# GROWTH AND CHARACTERISATION OF $Cu(In,Ga)Se_2$ THIN FILMS FOR SOLAR CELL APPLICATIONS

A thesis presented for the degree of

**DOCTOR OF PHILOSOPHY**

in the University of Salford

By

**Ejaz Ahmed**

Department of Electronic and Electrical Engineering
University of Salford, U.K.

1995

## Abstract

The development of low cost, efficient photovoltaic devices is a major technological challenge which demands suitable materials and fabrication processes. Thin film polycrystalline heterojunction solar cells appear to be most appropriate with respect to cost and ease of manufacture, and it is anticipated that the next generation of photovoltaic devices will be based entirely on thin film technologies.

Copper based ternary and multinary compounds are well established as exceptional semiconductors with potential applications in the fields of solar cells for both terrestrial and space applications, infra-red detectors, light emitting diodes etc. The chalcopyrite forms of these compounds have large absorption coefficients and exhibit superior radiation resistance. Among these compounds, $CuInSe_2$ (CIS) and $CuIn_{1-x}Ga_xSe_2$ (CIGS) have raised the most interest and recent thin film heterojunction photovoltaic devices based on these materials have achieved efficiencies of the order 15.5% and 16.9% respectively. The higher efficiencies realised in CIGS based devices is due to the fact that the band gap of the material can be adjusted towards the optimum value (1.45 eV) by the partial substitution of gallium for indium.

In this work, thin films of both CIS and CIGS were deposited onto glass substrates by flash evaporation of the respective pre-reacted source materials. The substrate temperature was varied between room temperature and 200°C. Two types of evaporation sources, a flat tungsten strip and a molybdenum twin chimney were used. The effect of the growth conditions on the film properties was observed. The structural, compositional and electro-optical properties were studied using a variety of analytical techniques

including x-ray diffraction (XRD), scanning electron microscopy (SEM), energy dispersive analysis with x-ray (EDAX), x-ray fluorescence (XRF), Rutherford backscattering spectroscopy (RBS), four point and thermal probe techniques, photoconductivity (PC) and photoacoustic spectroscopy (PAS).

The as-grown films were found to have a columnar structure and a strong preferred orientation with the <112> plane parallel to the substrate. Results from EDAX, XRF and RBS indicated that the as-grown films were slightly deficient in selenium, otherwise the composition was comparable with that of the starting polycrystalline material. Electrical measurements revealed both n- and p-type conductivities with resistivity values in the range $10^{-2}$ to $10^{6}$ Ωcm.

The as-grown films were subsequently processed under several sets of conditions including vacuum, selenium, inert and forming gas ambients at different temperature and times. A two stage post-deposition heat treatment of the films was developed to improve the composition and crystal structure and to optimise the electro-optical properties. It was observed that the first annealing stage (in a selenium ambient) produced an excellent improvement in the composition of the film. An increase in the film grain size (to > 2μm) was observed when the films were subsequently annealed in a forming gas ambient. Significant improvements were also observed in the optical properties.

The as-grown and annealed films were analysed using the PAS technique which revealed the existence of several donor and acceptor states originating from intrinsic defect levels. The results were compared with those obtained from single crystals. Photoconductivity measurements were also performed on the as-grown thin films.

## Table of contents

List of figures .......... i
List of tables .......... vii
List of symbols .......... ix
Acknowledgements .......... x

Chapter 1 Introduction

1.1 Introduction .......... 1
1.2 Photovoltaic materials .......... 1
1.3 Aims and objectives .......... 9
1.4 Preview of the thesis .......... 10

Chapter 2 Literature survey of Cu(In,Ga)Se2 thin films photovoltaic materials and their preparation techniques

2.1 Introduction .......... 13
2.2 $CuInSe_2$ .......... 14
2.2.1 Structural properties .......... 18
2.2.2 Electrical properties .......... 21
2.2.3 Optical properties .......... 23
2.2.4 Heterojunctions .......... 24
2.3 $CuGaSe_2$ .......... 25
2.3.1 Structural properties .......... 28
2.3.2 Optical properties .......... 29
2.3.3 Electrical properties .......... 30
2.3.4 Heterojunctions .......... 30
2.3.5 Photoconductivity .......... 31
2.4 $CuIn_{1-x}Ga_xSe_2$ .......... 32
2.4.1 Structural properties .......... 33
2.4.2 Electrical properties .......... 34
2.4.3 Optical properties .......... 34
2.4.4 Heterojunctions .......... 35
2.5 Post deposition processing .......... 35
2.6 Thin film deposition techniques .......... 37
2.6.1 Physical methods .......... 38
i) Flash evaporation .......... 38
ii) Single/double source evaporation .......... 39
iii) Co-evaporation technique .......... 39
iv) Electron beam evaporation .......... 40
v) Laser beam evaporation .......... 40
vi) Molecular beam epitaxy (MBE) .......... 41
vii) Sputtering process .......... 42

2.6.2 Chemical methods ........................... 42
i) Chemical vapour deposition (CVD) ........... 43
ii) Electrodeposition ........................ 44
iii) Chemical spray pyrolysis .................. 45
iv) Screen printing ......................... 45
2.7 Conclusions ................................. 46

Chapter 3 Experimental

3.1 Introduction ................................. 48
3.2 Preparation of stoichiometric mixture ............. 48
3.3 Flash evaporation system ....................... 51
3.3.1 Vacuum system ........................ 51
3.3.2 Working chamber ....................... 53
3.3.3 Control unit .......................... 53
3.3.4 Evaporation sources ..................... 55
3.3.5 Improvements made in the system ............ 55
3.4 Preparation of thin films ....................... 61
3.5 Post deposition heat treatments .................. 61
3.6 X-ray diffractometer .......................... 63
3.7 Raman scattering spectroscopy ................... 66
3.8 Rutherford backscattering spectroscopy ............ 69
3.9 Energy dispersive x-ray analysis (EDAX) ........... 71
3.10 X-ray fluorescence ........................... 74
3.11 Dektak measurements ......................... 75
3.12 Resistivity and carrier type measurements .......... 76
3.13 Photoconductivity system ....................... 81
3.14 Photoacoustic spectroscopy ...................... 86
3.15 Conclusions ................................. 88

Chapter 4 Effects of deposition parameters on the properties of as-grown thin films

4.1 Introduction ................................. 89
4.2 Investigation of the starting material .............. 90
4.2.1 $CuIn_{0.75}Ga_{0.25}Se_2$ ........................... 91
4.2.2 $CuInSe_2$ ............................... 97
4.3 Effect of source temperature .................... 102
4.4 Source geometry ............................ 113
4.5. Effect of substrate temperature .................. 119
4.5.1 X-ray diffraction analysis ................ 120
4.5.2 Raman spectroscopy ..................... 124
4.5.3 Scanning electron microscopy .............. 130
4.6 Depositions under optimised conditions ............ 134
4.6.1 Structural properties ..................... 135
XRD analysis ........................... 135

Scanning Electron Microscopy .................. 138
4.6.2 Compositional analysis .................. 140
X-ray fluorescence spectroscopy .................. 140
Energy dispersive x-ray analysis .................. 142
Rutherford backscattering spectroscopy .................. 147
4.6.3 Comparison of XRF, EDAX and RBS results .................. 153
4.7 Electrical Properties .................. 154
4.8 Conclusions .................. 157

Chapter 5 Effect of post-deposition annealing on the film properties

5.1 Introduction .................. 159
5.2 Structural properties .................. 160
5.2.1 X-ray diffraction analysis .................. 160
CIGS .................. 160
CIS .................. 167
5.2.2 Scanning electron microscopy .................. 170
5.2.3 Raman spectroscopy .................. 176
5.3 Compositional properties .................. 181
5.3.1 Energy dispersive x-ray analysis .................. 181
CIGS .................. 181
CIS .................. 183
5.3.2 Rutherford backscattering analysis .................. 185
5.4 Electrical properties .................. 191
5.5 Conclusions .................. 197

Chapter 6 Photoacoustic spectroscopy and Photoconductivity analysis

6.1 Introduction .................. 199
6.2 Photoacoustic Spectroscopy (PAS) .................. 200
6.2.1 The RG theory .................. 201
6.2.2 Determination of the absorption coefficient $\alpha$ .................. 206
6.2.3 Modifications to the standard PAS theories - applications to this work .................. 209
6.3 PAS experimental analysis and results .................. 215
6.3.1 The effect of annealing on the observed defect levels .................. 223
Selenium anneal .................. 223
Two stage anneal .................. 231
Laser anneal .................. 242
6.4 Effect of ion-implantation .................. 250
6.5 Transmission PAS analysis .................. 254
6.6 Photoconductivity analysis .................. 257
6.7 Conclusions .................. 271

Chapter 7 Summary and future work recommendations

7.1 Conclusions ........................................ 273
7.2 Future recommendations ................................ 276

References ................................................ 280
Appendices
Appendix A ................................................ 300
Appendix B ................................................ 301
Appendix C ................................................ 308

# List of figures


## Chapter 2

Figure 2.1: The tetragonal chalcopyrite structure illustrated for ternary and multinary compounds.

Figure 2.2: The pseudobinary phase diagram of the $Cu_2Se$-$In_2Se_3$ system [35].

Figure 2.3: The pseudobinary phase diagram of the $Cu_2Se$-$Ga_2Se_3$ system [115].

## Chapter 3

Figure 3.1: Schematic arrangement of the vacuum system.

Figure 3.2: Internal arrangement of the vacuum chamber.

Figure 3.3: Design of the molybdenum twin chimney evaporation source.

Figure 3.4: Design of the substrate holder/heater

Figure 3.5: Pyrex ampoule used for post-deposition annealing of thin films.

Figure 3.6: Schematic diagram of the x-ray diffractometer.

Figure 3.7: Block diagram of the Raman spectroscopy experimental.

Figure 3.8: Rutherford backscattering spectroscopy setup.

Figure 3.9: Thermal probe apparatus to measure the conductivity type of the sample.

Figure 3.10: Four point probe apparatus to measure the resistivity of the sample.

Figure 3.11: Correction divisor for probes on a thin film (non-conducting substrate).

Figure 3.12: Photoconductivity experimental setup.

Figure 3.13: Cross-sectional view of the cryostat used for low temperature photoconductivity measurements.

## Chapter 4

Figure 4.1: XRD spectrum of the polycrystalline $CuIn_{0.75}Ga_{0.25}Se_2$ pre-reacted starting material.

Figure 4.2: EDAX spectrum of the polycrystalline $CuIn_{0.75}Ga_{0.25}Se_2$ pre-reacted starting material.

Figure 4.3: XRD spectrum of the polycrystalline $CuInSe_2$ pre-reacted starting material.

Figure 4.4: EDAX spectrum of the polycrystalline $CuInSe_2$ pre-reacted starting material.

Figure 4.5: Effect of source temperature on the composition of polycrystalline CIGS thin films.

Figure 4.6: Different regions of indium, gallium and selenium curves exhibiting the behaviour of polycrystalline CIGS film composition with respect to source temperature.

Figure 4.7: Vapour pressure data of copper, indium, gallium and selenium [196].

Figure 4.8: Normalised concentration of copper, indium, gallium and selenium in CIGS thin films against the normalised temperature (Normalisation temperature for; copper - 1150°C; indium - 1300°C; gallium - 1200°C and selenium - 1200°C) to indicate the dilution effect.

Figure 4.9: Surface roughness (Ra=214Å) of polycrystalline CIGS thin film sample prepared by flat strip tungsten source.

Figure 4.10: Surface roughness (Ra=12Å) of polycrystalline CIGS thin film sample prepared by twin chimney molybdenum source.

Figure 4.11: Thickness profile of the polycrystalline CIGS thin film measured by Dektak.

Figure 4.12: X-ray diffraction spectra of CIGS films deposited at different substrate temperatures.

Figure 4.13: Raman spectra of CIGS thin films deposited at 200°C (a), at 100°C (b), at room temperature (c) and standard CIGS single crystal (d).

Figure 4.14: Effect of film composition on the Raman spectra of CIGS samples.

Figure 4.15: Scanning electron micrographs of CIGS films deposited at substrate temperature of 200°C (a), at 100°C (b) and at Room temperature (c).

Figure 4.16: Nucleation and physical film growth process.

Figure 4.17: Representative x-ray diffraction spectra of three CIGS thin films prepared under optimised deposition conditions.

Figure 4.18: Representative x-ray diffraction spectra of three CIS thin films prepared under optimised deposition conditions.

Figure 4.19: Scanning electron micrographs of CIGS (a) and CIS (b) thin films prepared under optimised deposition conditions.

Figure 4.20: Weight percent of elements in polycrystalline CIGS films as measured by XRF technique.

Figure 4.21: Weight percent of elements in polycrystalline CIGS films as measured by EDAX technique.

Figure 4.22: Compositional triangle of CIGS and CIS thin films measured by EDAX technique; filled circles (CIGS thin films), filled square (CIGS source material), empty circles (CIS thin films) and empty square (CIS source material).

Figure 4.23: EDAX spectrum of the polycrystalline CIGS thin film.

Figure 4.24: EDAX spectrum of the polycrystalline CIS thin film.

Figure 4.25: Measured and calculated RBS spectra of CIGS thin film.

Figure 4.26: Effect of thickness on the RBS spectrum of CIGS thin films.

Figure 4.27: Effect of thickness on the RBS spectrum of CIS thin films.

**Chapter 5**

Figure 5.1: XRD spectra of CIGS thin films; (a) vacuum annealed at 300°C for one hour, (b) the as-grown.

Figure 5.2: XRD spectra of CIGS thin films; (a) annealed in selenium at 300°C for two hours, (b) $N_2$:$H_2$ annealed at 300°C for 2 hours and (c) the as-grown.

Figure 5.3: XRD spectra of CIGS thin films; (a) selenium annealed at 300°C for two hours + argon annealed at 300°C for half hour, (b) selenium annealed at 300°C for two hours + $N_2$:$H_2$ annealed at 300°C for half hour and (c) the as-grown.

Figure 5.4: XRD spectra of CIS thin films; (a) selenium annealed at 300°C for two hours + $N_2$:$H_2$ annealed at 300°C for two hours and (b) the as-grown.

Figure 5.5: Scanning electron micrographs of CIGS thin films annealed in selenium a) at 400°C, b) at 300°C and c) at 250°C for two hours.

Figure 5.6: Scanning electron micrographs of CIGS thin films; (a) annealed under 9:1 mixture of $N_2$:$H_2$ ambient at 300°C for two hours and (b) at 300°C for one hour.

Figure 5.7: Scanning electron micrographs of CIGS thin films; (a) selenium annealed at 300°C for two hours + $N_2$:$H_2$ annealed at 300°C for two hours in a infra-red heater, (b) in a constant resistive heater at 300°C for two hours and (c) the as-grown.

Figure 5.8: Scanning electron micrographs of CIS thin films; (a) selenium annealed at 300°C for two hours + $N_2$:$H_2$ annealed at 300°C for two hours, (b) selenium annealed at 300°C for two hours and (c) the as-grown.

Figure 5.9: Raman spectra of CIGS thin films; (a) selenium annealed at 300°C for two hours and (b) the as-grown.

Figure 5.10: Raman spectra of CIGS thin films; (a) selenium at 300°C for two hours + $N_2$:$H_2$ annealed at 300°C for two hours, (b) the as-grown and (c) a standard CIGS single crystal.

Figure 5.11: Raman spectra of CIGS thin films; (a) $N_2$:$H_2$ annealed at 200°C for two hours, (b) selenium annealed at 300°C for two hours + $N_2$:$H_2$ annealed at 300°C for two hours and (c) a standard CIGS single crystal.

Figure 5.12: Compositional triangle for CIGS thin films; (a) the as-grown, (b) vacuum annealed at 300°C for one hour, (c) annealed under selenium ambient at 300°C for two hours, (d) two stage annealed at 300°C for two hours and (e) annealed under $N_2$:$H_2$ ambient at 300°C for two hours.

Figure 5.13: RBS spectra of CIGS thin films before and after vacuum anneal at 300°C for one hour.

Figure 5.14: RBS spectra of CIGS thin films; the as-grown (full line), annealed under 9:1 mixture of $N_2$:$H_2$ (dashed line) and annealed under selenium ambient (dotted line) at 300°C for two hours.

Figure 5.15: RBS spectra of CIGS thin films annealed under selenium ambient at 300°C for two hours followed by an anneal in 9:1 mixture of $N_2$:$H_2$ (dotted line) or argon (dashed line) at 300°C for half an hour.

Figure 5.16: RBS spectra of CIS thin films annealed under selenium ambient at 300°C for two hours followed by an anneal in $N_2$:$H_2$ ambient at 300°C for one hour.

Figure 5.17: Resistivity against the annealing temperature for CIGS film annealed under selenium ambient.

Figure 5.18: Log of resistivity against the annealing temperature for CIGS film annealed under selenium ambient.

**Chapter 6**

Figure 6.1: Schematic of a standard photoacoustic spectrometer cell [233].

Figure 6.2: Dependence of the absorption coefficient $\alpha$ on the normalised photoacoustic amplitude signal Q; ■ - present work, ▲ - [240] and o - [241].

Figure 6.3: The effect of interference from a two layer structure (CIGS thin film deposited onto molybdenum coated glass substrate).

Figure 6.4: Comparative room temperature normalised photoacoustic amplitude signal from p-type CIGS thin film and a specimen of un-coated glass slide.

Figure 6.5: Normalised photoacoustic spectra for three representative polycrystalline as-grown CIGS thin films.

Figure 6.6: Semi logarithmic plot of the absorption coefficient as a function of photon energy.

Figure 6.7: Plot of $(\alpha h\nu)^2$ against the photon energy to calculate the band gap of the as-grown polycrystalline CIGS thin films.

Figure 6.8: Photoacoustic spectra of the as-grown and selenium annealed at 300°C for two hours CIGS thin films.

Figure 6.9: Photoacoustic spectra of p-type single crystal and selenium annealed polycrystalline thin film of CIGS.

Figure 6.10: Semi logarithmic plot of the absorption coefficient as a function of photon energy (0.9 eV to 1.3 eV) for a selenium annealed CIGS thin film.

Figure 6.11: Spectral response of the absorption coefficient in the tail of the spectra (0.7 eV to 1.0 eV) exhibiting the deeper state transitions.

Figure 6.12: Plot of $(\alpha h\nu)^2$ against the photon energy to calculate the band gap of the selenium annealed polycrystalline CIGS thin films.

Figure 6.13: Comparative plots of the spectral distribution of CIGS thin films annealed under selenium and $N_2$:$H_2$ (FG) ambient at different temperatures.

Figure 6.14: Comparative plots of the spectral distribution of CIGS thin films annealed under selenium and argon ambient at different temperatures.

Figure 6.15: Comparative plots of the absorption coefficient of CIGS thin films annealed under selenium and argon ambient at different temperatures.

Figure 6.16: Plot of $(\alpha h\nu)^2$ against the photon energy to calculate the band gap of selenium and argon annealed polycrystalline CIGS thin films.

Figure 6.17: Normalised photoacoustic spectrum of selenium annealed CIGS thin film in the photon energy range between 0.7 eV to 3.1 eV.

Figure 6.18: Comparative plot of the normalised photoacoustic amplitude signal for polycrystalline CIS thin films before and after laser annealing.

Figure 6.19: Comparative plot of the absorption coefficient of a single crystal (a), polycrystalline CIS thin film before (c) and after laser annealing (b).

Figure 6.20: Plot of $(\alpha h\nu)^2$ against the photon energy to calculate the band gap of CIS thin films before and after laser annealing.

Figure 6.21: Comparative plots of the spectral distribution of CIGS thin films annealed under $N_2$:$H_2$ (FG) ambient at 400°C and $H^+$ implanted.

Figure 6.22: Comparative plots of the spectral distribution of CIGS thin films annealed under argon ambient at 400°C and $H^+$ implanted.

Figure 6.23: Transmission photoacoustic spectra of un-coated glass slide and the as-grown CIGS thin film.

Figure 6.24: Photoconductivity spectrum of n-type CIS single crystal.

Figure 6.25: Photoconductivity spectrum of n-type CIS single crystal.

Figure 6.26: Photoconductivity spectrum of p-type CIS single crystal.

Figure 6.27: Photoconductivity spectrum of p-type CIS thin film.

Figure 6.28: Photoconductivity spectrum of p-type CIGS thin film measured at room temperature.

Figure 6.29: Photoconductivity spectrum of p-type CIGS thin film measured at 250°K.

Figure 6.30: Photoconductivity spectrum of p-type CIGS thin film measured at 150°K.

Figure 6.31: Photoconductivity spectrum of p-type CIGS thin film measured at 77°K.

Figure 6.32: Photoconductivity spectral distribution of CIGS single crystal using the photoacoustic spectrometer.

# List of tables

Table 2.1: Physical and electro-optical properties of $CuInSe_2$ semiconducting compound.

Table 2.2: Properties of $CuGaSe_2$ semiconducting compound.

Table 3.1: A calibration table to obtain an accurate estimate of the evaporation temperature.

Table 4.1: X-ray powder diffraction data of CIGS pre-reacted starting material.

Table 4.2: EDAX compositional analysis of CIGS pre-reacted starting material.

Table 4.3: X-ray powder diffraction data of CIS pre-reacted starting material.

Table 4.4: EDAX compositional analysis of CIS pre-reacted starting material.

Table 4.5: Enthalpies and Gibb's free energies [197].

Table 4.6: Comparison of the surface roughness of CIGS thin films prepared by flat strip type tungsten source and twin chimney type molybdenum source.

Table 4.7: Comparative analysis of the structural properties of $Cu(In,Ga)Se_2$ thin films using XRD technique.

Table 4.8: Comparative compositional analysis of CIGS thin films using EDAX, XRF and RBS techniques.

Table 4.9: Electrical properties of flash evaporated CIGS and CIS thin films.

Table 5.1: Comparison of the x-ray powder diffraction data of the polycrystalline pre-reacted starting material and CIGS thin films.

Table 5.2: Comparison of the x-ray powder diffraction data of the polycrystalline pre-reacted starting material and CIS thin films.

Table 5.3: Compositional analysis of the as-grown, annealed under selenium ambient and two stage annealed thin films of CIS.

Table 5.4: Electrical properties of CIS thin films before and after annealing under selenium ambient at 300°C for two hours followed by an anneal under $N_2$:$H_2$ ambient at 300°C for two hours.

Table 6.1: The gap energy and the ionisation energies of the defect levels of the as-grown and annealed (under different ambient and temperatures) CIGS thin films.

Table 6.2: Energy band gap values of annealed (under different ambient and temperatures) thin films of CIGS at different modulating frequencies.

Table 6.3: The fundamental energy band gap $E_g$ and different defect ionization energies ($E_1$ - $E_5$) of p-type CIS single crystal and thin films as determined by photoacoustic spectroscopy.

## List of symbols

$I_o$ : Incident monochromatic light flux
$\alpha$ : Absorption coefficient
h : Planck's constant
$\nu$ : Frequency of light
$h\nu$ : Photon energy
$\lambda$ : Wavelength of the incident light
f : Chopping/Modulating frequency
$\omega$ : Radian frequency
$T_o$ : Ambient temperature
$l_s$ : Thickness of the sample
$l_g$ : Thickness of the gas column
$l_b$ : Thickness of the backing material
$\varrho_j$ : Density of material j
$C_j$ : Specific heat of material j
$\phi_j$ : Temperature of medium j
$\beta_j$ : Thermal diffusivity of material j
$\varkappa_j$ : Thermal conductivity of material j
$a_j$ : Thermal diffusion coefficient of material j
$\mu_j$ : Thermal diffusion length of material j
$P_g$ : Photoacoustic amplitude signal
g : Ratio of thermal conductivity & diffusivity of gas and sample
b : Ratio of thermal conductivity & diffusivity of backing material & sample
R : Reflectance from the gas to the sample
$R_b$ : Reflectance from the sample to the backing material
q : Normalised photoacoustic amplitude signal
$\eta$ : Non-radiative quantum efficiency

# Acknowledgements

The author wishes to thank Dr. A.E. Hill for his invaluable guidance and supervision given throughout this work. Special thanks are due to Dr. R.D. Tomlinson and Dr. A. Zegadi for their helpful suggestions, advice, help and encouragements.

My sincere thanks goes to Dr. R.D. Pilkington for his great help and moral support during the period of this work. Many thanks are due to Professor H. Neumann for his informative discussions on my research topic, and to Professor S Leppävuori of the University of Oulu, Finland for organising the Raman analysis.

It is a great pleasure to acknowledge the valuable technical advice, assistance and friendship that I have had from Mr. J.J. Smith, Mr. E. Brimble, Mr. K. Bullock and Mr. P. Cardwell.

I am also extremely grateful to the Ministry of Education, Government of the Islamic Republic of Pakistan for awarding me the Central Overseas Training scholarship and the Bahauddin Zakariya University, Multan, Pakistan for granting me study leave. Without their support none of this work would have been possible.

# Chapter 1

# Introduction

## 1.1 Introduction

Shortly after the discovery of photovoltaic effect in single crystal Silicon p-n junction [1] and CdS-Cu schottky barriers [2] in mid 1950's, the replacement of fossil energy resources seemed feasible and highly attractive [3]. Considerable research efforts started worldwide and led to a large number of relevant publications. It therefore appears highly likely that major advances will be made by the use of new advanced materials and processes. A number of materials such as copper (I) sulphide, silicon, gallium arsenide, cadmium telluride and copper indium gallium diselenide, are being studied for the efficient harnessing of solar energy through solid state solar cells in an cost effective manner [3].

The aim of this chapter is to describe briefly the historical development of photovoltaic materials. The most promising of these materials are compared in terms of their properties and applications. The aims and objectives and a brief introduction of this thesis are outlined in the last section of this chapter.

## 1.2 Photovoltaic materials

The sun has always been the main source of energy for life on earth. However, it is only during the last two decades that man has learned to convert solar radiations directly into electrical energy with a reasonable degree of efficiency. The efforts that went into space technology led to an intensified and systematic development of photovoltaic power

generation. The present technological level of this type of power generation reflects the high requirements of space technology. The ever increasing scope of space-craft missions, satellite power and life, necessitates further development. In addition, the terrestrial applications of solar energy have become increasingly more important throughout the world which has given further impetus to research and development in this area.

The limited resources of the earth has forced man to search for and develop new sources of energy. Photovoltaic power generation is one attractive alternative way to produce energy. A major advantage of solar energy is that it is renewable and, unlike fossil fuels, will not run out. Solar energy is also a much cleaner and non-polluting source of power as it does not have any dangerous by-products. Since the amount of energy that reaches the earth surface is approximately 10,000 times than that of it's total energy consumption, the global potential for solar energy is large and rapidly growing due to our ability to harness it efficiently.

Photovoltaic conversion systems require special forms of semiconductor materials or compounds which can be fabricated to contain a junction or interface with the necessary electronic characteristics. In general, when light penetrates into the material, it is absorbed and generates free electrical charges. As these charges drift across the junction they are collected by contacts applied to the exterior surface of the semiconductor and thus produce a current. By combining a number of solar cells in an appropriate way it is possible to develop power sources of various capacities. The generation of photovoltaic power depends upon the employment of solar photons for the production

of electrons and holes. This can be most readily done by the absorption of solar radiation in a suitable semiconducting material. Since the solar photons have specific energies the efficient creation of electron-hole pair is thus highly dependent on the type of materials employed and their properties.

A material is considered to be suitable for use as an absorber layer in photovoltaic devices if it has the following properties:

* direct band gap
* high absorption coefficient
* few and inactive grain boundaries
* good mobility and minority carrier life time
* long term stability i.e. radiation resistant

For practical purposes the availability of suitable materials for large area deposition with high throughput and high material yield on inexpensive substrates must also be considered. Many materials and processes are being studied in order to fulfil these important objectives [3].

Solar cells have been mainly developed in either single crystal or thin film form. Although single crystal solar cells of Silicon (Si) and Gallium Arsenide (GaAs) have achieved high conversion efficiencies, their production costs are still very high and with existing technologies it is difficult to achieve further cost reductions. The effects of radiation [4,5] and ambient temperature [6] on the device properties showed these

materials to be highly susceptible with their conversion efficiencies degrading with time. Alternatively, thin film technologies offer an important option for low cost devices and have recently become the focus of increased attention [7]. Considerable progress has been made with respect to high conversion efficiencies and low cost manufacturing. Furthermore, thin film solar cells have exceptionally high radiation tolerances when compared to conventional single crystal cells [4].

General analysis shows that there is a range (1.15 eV to 1.4 eV) of optimum energy band gaps for photovoltaic conversion [8]. Although, the band gap of silicon lies at 1.12eV, just below the optimum band gaps range. However, a large amount of research work done on this material has resulted in a large conversion efficiencies [9]. A major disadvantage for photovoltaic use is that the band gap in silicon is indirect. To excite an electron from the valence band of silicon to the conduction band both the energy and momentum must be changed. Since sunlight supplies only the required energy the momentum change must originate from the lattice vibrations (phonons). Due to the need for both a photon and phonon to be involved, the absorption of light in silicon is therefore much weaker than in direct band gap semiconductor materials such as gallium arsenide [10].

Thin film polycrystalline silicon is used for low cost solar cells. However there is a need for further development in order to improve it's stability and conversion efficiencies. The main advantages of thin film solar cells comes from the lower production costs, the potential for higher conversion efficiencies and a reduction in the material requirements compared to single crystal based devices [7]. The use of polycrystalline silicon for solar

cells offers the potential for high performance in conjunction with low cost manufacturing. However, both theoretical and experimental investigations [11] have identified issues of grain size and film thickness as limiting factors and further work on these and back-surface passivation is necessary to raise this technology to the next technological level.

Initial research [12] reported that amorphous silicon, when deposited by vacuum evaporation or sputtering, showed a high degree of conformational disorder with a large number of unsaturated dangling bonds which affect the electronic properties due to electrically inactive dopants. However, in 1972, Spear [13] used hydrogen during the deposition process, saturating most of the dangling bonds producing hydrogenated amorphous silicon with good electronic properties. The effective band gap of this material can be varied, depending on the deposition parameters, within a range of about 1.6 - 1.7 eV. It can further be tailored, by the addition of carbon to raise, germanium or tin to reduce, the band gap. However, the resultant performance of the devices based on these materials was poor compared to that of pure a-Si. Band gap engineering is thus the key to optimising the devices fabricated. To date glow-discharge techniques have produced the most efficient devices with conversion efficiencies of about 13% [14].

A significant difficulty with a-Si solar cell technology is that it suffers from an intrinsic degradation effect [4]. The first generation a-Si modules experienced about 20% degradation in peak power over two years of exposure to light [4]. The most recent a-Si solar cells are more stable, but still experience a 10-15% loss of performance [4]. Further improvements and better understanding of the physics of these devices are

necessary in order to reduce this degradation effect.

For many years copper (I) sulphide was known to be one of the most suitable material for hetero-junction solar cells [3]. From the late 1950's, for almost two decades, the only available all thin film solar cells were p-$Cu_2S$/n-CdS [3]. The $Cu_2S$ was prepared with reasonable electronic properties using simple preparation technologies such as thermal evaporation, sputtering, sintering, spraying, etc. However, all these processes have failed to achieve the desired conversion efficiencies. Only the topotaxial processes [3] based on ion exchange reactions were successful in the production of $Cu_2S$ layers with high cell efficiencies. Simple heat processing in various atmospheres and several other treatments had also resulted in significant improvements in the performance of these devices. Further details and the historical developments of this type of hetero-junction devices can be found in various articles [3,15,16].

During the development of $Cu_2S$/CdS thin film solar cells, a number of degradation problems [3] were observed due to the complex nature of this type of device. These included:

(i) The interface between two materials with different electron affinities, band gaps and crystal structures.

(ii) The lattice mismatch and the inter-diffusion of components, in particular copper, resulting in defect states at or near the interface.

(iii) A variety of $Cu_2S$ phases at room temperature.

(iv) Interface roughness, grain boundaries and random crystal orientation.

Due to limited efficiency poor reproducibility and long term instability, minimal work on the development of this type of device has been carried out.

Thin film solar cell devices based on II-VI and I-III-$VI_2$ compounds are currently being studied extensively [17] and have the following advantageous properties:

* Direct band gap
* High optical absorption coefficient.
* Moderate surface recombination velocities.
* Radiation hardness.
* Low cost.

For example, CdTe as an absorber material in thin film photovoltaic devices offers significant advantages due to its optimal direct band gap value of 1.45 eV. Since this material can be doped p- or n-type there is the possibility of forming homo-junctions. However hetero-junctions are generally used for solar cells. A wide variety of thin film deposition techniques including vacuum processes, screen printing, chemical vapour deposition and electrodeposition have been utilised for the preparation of this material [17]. All of these processes typically require a high temperature step at 400-450°C [18] to achieve the desired material properties.

Of considerable interest are two problems which are particularly relevant in preparing these devices i.e. CdTe doping and suitable ohmic contacts [19]. Various solutions to the doping problem have been proposed including ion assisted doping by PVD, arsenic

CVD and diffusion of copper [19]. The ohmic contact problem can be overcome by using semi-metal HgTe as a contact material or by considering mixed ternary alloys of HgCdTe for which preparation of ohmic contacts is easier than CdTe [4].

Other materials which are being extensively studied for use as absorber layers in thin film photovoltaic devices are copper based ternary and multinary compounds [7].

Copper Indium Diselenide ($CuInSe_2$) is a member of the I-III-$VI_2$ semiconductor family with a chalcopyrite structure and a direct energy band gap of approximately 1.02 eV, at 300°K [20]. Its excellent thermal stability, radiation hardness and high optical absorption coefficient make it an ideal candidate material in efficient and low cost thin film solar cells for both single and tandem junctions [21]. Solar cells based on vacuum evaporated CIS films have been fabricated with a conversion efficiency of more than 16% [22]. The main limits to CIS based device efficiency are reproducibility, large area uniformity and the slightly less than optimum band gap. However, research is in progress to improve the efficiencies of the devices by improving the uniformity and developing better deposition techniques.

Copper gallium diselenide ($CuGaSe_2$, CGS) is another member of the I-III-$VI_2$ semiconductor family and has very similar properties to CIS in terms of structural and electrical behaviour. It has a direct band gap of 1.68 eV [23], slightly higher than the optimum value. Cell efficiencies better than 6% have been reached for $CuGaSe_2$/(Cd Zn)S structures [24].

Thin film polycrystalline solar cells based on the ternary chalcopyrite compounds CIS and CGS have shown good photovoltaic properties. However, the fundamental limit on the efficiency of $CuInSe_2$ based solar cells is the small open circuit voltage due to the band gap value (1.02 eV) of the absorber layer, the optimum value being ≈ 1.5 eV. The band gap of CIS can be adjusted towards the optimum value by the partial substitution of Gallium for Indium. The band gap of the resultant $CuIn_{1-x}Ga_xSe_2$ (CIGS) can be increased continuously from 1.02 eV (for pure CIS) to 1.68 eV (for pure CGS) by varying 'x' between zero and one [25]. Hetero-junctions with (Zn,Cd)S as a window material have yielded more than 16% efficient cells [22].

## 1.3 Aims and objectives

Although, the I-III-$VI_2$ family of semiconducting compound appear to be a promising candidate for use in optoelectronic devices, there are some members of this family, such as $CuIn_{1-x}Ga_xSe_2$, for which the information concerning the electro-optical properties is scarce. In addition, these properties are highly dependent on their structure and composition, which in turn are strongly related to the film growth parameters. Therefore, the choice of the processing approach is very important to obtain compound films with good properties. A number of deposition techniques have been used in order to produce thin films of these materials. Whilst these have generated a great deal of scientific information none of the technologies employed have been widely accepted due to problems associated with stoichiometric non-uniformities and poor reproducibility. Initial studies have shown flash evaporation to be a technique with potential for producing

stoichiometric films of CIS and has been the subject of this investigation.

The objectives of the present work can be summarised as follows:

1. To investigate and develop the flash evaporation system to deposit reproducibly good quality CIS and CIGS films suitable for use in solar cells.
2. To obtain a better fundamental understanding of the effect of deposition parameters on the properties of thin films.
3. To characterise fully the compositional, structural and electro-optical properties using a variety of techniques.
4. To improve the reproducibility by optimising the deposition conditions.
5. To study and optimise the properties of thin films by the use of various post deposition processes.
6. To study the defect chemistry using optical techniques such as photoconductivity and photoacoustic spectroscopy.
7. To assess CIS and CIGS film properties required for the future fabrication of solar cells.

## 1.4 Preview of the thesis

Many advances in the technology of semiconductor devices were made possible by fundamental research concerned with both qualitative and quantitative descriptions of the physical and chemical phenomena in the semiconducting materials for their

photovoltaic applications. The use of materials, such as $Cu(In,Ga)Se_2$, in device technology provide motivation as well as a basic frame work for the investigation of many research problems. Extensive basic and applied research on $Cu(In,Ga)Se_2$, both in thin film and single crystal form, have shown a considerable potential for success. However, there is a need for further investigations in order to gain a better understanding of the fundamental properties.

Chapter 2 highlights existing research literature of $Cu(In,Ga)Se_2$ ternary and quaternary chalcopyrite semiconducting compounds followed by the review of some of the more frequently employed deposition techniques used for the growth of this material in thin film form. There have been a number of perspectives employed by different researchers towards the ultimate objective of understanding the properties of this material. This chapter reviews the research by dividing the discussion into structural, electrical and optical properties and application of the materials in device preparation. Thin film deposition technologies are considered with respect to their use for the deposition of copper based ternary and quaternary compounds.

Chapter 3 gives a survey of the experimental techniques for the measurement of different properties of thin films along with the preparation of pre-reacted starting material and the experimental apparatus for the deposition of $Cu(In,Ga)Se_2$ thin films. The modifications made in the experimental system have also been considered. The analyzing techniques are explained in terms of their working principle preceded by a brief introduction about the technique.

A major consideration for most deposition processes is the effects of deposition parameters on the film properties. Therefore, the effects of deposition parameters such as source temperature, substrate temperature, source to substrate distance and source design, on the properties of deposited thin films are considered in chapter 4. The results obtained are explained in view of the existing literature.

In many cases thin film properties can be tailored to achieve the required specifications for solar cells and this therefore merits investigation. Chapter 5 discusses the effect of post deposition heat treatments on the properties of thin films. The film's characteristics are compared with respect to the different ambients under which post deposition heat treatments are carried out. Results are explained by considering different mechanisms.

Chapter 6 is devoted to the photoconductivity and photoacoustic studies on both the as-grown and annealed thin films. The mathematical analysis for the determination of carrier life time in photoconductivity measurements and the absorption coefficient and band gap calculations used in photoacoustic analysis is also considered.

Finally, conclusions and future work recommendations are considered in chapter 7.

# Chapter 2

# Literature survey of Cu(In,Ga)Se2 thin films photovoltaic materials and their preparation techniques

## 2.1 Introduction

The potential of the ternary and multinary family of compound semiconductor materials, such as CIS, CGS and CIGS, for use in various electronic devices continues to attract an increasing amount of interest. This has led to an extensive study of the growth and characterisation of these materials both in thin film and single crystal forms. Compound semiconductors have become leading candidates amongst photovoltaic materials because a wide range of physical, optical and electrical properties can be achieved compared to elemental materials. However, for cost effectiveness and high throughput required for large scale and large area production, the preparation of these materials in thin film form is necessary. It is generally accepted, therefore, that the next generation of high quality, low cost photovoltaic devices will be based largely on current and future developments in thin film technologies.

The purpose of this chapter is to review relevant existing literature on copper based ternary and multinary compounds. The first section describes important work on the structural, electrical and optical properties of CIS, CGS and CIGS thin film materials along with their applications in heterojunctions. The deposition techniques used in the preparation of these thin film photovoltaic materials are also considered in the last section.

## 2.2 $CuInSe_2$

CIS, one of many I-III-$VI_2$ ternary semiconducting compounds, was first reported by Hahn et al. [26] and later studied by Tomlinson [27,28]. This material crystallises in a chalcopyrite structure [29] which has a diamond like lattice with a face centred tetragonal unit cell (space group I42d). The chalcopyrite structure is a super-structure of sphalerite (see figure 2.1), which arises from the ordered substitution of the zincblende lattice, resulting in the doubling of the c-axis [29]. The lattice structure of chalcopyrite CIS is shown in figure 2.1. The detailed calculations of the lattice gave values of a = 5.782Å and c = 11.621Å [30].

In general, vacuum evaporation of many compounds, alloys and mixtures is a difficult process requiring a careful consideration of factors effecting their dissociation, which can take place below their melting points. Thus the condensate does not necessarily have the same composition as that of the source material. Many workers [31,32] have observed this dissociation in the deposition of CIS. Partial vapour pressures of $In_2Se$ and $Se_2$ in the temperature range 900-1160°K using a mass spectrometer have been measured [33]. Thermal dissociation [34] can thus occur via the following route:

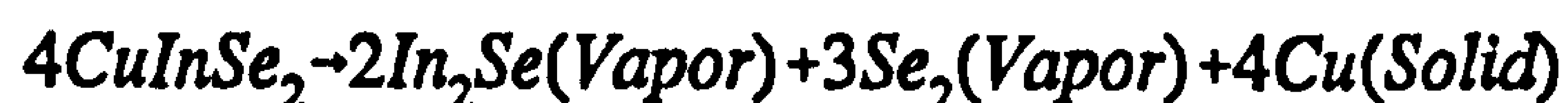

$$4CuInSe_2 \rightarrow 2In_2Se(Vapor) + 3Se_2(Vapor) + 4Cu(Solid)$$

The pseudobinary phase diagram [35] of Cu-In-Se is shown in figure 2.2. This shows that CIS melts congruently at 986°C. Above 810°C, CIS lies in the δ-phase and crystallizes with the sphalerite structure, while below 810°C, it lies in the γ-phase and crystallises with the chalcopyrite structure. During the transformation from sphalerite to

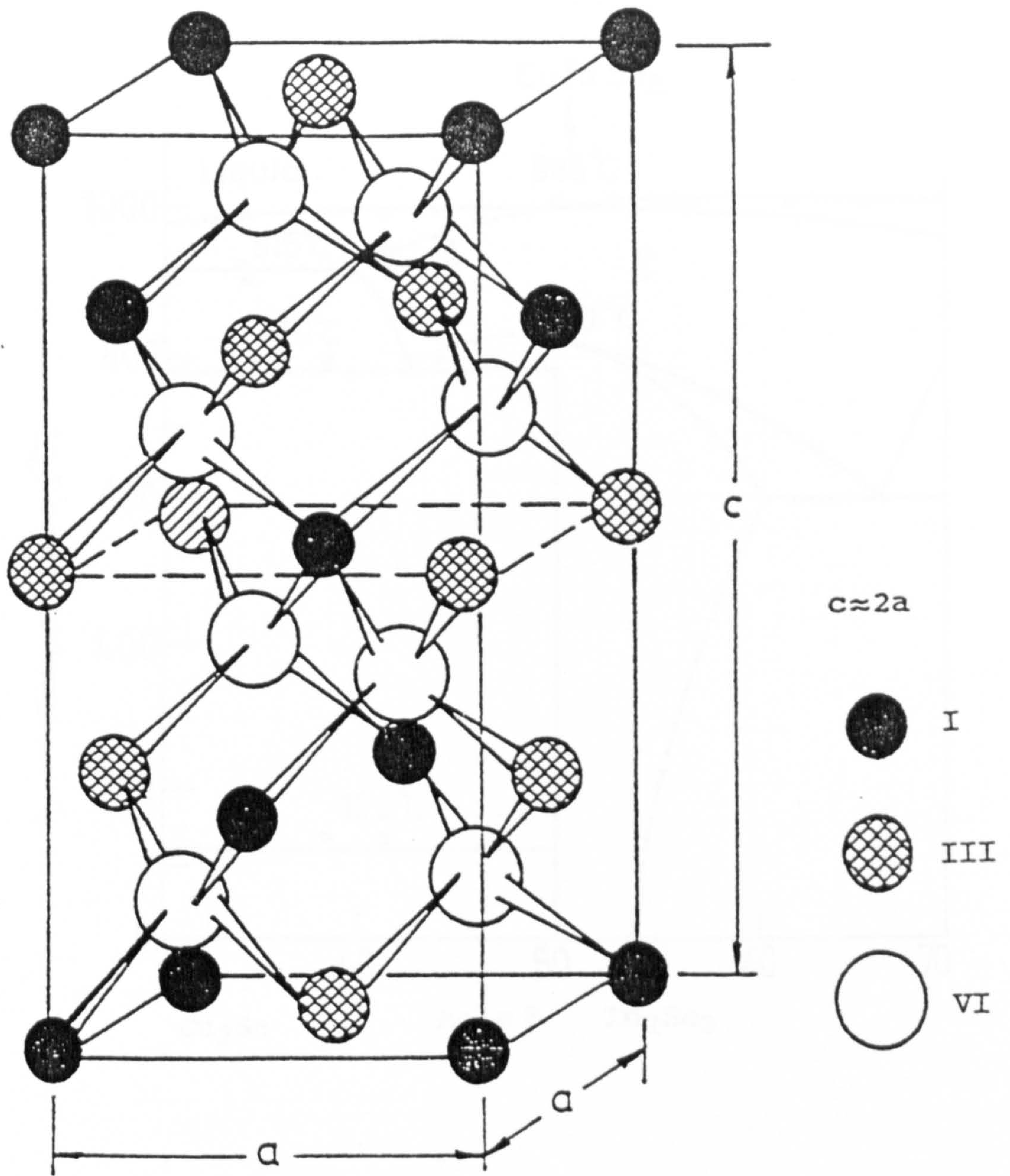


Figure 2.1: The tetragonal chalcopyrite structure illustrated for ternary and multinary comounds.

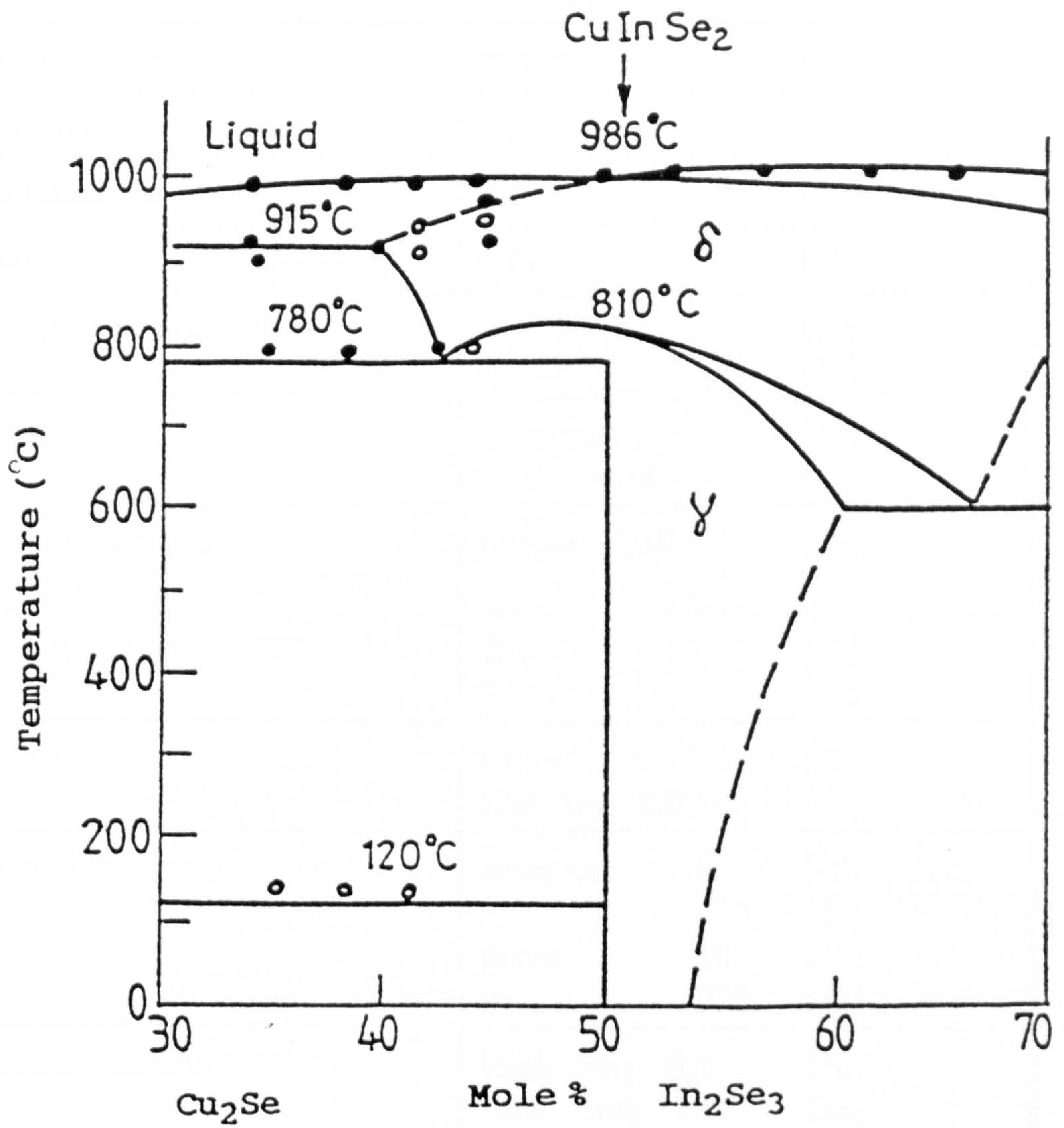


Figure 2.2: The pseudobinary phase diagram of the $Cu_2Se$-$In_2Se_3$ system [35].

| Formula | | $CuInSe_2$ | |
|---|---|---|---|
| Molecular weight | | 336.28 | [36] |
| Melting point | (°C) | 986 | [37] |
| Phase transition | (°C) | 810 | [37] |
| Density | (gm $cm^{-3}$) | 5.77 | [38] |
| Lattice parameters | (Å) | a=5.782<br>c=11.620 | [30]<br>[30] |
| Symmetry | | Sphalerite<br>Chalcopyrite | [39]<br>[36] |
| Thermal expansion coefficient | (at 273°K) | (7.89-8.32)10 | [40] |
| Deby temperature | (°K) | 207<br>221.9 | [41]<br>[42] |
| Effective mass | | Holes 0.73 $m_e$<br>Electrons 0.09 $m_e$ | [43]<br>[43] |
| Ionization energy | (meV) | acceptor 85<br>400<br>donor 10<br>225 | [44]<br>[45]<br>[45]<br>[45] |
| Dielectric constant | | High freq. 8.1<br>Low freq. 13.6 | [36]<br>[36] |
| Refractive index | | 2.7-3.0 | [46] |
| Thermal conductivity | (mW/Cm-K) | 86 | [47] |
| Electron affinity | (eV) | 3.97 | [36] |
| Mobility | ($cm^2$/V.s) | electrons 800<br>holes 20 | [48]<br>[49] |
| Conductivity type | | both n- and p-type | [50] |
| Band gap | (eV) | 1.02 ± 0.01<br>1.03 n-type crystal<br>1.04 n-type film | [49,51,52-54]<br>[55]<br>[56] |

Table 2.1: Physical and electro-optical properties of $CuInSe_2$ semiconducting compound.

chalcopyrite, high cooling rates lead to micro-cracking due to thermal stresses and/or different expansion coefficient. Table 2.1 summarises some measured and estimated properties of CIS.

### 2.2.1 Structural properties

Researchers at Salford University [57] reported the preparation of the first CIS thin films by the flash evaporation method. Since then the technique has been used widely [58-61]. A systematic study of the effect of source temperature on the composition of $CuInSe_2$ thin films has been carried out [62]. These films were copper deficient at source temperatures below 1200°C. Comparable thin film composition to that of bulk material was realised at source temperatures greater than 1300°C. This was later confirmed by Neumann et al. [63] and Hanemann et al. [64]. The effect of substrate temperature (27-500°C) on the elemental composition of flash evaporated thin films was examined [65]. Nearly stoichiometric films were obtained at 447°C. Both lower and higher substrate temperatures resulted in depleted and enriched copper content respectively. Copper deficiency could be due to the reported source temperature just under 1300°C. This temperature value is on the bottom edge of the source temperature range reported by Tomlinson et al [62]. On the other hand, higher substrate temperatures resulted in enriched copper samples (deficient in indium and selenium) which could be due to the re-evaporation of In-Se compound.

Deposition of the first amorphous thin films with thicknesses in the range of 200-1000Å

was reported in 1980 [66]. A vibrating hopper and resistively heated tantalum source were used in order to deposit thin films onto glass substrates at 77°K. X-ray analysis confirmed the amorphous nature of the deposited films since no preferred crystalline direction was observed. Rutherford backscattering spectroscopy (RBS) confirmed the films to be copper deficient.

Dissociation and decomposition of compounds and alloy evaporants made the single source evaporation technique very difficult for thin film deposition of $Cu(In,Ga)Se_2$ [67,68]. However, some researchers [69,70] have reported successful growth of CIS by this technique. Single phase films were obtained at a substrate temperature of 500°K. X-ray and electron diffraction analysis of the films showed a preferred orientation dependent on substrate temperature and thickness [69]. The loss of selenium (the most volatile element in CIS) was compensated for either by using an additional selenium source [71] or by using excess elemental selenium in the source material [72,73].

Co-evaporation of copper, indium and selenium is a most widely used technique and is generally considered to be the most successful [36,48,74]. It has also been used by Dhere et al. [75]. Indium rich samples showed a sphalerite structure with <111> orientation and a small proportion of the chalcopyrite phase. Don et al. [76] reported the growth of CIS layers, with different compositions, onto glass substrates and GaAs single crystals. Additional phases such as $Cu_2Se$ were observed in copper rich films deposited on glass substrates. A second phase, identified as CGS, due to out-diffusion of gallium from GaAs substrates was observed in Cu-rich films. Grain size, crystalline phase and crystalline orientation have been found [77] to be strongly dependent on the deposition

rate and substrate temperature. When electron bombardment heating methods were employed for copper and indium and with selenium being heated using a coil heater, similar effects were observed [78]. However, the substrate (either gold coated glass slides or gold metallized polycrystalline alumina discs) temperature range was varied between 200-500°C. The films were amorphous below 300°C and chalcopyrite at substrate temperatures higher than 420°C.

Thin films have also been deposited [79-81] by r.f sputtering from CIS targets. However, sputtering from compound targets is reported to be limited in terms of reproducibility, due to difficulties in reliably fabricating large area targets [82]. Near-stoichiometric but amorphous films were produced [80] at low substrate temperatures. It was observed that r.f voltage and r.f power and substrate temperature have significant effect on the film structure. Chalcopyrite structure was observed at substrate temperatures greater than 673°K. Further temperature increases showed a rise in crystallite size at the expense of film quality. Piekoszewski et al. [83,79] however, reported that the composition of their films was insensitive to r.f voltage, argon pressure and target to substrate distance. A fine powder produced In rich and Se-deficient multiphase films whereas single phase and stoichiometric films resulted from targets made of coarse powder.

CIS has been deposited onto CdS substrates using molecular beam epitaxy (MBE) [84-86]. A minimum substrate temperature of about 573°K was found to be necessary to achieve epitaxial growth. The ratio of arrival rates of Cu and In are critical in governing layer stoichiometry [86]. The use of an ion gauge beam flux monitor, to control the

elemental fluxes, in an MBE system has resulted in a good layer stoichiometry [87].

Many workers [88-90] have reported the use of the Chemical Spray Pyrolysis technique in the preparation of CIS films. Initial investigations [88,89] showed either a sphalerite or chalcopyrite structure along with secondary phases such as $In_2O_3$ in the as sprayed films. Higher substrate temperatures (250-350°C) revealed only sphalerite structure without any additional phases. However, Bates et al. [90] observed the conversion of sphalerite structure to the chalcopyrite when annealed for a short time in nitrogen at temperatures of 400-600°C. It was later reported [91] that the chalcopyrite phase in the as-sprayed films resulted from increase in pH of the original solution.

Several other methods such as screen printing [92], electro-deposition [93], synthesization of stacked elemental layers by thermal [94] and laser annealing [95], close space chemical vapour transport (CSCVT) [96] and metal oxide chemical vapour deposition (MOCVD) [97,98] have also been used with varying degree of success to deposit CIS thin films.

### 2.2.2 Electrical properties

P-type polycrystalline films (600-800 Ωcm) were deposited at substrate temperatures above 700°K [57,99], whereas, highly resistive n-type deposits were obtained at low temperatures (520-620°K). The resistivity of the first flash evaporated amorphous CIS films [66], measured by Van der Pauw's technique, was in the range $2.2\text{-}8.5\times10^6$ Ωcm.

Flash evaporated films of 1.2-1.6μm thickness were p-type with a hole concentration of $2\times10^{21}$ $cm^{-3}$ when the charge contained 20% excess selenium. For low, and sometimes for high, percentages of excess selenium, n-type conductivity was observed [73]. A substrate temperature of 523°K was found to be the boundary between low and high resistivity films with p-type conductivity. Kazmerski et al. [69] observed n to p-type change in conductivity when films were annealed in $Ar/H_2Se$ atmosphere. Haneman et al. [64] however, noticed p to n-type conductivity change in electro-deposited films by annealing at 350°K in the presence of indium, with an increase in resistivity.

Electrical properties of co-evaporated thin films were dependent on Cu:In ratios [75]. P-type films with resistivities in the range 0.02-27 Ωcm with a variation of ±3 atm.% of In and Cu around stoichiometry were reported. Highly resistive films were realised when the indium content was 5 atm.% higher than the stoichiometric value. Similar dependence of electrical properties on the Cu:In ratios was observed in CIS layers deposited by MBE [87]. The selenium arrival rate was also found to be important as low selenium rates always produced n-type layers.

It has been reported that films were p-type when selenium was more than 45 wt% with a change to n-type for lower values [100]. However, films deficient in copper were always n-type even though they contained excess of selenium [101]. The resistivity of the sputtered [80] and screen printed films [92] produced from starting materials containing extra selenium was found to be lower than those made from stoichiometric CIS materials.

### 2.2.3 Optical properties

The highest absorption co-efficient ($6\times10^5$ $cm^{-1}$) for films of thickness nearly 2000Å grown by the three source technique has been reported by Kazmerski et al. [102]. An improvement in the optical properties after heat treatments in argon, nitrogen and oxygen was also noted. High vacuum annealing, however, produced selenium deficiencies near the film surface which in turn degraded the absorption characteristics.

A shift of the characteristic peak from the near absorption edge towards shorter wavelengths was observed as the percentage of excess selenium was raised in the source material [73]. For a near stoichiometric film an energy gap of 1.04 eV was found, whereas films with Cu:In ratio ≥1.25 showed the presence of an additional phase with an energy gap of 1.23 eV, which was attributed to the $Cu_2Se$.

A detailed study [103] of optical properties of co-evaporated CIS films has been made in relation to the composition and deposition process parameters. The films showed a direct optical transition gap with an energy near 1.0 eV. For some films there was a forbidden direct transition with an energy of 1.2 eV and strong dependencies of refractive index, absorption co-efficient and optical gaps on Cu:In ratio. The measured absorption coefficient was in the range $1\text{-}6\times10^4$ $cm^{-1}$ for different atomic percentages of constituent elements [104]. The energy gaps for these films ranged from 0.94±0.01 to 1.02±0.01 eV. A mild dependency of band gap on composition was found only in films deposited at 723°K.

Molecular beam deposited epitaxial p-type films [85] showed an increase in absorption below the edges as well as shoulder which can be attributed to the copper vacancy band. A higher band gap of 1.10 eV was formed in the as-grown electro-deposited films which after post deposition heat treatments was decreased [64]. Optical band gaps of relatively rough polycrystalline films of CIS were examined using photothermal deflection spectroscopy [105]. A slight shift in band gap towards lower energies occurred for air annealed samples.

### 2.2.4 Heterojunctions

The fabrication of solar cells utilizing CIS as an absorber layer has been reported by a number of researchers [106-108,79]. Among the many possible materials, cadmium sulphide is promising as high band gap window material, due to the fact that the lattice mismatch is very small, especially with ZnCdS. The fabrication of p-$CuInSe_2$/n-CdS heterodiodes with 70% quantum efficiency in the wavelength range between 550 to 1250 nm has been reported [106]. These heterodiodes in solar cell configuration reached a power conversion efficiency of 12%.

A 5% efficient solar cell was produced by depositing CdS films onto rf-sputtered CIS film deposited on Au metallized alumina substrates [79]. Heterojunctions made by molecular beam epitaxy of CIS layers onto single crystal CdS have also shown a maximum conversion efficiency of 5% [85]. An improved efficiency of 8.7% has been reported [109] for solar cells made entirely by screen printing.

The photocurrent of a thin film CIS solar cell was improved by 25% when a wide band gap conducting window layer of ZnO on top of an un-doped CdS layer over CIS was employed [110]. A post deposition heat treatment in air at 200°C was shown to be necessary to increase the efficiency of a CdS/CIS solar cell [111].

## 2.3 $CuGaSe_2$

Copper gallium diselenide (CGS), is a member of I-III-$VI_2$ group of semiconducting compounds, and in thin film form it has not been investigated in detail. CGS has shown less promise in stand alone devices, with only 6% efficient solar cells having been fabricated [24]. However, it is an ideal high bandgap partner for copper indium diselenide in tandem structures, for which the theoretical maximum achievable efficiency is as high as 33% [112].

Like CIS, this is also a direct band gap material of 1.68 eV [113] with a chalcopyrite structure [29] and belongs to the tetragonal system (space group I42d). Crystallographic parameters of a = 5.612Å, c = 11.032Å and c/a = 1.966 for CGS have been reported [114]. Various sections of the phase diagram of I-III-$VI_2$ ternary system have been published by Platnik and Belova [115]. A part of the pseudobinary phase diagram with reference to the binary compounds $Cu_2$ and $Ga_2Se_3$, in the concentration range 40-100 mol% $Ga_2Se_3$, is shown in figure 2.3. The melting point has been established as 1070°C [116]. Unlike CIS, CGS can only be made with p-type conductivity [117,118], therefore it can only be used as an absorber layer with certain n-type window materials in

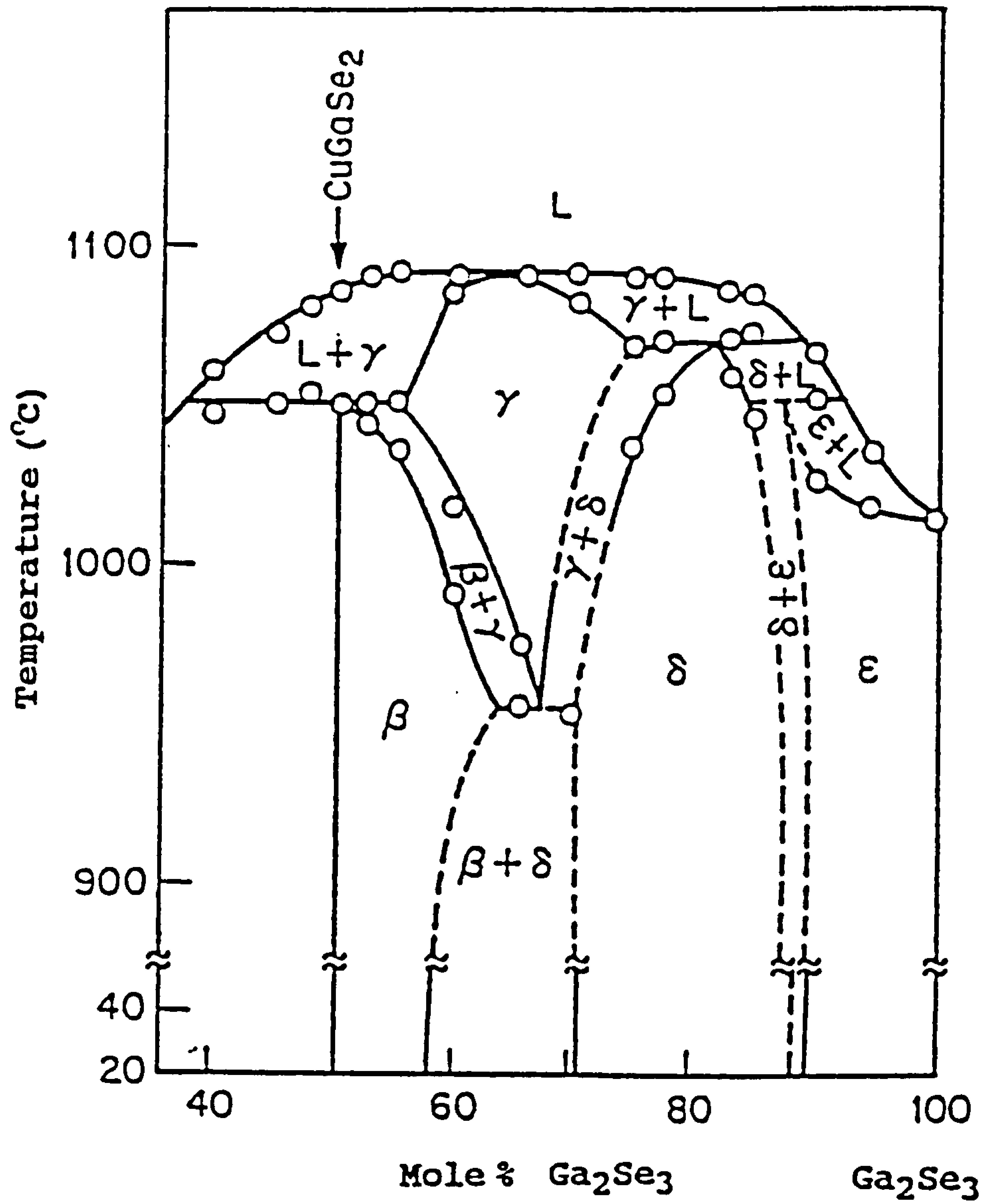


Figure 2.3: The pseudobinary phase diagram of the $Cu_2Se$-$Ga_2Se_3$ system [115].

| Compound properties | $CuGaSe_2$ | |
|---|---|---|
| Melting Point (°C) | 1040 | [116] |
| Density (gm $cm^{-3}$) | 4.35 | [119] |
| Lattice Parameters | a=5.635 Å<br>c=11.035 Å | [120]<br>[120] |
| Carrier Type | p-type only | [121] |
| Hole Concentration (cm) | $4x10^{15}$ as-grown<br>$3x10^{16}$ annealed | [122]<br>[122] |
| Electro-conductivity (Ω-cm) | $1-10^{-5}$ | [117] |
| Mobility ($cm^2$/V.s) | 2-5 | [123] |
| Energy Gap (eV) | 1.66<br>1.69 | [123]<br>[124] |

Table 2.2: Properties of $CuGaSe_2$ semiconducting compound.

heterojunctions. Fundamental properties of CGS are listed in table 2.2.

### 2.3.1 Structural properties

A number of techniques, such as flash evaporation [125], electron beam evaporation [113], laser beam evaporation [126], elemental constituent evaporation [127], selenization [128], etc. have been used for the deposition of CGS thin films. Epitaxial layers were prepared by flash evaporation onto <100> oriented GaAs and GaP substrates [129]. The orientation of the epitaxial layer was different for different types of substrate. For example, for GaP the c-axis of the deposit is parallel to the substrate surface. On the contrary, the c-axis of the deposit is perpendicular to the GaAs substrate surface. The temperature range for epitaxial growth was larger for GaP (795-895°K) compared to GaAs (870-895°K).

The structure of sputtered CGS films [124] was amorphous with binary phases at low substrate temperatures and became single phase with (112) preferred orientation at temperatures more than 573°K. The measurement of granular structure with average grain size of 5000 to 7000 Å was only possible in the films grown at about 623°K whereas temperatures lower than 573°K showed no surface structure. The application of electron beam evaporation in the temperature range of 673 to 723°K for the deposition of CGS thin films resulted in a change of sphalerite structure to chalcopyrite [120].

To study the composition and substrate effect on the structure of CGS films, samples were prepared on four different substrates by the co-evaporation of elemental constituents [130]. The resultant film thickness was in the range of 1.0-2.0 μm. The 2θ value for the <112> peak was found to increase with increasing molecularity for $Al_2O_3$ and glass substrate while a decrease was observed for Mo-coated substrates. Dittrich et al. [131] introduced a new selenization method to produce single phase chalcopyrite thin films. Elemental layers of Cu, Ga and Se were deposited onto molybdenum coated glass substrates by sequential thermal vacuum evaporation and were subsequently heat treated in a quartz tube flooded with argon. The surface morphology of metal films depends strongly on the sequence of deposition. For example, Cu on Ga films showed a granular agglomeration of the Cu rich phase on the liquid Ga. On the other hand Ga on Cu films exhibited polycrystalline appearance.

### 2.3.2 Optical properties

The optical absorption data of electron beam evaporated CGS thin films [120] showed three energy gaps corresponding to fundamental, band splitting and copper 3d level transitions at 1.66, 1.76 and 2.45 eV respectively. The dependence of absorption coefficient on substrate temperature was also observed and found to decrease with increasing substrate temperature. Similar observations have been reported [126] for laser evaporated CGS thin films.

A study [23] of the optical properties of CGS thin films near and above the fundamental

absorption edge for the flash evaporated films, deposited onto glass substrates at 920°K was carried out by Horig et al. The characteristic energy gaps at 1.67, 1.78 eV are similar to those observed later by Reddy et al [120,126]. However, transition at 2.8 eV is higher and attributed to the p-d hybridization of the valence band predicted in a theoretical model [132].

### 2.3.3 Electrical properties

A change in resistivity from $10^3$ to 1 Ωcm corresponding to the variation in growth temperature was observed in r.f. sputtered films of CGS [121] due both to changes in compositional and structural properties. The conductivity of the films was always p-type with no measurable Hall effect. Similar effects were observed for co-evaporated films with a corresponding change in resistivity from $10^6$ to 0.1 Ωcm [134].

### 2.3.4 Heterojunctions

Gopalswamy and Reddy [123] reported the fabrication of an all thin film ZnO/ZnCdS/CGS heterojunction, in which a window layer of ZnO was deposited by spray pyrolysis and a CGS absorber layer by electron beam evaporation. A thin film of ZnCdS was used as the buffer layer to reduce the lattice mismatch between window and absorber films. The measured open circuit voltage was 400 mV and the short circuit current was 10.5 mA/cm$^2$, giving an electrical conversion efficiency of about 2%.

A p-type thin film of CGS was laser evaporated onto vacuum deposited n-type CdS films at a temperature of 643°K to prepare a thin film heterojunction [122]. This was then heat treated in Se-atmosphere to compensate for the loss of selenium in the films. From the dark I-V measurements on these junctions at different temperatures it was found that tunnelling is the predominant current transport mechanism below room temperature, while recombination of charge carriers is observed above 303°K.

A significant increase in efficiency of a solar cell consisting of CGS as the absorber layer was found [134] when CGS layers were chemically etched in $Br_2$-MeOH and KcN solutions, before the deposition of window layers. The cell properties were investigated by quantum efficiency, electron beam induced current and capacitance measurements. A significant increase in fill factor (FF) up to 56% for a CGS/(Cd,Zn)S cell has also been reported [135]. Measurements of conductivity and carrier density showed the removal of secondary phases, by KCN dip, from Cu-rich films.

### 2.3.5 Photoconductivity

Laser evaporated films [136] showed a dependence of photoconductivity on thickness and a maximum photoresponse at 750 nm was observed for a thickness of 1.2 μm. Annealing in selenium ambient showed no change in the position of the peak but the photoconductivity increased sharply. Analysis of the shoulder observed on the high energy side at 720 nm revealed that the transition originated from the split p-state. A variation of photocurrent with applied bias voltage and temperature (303 to 373°K) can

also occur. Highly resistive, p-type copper deficient films deposited by the co-evaporation technique were used in the photoconductivity experiments to measure the mobility life time products [137]. The mobility life time product $\mu\tau=6x10^{-6}cm^2/V$ for holes and $2.6x10^{-9}cm^2/V$ for electrons were found at an illumination of about 0.25 AM1. Much improved photoresponse due to the decrease in effective doping levels and increased effective minority carrier diffusion lengths on chemical and electrochemical etched CGS thin films was revealed [138].

## 2.4 $CuIn_{1-x}Ga_xSe_2$

Copper Indium gallium diselenide is another member of I-III-$VI_2$ family of chalcopyrite semiconductors [29]. This material has received an increasing amount of attention recently due to the fact that it's band gap is direct and can be varied from 1.02 to 1.68 eV [67], the range of maximum efficiency for photovoltaic conversion, by varying the composition. The lattice parameters are a = 5.696, c = 11.322 for 50% gallium [139]. Other values of lattice parameters, corresponding to different values of x composition, has also been reported by the same author [140].

Except for some investigations about the lattice parameters, composition dependence of energy band gaps, preparation in the form of single crystal and thin film and some characterization of the electrical and optical properties, only a very small amount of information is available in the literature about the properties of $CuIn_{1-x}Ga_xSe_2$.

### 2.4.1 Structural properties

The deposition of $CuIn_{0.5}Ga_{0.5}Se_2$ thin films by flash evaporation onto glass substrates at 30-400°C has been demonstrated [139]. A molybdenum boat source was heated to about 1500°C for the evaporation of pre-synthesized powder. Films were amorphous at substrate temperatures lower than 200°C. Above 200°C, single phase and polycrystalline films with strong <112> orientation were observed. However, the XRD clearly showed a small peak at about 23° which the authors failed to identify. For chalcopyrite structure there should not be any peaks other than <112> and <103> between $2\theta$ values of 20 and 30°. Hence, it appears that this peak was due to the presence of secondary phases such as $Cu_2Se$. EDAX analysis of the films revealed that film composition depends critically on the deposition temperature.

The preparation of thin $CuIn_xGa_{1-x}Se_2$ films onto mica substrate (with x=30 and 50%) by single source evaporation and flash evaporation techniques has been investigated [68]. The temperature of the substrates was varied between 200-300°C and 200-250°C respectively. The flash evaporation method was found to be better in terms of reproducibility. Similar conclusion was drawn by Romeo et al. [67]. They used a tantalum source temperature greater than 1500°C to deposit CIGS films. Mica sheets were used as substrates heated at temperatures in between 473-523°K. Successful growth of $CuIn_{0.5}Ga_{0.5}Se_2$ thin films by the single source evaporation method has also been reported [141]. In order to compensate for the loss of selenium during film growth polycrystalline powder with 3 mol.% excess selenium source material was used in a resistive heated molybdenum boat at about 1650°K . The substrates used were glass

slides, maintained at constant temperature in the range between 303-700°K.

### 2.4.2 Electrical properties

Romeo et al. [67] reported that their films were always p-type with resistivities in the range of 1-100 Ω-cm. Hole mobility was found to be 1-2 $cm^2/V.s$. P-type films with resistivities ranged from 0.1-10 Ωcm were obtained [68,142] by flash evaporation. The effect of higher evaporation rate on the film resistivities was also observed. The influence of copper diffusion from the film to the ZnSe single crystal was enhanced at elevated substrate temperatures [142].

The effects of deposition temperature and film thickness on the electrical resistivity and Hall mobility of flash evaporated $CuIn_{0.5}Ga_{0.5}Se_2$ thin films have been investigated [138]. An increase in film thickness and substrate temperature resulted in a decrease in resistivity, from $10^4$ to $10^2$. However, Hall mobility changed inversely with substrate temperature and directly with film thickness.

### 2.4.3 Optical properties

Optical absorption studies [143] on flash evaporated p-$CuIn_{0.75}Ga_{0.25}Se_2$ thin films revealed three energy gaps of 1.16, 1.22 and 1.38 eV, due to the fundamental edge, band splitting by crystal field and spin-orbit effects, respectively. The forbidden gap of

$CuGa_xIn_{1-x}Se_2$ films [68], measured from absorption spectra was reported as 1.29 eV for x=0.5 and 1.36 eV for x = 0.7. Determination of the optical constants of CIGS thin films [141] by transmittance and reflectance measurements in the wavelength range from 0.4 to 1.2 μm revealed three characteristic energy gaps of 1.30, 1.55 and 2.46 eV.

### 2.4.4 Heterojunctions

Thin film polycrystalline $ZnCdS/CuIn_{1-x}Ga_xSe_2$ solar cells produced by elemental vacuum evaporation have been reported [144]. The best cell, made from the selenide films with 23% Ga and anti-reflection coating, showed a total area efficiency of 10.7%. Improvements in open circuit voltage and fill factor after 5 minutes bake in oxygen environment have also been observed. As deposited cells without anti-reflection coatings showed an efficiency of 9% which was increased up to 10.06% after post deposition annealing [145]. Heterojunctions with nearly zero mismatch between flash evaporated CIGS thin films and Al-doped ZnSe single crystal have been reported [68].

## 2.5 Post deposition processing

Post deposition treatments can considerably improve the properties of absorber layers and hence the parameters of photovoltaic devices [146]. The literature contains a number of reports on post deposition heat treatments of $Cu(In,Ga)Se_2$ compound material prepared by different deposition techniques. However, they are mostly concerned with

the structural properties.

Two stage processing of compound thin films involves two distinct processing steps. During the first stage of the process a precursor film which contains all or some of the constituent elements of the compound is deposited on a substrate which may or may not be heated. During the second stage of the process the constituents are reacted with each other and/or with other species introduced from a reactive atmosphere to form a continuous and compact compound film of CIS.

Rapid thermal annealing of stacked elemental layers (SEL) in different gas ambients at 50-600°C for a range of annealing time (from a few seconds to two hours) have been reported by Oumous et al. [94]. Reaction mechanism studies [147] showed that, prior to the formation of CIS, the material goes through different phases such as $Cu_2Se$ and $\beta$-$In_2Se_3$. Sphalerite or chalcopyrite phase was only observed at annealing temperatures of > 300°C.

Effects of thermal and chemical post deposition treatments on the composition and structure of one-step electro-deposited thin films of CIS have been reported by Guillén and Herrero [148]. In this process, co-deposited copper, indium and selenium were first heat treated at or above 400°C to eliminate the $Cu_xSe$ and $In_ySe$ phases, followed by a subsequent KCN treatment to remove the remaining secondary phases. An increase in grain size of about 50nm has also been observed. The properties of treated thin films showed a strong dependence on the sequence of annealing and chemical treatments used. Laude et al. [149] have demonstrated the synthesis of CIS by laser irradiation of vacuum

evaporated multilayer sandwiches of copper, indium and selenium in an atomic ratio of 1:1:2. Electron diffraction analysis revealed that CIS was formed, apparently in isolated areas. However, no detailed optical and electrical data was presented.

Another approach for the preparation of good absorber layers for photovoltaic applications is selenization. Copper and indium/gallium layers prepared by co-evaporation [150] are selenized in a selenium environment to form the required CIS of chalcopyrite structure. This approach, however, has a problem due to the use of toxic $H_2Se$. To avoid this problem, several routes have been demonstrated including annealing of elemental layers of Cu/(In or Ga)/Se in an inert gas environment [151,152,94] and annealing of copper, indium alloy layers in the presence of selenium vapour [153].

## 2.6 Thin film deposition techniques

To a large extent, the choice of any one of the many available methods for growing thin films of the I-III-$VI_2$ compounds is dependent upon the application which dictates the desired material properties such as crystalline order, perfection and the impurity concentration in the film.

A wide variety of deposition techniques are available. For the formation of high quality thin films for photovoltaic applications, the preferred techniques are generally vacuum deposition processes. These can be classified into two categories, **Physical Vapour Deposition** such as evaporation, sputtering, laser, electron and molecular beam

evaporation, and **Chemical Vapour Deposition** such as laser or plasma assisted deposition, spray pyrolysis, screen printing, etc. The following section discusses some of the thin film deposition techniques.

### 2.6.1 Physical methods

Physical methods have been widely used to deposit thin films by condensation of vapours in high vacuum, $10^{-8}$ to $10^{-1}$ mbar, atomistically at the substrate surface. The technique is extremely versatile and covers a wide range of variants including thermal evaporation, activated reactive evaporation, ion-beam sputtering and ion-plating. Virtually any metal, alloy, ceramic, inter-metallic and some polymeric type materials and their mixtures can be easily deposited on to virtually any substrate material which are stable at operating temperatures in vacuum.

#### i) Flash evaporation

This method involves rapid evaporation of multi-component compound or alloy (powder) by dropping it continuously onto a source, heated at a temperature high enough to evaporate all the disassociation products of the compound. Historically, flash evaporation was described in 1948 for the first time, in connection with the evaporation of brass and other alloy metal films [154]. Since then, this method has been applied to the deposition of a large number of alloys and compounds such as copper ternary and multinary compounds.

### ii) Single/double source evaporation

Single source evaporation is the simplest method for the evaporation of required material in thin film form. The suitability of this technique is limited for single element evaporation, because, in compound and alloy evaporants the constituent elements have different vapour pressures and may evaporate at different rates with respect to the rate of increase of source temperature, which makes it very difficult to produce stoichiometric films. However, the successful growth of CIS thin films by single source evaporation method has been reported [69]. The disadvantages of disassociation and decomposition leading to the loss of the most volatile components (selenium) can be overcome by using another source in the system [67], known as double source evaporation technique.

### iii) Co-evaporation technique

Multi-component compounds or alloys of thin films with precisely controlled composition can be prepared by evaporating each component from a separate source. This technique has been developed [155] and used most successfully by workers at Boeing Aerospace Company [156], University of Stuttgart [157] and Swedish Institute of Microelectronics [158]. The temperatures of the sources can be controlled by using an appropriate thermocouple spot welded onto the base of each evaporation boat. Thickness of the deposited films can be monitored by frequency controlled quartz crystals.

Three source evaporation technique has been greatly successful in producing large area $Cu(In,Ga)Se_2$ thin film solar cells modules, and devices with efficiencies of more than 16% have been fabricated [22].

### iv) Electron beam evaporation

The use of a focused beam of electrons to evaporate the material under vacuum has broken many barriers in the field of thin film deposition. Materials can be evaporated by focusing a beam of high voltage electrons, provided by an electron gun, onto a small area of the material. The energy of the electrons which strike this area heats the material directly, causing it to evaporate. The advantage of this technique is that crucibles or boats, which might contaminate or react with the materials, are not required.

### v) Laser beam evaporation

The use of pulsed laser deposition (PLD) was first reported [159] in the mid 1960's to investigate the deposition of thin films of a variety of materials including semiconductors, dielectrics, organometallics and chalcogenides [160]. However, it is only relatively recently with the success of the technique for the deposition of an important class of materials called high temperature superconductors, that it has been widely accepted by industry as a viable process technology for industrial use. The technique has the ability to deposit almost any material and preserve the stoichiometry of multi-

component compounds. Recently it has been used successfully to deposit $Cu(In,Ga)Se_2$ thin film semiconducting compounds [161-163].

A laser pulse enters the vacuum chamber through a window and impinges on the target of material to be deposited. The pulse is about 20-30 nanoseconds wide with an energy density of approximately 1-10 $J/cm^2$. It vaporises the target material in the form of a plasma plume containing neutral, ionic and molecular species, which have a kinetic energy of a few electron volts which travel towards the substrate and deposit to form a coating.

### vi) Molecular beam epitaxy (MBE)

MBE is defined as epitaxial growth onto a substrate resulting from the condensation of directed beams of molecules or atoms in a vacuum system. This is basically a vacuum evaporation system consisting of effusion cells in a source-shroud assembly which provides water cooling around the cells and a liquid nitrogen shroud to separate the beams, around the entire assembly. The emergent beam of molecules produced by heating the material contained in an evaporation cell are monitored periodically by using a mass spectrometer. Molecular beam epitaxy has been used to deposit a variety of thin films of semiconducting compounds including $Cu(In,Ga)Se_2$ [165].

### vii) Sputtering process

Sputtering is a process which involves the ejection of atoms from the surface of a target material by bombardment with energetic particles and condensation of ejected material onto a substrate to form a thin film. The fast moving atomic sized particles knock out the surface atoms of the target material by the transfer of energy. The atoms that leave the target surface are able to travel in straight lines to condense on a substrate, because both the target and substrate are under a vacuum. The large number of atomic sized bombarding particles can be obtained by putting the target in a plasma and by applying negative high voltage to the target surface. This negative voltage attracts the ions from the plasma to the target surface. The ejection of atoms due to positive ion-bombardment is known as cathodic sputtering whereas sputtering done in the presence of mixture of inert and reactive gases is referred to as reactive sputtering. RF [165], DC [71] and ion beam sputtering [60] have all been used in the preparation of CIS thin films.

The deposition rate, system pressure, power density, target size and target to substrate separation are some of the parameters which can affect the quality of films. The advantage of sputtering is that it can also be used for the etching of oxide layers from the surface of a metal target and pure metal can be readily sputtered onto the substrate.

## 2.6.2 Chemical methods

Chemical processes utilise volatile components of coating materials which are

chemically decomposed or reacted with the substrate to form a coating atomistically on the hot substrate. The chemical reactions, generally, take place in the temperature range of 150 to 2200°C at pressures ranging from a few mbar to atmospheric pressure. These methods are highly versatile and flexible in producing a wide range of thin films with excellent adhesion.

### i) Chemical vapour deposition (CVD)

CVD is the formation of thin films from the decomposition of chemical precursors onto heated substrate. The occurrence of a chemical reaction is an essential part of the CVD method. Mostly, the deposition reaction at the surface of the substrate is heterogeneous, but sometimes homogeneous reactions (which usually affect the composition of the gaseous phase) can produce powdery or flaky deposits, which should be avoided. The following is a sequence of events which occur during the deposition process.

1. Transport of precursors to the substrate surface.
2. Adsorption of precursors onto substrate surface.
3. De-composition of precursors to solid films and gaseous by-products.
4. Desorption of gaseous products and un-reacted precursor molecules.
5. Transport of un-reacted and gaseous by-products away from the substrate surface into main gas stream.

In any CVD set-up, the reactor plays an important role. The physical and chemical

characteristics of the system determine the reactor geometry employed for a particular process. The provision of sufficient energy to decompose the chemical precursors at the site of reaction (substrate surface) is essential in all types of reactors, and this can be accomplished in different ways. The most frequently and successfully used method is resistive heating. The reaction at the surface of the substrate can be enhanced by the use of a laser beam (in laser assisted CVD), an ion beam (in ion assisted CVD) or by r.f/d.c (in plasma CVD) etc. Recently, thin films of polycrystalline chalcopyrite CIS have been grown successfully by using plasma enhanced and metal organic chemical vapour deposition techniques [166,167].

### ii) Electrodeposition

Electrodeposition is a process of depositing films onto an electrode, with the chemical changes in a solution. Metals in solutions may be either in cationic or anionic forms, and ions move with individual mobilities toward the electrodes under the influence of an electric charge. Since the mobilities of various ions are different, it follows that, in a given solution, more current may be carried by cations than by anions or vice versa. Different factors like pH, current density, bath composition etc. can influence the properties of electrodeposited material. Bhattacharya [168] first made electrodeposited CIS thin films in 1984. This technique, although, at early stages in its development for CIS, has considerable potential for coating large area substrates.

### iii) Chemical spray pyrolysis

Spray pyrolysis is a chemical process in which metal compounds are dissolved in a solvent and atomized into fine droplets which are then blown onto the hot surface of the substrate with the aid of a carrier gas, where they react and form the desired chemical compound. Chemical reactants are selected such that all the products other than the desired compound, are volatile. This method was described by Chamberlin and Skarman [169] for the production of CdS films onto heated substrate following a patent by Hill and Chamberlin [170]. The preparation of copper ternary compound films by chemical spray deposition was first reported by Pamplin and Feigelson [39].

The spraying solutions normally contain CuCl or $CuCl_2$ as the Cu source, sulphur and selenium in the form of dimethyl thiourea and dimethyl selenourea respectively and trichloride sources for gallium and indium. The major advantage of spray pyrolysis is its ability to produce thin films from a simple and low cost apparatus as compared to vacuum deposition techniques. A disadvantage of this method is the wastage of high cost material during spraying due to the deflection of gas flow out of the coating region and the vaporization of significant amount of small droplets before reaching the substrate.

### iv) Screen printing

Screen printing is a cheap and scalable thin film fabrication technique which includes

the printing of semiconducting material (pastes) through a screen onto a substrate followed by sintering. The elemental powders or pre-reacted compound materials (in the form of powder) can be mixed with an appropriate amount of glycol (which acts as a binder) to form a screen printable paste. The screen printed films then need sintering which can be achieved in an inert atmosphere over a period of time at an appropriate temperature. This method can also be used in making the front grid and back metal electrodes for solar cells. Hetero-devices of (Zn,Cd)S/CIS, have achieved efficiencies of 8.75% [109].

## 2.7 Conclusions

In the last two decades, extensive research has been done on the growth, structural and electro-optical characterization of I-III-$VI_2$ semiconducting compounds and their applications in opto-electronic devices. Among these compounds, CIS has raised the most interest and represents the major part in existing literature. In comparison other members of this family of compounds, for example CGS and CIGS, have attracted less interest.

Some very promising deposition techniques used for the preparation of thin films of copper ternary and multinary compounds have been reviewed. Each method has its specific advantages and disadvantages with respect to film quality, reproducibility, production costs and need for post deposition treatments. Therefore, the selection of a particular technique is dependent upon a complicated set of factors including the

application requirements. Physical vapour deposition techniques, particularly co-evaporation, have shown the capability of producing good quality films for efficient solar cells. Other methods have not yet produced devices with comparable efficiencies. However, results from initial studies are promising and require further research and development.

For the production of suitable devices precise control of the deposition process is necessary and is proving to be major obstacle in most thin film technologies employed. In particular, good stoichiometric uniformity over large areas is a difficult issue which needs to be resolved. The simplest solution has been to use a two stage process, such as selinization. However, this involves the use of toxic chemicals and a more attractive alternative is to use a PVD based technique employing solid sources. Of the PVD processes investigated, flash evaporation appears to be suitable from the point of view of stoichiometric control. This technique has therefore been the focus of this work. However, preparation of uniform and pin hole free thin films with suitable characteristics cannot be achieved without controlling the deposition parameters. Although some success with this technique has been reported by various workers further study is necessary.

# Chapter 3

# Experimental

## 3.1 Introduction

Numerous experimental investigations have shown that the properties of the ternary chalcopyrite semiconductor are dominated by various types of defects [171] which can be due to variations from the ideal stoichiometry of the compound. The compositional, structural, and electro-optical properties of the films can in most cases be determined by conventional measurement techniques used on bulk material. However, for thin films, due considerations must be given to the small mass of the films, their irregular topography, the strong effect of micro-inhomogenities, the large surface-to-volume ratio and the effect of substrate material [172]. It is, therefore, useful to employ several different measurement procedures to determine accurately the same film parameters.

In the following section, some of more frequently employed measurement techniques used in the characterisation of $Cu(In,Ga)Se_2$ thin films are described. A brief introduction to each technique, it's working principle and the experimental conditions are considered. The first part, however, describe the preparation of pre-reacted starting material and the deposition of thin films of $Cu(In,Ga)Se_2$ semiconducting material.

## 3.2 Preparation of stoichiometric mixture

Direct vacuum fusion [173] of a stoichiometric mixture of the elements was employed for the preparation of $CuInSe_2$ and $CuIn_{1-x}Ga_xSe_2$ compounds. Elements of copper, indium, gallium and selenium with a 6N purity were used instead of compounds because

of low price and purity advantages. The following steps were used in the preparation of the stoichiometric mixture.

### Cleaning of ampoule

The quartz ampoule was:

* etched with 15% HF for one hour to remove dirt, grease, finger prints etc.
* washed with running water.
* filled with diluted $HNO_3$ and left for two hours to remove metallic impurities.
* soaked in cleaning agent (RBS-35) followed by washing in deionized water.
* outgassed in a vacuum oven at 800°C for 15 hours.

### Weighing of elements

* Copper bars were cut into small pieces, etched in diluted nitric acid, rinsed in deionized water and, after weighing, were stored in the cleaned ampoule.
* The weights of other elements were calculated according to the following relations [173], with respect to the weight of etched copper.

$$Tot.Wt.(Se) = 2\frac{Tot.wt.(Cu)}{At.wt.(Cu)}At.wt.(Se) \tag{3.1}$$

$$Tot.Wt.(1n) = (1-x)\frac{Tot.wt.(Cu)}{At.wt.(Cu)}At.Wt.(1n) \tag{3.2}$$

$$Tot.wt.(Ga) = (x)\frac{Tot.wt.(Cu)}{At.wt.(Cu)}At.wt.(Ga) \tag{3.3}$$

* After weighing, each element was put inside the ampoule, which was then mounted onto the vacuum system.

**Preparation of compound**

* The ampoule and elements were baked under a vacuum of $10^{-6}$ mbar at 100°C. During this process, dry nitrogen from a liquid nitrogen boiler was used to remove the moisture both from the ampoule and elements.
* The ampoule was then sealed and further processed in a furnace whose temperature was accurately controlled using a Eurotherm 818 controller. The temperature was first raised to 200°C for 8-10 hours and then raised to 1100°C at a rate of 5°C/min.
* The temperature was maintained at 1100°C for a further 8-10 hours.
* The furnace was rocked mechanically at regular intervals to ensure that all the elements were well mixed.
* In the final step, the furnace was rapidly cooled down to room temperature simply by switching off it's power.

## 3.3 Flash evaporation system

As described earlier, thermal evaporation can be achieved by a variety of physical methods. The flash evaporation technique has the advantage of producing stoichiometric films of multi-component compounds. The evaporation apparatus can be divided into three main parts; the vacuum system, the working chamber and the electrical control unit. In the following section, these units and the improvements made to them are discussed.

### 3.3.1 Vacuum system

The vacuum system, including a chamber or bell jar, is an important part of the deposition system because the properties of films may be influenced by the residual gases and their partial pressures. The vacuum quality may also affect the adherence of the film to the substrate. Therefore, a high vacuum must be maintained in the reaction chamber in order to suppress any undesirable impurities which can reduce the ultimate purity attainable in the deposited films.

A schematic arrangement of the vacuum system is shown in figure 3.1. It consists of a main working chamber coupled with a water cooled oil diffusion pump backed by a Speedivac rotary pump, also used to obtain a roughing vacuum. The diffusion pump is connected with the system via an oil vapour baffle which prevents oil vapour molecules entering the vacuum chamber. A Pirani gauge connected in the rotary pump line was

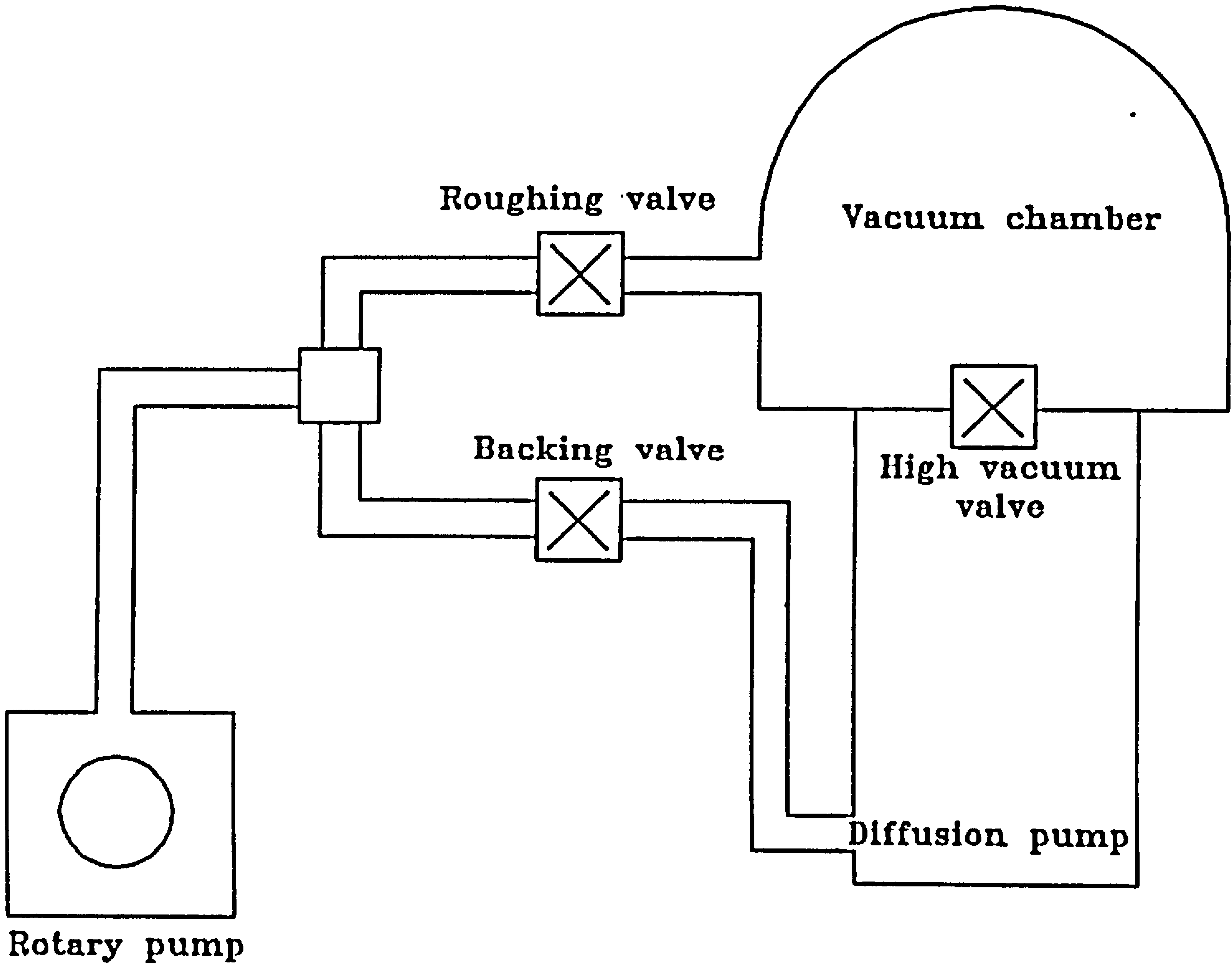


Figure 3.1: Schematic arrangement of the vacuum system.

used for the high pressure range of the working chamber whereas the low pressure was measured with a Penning gauge. Some successful attempts were made to increase the ultimate vacuum attained after extensive exhaustion by increasing the temperature of the chamber temporarily both from inside and outside to desorb trapped vapour gases. A vacuum of $10^{-6}$ mbar in the chamber was achieved. The system was also protected against vacuum and water supply failure by means of a magnetic valve.

### 3.3.2 Working chamber

A glass bell jar working chamber with a metal protective cage and a moulded rubber gasket (vacuum seal) was used in the flash evaporation system. The baseplate was fitted with several feedthroughs which were used to connect power supplies, thermocouple wires, vibratory hopper supply, etc. This enabled the measurements of important system parameters such as, source and substrate temperatures. Most of the material used in this unit was made of stainless steel. The internal arrangement is shown in figure 3.2.

### 3.3.3 Control unit

The control unit used with the flash evaporation system consisted of a temperature monitoring system and power supplies. The temperature of the source was monitored with a B-type Pt-6%Rh/Pt-30%Rh thermocouple placed just under the source boat inside a small basket of Molybdenum. This thermocouple was connected to a Eurotherm

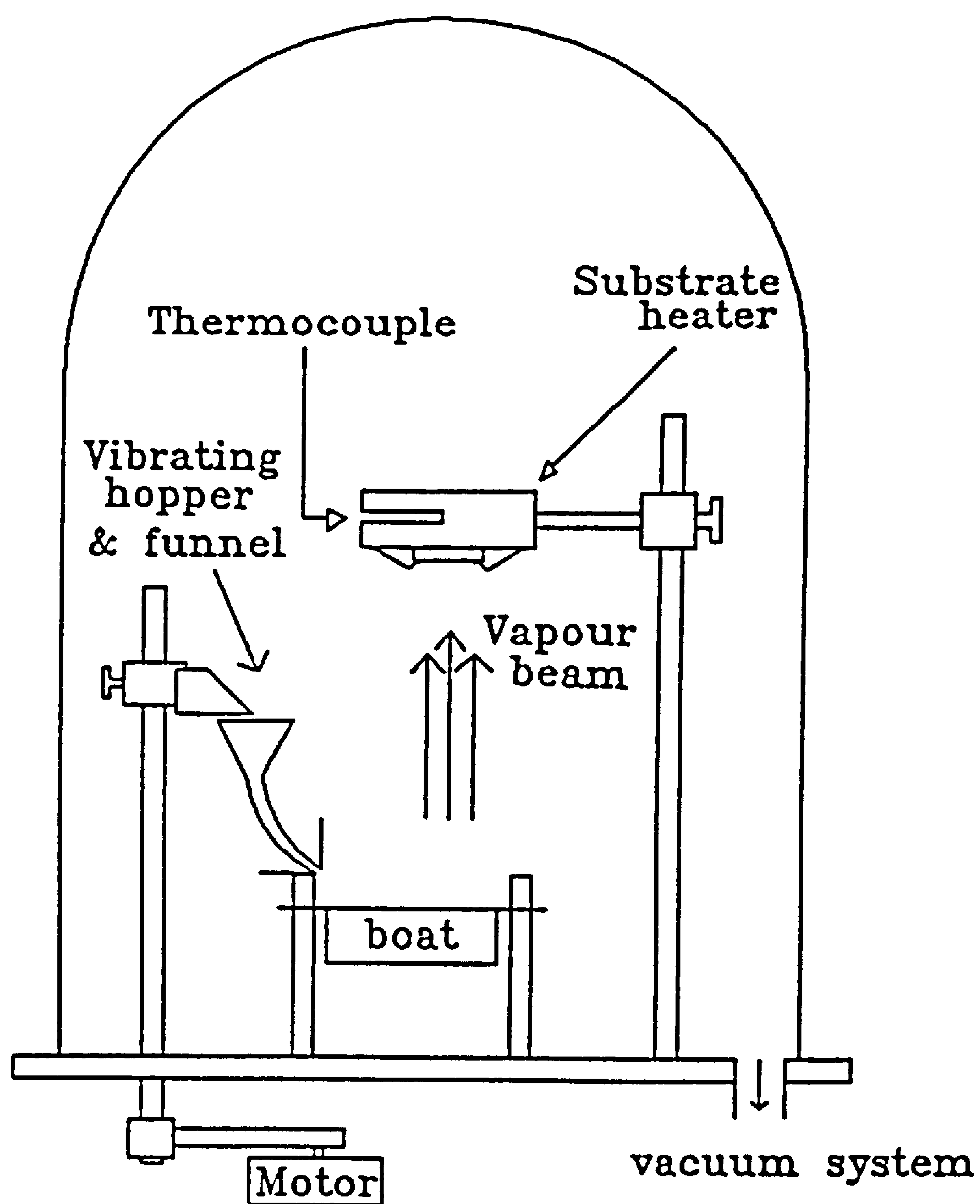


Figure 3.2: Internal arrangement of the vacuum chamber.

controller. The power supply used for the evaporation boat heating was a 6V-300 Amps transformer controlled by a variac. The temperature of the substrate block was measured and controlled by the Eurotherm temperature controller via a NiCr-NiAl thermocouple.The power supply used for the substrate heater was a transformer, controlled by a variac.

### 3.3.4 Evaporation sources

In this study a flat tungsten sheet was initially used as a source but it was found to be unsatisfactory as it always produced films with non-uniform thickness. Therefore, a twin chimney type boat made of Molybdenum was used. Although these types of sources are commercially available in the market, due to their high costs it was decided to make these in the laboratory. Different materials such as Tungsten, Tantalum, Molybdenum etc. were used to make a number of sources and finally Molybdenum was found to be the most suitable material. Twin chimney type boats as shown in figure 3.3, were designed and made in accordance with the requirements for evaporation and facilities available in the department.

### 3.3.5 Improvements made in the system

It is well known that, even under ideal conditions of high vacuum, position of source and substrate and optimum choice of temperature, the deposited film can have a non-

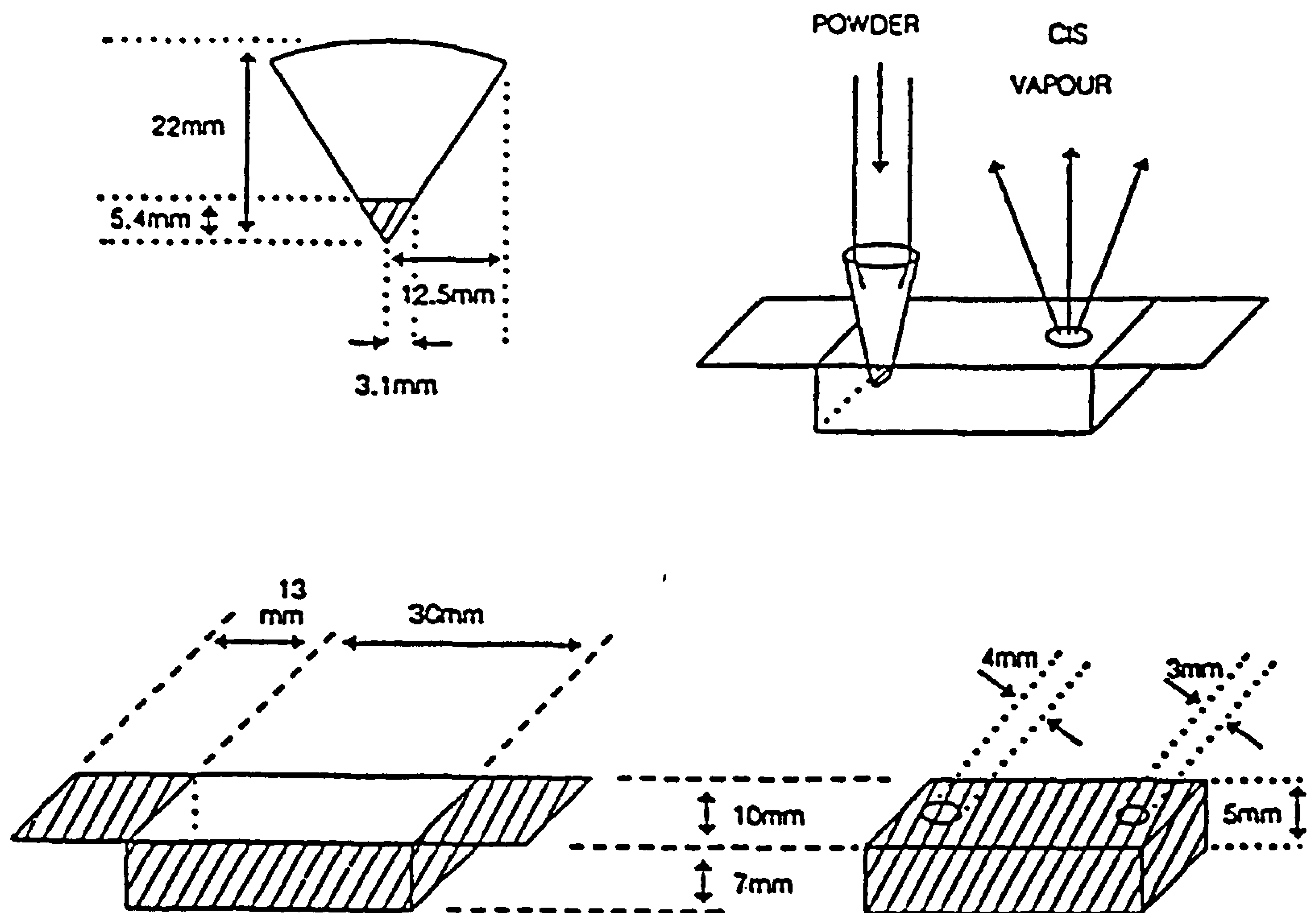


Figure 3.3: Design of the molybdenum twin chimney evaporation source.

uniform thickness [172]. This problem is more severe when using a single evaporation source, whose size is small in relation to the distance from different points on the substrate and where this distance is not identical for all of these points. As mentioned earlier in section 3.3.4, to overcome this problem of non-uniform thickness, a twin chimney type boat was designed and manufactured from Molybdenum. The custom-designed boat is shown in figure 3.3. It consists of a top section, with the same dimension as that for the base excluding wings, incorporated two holes, one used for the entry of the pre-reacted material, other for the exit of vapour.

At the start of this work, there was no heating arrangement for the substrate. However, it has been shown for a large number of materials that the fundamental film properties such as adherence and microstructure are strongly dependent on the substrate temperature. In general, at low substrate temperatures, the adherence of the film to the base material is relatively poor and grain size comparatively small [172]. In order to achieve a better adherence and large grain sizes, it is necessary for an experimental system to be able to function over a range of temperatures. Therefore, a substrate holder/ heater was made from a copper block which was resistively heated by means of 10V - 60A power supply. A K-type NiCr/NiAl thermocouple was placed in a blind hole, drilled on one side of the copper block as shown in figure 3.4. Due to the low resistance of the wire used and the thermal mass of the heater block, the maximum temperature of 200°C was recorded within a reasonable time (≈ 30-40 mins.). Higher temperatures (≈300°C) could be achieved, but longer times (≈ 2 hours) were necessary.

The facility of measuring the source (twin chimney type boat) temperature was also

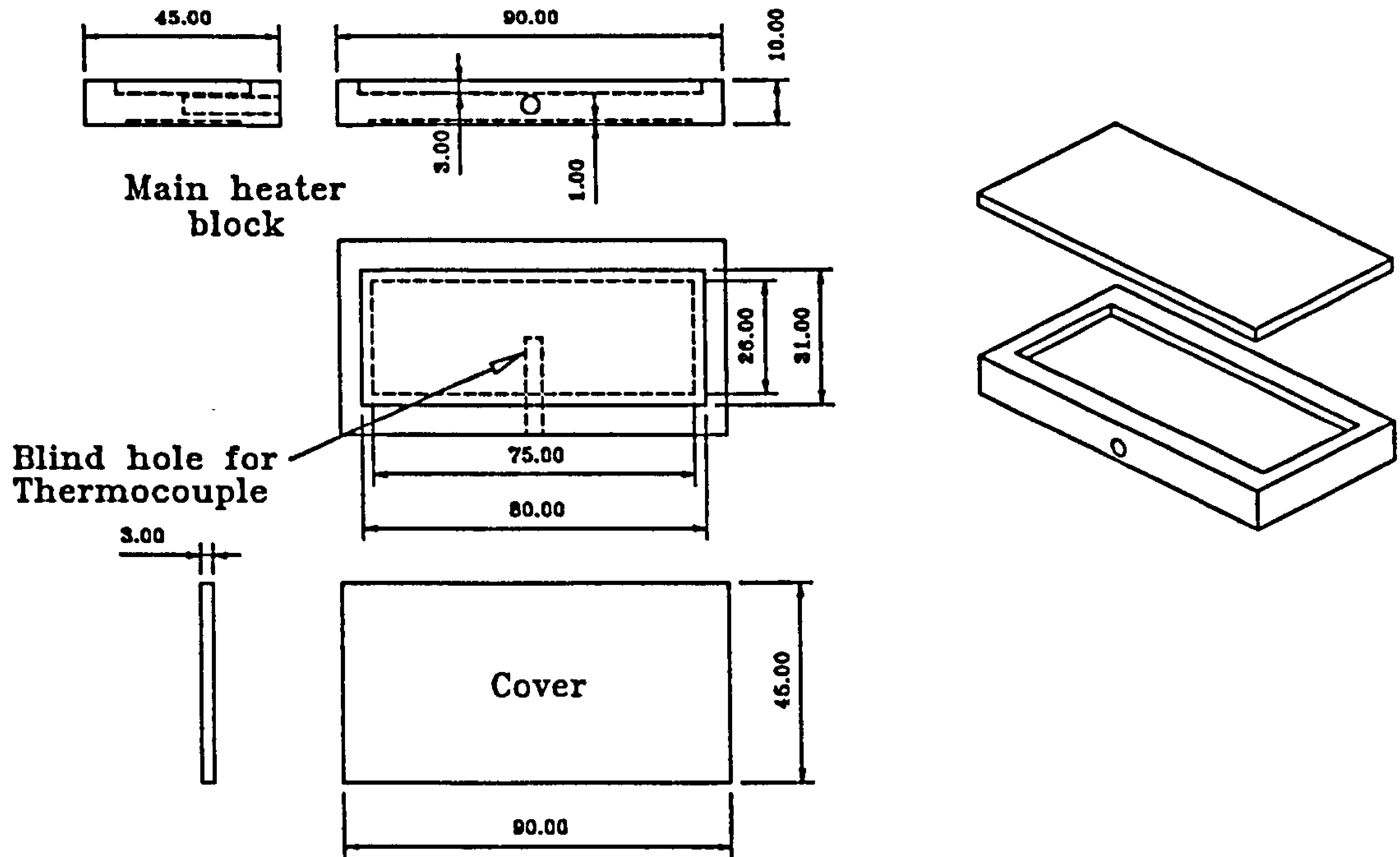


Figure 3.4: Design of substrate holder/heater

arranged by placing a Pt-6%Rh/Pt-30%Rh thermocouple in a small basket under the source. For accurate measurements of source temperature it is necessary to achieve a good contact between thermocouple and the base of the evaporation source. However, considerable difficulties were encountered in spot welding the thermocouple to the base of the molybdenum boat. The basket was made of the same material as the evaporation source. In this type of arrangement, there is a possibility of a temperature gradient between the top side of the boat and the thermocouple. A calibration table was constructed (see table 3.1) in order to obtain an accurate estimate of the evaporation temperature. Thermocouple temperature measurements were compared with those obtained using an optical pyrometers focused on the top of the source. In general a difference of 250°C was observed over the temperature range considered. The measured thermocouple temperatures were therefore adjusted in order to compensate for the temperature gradient effect.

In the flash evaporation of Cu-ternary compounds, fluctuations in grain delivery into the boat produce corresponding deviations from homogeneity in the deposited films. When a grain of the Cu-compound strikes the hot boat, it first gives off a vapour consisting mostly of it's more volatile elements followed by a vapour whose composition changes such that it is gradually richer in the less volatile elements. The final composition of the vapour consists almost completely of copper (the least volatile element). A non constant delivery rate of the powder to the source can result in alternating layers of the component elements on the substrate. To obtain a uniform feed of compound to the boat, a vibrating hopper and funnel arrangement was designed which maintained a continuous feed of compound into the boat. Initially, the hopper was controlled by hand which led

| Supplied current (Amps) | Thermocouple Temp. (°C) | Pyrometer Temp. (°C) | Difference of Temp. (°C) |
|---|---|---|---|
| 170 | 880 | 1140 | 260 |
| 200 | 950 | 1210 | 260 |
| 240 | 1050 | 1290 | 240 |
| 270 | 1120 | 1360 | 240 |
| 300 | 1200 | 1470 | 270 |
| 320 | 1300 | 1560 | 260 |

Table 3.1 A calibration table to obtain an accurate estimate of the evaporation temperature.

to a discontinuous feed of compound into the boat resulting in non-homogeneous films.

## 3.4 Preparation of thin films

The fine grain (150-250 μm) starting material for the flash evaporation process was made by repeated grinding and sieving of polycrystalline $CuIn_{0.75}Ga_{0.25}Se_2$ and $CuInSe_2$ ingots (preparation method described earlier in section 3.2). Both flat tungsten strip and molybdenum twin chimney boats were used as the evaporation sources. The non compensated temperature of the source was varied between 900-1300°C, as measured by a Pt-6%Rh/Pt-30%Rh thermocouple placed directly below the source. The continuous feeding of fine grain CIGS onto the hot source was established by means of a motor-controlled vibrating hopper and a specially designed feeder tube. A source-to-substrate distance of 12 cm and a measured pressure lower than $10^{-6}$ mbar were found to be optimum for the successful growth of CIGS thin films. These were deposited on to ultrasonically cleaned glass slides (cleaning process is explained in Appendix A), the temperature of which was varied between room temperature and 200°C.

## 3.5 Post deposition heat treatments

In order to investigate the effect of annealing on the physical and electro-optical properties of the thin films, selected as-grown films were heat treated in different ambients. Four main annealing regimes were adopted: annealing in vacuum, annealing

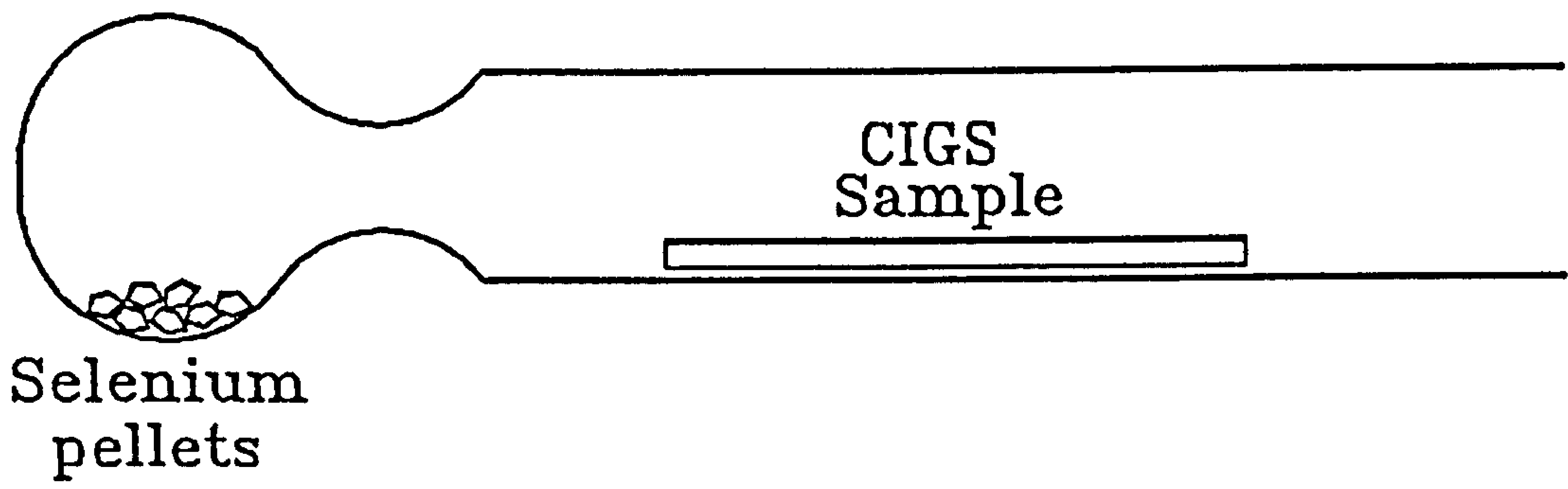


Figure 3.5: Pyrex ampoule used for post-deposition annealing of thin films.

in an ambient of 9:1 mixture of $N_2$:$H_2$, annealing in the presence of an inert gas such as argon and annealing in a selenium atmosphere. The influence of various temperatures in the range 200 to 500°C was investigated. Two stage annealing was then employed to optimise the compositional, structural and electro-optical properties.

Post deposition annealing in vacuum and selenium atmospheres was carried out in closed ended pyrex tubes evacuated by means of rotary pump. The shape of the ampoule allowed the sample and selenium to be physically separate (see figure 3.5). However, at elevated temperatures the selenium vapour was able to pass through the narrow neck of the ampoule from the selenium source to the sample by a diffusion process.

## 3.6 X-ray diffractometer

X-ray diffraction (XRD) is a technique used to identify the crystalline phases present in materials and to measure the structural properties such as grain size, preferred orientation and defect structure of the phases [174]. XRD is a non-contact and nondestructive technique which can be used for the analysis of materials composed of almost any element. However, it is more sensitive to high atomic number (Z) elements, since the diffracted intensity from these is much larger than from low Z-elements. Most of the laboratory based equipments have sensitivities down to a thickness of 50Å [174].

Figure 3.6 shows the basic operating principle of an XRD setup where the diffraction angle 2θ is the angle between the incident and diffracted X rays. In a typical experiment

[174], x-ray beams from the target are incident on the sample which rotates about a goniometer axis. The radiation diffracted at an angle 2θ is measured by goniometer and a detector in the form of a moveable counter assembly. The detector is rotated about the same axis as the sample but at twice the angular velocity of the latter. The diffraction spectrum of the samples is then plotted on a chart recorder as a function of 2θ. The inter-planar spacing $d_{(hkl)}$, corresponding to each diffraction line is calculated by the following relation:

$$d_{(hkl)} = \frac{\lambda}{2Sin\theta_{(hkl)}} \tag{3.4}$$

where θ is Bragg's angle of diffraction and λ is the wavelength of monochromatic radiation. For a tetragonal lattice, the relationship between inter-planar 'd' values and lattice parameters a & c, given below, can be used to estimate the 'hkl' miller indices:

$$d_{(hkl)} = \frac{1}{\sqrt{\frac{h^2+k^2}{a^2}+\frac{l^2}{c^2}}} \tag{3.5}$$

The XRD apparatus used in this work, consisted of a Phillips x-ray generator, type PW 1010 and a goniometer, type 1-050/25 with a detector probe (Geiger Muller Counter) type PW 1965/30. Copper $K_\alpha$ radiation of wavelength 1.54178Å was used and a nickel filter was employed to suppress the intensity of the $K_\beta$ component in the characteristic spectrum. A working tube voltage of 40 kV and a current of 40 mA were employed. The resultant patterns of diffracted x-rays were recorded using either a chart recorder or a computer. The peak positions of phases likely to occur in $Cu(In,Ga)Se_2$ systems

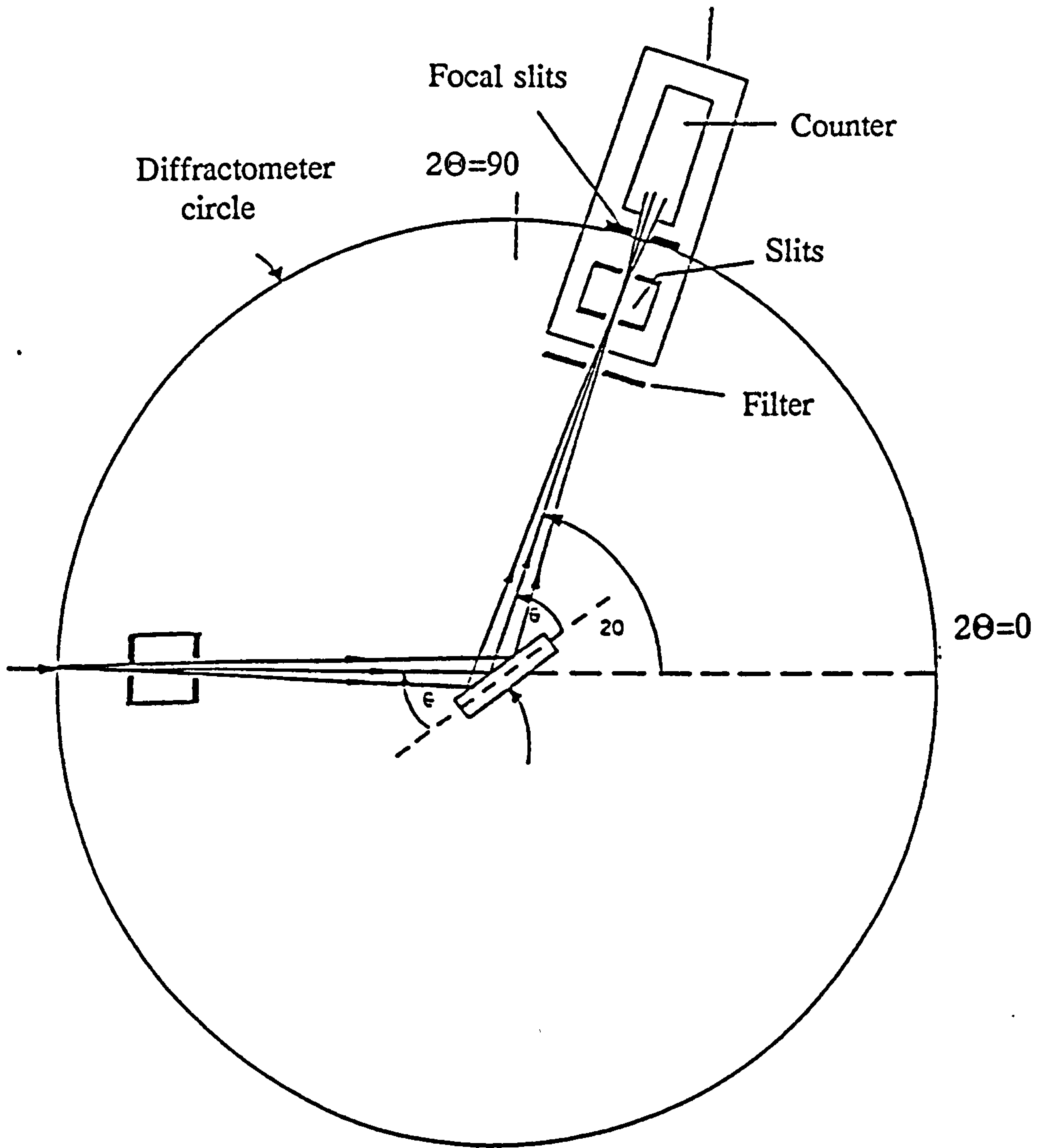


Figure 3.6: Schematic diagram of the x-ray diffractometer.

were then compared with that of the starting pre-reacted material, Joint Council on Powder Diffraction Studies (JCPDS) diffraction powder index file, card no. 35-1102, as well as with published research.

## 3.7 Raman scattering spectroscopy

Raman scattering spectroscopy has emerged as one of the principle characterisation techniques for the non-destructive investigation of the structure and composition of a wide range of materials [175]. The early applications of Raman spectroscopy, utilising mercury arc excitation and photographic detection, was limited [176]. However, as a result of the development of powerful sources of monochromatic radiation, such as lasers, and the substantial improvements in detection techniques, Raman spectroscopy may now be used for almost any type of material under almost any physical conditions.

The block diagram of figure 3.7 shows the components of the equipment necessary for the observation of Raman spectra [175,176]. The gas laser provides the highly monochromatic, self collimated and plane polarized radiation, further focused to produce a beam of much smaller diameter, giving a high irradiance at the sample. Focused laser beams are normally used for the production of Raman spectra except in the special case where the high irradiance may be damaging to the sample. For high resolution studies, the single mode of a laser can be achieved by using a mode-selecting device. The intensity of the scattered radiation can then be increased by additional optical devices. The subsequent dispersion is accomplished by a grating dispersing system. Finally, the

photomultipliers detect these scattered radiations which subsequently pass through electronic devices such as a lock-in amplifier to discard the thermally generated unwanted signal before recording in a computer.

In the present study, the Raman analysis was carried out at the Microelectronics and Material Physics Laboratories, University of Oulu, Finland. Unpolarised Raman spectra of the $Cu(In,Ga)Se_2$ films and target materials were measured on a Jobin-Yvon T 64000 triple Raman spectrometer equipped with a CCD detector. The spectrometer was used in a configuration where the first two stages were in a double subtractive mode and the last stage worked as a spectrometer. The slits were chosen to give a resolution of $5cm^{-1}$. Excitation was by means of the 514.5nm and 488nm lines of an argon ion laser in the backscattering configuration using a 50x microscope lens. To avoid heating effects, the measurements were done using a defocused spot of approximately 15μm diameter. The power on the sample was estimated to be about 30mW. The measured spectral region was from $75cm^{-1}$ to $300cm^{-1}$. A 300s integration time was generally used for each region of the CCD coverage. The full wave half maximum (FWHM) values for thin films were calculated from the room temperature Raman spectra and compared with those obtained from a standard single crystal sample grown with the same compositions. Some useful informations concerning the structure and composition of the samples can be obtained from these values. In general, a sample indicating lower values of FWHM is considered to be better in the structure and composition.

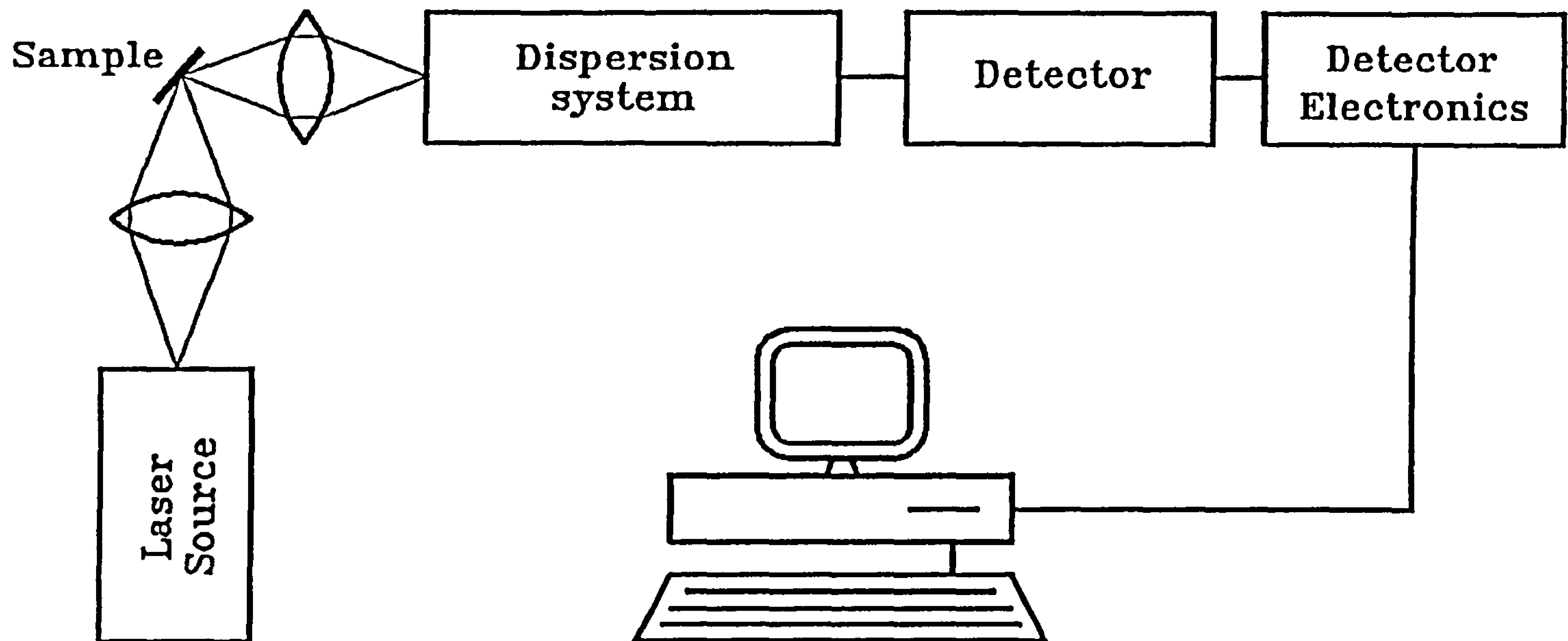


Figure 3.7: Block diagram of the Raman spectroscopy experimental.

## 3.8 Rutherford backscattering spectroscopy

Rutherford backscattering spectroscopy (RBS) is a very useful technique for gaining qualitative information about the compositional uniformity (through the sample), quantitative information about the surface composition and for the identification of surface and bulk impurities [177]. This technique is also non-contact and has been reported [178] not to affect the distribution of atoms within the target. It can be used for the analysis of single and multi-element materials. In multi-element materials the measurement accuracy is high (0.2%) for thin samples (<500nm) in which the individual peaks of each element are well resolved [179,180]. However, for thicker films the accuracy deteriorates to ±5% [179] due to the overlapping of respective peaks of constituent elements in a multi-component compounds. The necessary conditions, required in this technique are the use of an intense beam of Helium ions and a highly evacuated chamber, to avoid the problems due to the absorption of scattering in air. The use of a liquid nitrogen cold shield around the sample can also reduce the chance of hydrocarbon build up on the target surface.

The schematic outline of the main parts used in this system is shown in figure 3.8 and the basic operating principles are described [177]. Helium ions produced from an ion source are accelerated up to 2 MeV by a Van de Graaff accelerator. This high energy beam then passes through a series of devices which collimate or focus and filter it for a selected type of particle and energy. The beam then enters the scattering chamber where it impinges on the sample. Backscattered particles from the sample then strike the detector and generate an electrical signal. This signal is amplified and processed with

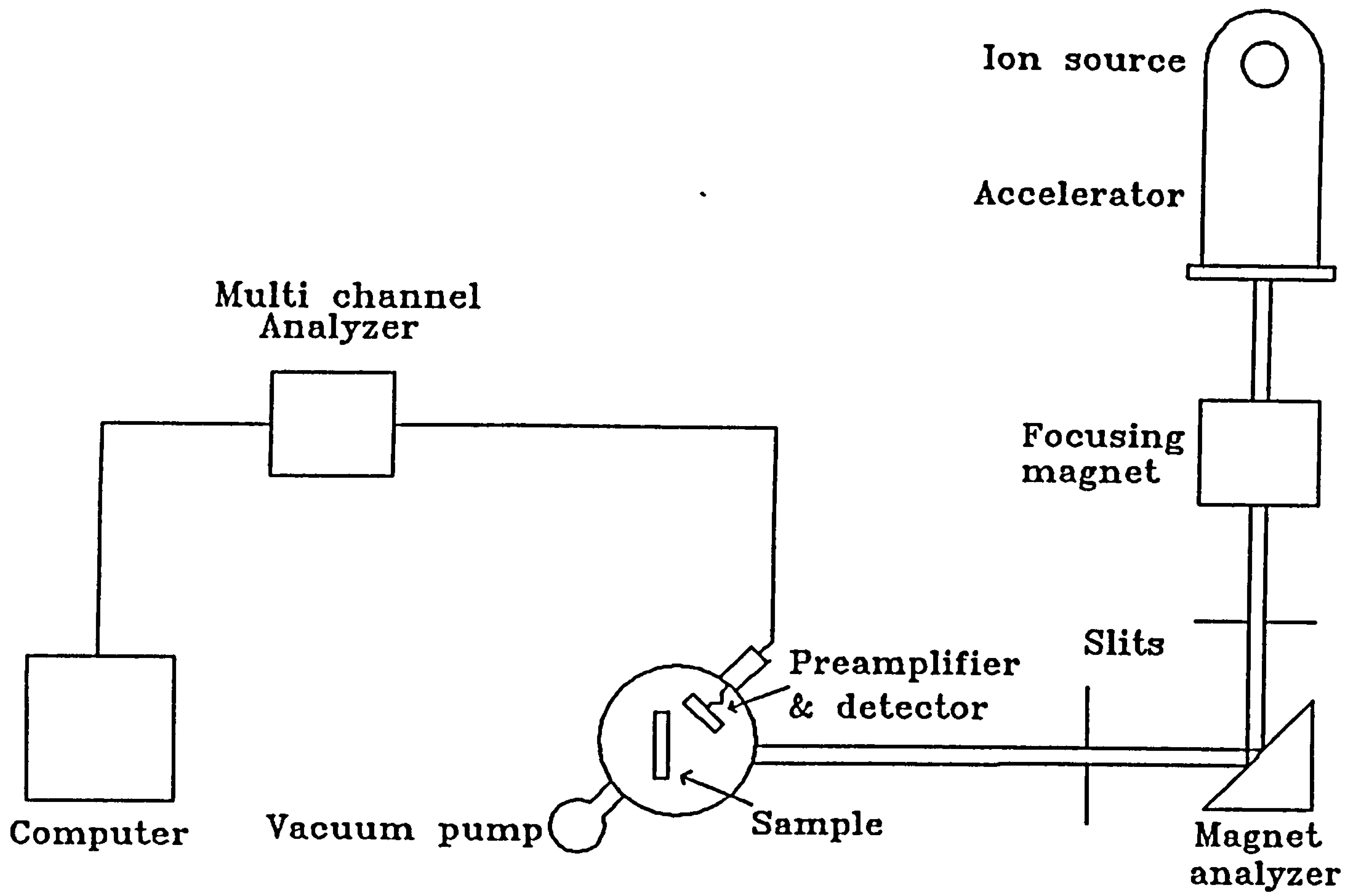


Figure 3.8: Rutherford backscattering spectroscopy setup.

fast analogue and digital electronics. The RBS spectra of the yield against energy can be recorded on a multichannel analyzer (MCA) and the composition of the sample can be estimated by using computer software. Theoretically, a signal generated from an element of heavy mass will appear in the backscattering spectrum at high energies and for light mass elements it will be placed at low energies [177]. The strength of the signal corresponding to that element estimates the composition in the material.

The present work involves the use of typical RBS equipment for the analysis of $Cu(In,Ga)Se_2$ thin film surface composition and depth profile. A 2 MeV $He^+$ ion beam from a Van de Graaff accelerator was focused down to 2 mm x 1 mm on the surface of the sample, incident at 90°, by using a series of slits. The chamber pressure was normally maintained at $10^{-6}$ mbar. The target chamber was separately pumped to allow quick changes of the samples. The backscattered $He^+$ ions were detected by a solid state detector with 15 keV resolution. The energy spectra of the backscattered particles was recorded on the multichannel analyser. For the estimation of composition, a RUMP simulation computer software [181] was used. This software works by generating successive simulations until a best fit is achieved.

## 3.9 Energy dispersive x-ray analysis (EDAX)

The detection and measurement of characteristic x-ray energies, for materials excited by energetic electrons is the basis of EDAX [182,183]. It can be utilized for the quantitative and qualitative analysis of the elemental composition of a wide range of materials. This

analysis is accomplished by the coupling of the x-ray analysis device with a scanning electron microscope (SEM). The resultant combination can allow the analysis of the microscopic and macroscopic composition of a sample simultaneously with the visual representation of the identical area. The entire analysis can be performed quickly, often with minimal specimen preparation. More importantly, it is non-destructive to the sample. In recent versions [183] of SEM-EDS, a thin metallic film is placed in the path of the primary electron beam in the SEM column, converting the electron beam to an x-ray beam. However, the generation of specimen x-rays is more efficient with an x-ray flux than with the use of the primary electron beam and with this arrangement a significant decrease of background radiation results which is more useful for the detection of trace amount elements.

The operation [183] of EDAX involves the use of a primary x-ray or an electron beam which when striking the specimen, removes an electron from the inner shell of an atom and creates a vacancy which may be filled by an electron from any shell of greater energy. This produces a spectrum of the specimen x-rays for each element. An x-ray which is created by the filling of a vacancy in the K shell is named a K x-ray. Similarly, the filling of an L shell creates an L x-rays. The x-ray is further distinguished by the size of the electron jump to fill the vacancy which created a particular type of x-ray. If the vacancy is filled by an electron from the adjacent shell, the created x-ray is termed as $\alpha$. If the electron filling the vacancy is coming from a difference of two shells, then it is known as a $\beta$ x-rays. Therefore, an electron that jumps from an L shell to a K shell will create a $K_\alpha$ x-rays. The specimen x-rays are then allowed to strike on a semiconductor detector, usually a Si(Li) crystal, to convert it into a purely electronic

signal. Finally the signal is processed with fast analogue and digital electronics before recording it. The quantification of elemental composition is a complicated task. However, developments in computer software have resulted in greater ease and flexibility of compositional analysis.

The basic operation [183] of SEM can be described as follows. A beam of electrons emitted and accelerated by the electron gun is focused by a number of electromagnetic condenser lenses onto the specimen and is systematically scanned across the surface of the specimen. The interaction of the electron beam with the specimen surface results in the generation of secondary and backscattered electrons from the specimen which are attracted to and pass through a positively charged grid to strike a scintillator where they are absorbed and lose their energy by generating light photons. The photons pass down a light guide to impinge on the photocathode of a photomultiplier where they in turn lose their energy in generating photo-electrons. The final amplified output is collected at the anode of the photomultiplier in the form of a voltage pulse. This voltage pulse is further amplified electronically. The series of voltage pulses produces a voltage wave form which, when applied to the brightness control of a cathode ray display (scanned in synchronisation with the scan on the specimen), produces lines of varying brightness which form a true picture of the specimen on the display. This information can be stored in the form of a photographic image.

In this present study, the $Cu(In,Ga)Se_2$ thin films were characterised for their elemental composition by using energy dispersive x-ray analysis in conjunction with a JEOL scanning electron microscope, model JSM-6400. An accelerating voltage of 20 kV was

used to accelerate the x-rays which in turn result in a penetration depth of 1 μm. The detector resolution was 150 eV. Other parameters were fixed at optimum operating conditions to give accurate information about the sample. In the compositional analysis, ZAF correction was used to compensate the effects of (Z) atomic number on initial x-ray generation, (A) absorption and (F) fluorescence effects.

## 3.10 X-ray fluorescence

X-ray fluorescence spectroscopy (XRF) is a non-destructive analytical technique to identify and determine the concentrations of elements present in solids, powders and liquid materials [184]. XRF can be used to determine all elements in the periodic table between boron and uranium - from trace levels often below one part per million, up to 100%. Its wide range application in research derives from the ability to deliver extremely accurate results at very high speeds. With modern computer - controlled instruments, analyses are typically completed within minutes.

The working principle is [184] similar to that of EDAX and consists of bombarding a sample with radiation from an x-ray tube (primary radiation) which causes the constituent atom to be energised, so that individual electrons move out of their normal positions and into orbitals further from the central nucleus. As the atom returns to a stable state, the electrons drop back into the inner orbits and give up their excess energy in the form of secondary radiation (fluorescence). Fluorescence radiation is emitted for each energy transition, with the wavelength inversely proportional to the difference

between the electron's initial and final energy levels.

XRF compositional analysis of CIGS thin film samples was carried out at the Health and Safety Exective (HSE) laboratory, Sheffield, UK. A Philips PW 1480 sequential wavelength dispersive x-ray spectrometer was used. A working tube voltage 100 kV and a current of 25 mA were employed. The XRF was calibrated for 25mm filters using one of two methods; sampling from a dust cloud or spotting solutions on filter papers. Analysis of deposits on glass slides was conducted with only 0.21cm$^2$ of the area on each slide irradiated by using a suitable mask (0.7cm x 0.3cm).

## 3.11 Dektak measurements

In most of the applications of thin films, particularly optical applications, it is desirable that the surface of the film be smooth. High roughness can introduce high scattering from the surface of the optical component thus degrading the response of the whole optical system. Since CIGS and related materials have potential applications in photovoltaic devices the surface of the coating have an important influence on the optical properties. These surface characteristics have been studied using surface profilometry described [185] in this section.

The stylus instrument operates on a very simple principle [185], involving the comparison of the movement of the stylus displaced at a constant velocity on the flat and smooth surface to be measured. The instrument consists of a stylus driven by a

traversing unit, an electronic amplifier to boost the signal from the stylus to a useful level and the associated computer which calculates all necessary surface roughness data. Most of the instruments in use nowadays have a video camera which can be focused on the desired part of the sample. In this way specific areas could be scanned and observed as the stylus moves across the sample. Diamond styli are universally used with a tip radius of 5 to 10 μm.

The Dektak ST 3010 was used for surface roughness as well as for thickness measurements of the $Cu(In,Ga)Se_2$ thin films deposited on glass substrates. For comparison, uncoated glass slides were also analysed for their surface roughness.

## 3.12 Resistivity and carrier type measurements

The resistivity and conductivity type are the basic material parameters whose measurement is required for determining the sign, density and interaction of charge carriers with impurities [172]. The measurement of conductivity type of semiconducting materials was carried out by the hot point probe method [186]. This apparatus, as shown in figure 3.9, consists of a low impedance galvanometer connected with two spring adjustable needle electrodes onto a sample holder. These can be brought into contact with the sample by adjusting the spring pressure. When a small area of sample around the contact is heated a local heating effect is produced which causes the flow of majority carriers from the hot to the cold junction. This in turn produces a potential difference across the electrode, whose polarity can be observed by the deflection of the

galvanometer. The direction of this deflection indicates the carrier type.

The surface resistivity of the sample can be measured by using the four point probe method. The main advantage of this method is that it is simple in operation and does not require the fabrication of permanent contacts. The basic arrangement shown in figure 3.10, consists of four equally spaced and in line probes which are lowered onto the surface of the sample. As a result a current passes through the outer probes while the potential difference is measured across the inner two probes. The resistivity of a thick sample [186] can be calculated simply by using the following relation:

$$\rho(\Omega\text{-}cm)=2\pi S\frac{V}{IG(\frac{W}{S})} \qquad (3.6)$$

Where S is the spacing between any two adjacent probes (the equipment being used had a probe spacing value of 1mm). A correction factor G(W/S) should be used for samples having thicknesses comparable to the probe spacing, where W is the sample thickness. A plot of G(W/S) against W/S is shown in figure 3.11. However, the resistivity of thin films [187] will include the thickness (t) of the sample and be:

$$\rho(\Omega\text{-}cm)=4.52\frac{V}{I}t \qquad (3.7)$$

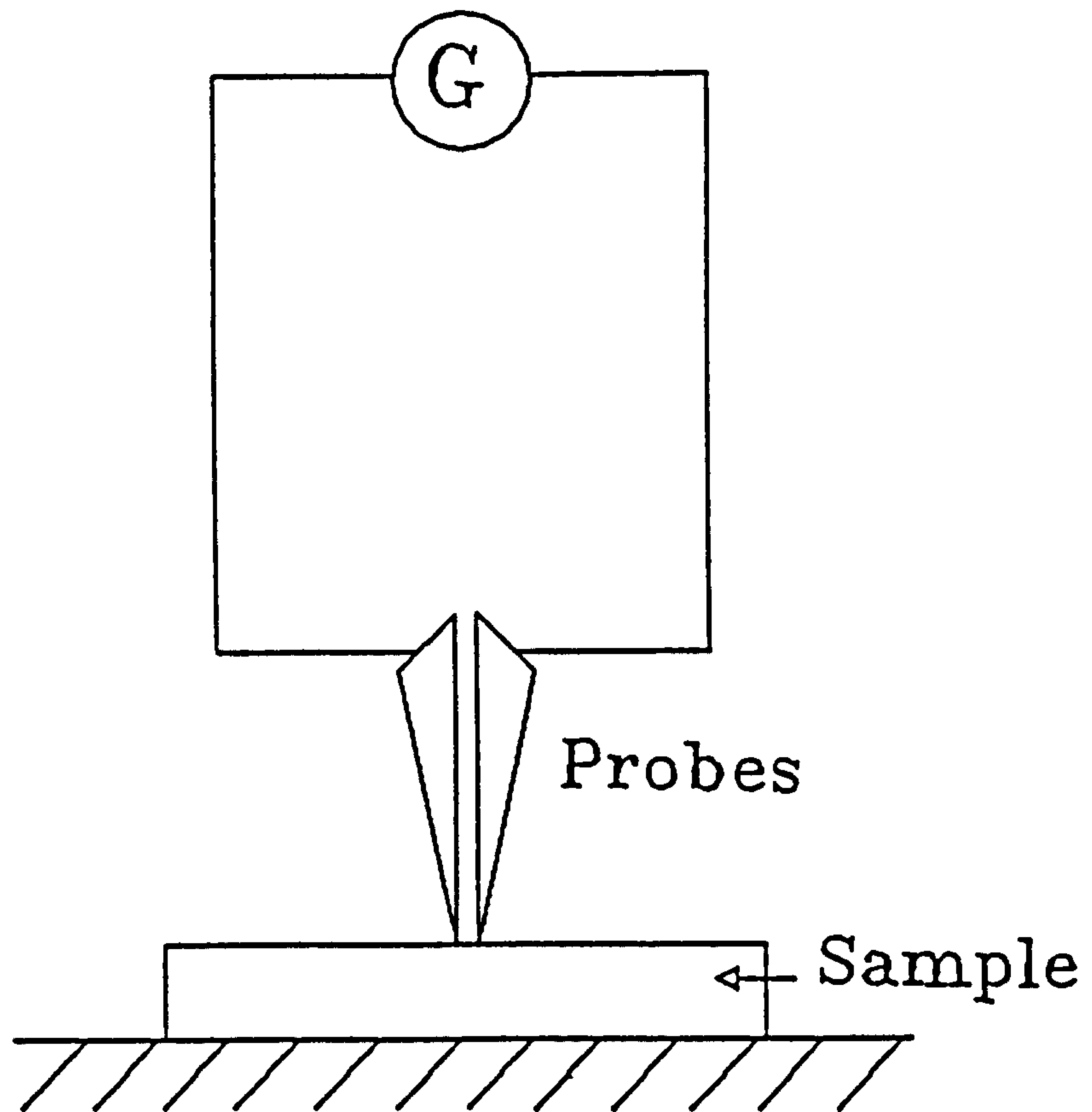


Figure 3.9: Thermal probe apparatus to measure the conductivity type of the sample.

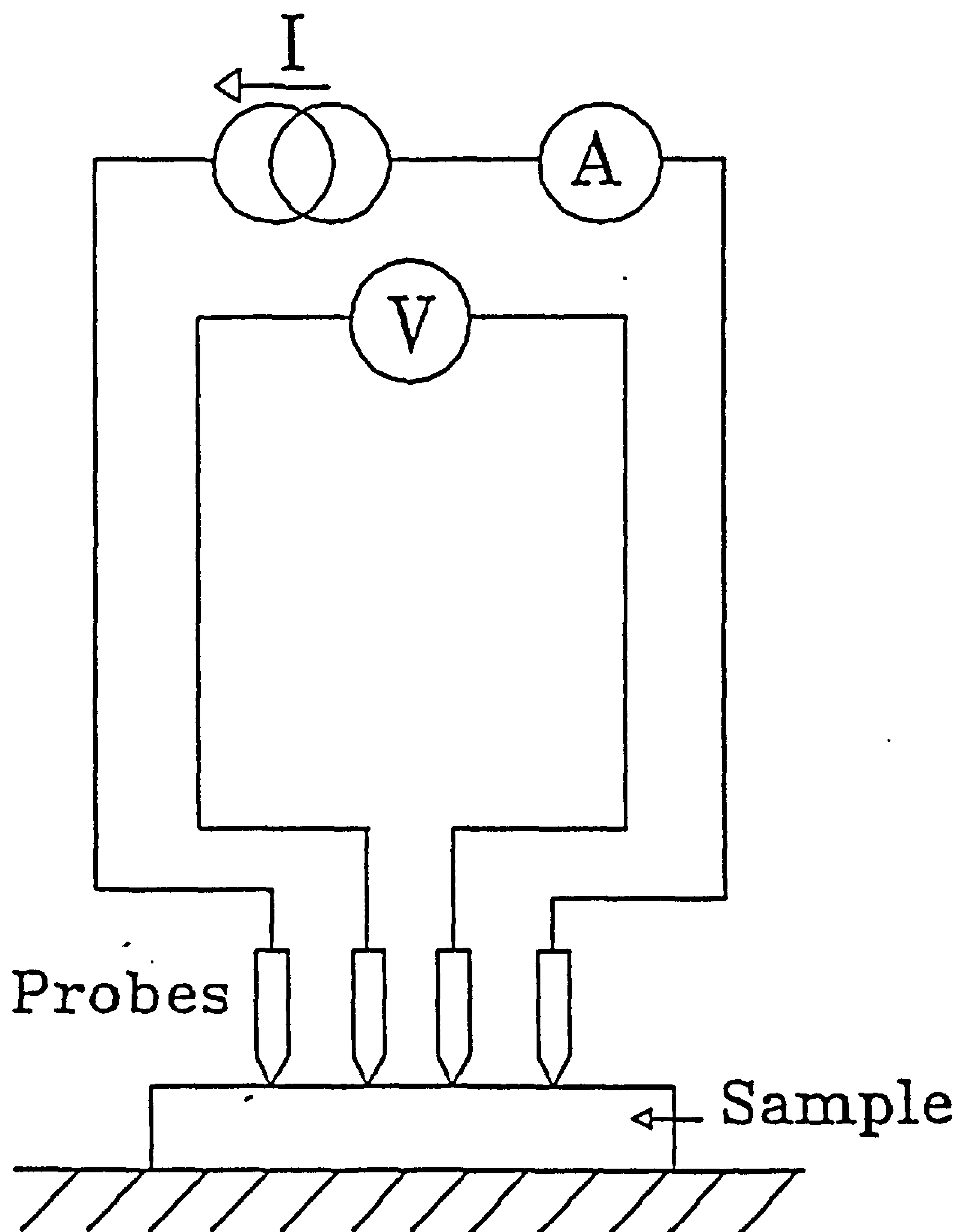


Figure 3.10: Four point probe apparatus to measure the resistivity of the sample.

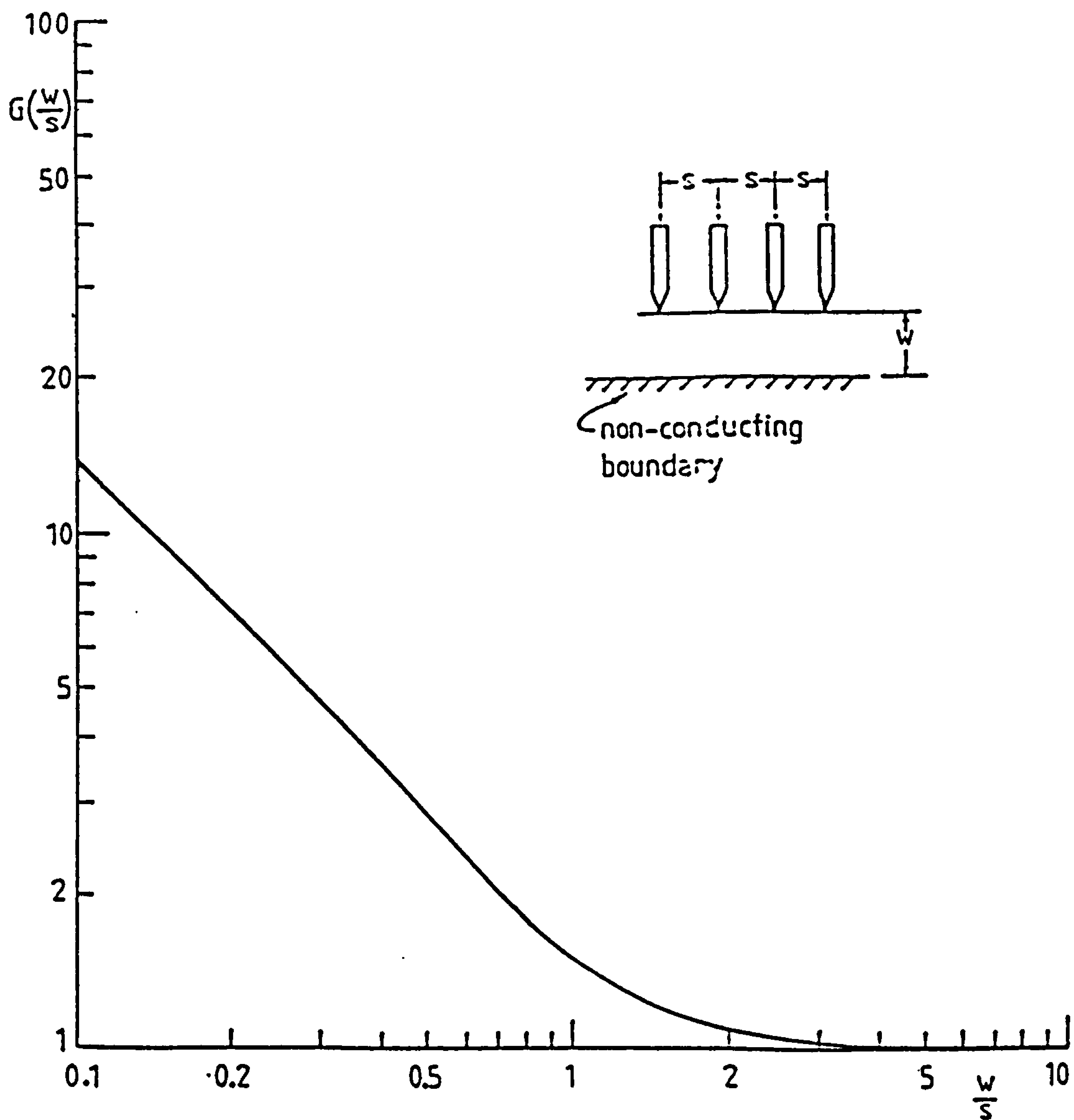


Figure 3.11: Correction divisor for probes on a thin film (non-conducting substrate).

### 3.13 Photoconductivity system

The phenomenon in which the conductivity of a semiconducting material increases due to the absorption of light is called photoconductivity [188]. Almost all semiconductors exhibit a certain degree of photoconductivity at room temperature, due to the partially filled conduction band. Their photoconductivity can be increased when they are exposed to photons having sufficient energy. In an intrinsic semiconductor, a photon may produce electron-hole pairs and both can contribute to current, whereas in extrinsic semiconductors, only one type of carrier is available for conduction, i.e. electrons for n-type material and holes for p-type [188]. The spectral response may be modified by doping, since donor or acceptor levels fall between the valence band and conduction band.

The apparatus for the photoconductivity measurements of single crystal and thin film samples is shown in figure 3.12. It consists of:

1. A 150 watt **quartz halogen lamp**, which is calibrated to provide a constant power density over the required wavelength range, followed by an **optical focusing lens**.

2. A Bentham 218 **optical chopper** consisting of a remote mounted chopping head linked with a control unit by means of a cable. The chopping frequency can be varied in the range between 10 Hz to 1 kHz by using blades with different numbers of slots.

3. A Jobin-Yvon H.10 **monochromator** incorporating a concave holographic 600 grooves/mm grating. Wavelength scanning is linear throughout the range from 200 to 800 nm with direct readout in nanometres on a mechanical counter. The readout counter is directly coupled to the grating and was initially calibrated for a 1200 grooves/mm grating. For the H.10 monochromator (600 grooves/mm), the counter display must be multiplied by 2 to get the actual wavelength.

4. An Oxford Instrument DN 1704 **cryostat** which operates on the principal of the controlled and continuous transfer of liquid nitrogen from a reservoir to a heat exchanger which surrounds the sample space. The sample temperature can be varied continuously from 77 to 300°K and is measured by a platinum temperature sensor connected to the heat exchanger. A sorption pump of charcoal is also fitted, which pumps out the residual gas when cooled by the liquid nitrogen reservoir. The main parts and dimensions of the cryostat are shown in fig. 3.13.

5. A Brookdeal 452 **precision ac amplifier** with very low short circuit noise and high input impedance. These specifications make it ideally suited to the amplification of low level signals from cryogenic sources.

6. A Bentham 211 broad band current input **lock in amplifier** suitable for applications where stray light or dark current drift make the normal current amplifier unacceptable. The unit includes a high gain ac amplifier followed by a synchronous detector and low pass filter. Other features include:- switched and

continuously variable sensitivity, rms deviation control, zero offset, zero check facilities, etc. It is operated by a built in 15 V, 100 mA power supply.

7. Finally the output can be recorded by chart recorder or computer. A computer connected at the output has an extra advantage that the recorded data can be further processed by using commercial software. In the present work a BBC computer was connected to run the monochromator and record output data through a laboratory built interface. The control software is shown in Appendix B.

The photoconductivity spectra were measured in the photon energy range hv=0.75-3.1eV as a function of temperature in the range T = 80-320°K. The optical system, as described earlier, consisted of a 150 W tungsten halogen lamp calibrated to provide constant power density over the photon energy range covered in the experiments, followed by a focusing lens, a Bentham 218 optical chopper and a Jobin Yvon H10 monochromator. The photocurrent was phase-sensitively detected using a Bentham 211 current input lock-in amplifier. The output of the phase sensitive detector was read with a Keithley 175 digital voltmeter. For the temperature dependent measurements the samples were placed in an Oxford Instruments DN 1704 liquid nitrogen cryostat equipped with an Oxford Instruments ITC-4 temperature controller. All the spectra were corrected for the spectral distribution of the optical system and normalized to constant photon flux and to the silicon photodetector.

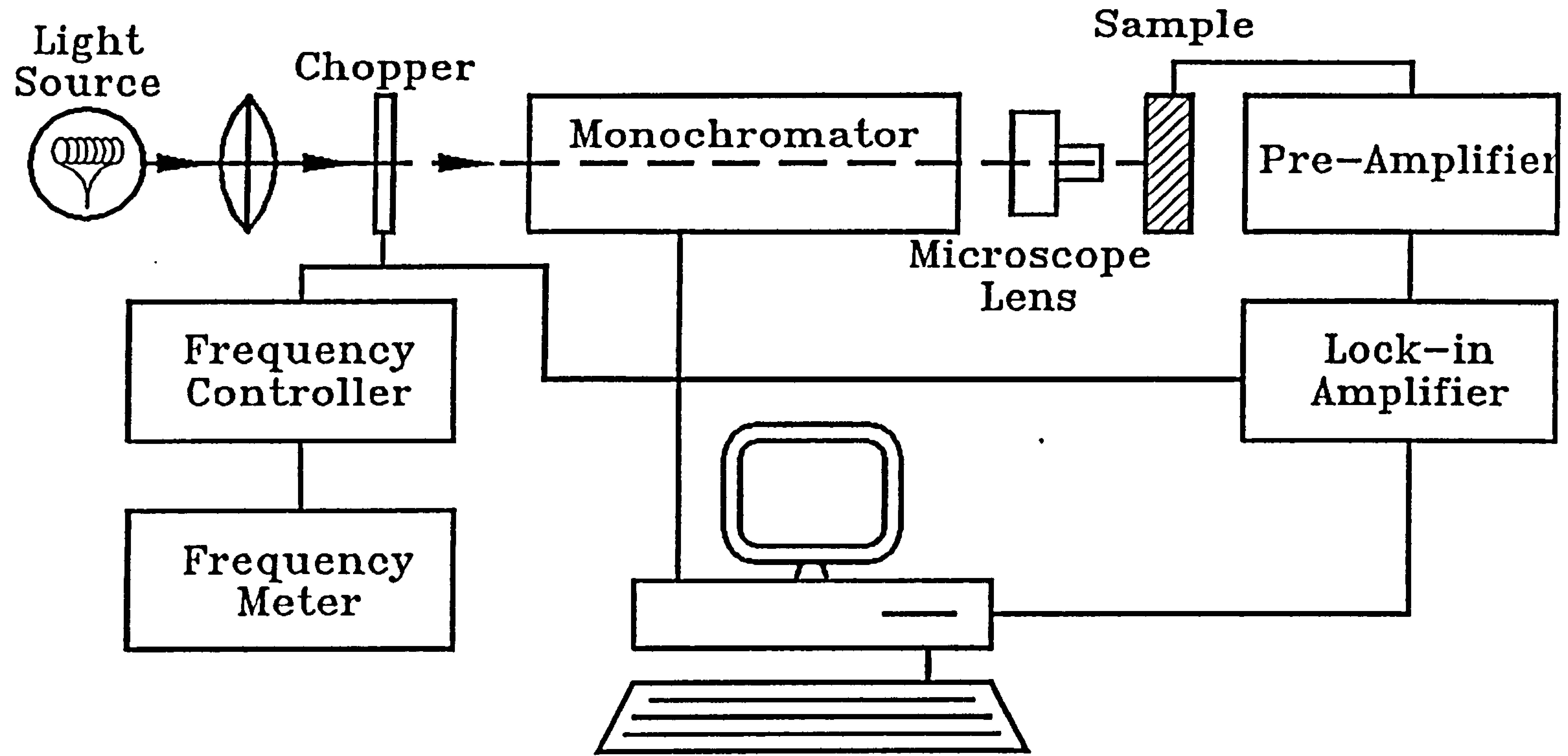


Figure 3.12: Photoconductivity experimental setup.

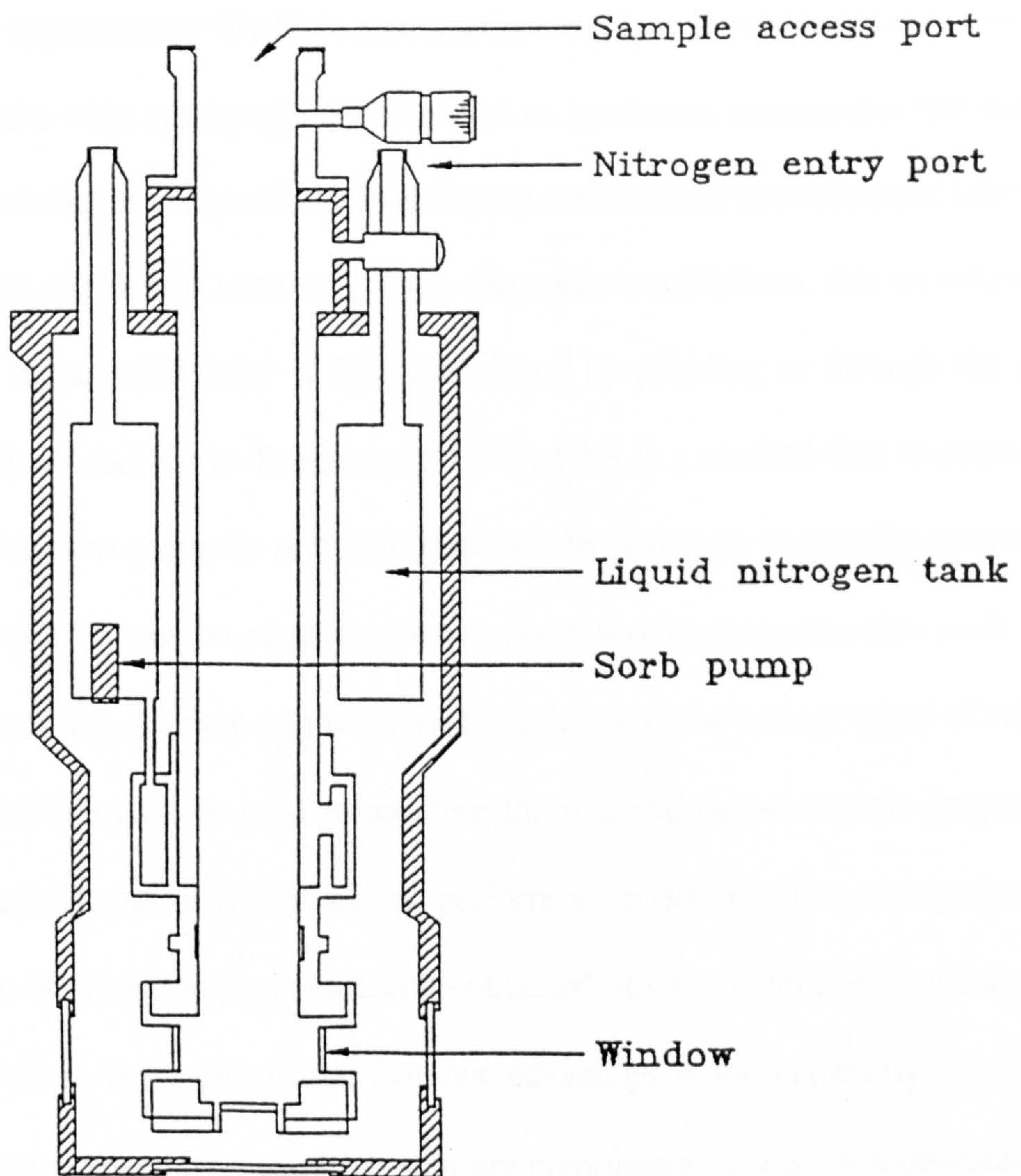


Figure 3.13: Cross-sectional view of the cryostat used for low temperature photoconductivity measurements.

## 3.14 Photoacoustic spectroscopy

Photoacoustic spectroscopy (PAS) is a contactless and hence non-destructive technique for the study of a wide variety of materials such as insulators, semiconductors and even metallic systems that can not be studied readily by conventional spectroscopic techniques [189]. However, for metals with very large absorption coefficients, this technique may be used only if the reflectivity is first diminished by grinding or through the use of powders [189]. According to Rosencwaig [189], PAS is a method that measures how much of the incident energetic radiation absorbed by a sample is actually converted to heat. As a result, it can be used to obtain spectroscopic measurements such as the absorption spectrum, lifetime of the excited species, and the energy yield of radiative processes. PAS can also be used to measure thermal and optoelectronic properties of materials, the thickness of layers, and to perform a variety of other non-spectroscopic investigations. Furthermore, spectra can be obtained quickly from gas, liquid and solid crystals as well as from thin films. Another advantage is the capability of obtaining optical absorption spectra on materials that are completely opaque to transmitted light, since the technique does not depend on the detection of photons. PAS yields direct information on non-radiative absorption processes which are usually associated with band structure and defect related energy loss mechanisms. Such information is necessary for materials which could find applications in electronic devices.

The basic theory behind the photoacoustic technique is quite simple [189]. Light absorbed by a sample is followed by non-radiative de-excitation-relaxation processes. These give rise to a heat source in the sample, which may be distributed throughout its

volume or confined to its surface. This heat source gives rise to both temperature and pressure fluctuations within the sample, which are then detected by thermal and/or acoustic sensing devices. Photoacoustic detection is unique in that it is a direct monitor of the non-radiative relaxation channel and, hence, complements absorption and other spectroscopic methods [190]. The schematic arrangement of the equipment is similar to that of the photoconductivity system. The only difference is that, in PAS, the sample is placed within a closed cell without any contacts on its surface.

The experimental conditions used in the present study were as follows. A 400 W Cermax xenon short arc lamp was used as the radiation source. The light source, after being modulated by a servo-controlled mechanical chopper, was dispersed through an f/4 Spex Minimate monochromator driven by a motor scanning at a speed equivalent to less than 0.5 nm/second. Modulated light from the monochromator, after passing through an infrared filter, was then directed by an f/0.7 off axis elliptical mirror to the photoacoustic cell. The elliptical mirror was used to concentrate and increase the efficiency of the system and makes it suitable for the characterisation of solids, powders and liquids. The cell was made of stainless steel with a geometry designed to give a non-resonant cavity configuration. The microphone output signal was phase detected using a Brookdeal 9454 precision a.c. amplifier with input filters (preamplifier) and a Brookdeal lock-in amplifier comprising of a 9412 Phase sensitive Detector and a 942 reference unit. The output of the phase sensitive detector was read using a Keithley 175 auto-range digital voltmeter. An IBM personal computer was used for the acquisition and processing of data from the digital voltmeter through an IEEE 488 interface card, also used for controlling the monochromator scanning motor via a laboratory-built

interface. All the measurements were recorded at room temperature using chopping frequency values of 30, 112, 185 and 312 Hz. The scans were recorded in the photon energy range hν=0.7 to 1.4 eV. The photoacoustic spectra were corrected for the spectral distribution of the optical system, cell and microphone response by normalising the output signal of the specimen to that of a fine grained powder of carbon black.

## 3.15 Conclusions

The experimental and the appropriate conditions for the preparation of pre-reacted starting material of Cu(In,Ga)$Se_2$ have been discussed. Key parts of the deposition system and their impact on eventual film characteristics have been considered. Modification to the flash evaporation system in order to achieve better film quality are described. The experimental conditions of various post-deposition annealing regimes and the effects of annealing parameters, such as ambients, time and temperatures, on the film properties have been considered.

Basic principles of analytical techniques for the characterisation of thin films of CIS and CIGS and specific conditions employed for this work have also been addressed.

# Chapter 4

# Effects of deposition parameters on the properties of as-grown thin films

## 4.1 Introduction

The development of low cost and efficient photovoltaic devices is a major technological challenge which could be met with the appropriate use of thin films of copper based ternary and quaternary photoactive materials. Devices made from these materials have shown high energy conversion efficiencies in the order of 16% [22]. However, researchers have constantly reported difficulties relating to the reproducible production of material with the desired properties [191]. A fundamental understanding of the growth processes is therefore essential if thin films of these compounds are to be commercially grown.

As previously discussed, one of the most promising thin film materials is copper indium/gallium diselenide (CIGS). To date, very little work has been carried out on the relationship between the growth conditions and the fundamental properties, although the degree of interest in these types of materials has greatly increased in recent years. A better fundamental understanding of the growth behaviour will have a major impact on the ultimate device performance.

In this chapter the effect of growth parameters on the properties of $CuIn_{1-x}Ga_xSe_2$ thin films with x=0 & 25% are described. It is shown that the film properties are highly dependent upon the deposition parameters such as source and substrate temperature, pressure, source geometry and feed rate etc. Common deposition problems, such as lack of control over the feed rate, source and substrate temperature can produce significant deviations in the film composition and create undesirable variations in the structural and

electro-optical properties of the films. These problems are discussed in detail.

When depositing thin films for a particular application it is necessary to outline the desired properties. In the case of CIGS for photovoltaic applications the films should have the correct composition (comparable to the starting material), structure (chalcopyrite), a large grain size (>1μm), the desired resistivity (<5 Ωcm) etc. [192,193].

Initially it was decided to optimise the deposition process to produce the desired structure, grain size and composition.

## 4.2 Investigation of the starting material

For the deposition of thin films of CIGS and CIS by flash evaporation, the source materials were prepared by the direct fusion of elements in a quartz ampoule as described in section 3.2. Since the flash evaporation technique involves the rapid evaporation of pre-reacted starting material it is necessary to characterise the starting material to compare and contrast it's properties with that observed in the deposited films. The elemental composition and structure of the starting materials were analyzed using EDAX and XRD respectively.

### 4.2.1 $CuIn_{0.75}Ga_{0.25}Se_2$

XRD analysis of the starting material of CIGS revealed a typical spectrum as shown in figure 4.1. It can be seen that the structure is chalcopyrite from the observed characteristic peaks <101> and <211>, at 2Θ values of 17.2° and 35.7° respectively. The most intense peak is the <220,204> with the <112> (the second most intense peak) observed along with the other CIGS related diffraction lines. Since the ionic radius of gallium is smaller than indium, a smaller unit cell is expected when gallium is substituted for indium. Therefore, CIGS has consistently lower d-spacing (higher 2Θ) values. The measured and calculated d-values from the spectra were compared with the reported data [186] to calculate the hkl values of the corresponding peaks, table 4.1. It is evident that the measured and calculated d-values of our material are in good agreement with each other. However, the reported [186] d-value of the <112> peak, 3.29, is slightly lower than the measured/calculated value of 3.31. This could be due to a small measurement error. In addition, peaks corresponding to <101>, <103>, <213,105> and <411,217> have not been reported, probably due to limited sensitivity of the XRD equipment used.

In order to perform the compositional analysis of the pre-reacted starting material, the powder was re-melted in an evacuated quartz ampoule for 6 hours at 1200°C. Mechanical rocking was performed regularly to completely homogenise the mixture. The resulting ingot was characterised using EDAX technique. Analysis was performed at several different sites on the ingot and the results are tabulated in table 4.2.

The average value of the copper content in the starting material was found to be 23.65 atm.%, approximately 5% lower than the theoretical value of 25 atm.%. The average atm.% contents of gallium and selenium were found to be 5.8 and 49.65 respectively. These values differ by approximately 6.4% and 0.7% from that of the theoretical values. The indium content of 20.8 atm.% was about 10% higher than the theoretical value of 18.76 atm.%. If we consider the accuracy of the EDAX technique which has a reported [194] measurement error of ±4%, the deviation in copper, gallium and selenium are within this measurement error. However, the variation between the theoretical and measured indium content is greater than this reported measurement error. This is to be expected due to copper segregation [195] (to the grain boundaries) giving a false indium content.

A representative EDAX spectrum for CIGS is shown in figure 4.2, illustrating the respective peaks of copper, indium, gallium and selenium. For each element there are two peaks that can be distinguished, these are designated alpha ($\alpha$) and beta ($\beta$). These peaks originate from the relaxation of excited electrons, see section 3.9. In the spectrum shown in figure 4.2, all elements except In show the $K_\alpha$ and $K_\beta$ peaks which indicates both the final place of the electron and also the type of transition that has taken place. For example, $K_\alpha$ indicates that the electron has jumped to a K shell from the nearest outer L shell. Since the probability of transition from the nearest shell is greater the peak intensities for $K_\alpha$ transitions are larger than that for $K_\beta$ peaks. This is observed for all elements except indium in which case the $L_\alpha$ peak is observed, this is due to the $K_\alpha$ peak being out of the considered range. In addition the $K_\alpha$ peak intensity for indium is very low and when combined with computer simulation the resultant errors are

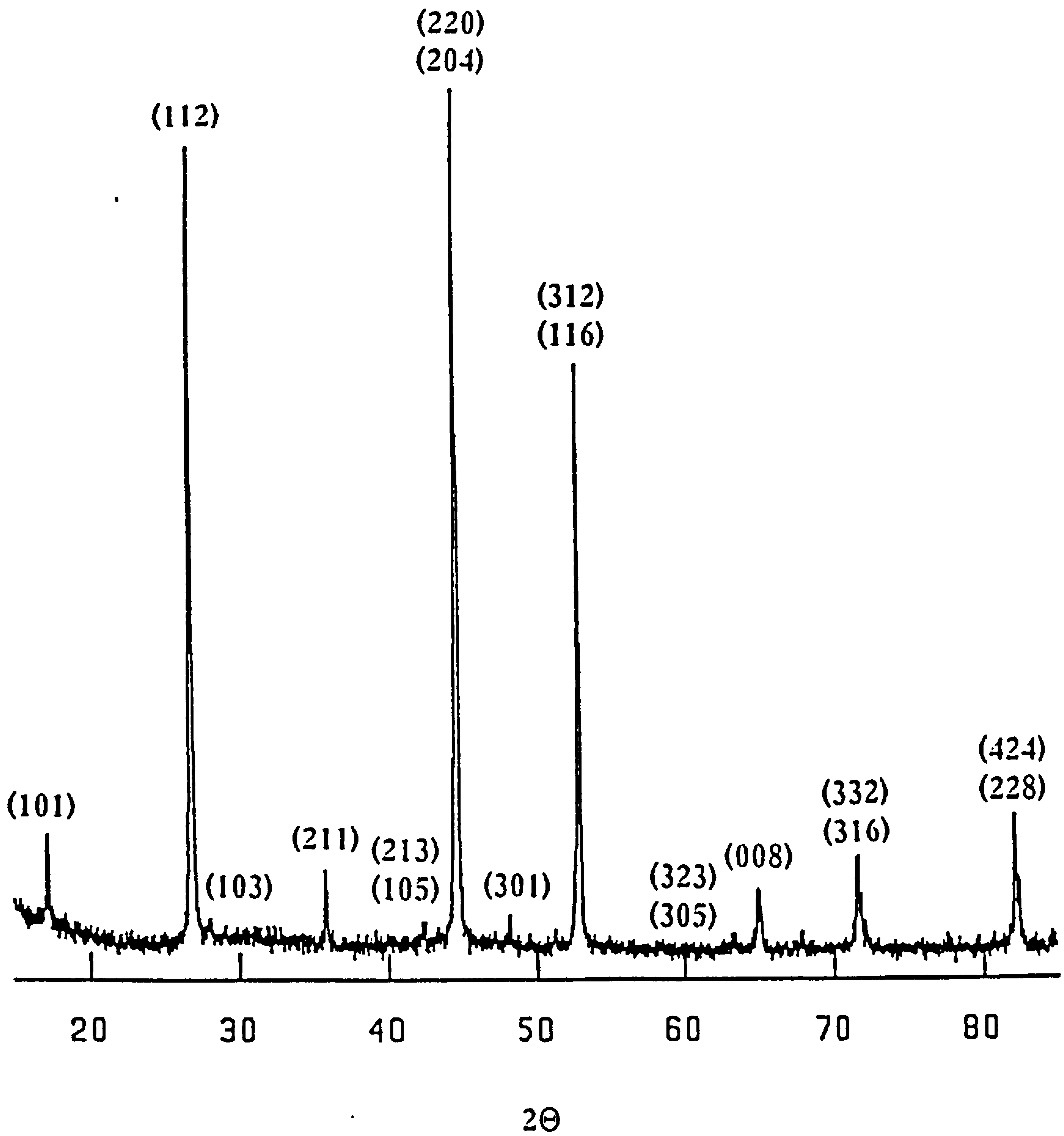


Figure 4.1: XRD spectrum of the polycrystalline $CuIn_{0.75}Ga_{0.25}Se_2$ pre-reacted starting material.

| Peak No. | d-value (meas.) | angle (2Θ) | $I/I_{max}$ (%) | d-value (calc.) | hkl | d-value [186] |
|---|---|---|---|---|---|---|
| 1 | 5.14 | 17.2 | 12.2 | 5.13 | 101 | - |
| 2 | 3.32 | 26.82 | 94.81 | 3.313 | 112 | 3.29 |
| 3 | 3.19 | 27.94 | 2.89 | 3.18 | 103 | - |
| 4 | 2.51 | 35.74 | 8.52 | 2.50 | 211 | 2.495 |
| 5 | 2.13 | 42.34 | 2.20 | 2.129 | 213,105 | - |
| 6 | 2.03 | 44.58 | 100 | 2.025 | 220,204 | 2.015 |
| 7 | 1.88 | 48.16 | 2.89 | 1.88 | 301 | 1.899 |
| 8 | 1.72 | 52.98 | 67.33 | 1.728 | 312,316 | 1.723 |
| 9 | 1.46 | 63.26 | 1.37 | 1.469 | 305,323 | 1.476 |
| 10 | 1.43 | 64.88 | 7.18 | 1.433 | 008 | 1.435 |
| 11 | 1.38 | 67.76 | 1.43 | 1.381 | 411,217 | - |
| 12 | 1.31 | 71.61 | 11.06 | 1.315 | 332,316 | 1.316 |
| 13 | 1.17 | 82.17 | 15.21 | 1.170 | 424,228 | 1.17 |

Table 4.1 X-ray powder diffraction data of CIGS pre-reacted starting material.

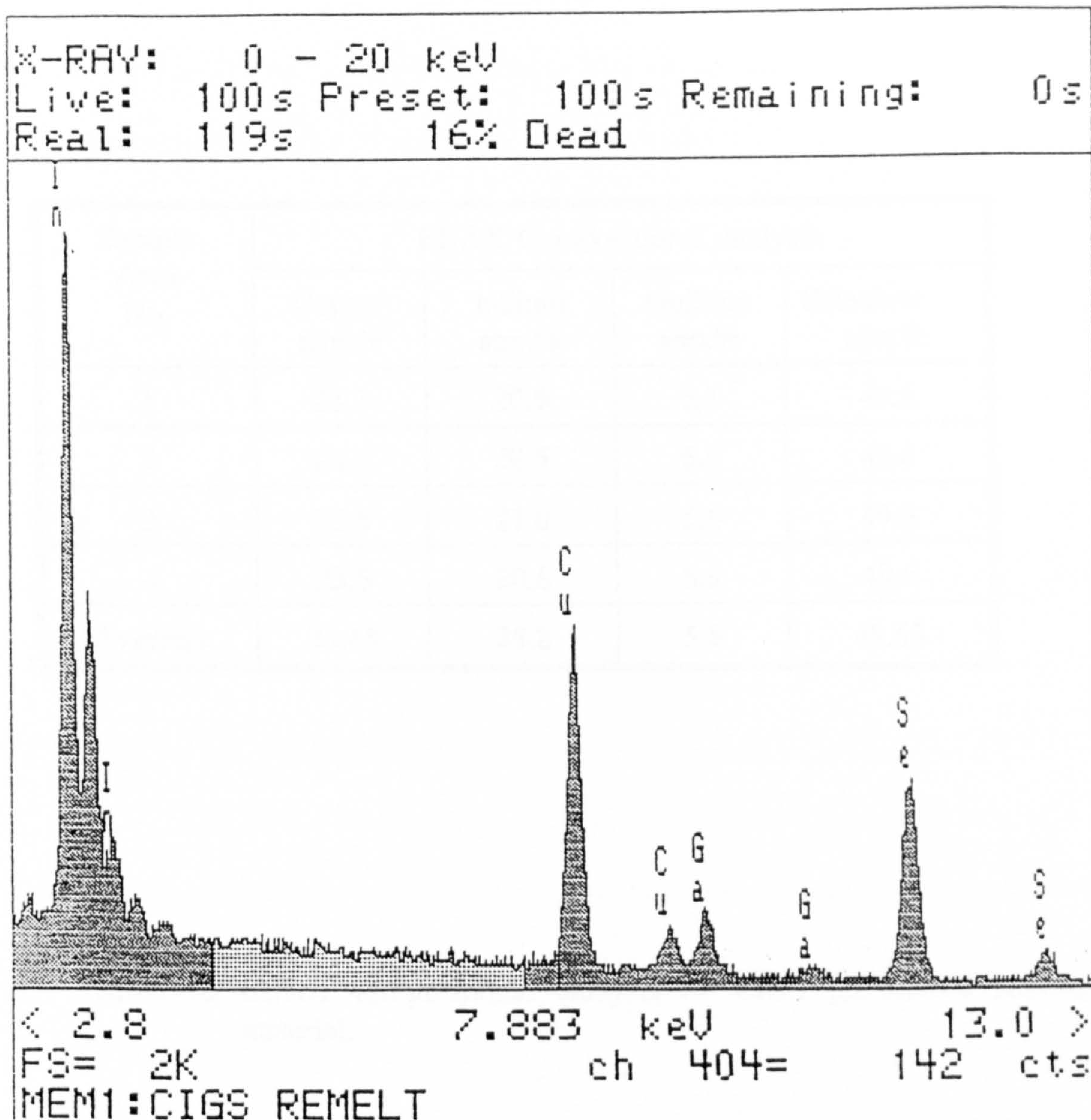


Figure 4.2: EDAX spectrum of the polycrystalline $CuIn_{0.75}Ga_{0.25}Se_2$ pre-reacted starting material.

| Sample Area No. | EDAX Compositional analysis | | | |
|---|---|---|---|---|
| | Copper atm.% | Indium atm.% | Gallium atm.% | Selenium atm.% |
| 1 | 23.3 | 20.9 | 6.1 | 49.6 |
| 2 | 24.3 | 20.5 | 5.6 | 49.6 |
| 3 | 23.5 | 21.0 | 5.6 | 49.8 |
| 4 | 23.5 | 20.8 | 5.9 | 49.6 |
| Average | 23.65 | 20.8 | 5.8 | 49.65 |

Table 4.2. EDAX compositional analysis of CIGS pre-reacted starting material.

unacceptably large [194].

Pre-reacted starting material of CIGS was p-type as measured by the hot probe technique. The observed value of resistivity was 13.21 Ωcm.

### 4.2.2 $CuInSe_2$

Pre-reacted starting material of $CuInSe_2$ was also analyses by XRD and EDAX. The observed XRD spectra is shown in figure 4.3. It can be seen that the structure is again chalcopyrite, the <101> and <211> diffraction peaks being present. The d-values corresponding to different diffraction peaks from the spectra were compared with those of Parkes et al. [173] and were found to be in good agreement. The only difference observed is in terms of the intensity of the diffraction peaks as shown in table 4.3. It is also evident from the spectra that the structure is oriented in the <112> plane as the <112> is the most intense peak.

A similar process of re-melting was performed to prepare a piece of ingot of CIS material for the EDAX compositional analysis. The EDAX results obtained from different areas of the ingot are shown in table 4.4. Once again the average value of indium was found to be 27.8 atm.%, approximately 2.8 atm.% (approximately 11%) higher than that of the theoretical value of 25 atm.%. The atm.% of copper and selenium were approximately 7% and 2% lower than that of theoretical values of 25 and 50 atm.%. The observed lower value of copper could again be due to the segregation

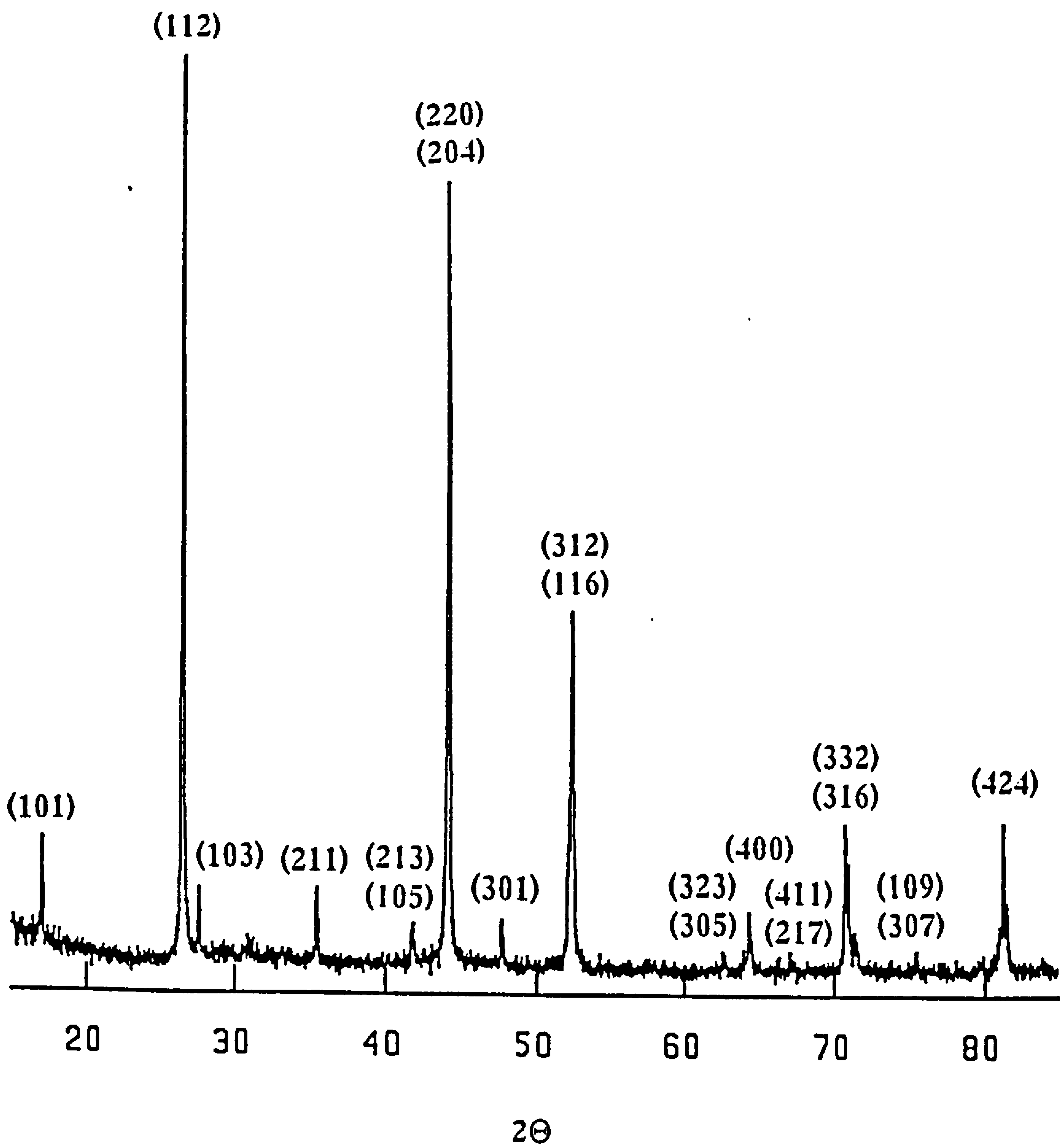


Figure 4.3: XRD spectrum of the polycrystalline $CuInSe_2$ pre-reacted starting material.

| Peak No. | d-value (meas.) | angle (2Θ) | $I/I_{max}$ (%) | d-value (calc.) | hkl | $I/I_{max}$ (%) | d-value [173] |
|---|---|---|---|---|---|---|---|
| 1 | 5.204 | 17.02 | 11.95 | 5.20 | 101 | 6 | 5.20 |
| 2 | 3.343 | 26.64 | 100 | 3.34 | 112 | 70 | 3.34 |
| 3 | 3.224 | 27.65 | 7.75 | 3.20 | 103 | 6 | 3.20 |
| 4 | 2.530 | 35.44 | 7.62 | 2.52 | 211 | 15 | 2.52 |
| 5 | 2.157 | 41.83 | 3.62 | 2.15 | 105,213 | 6 | 2.15 |
| 6 | 2.047 | 44.20 | 87.43 | 2.04 | 204,220 | 100 | 2.04 |
| 7 | 1.899 | 47.85 | 3.45 | 1.90 | 301 | 6 | 1.900 |
| 8 | 1.747 | 52.31 | 37.52 | 1.74 | 116,312 | 85 | 1.743 |
| 9 | 1.482 | 62.63 | 1.40 | 1.48 | 305,323 | 6 | 1.480 |
| 10 | 1.447 | 64.30 | 6.75 | 1.44 | 400 | 25 | 1.446 |
| 11 | 1.395 | 67.02 | 1.35 | 1.39 | 217,411 | 4 | 1.393 |
| 12 | 1.328 | 70.91 | 15.74 | 1.32 | 316,332 | 35 | 1.327 |
| 13 | 1.257 | 75.54 | 1.09 | 1.25 | 109,307 | 2 | 1.256 |
| 14 | 1.200 | 79.84 | 1.09 | 1.20 | 415 | 2 | 1.200 |
| 15 | 1.182 | 81.31 | 17.44 | 1.18 | 424 | 60 | 1.181 |

Table 4.3 X-ray powder diffraction data of CIS pre-reacted starting material.

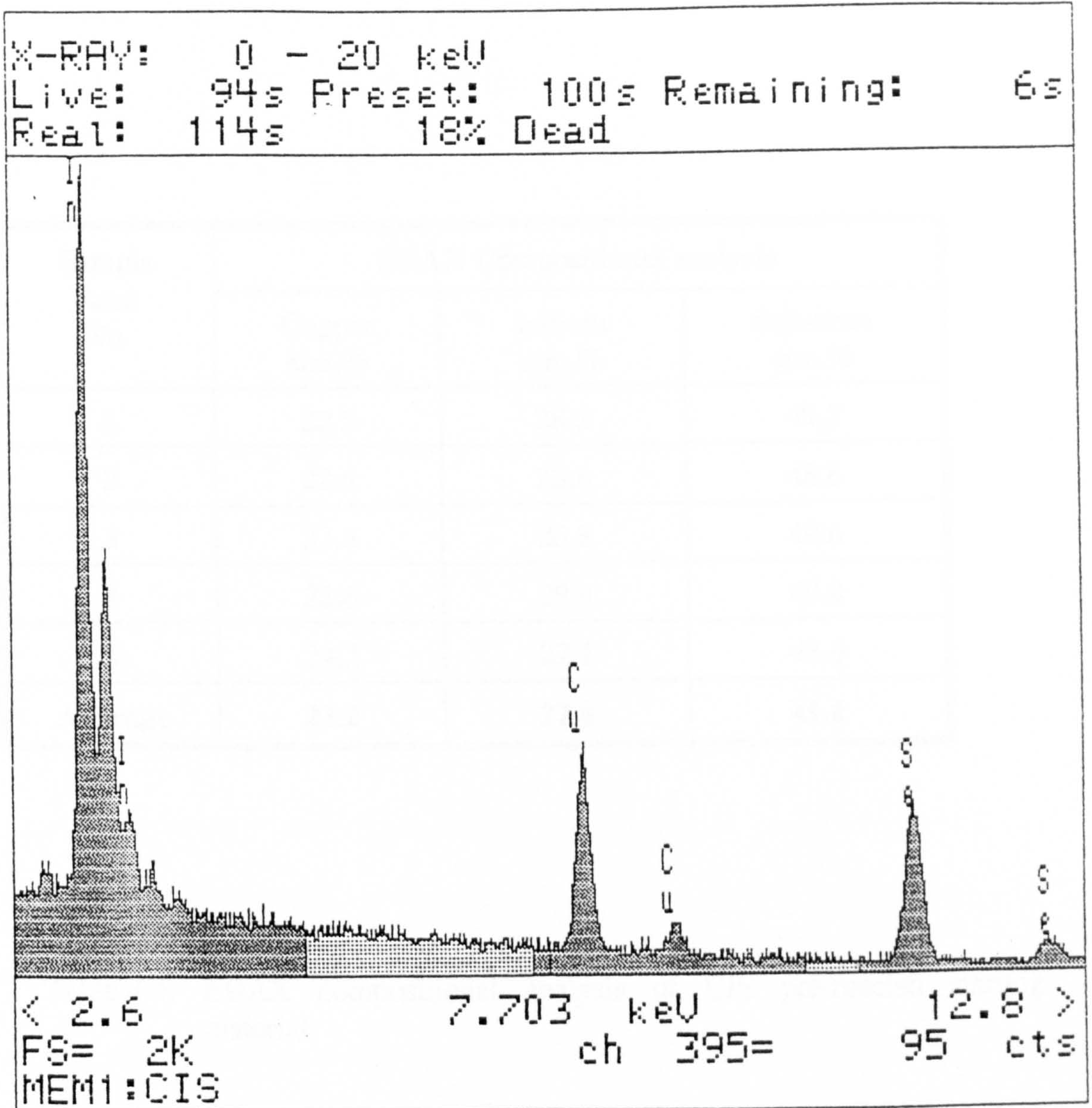


Figure 4.4: EDAX spectrum of the polycrystalline $CuInSe_2$ pre-reacted starting material.

| Sample Area No. | EDAX Compositional analysis | | |
| --- | --- | --- | --- |
| | Copper atm.% | Indium atm.% | Selenium atm.% |
| 1 | 22.5 | 28.2 | 49.3 |
| 2 | 22.6 | 28.6 | 48.8 |
| 3 | 23.6 | 26.8 | 49.6 |
| 4 | 22.6 | 28.4 | 49.0 |
| 5 | 24.3 | 27.1 | 48.6 |
| **Average** | **23.2** | **27.8** | **49.0** |

Table 4.4. EDAX compositional analysis of CIS pre-reacted starting material.

process as reported in literature [186,195].

The EDAX spectrum of the remelted CIS is shown in figure 4.4. This spectrum is identical to the one for CIGS starting material except for the missing gallium peaks. Once again the $\alpha$ and $\beta$ peaks corresponding to copper, indium and selenium are identified.

Electrical characterisation revealed that the pre-reacted material was p-type with an average bulk resistivity value of 5.56 $\Omega$cm.

## 4.3 Effect of source temperature

It is an established fact that the properties of vacuum evaporated thin films depend upon the deposition conditions. The source temperature, in particular, is a critical factor in determining the composition and structure of the films deposited. Therefore, for the preparation of homogeneous and stoichiometric thin films of the multi-component alloys and compounds of interest here, the source temperature must be precisely controlled and should be high enough to evaporate all the constituent elements.

A systematic study of the effect of the evaporation temperature, on the composition of CIGS thin films has been carried out and the results are shown in figure 4.5. The source temperature was systematically varied from 1100°C to 1550°C in 50°C steps. The original pressure of $10^{-7}$ dropped to $10^{-5}$ mbar during deposition. This pressure was

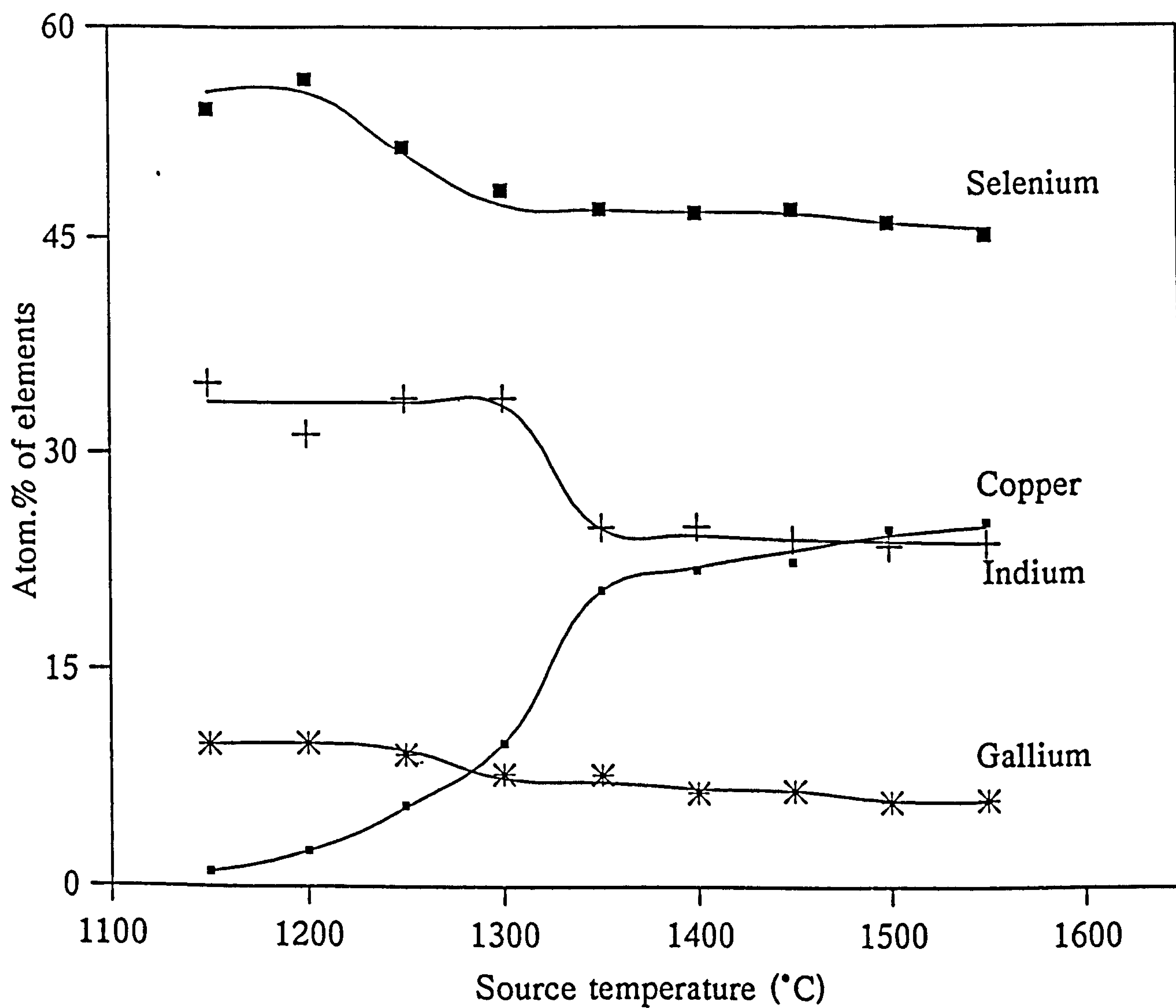


Figure 4.5: Effect of source temperature on the composition of polycrystalline CIGS thin films.

maintained throughout the deposition process. A flat tungsten strip type source was used for the initial flash evaporation experiments. Pre-reacted CIGS powder was dropped onto the source from a hand driven vibratory hopper. The composition of the films were determined using the EDAX technique.

A complete absence of copper was found in films deposited at source temperatures less than 1100°C. At elevated temperatures from 1100 to 1400°C, the copper content gradually increased from 2 to 20 atm.%. Increasing the temperature to 1550°C resulted in a film content of 25 atm.%, this is comparable to that of the starting pre-reacted CIGS material. One of the major objectives of this study was to reproduce the composition of the starting material. These results thus demonstrate that the efficiency of mass transfer at this temperature is at its optimum for copper.

A consideration of the indium content from figure 4.5 shows that it is relatively constant at about 35 atm.% between the temperatures of 1150°C to 1300°C. The indium content then decreased rapidly to a level of 24 atm.% with a further 50°C increase in temperature and then decreased very slowly to 23 atm.% up to a temperature of 1550°C. Between the temperatures of 1150°C and 1250°C the gallium content remained relatively constant at approximately 10 atm.%. A further 50°C increase in temperature caused the gallium content to decrease to about 7 atm.%. The change in gallium content was insignificant at between 1300°C to 1550°C as only a 1 atm.% decrease was observed. The atomic percentage of selenium (the most volatile component) was initially 55 atm.% at a temperature of 1200°C, this slowly decreased to 47 atm.% between the temperature range of 1200°C to 1300°C. At 1550°C a value of 46 atm.% was recorded.

It is evident from figure 4.5 that the temperature at which indium and gallium starts to decrease is at about 1350°C. At this temperature the copper content is also approaching that of the starting material. However, in the case of selenium, the temperature at which the film composition matches that of the starting is about 150°C lower than that for gallium and indium. The films produced at temperatures greater than 1300°C can be considered to be close to the bulk composition. This is in good agreement with the observations reported by Tomlinson et al. [62] who also proposed a minimum source temperature of 1300°C while studying the effect of source temperature on the composition of CIS thin films.

Careful examination of data plotted in figure 4.6 reveals that for all the constituent elements of the CIGS films there are 3 main regions. There exists a low temperature region where the composition is relatively constant, a transition region where there are significant changes occurring and a high temperature region where once again the elemental variations become minimal. When comparing the temperature ranges of the transition regions for gallium, indium and selenium with the published vapour pressure data it appears highly likely that there is a relationship between them. The elements with the higher vapour pressure have lower average transition temperature values compared to elements with a lower vapour pressure. Figure 4.7 shows the vapour pressure data [196] for copper, indium, gallium and selenium. The elements copper, indium and gallium show a similar rate of increase of vapour pressure with increased temperature, whereas, the rate of increase of selenium is much more rapid. In addition, in order to obtain a vapour pressure of $10^{-2}$ mbar for copper, gallium, indium and selenium, temperatures of 1240°C, 1030°C, 900°C and 228°C respectively have to be attained.

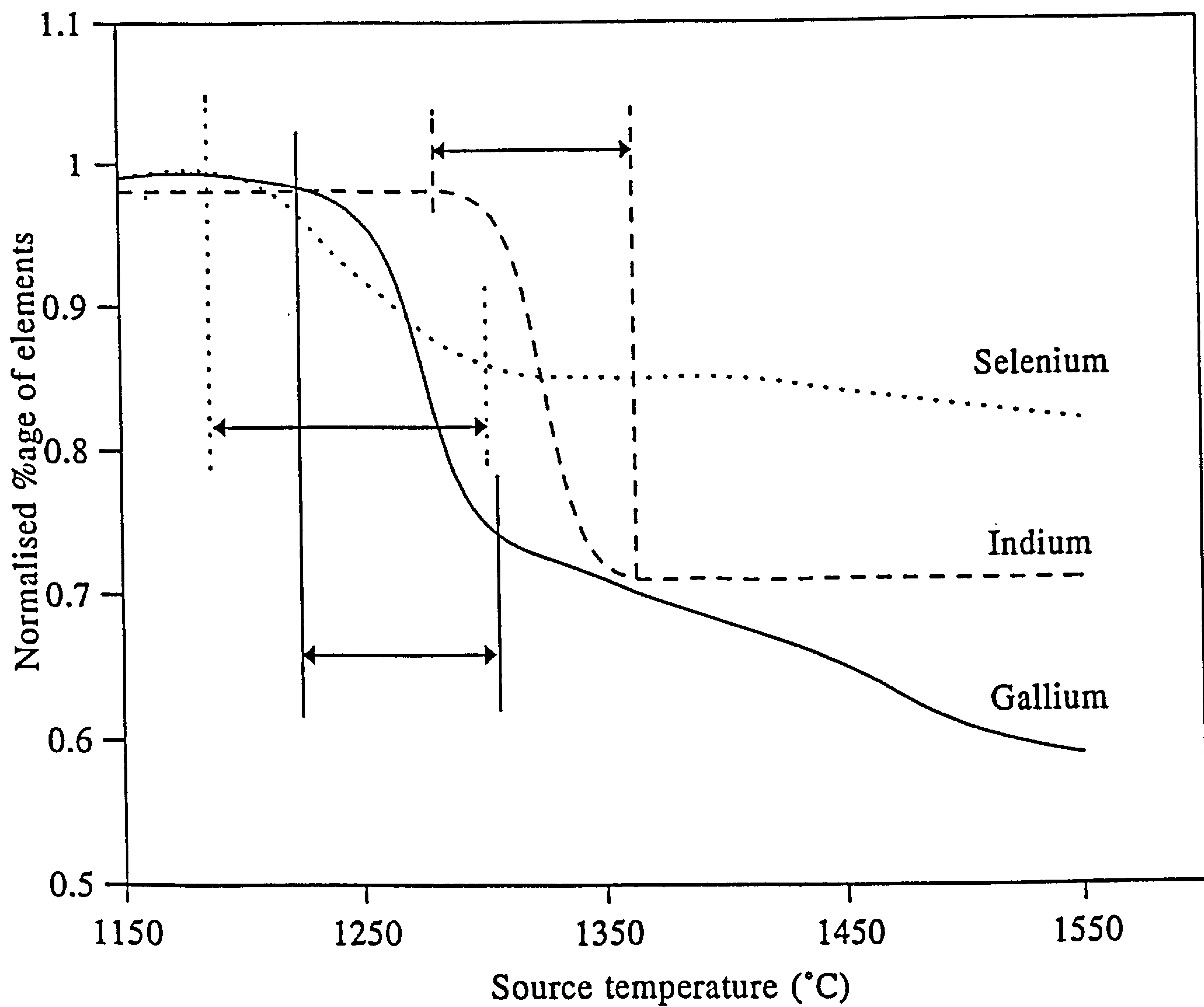


Figure 4.6: Different regions of indium, gallium and selenium curves exhibiting the behaviour of polycrystalline CIGS film composition with respect to source temperature.

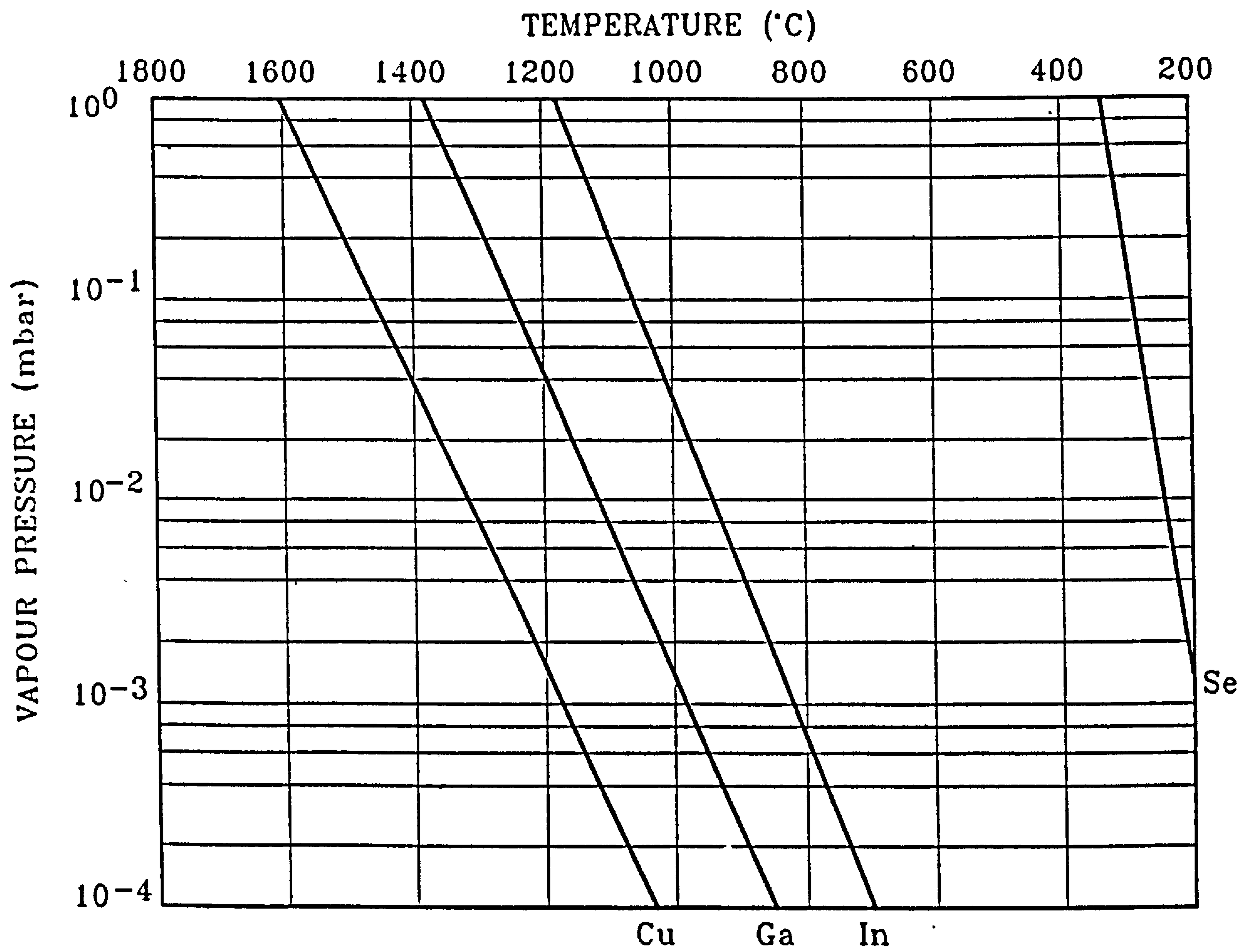


Figure 4.7: Vapour pressure data of copper, indium, gallium and selenium [196].

| Element/Compound | $\Delta_f H^\circ_{298}$ | $\Delta_f G^\circ_{298}$ |
|---|---|---|
| | kJ mol$^{-1}$ | kJ mol$^{-1}$ |
| $Cu_{(g)}$ | 338 | 299 |
| $Cu_{2(g)}$ | 484 | 432 |
| $Cu_{(s)}$ | 0 | 0 |
| $CuSe_{(g)}$ | 309 | 253 |
| $CuSe_{(s)}$ | -40 | -40 |
| $Cu_2Se_{(s)}$ | -59 | -74 |
| $CuSe_{2(s)}$ | -43 | -40 |
| $In_{(g)}$ | 243.3 | 209 |
| $In_{2(g)}$ | 381 | 340* |
| $In_{(s,l)}$ | 0* | 0 |
| $InSe_{(g)}$ | 234 | 185 |
| $InSe_{(s)}$ | -117 | -112 |
| $In_2Se_{(g)}$ | 153 | 102 |
| $In_2Se_{(s)}$ | -130 | -122 |
| $In_2Se_{2(g)}$ | 101 | 59 |
| $In_2Se_{3(g)}$ | -343 | -331 |
| $Se_{(g)}$ | 227 | 187 |
| $Se_{2(g)}$ | 146 | 96 |
| $Se_{(s,l)}$ | 0* | 0* |
| $CuInSe_{2(s)}$ | -204 | -201 |

Table 4.5 Enthalpies and Gibbs free energies [197].

This illustrates clearly the order in which the evaporation can occur if the temperature of the source is raised slowly; selenium first, followed by indium, gallium and then copper. From this analysis it can be seen that at low temperatures (<1300°C), phases of In/Se and Ga/Se can form readily. The formation of Cu/Se phases at these temperatures are less likely to occur as insufficient copper is evaporated, as reported by Neumann et al [32]. This supposition is further supported when one examines the free energies of formation of the various phases. Cahen and Noufi [197] formulated a table (see table 4.5) including data collected from different references along with their own work (indicated by *) to represent the free energies of formation of different phases. It can be seen that the In/Se phases form much more readily than Cu/Se phases due to their much lower free energies of formation. It is interesting to note that the free energy of formation of $In_2Se_3$ compared to $CuInSe_2$ (-331 and -201 kJ mole$^{-1}$ respectively) indicates the ease with which secondary phases can be formed during the deposition of CIS. Experimental observations [32] show that $In_2Se_3$ and related phases were predominant in the CIS films at low temperatures supporting the above arguments. This is not unexpected as elements with lower vapour pressures require more thermal energy to evaporate than those with higher vapour pressure.

The widths of the transition regions were calculated and found to be 85, 85 and 114. It is interesting to note that the widths of the gallium and indium regions are the same. It can be postulated that these two elements substitute for one another in the lattice structure, this is not surprising as they have similar physical properties (both are group III elements). The atomic radii of both gallium and indium are identical (0.081 nm) making substitution a relatively simple process. The changes in the elemental

composition can be considered in terms of percentage changes in each of the constituents (fig 4.6). If we consider gallium and indium, the percentage decrease in composition is approximately 38% and 31% respectively, further supporting the case for substitution discussed above. The selenium decrease is approximately 17%; this can be partially attributed to a radiation effect, heat being transferred from the source to the substrate and/or a dilution effect as the amount of the other elements increases. It has been reported that radiation effects are likely [62], as the substrate temperature is increased by approximately 100 - 200°C [62], which is very close (approximately 212°C) that require to re-evaporate selenium from the substrate. This effect could be more significant in the case of heated substrates. In the present case, since these particular films were deposited at room temperature, a dilution effect can arguably be considered.

In order to compare the variation of elemental composition with temperature and with one another the data was mathematically treated by the process of normalisation. The following discussion focuses only on the central transition region mentioned above where considerable changes took place. For the elements being considered the starting of the central transition region occurred at different points and therefore normalised temperatures given in the figure caption where used in order to mathematically eliminate vapour pressure effects. The atm.%'s of indium, selenium and gallium were normalised against the maximum composition value. To make it easier to compare and quantify the changes observed the copper atm.% values were both normalised and inverted. In figure 4.8 all the elemental curves follow a similar trend. As the amount of copper in the film increased there was a corresponding decrease in all of the other constituent elements

namely indium, gallium and selenium.

The objective of this analysis was to compare and quantify the transition region for each element irrespective of the starting point. The change in the amount of copper in the film as a function of source temperature was most pronounced. The selenium, gallium and indium data followed similar trends with the change being less pronounced. It was postulated that the rate of increase of copper temperature was directly proportional to the decrease in the other elements. To quantitatively compare this effect the rates of change of selenium, indium and gallium were added together and shown on the same plot (dotted line). It can be seen that there is good agreement between the rates of increase of copper and the overall rate of decrease of the other elements. It can be seen that the total change in concentration for indium, gallium and selenium are about 38, 31 and 17% respectively compared to 96% for copper. Thus it appears the incorporation of copper is at the expense of selenium, gallium and indium. The apparent difference is within experimental errors of the techniques used.

Under our experimental conditions, a source temperature of approximately 1550°C (measured by the optical pyrometer) was found to be the optimum evaporation temperature for the successful deposition of CIGS thin films. This is in good agreement with the reported source temperature of 1500°C [143]. However, the reported source temperature in the literature is 200°C higher than our source thermocouple temperature measurement. This difference may be due to the fact that the temperature within the CIGS material (on the top surface of the source) is certainly higher than the temperature measured by the thermocouple positioned below the source. This was also supported by

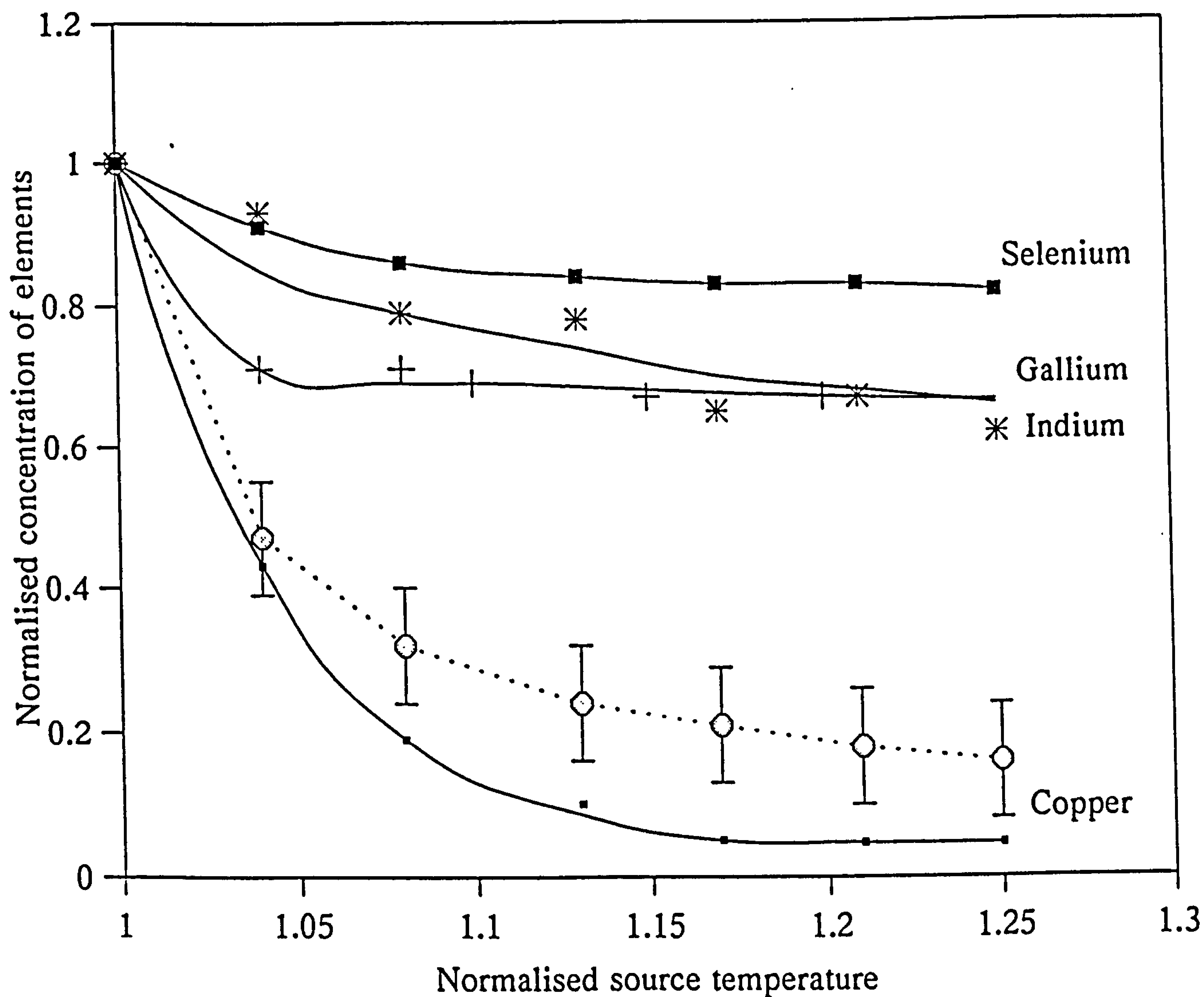


Figure 4.8: Normalised concentration of copper, indium, gallium and selenium in CIGS thin films against the normalised temperature (Normalisation temperature for; copper - 1150°C; indium - 1300°C; gallium - 1200°C and selenium - 1200°C) to indicate the dilution effect.

the measurement of the source temperature by an optical pyrometer focused on the top surface of the evaporation source as explained in section 3.3.5. The pyrometer measurements confirmed that the source temperature was approximately 250°C higher than that determined with the source thermocouple. The actual source temperature was calculated to be the measured thermocouple temperature plus 250°C.

## 4.4 Source geometry

Flash evaporation is a directional process in which the material is evaporated from a hot source towards the substrate. The gaseous concentration of species varies across the plasma region and therefore, in order to achieve high quality deposition the geometrical consideration are of significant importance. For an efficient process most of the material needs to be vaporised and deposited in thin film form. The source thus needs to be heated to a sufficiently high temperature using a suitable heating method. Resistance heating is perhaps the simplest way to do this where a filament or boat of suitable source material is used. In the present study two types of sources, a flat tungsten strip type and Molybdenum twin chimney type, were used and their effect on the film properties was observed.

Initial experiments using the simple flat strip tungsten source produced CIGS thin films which were both powdery and contained pinholes. There could be several possible reasons for the observed characteristics including source geometry, grain size and grain delivery.

If we assume that the grain size and grain delivery were correct then the remaining factor which can affect the surface properties of the deposits is source type. When using a flat strip type source it is possible that un-vaporised powder can be propelled onto the substrate due to the upward source temperature thrust. This is more pronounced if the grain size is too small. Detachment of the un-vaporised powder during and after the deposition results in a surface containing pinholes.

In the evaporation of compound materials fluctuations in grain delivery in the source would be expected to produce corresponding deviations from homogeneity in the deposited films. When a grain of material, such as CIGS, strikes the hot source it first gives off a vapour that consists of the more volatile elements, this changes to a composition that is richer in the less volatile elements. The final composition of the vapour consists almost completely of copper. Also if the powder delivery is slow, a grain which is dropped into the boat is completely vaporized before the next one arrives and the deposited film onto a substrate. Under these conditions the final film would consists of alternating layers of the component elements.

To alleviate these problems it was necessary to use an indirect evaporation technique incorporating a twin chimney molybdenum source. The pre-reacted CIGS powder was fed through an entrance hole and the evaporant was emitted through an exit hole. The use of this modified source resulted in films which were both "smooth" and pinhole free. The surface roughness of films grown using both sources was measured and the results are given in table 4.6. The respective surface roughness profiles of the films deposited by flat strip tungsten and twin Molybdenum chimney type sources, measured by Dektak,

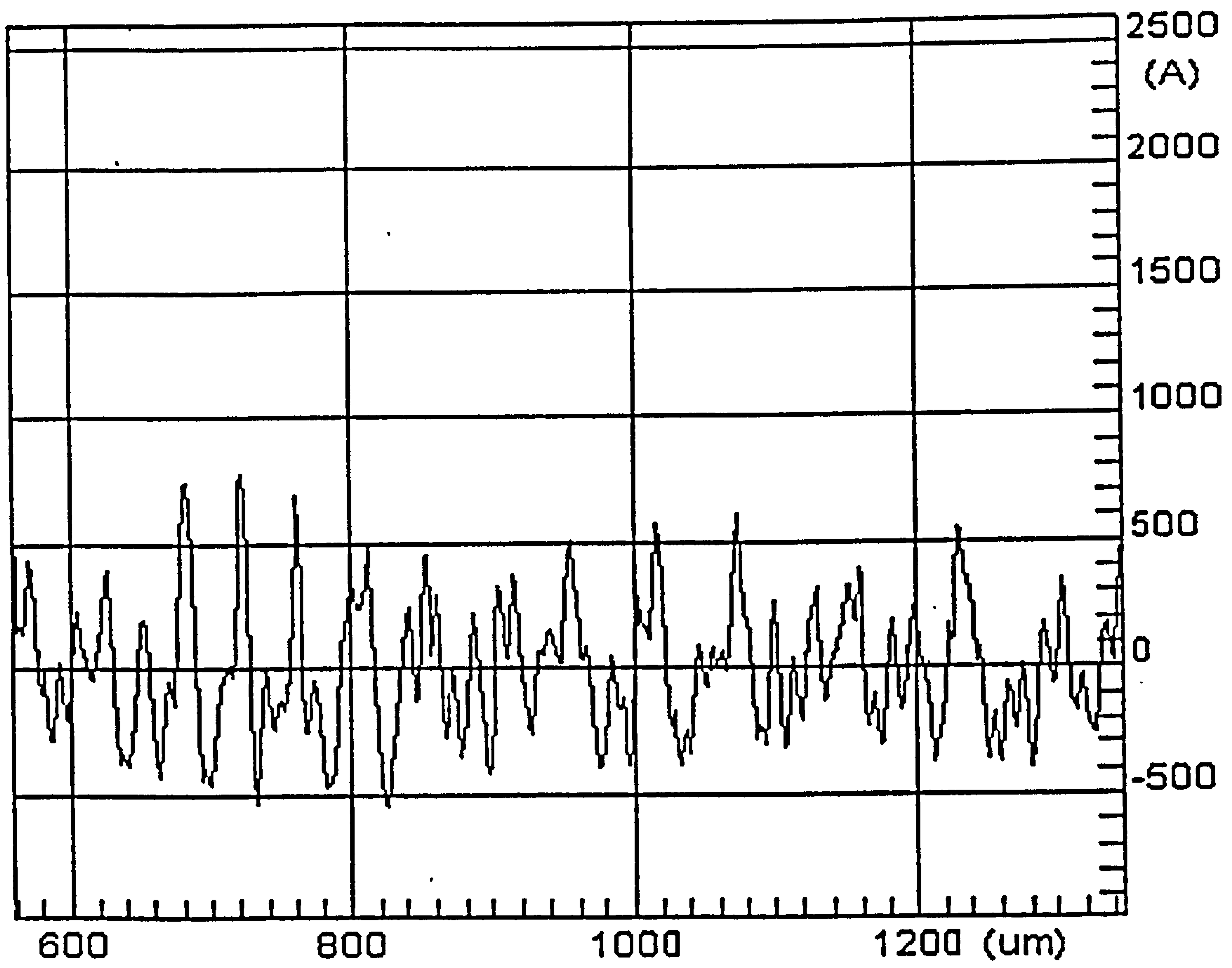


Figure 4.9: Surface roughness (Ra=214Å) of polycrystalline CIGS thin film sample prepared by flat strip tungsten source.

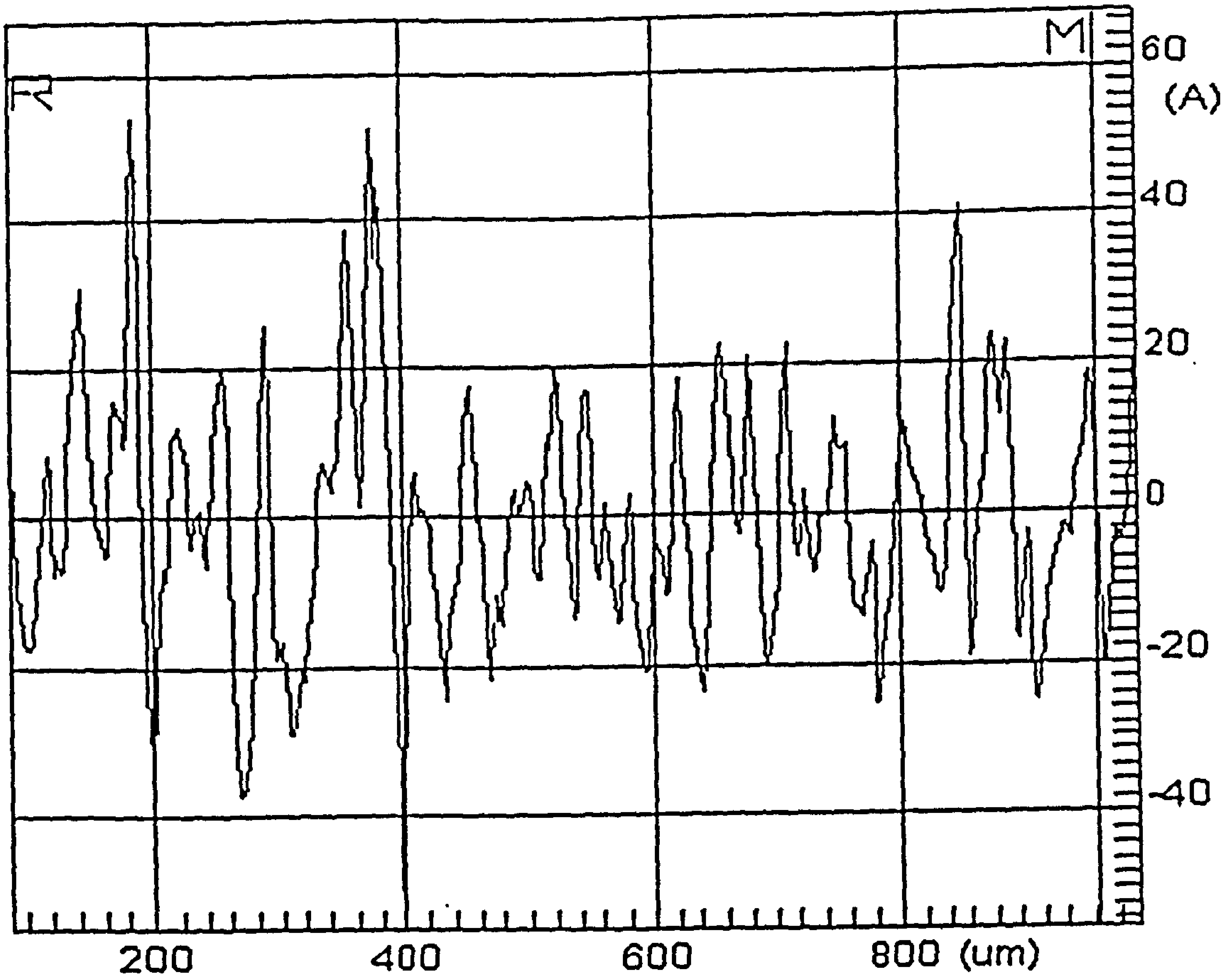


Figure 4.10: Surface roughness (Ra=12Å) of polycrystalline CIGS thin film sample prepared by twin chimney molybdenum source.

| FLAT STRIP SOURCE | | | | TWIN CHIMNEY SOURCE | | | |
|---|---|---|---|---|---|---|---|
| Sample No. | Thickness (Å) | Surface roughness (Å) | Scan length (μm) | Sample No. | Thickness (Å) | Surface roughness (Å) | Scan length (μm) |
| FEO8 | 6800 | 53 | 746 | FE7 | 4975 | 11 | 922 |
| FEO9 | 8450 | 214 | 821 | FE12 | 5051 | 14 | 1545 |
| FEO16 | 6110 | 47 | 1260 | FE18 | 7360 | 12 | 878 |
| FEO17 | 4415 | 170 | 353 | FE23 | 5765 | 10 | 1800 |

Table 4.6 Comparison of the surface roughnesses of CIGS thin films prepared by flat strip type tungsten source and twin chimney type Molybdenum source.

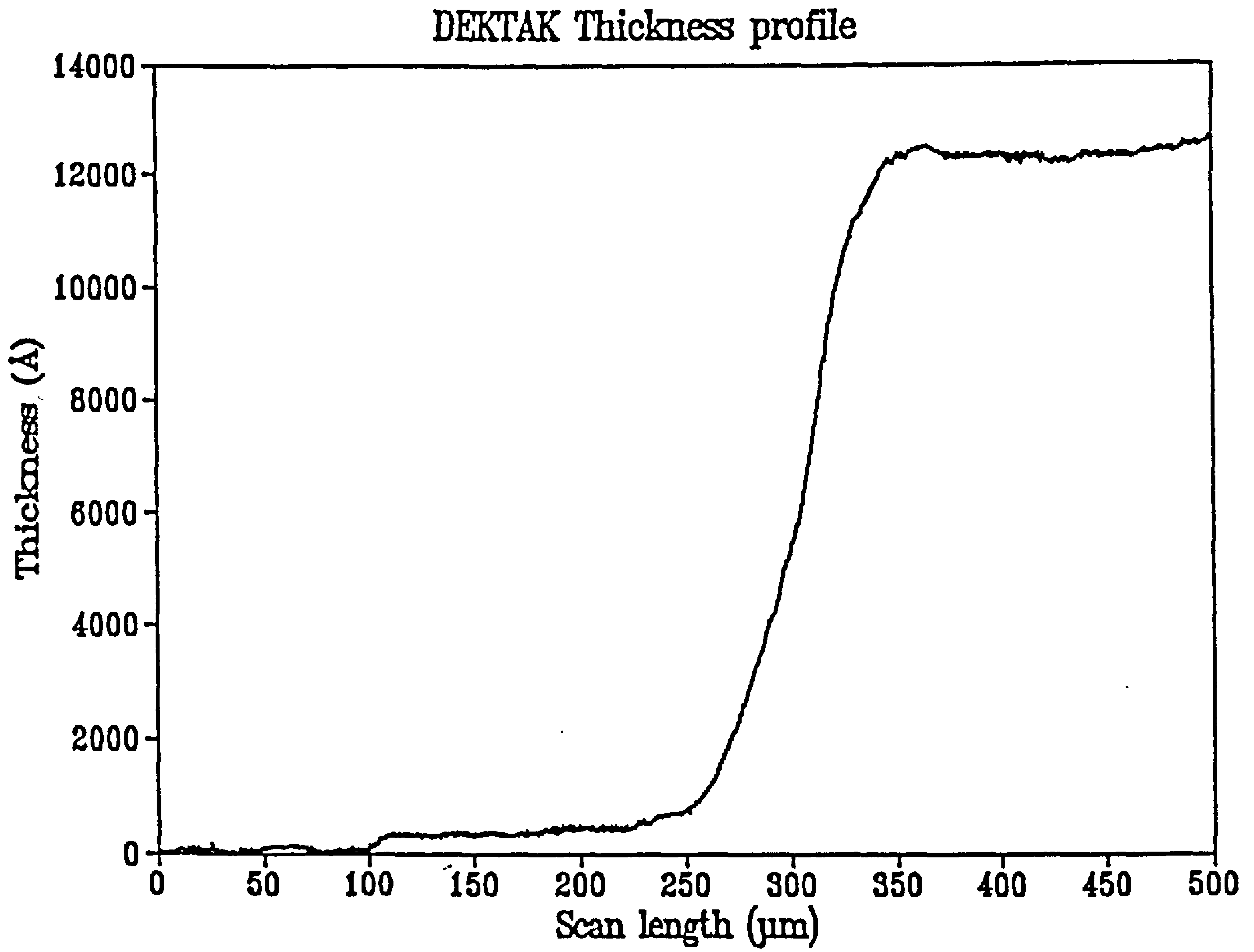


Figure 4.11: Thickness profile of the polycrystalline CIGS thin film measured by Dektak.

are shown in figures 4.9 and 4.10. Prior to these measurements the surface roughness of the glass substrates were ascertained. It was found that films grown using the twin chimney source had a surface roughness of approximately 12Å which is comparable to that of glass slides. In contrast, the films deposited using the flat strip source were uneven.

Thin film samples of CIGS were also analyses by Dektak for thickness. During the deposition of thin films, the area on the glass substrate covered by the holding wire clip, produced a natural step. This step was scanned by Dektak stylus and the resultant thickness step profile is shown in figure 4.11. A comparison was made between these results and those obtained by EDAX and RBS. The measured values of thickness were found to be in good agreement with the values determined by EDAX on the same area of the same sample. However, thickness values determined by RBS were different, probably due to the higher measurement error associated with the RBS technique (discussed in section 4.7.3).

## 4.5. Effect of substrate temperature

An important parameter in the deposition of thin films, regardless of the materials to be deposited or the technology employed, is the substrate temperature. It is well known [69,198,199] that the substrate temperature plays an important role in determining the final film properties. To ascertain the effect of the substrate temperature on the properties of CIGS thin films a series of samples was produced at different substrate

temperatures in the range of room temperature to 200°C. The effects of the substrate temperature on the film structure, surface morphology and electrical properties was investigated using a variety of analytical techniques including XRD, Raman spectroscopy and SEM. As previously discussed, the source geometry can have a significant effect on the way in which heat is transmitted to the substrate, influencing the film characteristics. In these experiments the source temperature was maintained at 1500°C and a molybdenum twin chimney type source was used.

### 4.5.1 X-ray diffraction analysis

In order to determine the effect of substrate temperature on the structure of the CIGS thin films, x-ray diffraction analysis (XRD) was carried out. Examples of the spectra obtained are shown in figure 4.12. An intense <112> diffraction line was observed for the range of substrate temperatures used. However, this peak is broader than that from the starting material. In general, peak broadening may arise from two causes: (a) small particle size and (b) micro-strain. Overall macroscopic strain results in changes in the unit cell dimensions and this leads to the diffraction peak being displaced. If the total film has no overall strain but instead contains small areas of inhomogeneous strain then this will result in peaks slightly displaced from their true position, the combined effect is a broadening of the peak. It can also be seen from figure 4.12 that the intensity and sharpness of diffraction lines depends on the substrate temperature. Samples deposited at low substrate temperature resulted in a less intense and comparatively broad diffraction line. However, a strong well resolved <112> diffraction line is observed as

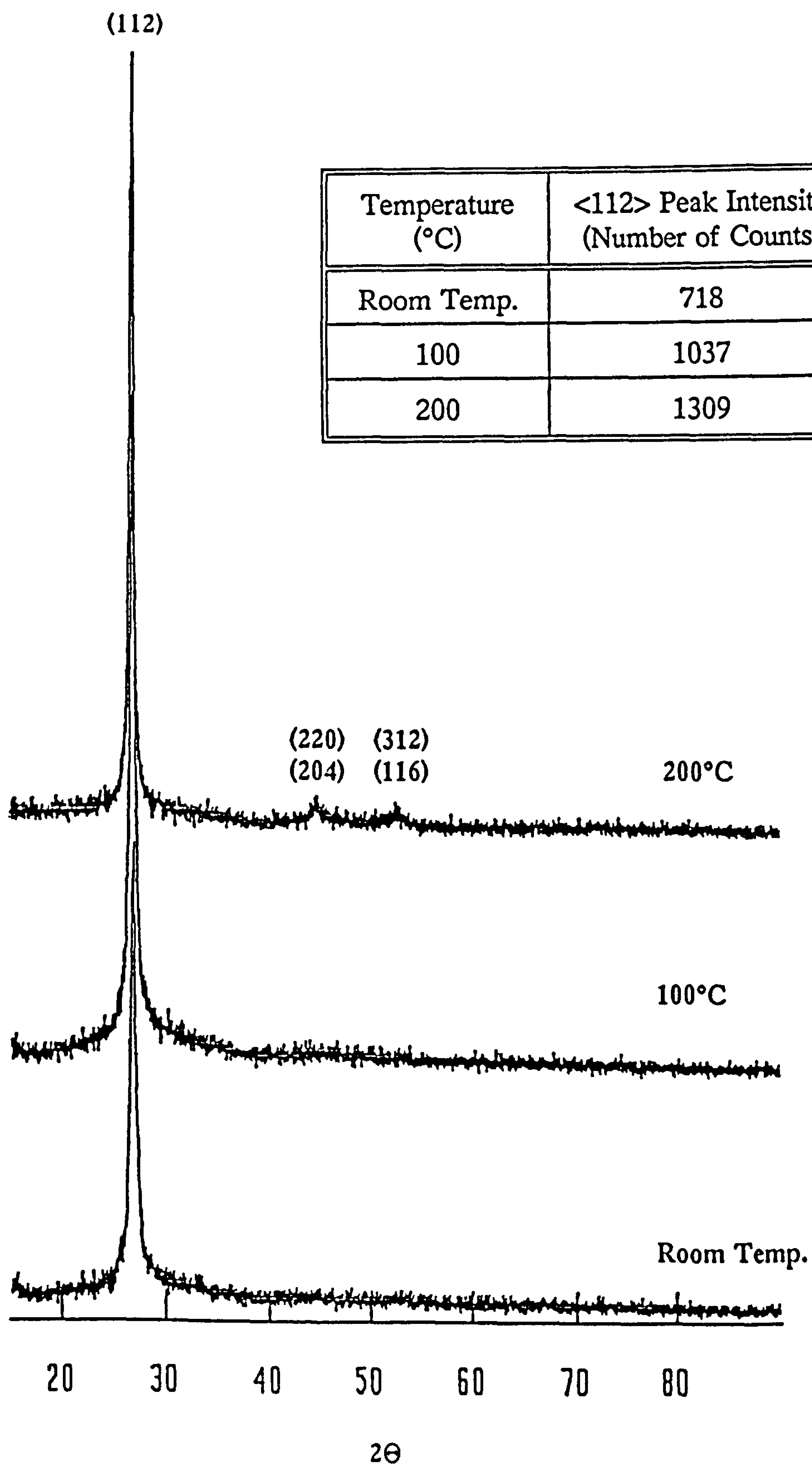


| Temperature (°C) | <112> Peak Intensity (Number of Counts) |
|---|---|
| Room Temp. | 718 |
| 100 | 1037 |
| 200 | 1309 |

Figure 4.12: X-ray diffraction spectra of CIGS films deposited at different substrate temperatures.

the substrate temperature is raised from room temperature to 200°C. In addition, a small increase of the other CIGS diffraction lines, for example the <220,204> and <312,116>, was also observed. This indicates that the flash evaporated films deposited at substrate temperatures less than 200°C are grown with a strong preferred orientation in the <112> plane parallel to the substrate. A small relaxation in the preferred orientation of the film structure was observed at a substrate temperature of 200°C.

It is worth noting that secondary phases are likely to be present in the textured <112> films but routine XRD analysis is not capable of distinguishing the presence of the various phases. According to Dhere et al [75], the sphalerite phase is likely to be present in nearly stoichiometric and copper rich films.

Contrary to the reported work [139], amorphous films were not observed at room temperature and only crystalline films with a strong preferred orientation of <112> were seen. This apparent contradiction can be understood by considering the nature of radiative effects likely to be operating in the experiments performed. Although there was not any active heating of the substrate, due to the small distance between the substrate and the heated source some heating of the substrate is inevitable from radiative transfer of energy. It is thus highly likely that these non-intentionally elevated substrate temperatures are responsible for the strongly observed <112> orientation observed in this work.

To further understand the effects of temperature, substrate structure and type on the degree of crystallinity and preferred orientation in thin film CIS, CGS and CIGS, table

| Process (material) | Substrate type | Substrate Temp. | Phases/ Orientation | Ref. |
|---|---|---|---|---|
| Flash evaporation (CIGS, 25% Ga) | Glass slides | 200°C | Strong <112> orientation | Present work |
| Flash evaporation (CIGS, 25% Ga) | 7059 corning glass | >350°C | Chalcopyrite <112> | 143 |
| Co-evaporation (CIS) | Alumina and glass coated with gold | 300°C<br>>420°C | Amorphous<br>Chalcopyrite with strong <112> | 78 |
| RF Sputtering (CIS) | Corning glass<br>Alumina | 50-300°C<br>>500°C | Sphalerite strong <112><br>Chalcopyrite strong <112> | 79 |
| E-beam evaporation (CGS) | Corning glass | <400°C<br>>400°C | Sphalerite strong <112><br>Chalcopyrite strong <112> | 120 |
| MBE (CIS) | Single Xtal<br>CdS,CIS, and Silica | <300°C<br>>300°C | Amorphous<br>Epitaxial | 164 |
| MOCVD (CIS) | Pyrex<br>Molybdenum | 400°C | Strong <112><br>Strong <112> | 200 |

Table 4.7 Comparative analysis of the structural properties of $Cu(In,Ga)Se_2$ thin films using XRD technique.

4.7 was constructed. In general, the preferred orientation is independent of the growth technology employed. For example, sputtering yielded similar films to electron beam evaporation on Corning glass substrates. If single crystal substrates are used, even at low growth temperatures, a preferred orientation is observed. It is reported by Szot et al [78] that depositions at room temperature onto glass substrates resulted in the production of amorphous films. At higher temperatures, regardless of the substrate structure and material, a high degree of crystallinity is observed by the majority of workers. For example, CIS growth on pyrex, alumina and GaAs substrates all show strongly preferred oriented deposition at high temperatures.

The crystalline structure of the as-grown flash evaporated films is in good agreement with that reported in the literature and has been shown to be dependent on the deposition temperature. Most thick (> 1 μm) coatings exhibit a strong preferred orientation at low deposition temperatures and tend towards more random orientations with increasing deposition temperature [201].

### 4.5.2 Raman spectroscopy

The structural properties discussed above were also investigated using Raman spectroscopy. Figure 4.13 shows examples of spectra obtained for: CIGS single crystal (a), room temperature deposited CIGS thin film (b), deposited at 100°C (c) and 200°C deposited films using flash evaporation (d).

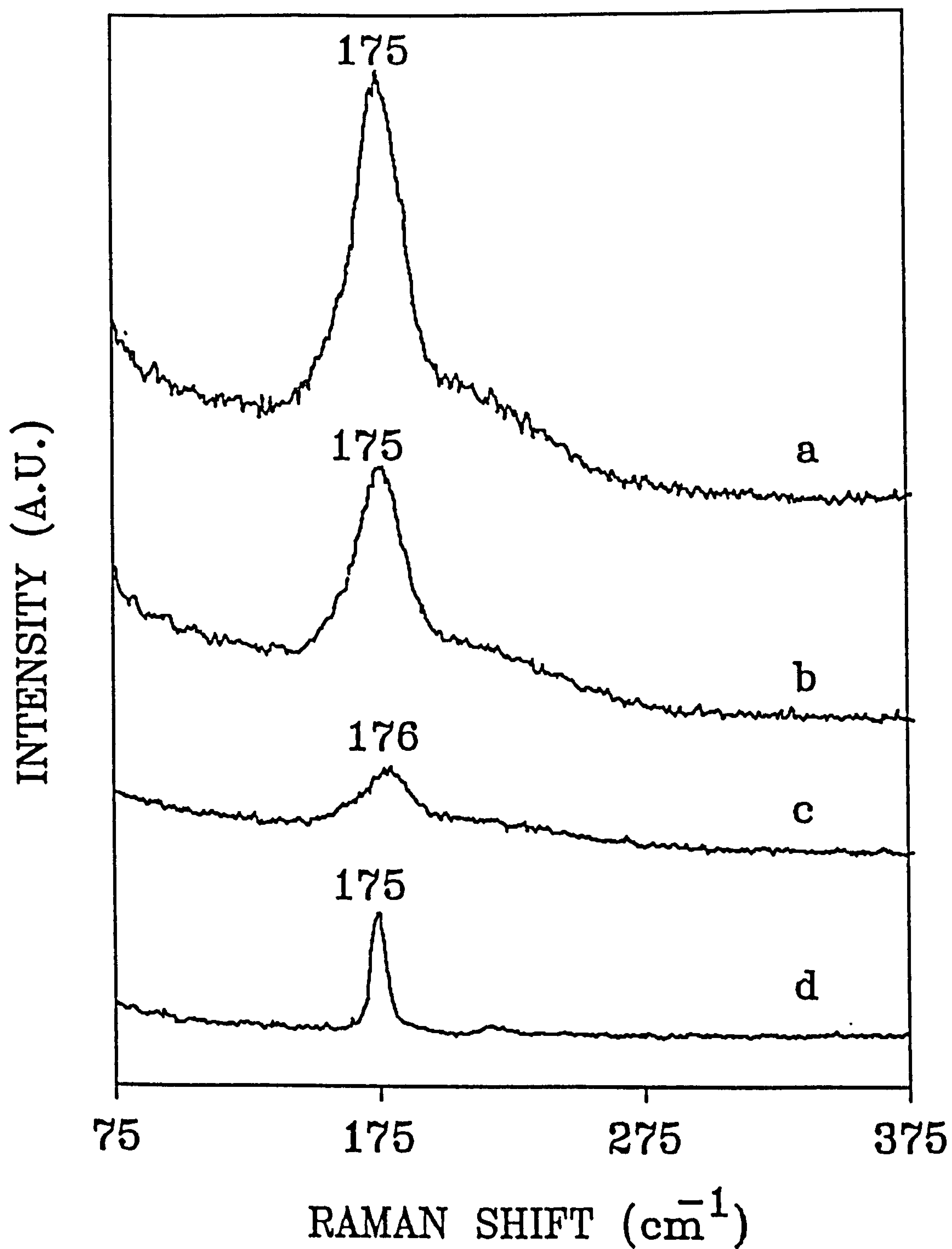


Figure 4.13: Raman spectra of CIGS thin films deposited at 200°C (a), at 100°C (b), at room temperature (c) and standard CIGS single crystal (d).

It can be seen that a single peak ($A_1$) was recorded at approximately 175 $cm^{-1}$ for all the samples. As the deposition temperature was raised the intensity of this peak also increased. From consideration of the full wave half height measurement (FWHM) the peak for the room temperature sample was small and relatively broad, suggesting that the structure of the film consists of very small grains (ca. 1000Å). This is not an unreasonable hypothesis as it is well established for a wide range of materials that the grain size is highly dependent upon deposition temperature [69,198,199]. To a first approximation it can be considered that the higher the deposition temperature the larger the grain size (within strict temperature limits). Flash evaporated films grown at 100 and 200°C demonstrated that the single Raman peak becomes larger and comparatively better resolved as the deposition temperature is increased. Although it is not conclusive, it appears that there is a very broad shoulder to the observed single peak at slightly higher frequency. It can be seen that for the single crystal sample (a), a well defined $A_1$ peak is observed at 175 $cm^{-1}$ with a very small $B_1$ peak at ≈ 215 $cm^{-1}$. It is believed that the shoulder, which is evident in the Raman spectra of thin films, is caused by the overlapping of the broad $A_1$ and $B_1$ peaks.

To understand the significance of the peaks in the Raman spectra let us consider the chalcopyrite unit cell structure. In this material two type of structure have been observed, namely sphalerite and chalcopyrite [48]. However, in all Raman investigations by various workers only the chalcopyrite structure has been considered to be of relevance. Therefore, we will restrict our discussions to chalcopyrite structure.

According to Neumann et al. [202], in a unit cell of chalcopyrite structure at room

temperature, eight atoms results in 21 optical vibrational modes which transform like $A_1$ + $2A_2$ + $3B_1$ + $3B_2$ + 6E. Out of these the $B_2$ and E modes are infrared and Raman active, the $A_1$ and $B_1$ are only Raman active and $A_2$ is Raman inactive [202]. The most intense peak is associated with the $A_1$ mode of the chalcopyrite lattice vibration, originating from the vibration of Se in the <001> plane [203]. This is generally observed in the I-III-$VI_2$ chalcopyrite compounds [204]. This peak is always observed in Raman spectra of both stoichiometric and non-stoichiometric films as long as the chalcopyrite structure is present [203]. However, the intensity and sharpness of this peak determines the composition and the degree of formation of chalcopyrite structure.

The $A_1$ mode peak in the as-grown flash evaporated CIGS samples was always observed at about 175 $cm^{-1}$. This observation is supported by the Raman spectrum of CIGS single crystal, labelled 'a' in figure 4.13, which also appeared at 175 $cm^{-1}$. However, the Raman $A_1$ peak for the sample deposited at room temperature appeared at a slightly higher frequency (176 $cm^{-1}$). It is felt that this higher value of Raman shift could be due to a measurement error.

The $A_1$ mode peak in CIS and CGS are reported to appear at 173 and 186 $cm^{-1}$ respectively [202,205]. For CIGS this peak lies in between these two values, as gallium is partially substituted for indium. The peak position can also be used as an effective tool for the analysis of film composition. The literature contains many reports about the Raman analysis of the copper ternary compounds CIS and CGS. However, Raman data for CIGS are relatively scarce. Recently, Tanino and Nakanishi [206] reported the position of the $A_1$ peak at 180 $cm^{-1}$ for CIGS (25% gallium). They analyzed a complete

range of $CuIn_{1-x}Ga_xSe_2$ single crystals with $0 \leq x \leq 1$. Their observations revealed that the position of the $A_1$ peak lay between 178 to 186 $cm^{-1}$ for x=0 (CIS) and x=1 (CGS) respectively. Their observed value for CGS is in good agreement with that previously reported [202], whereas, the observed values for CIS and partially gallium substituted CIGS are higher (by approximately 5$cm^{-1}$) than the reported values [205 + our present work]. If one assumes that this discrepancy is due to the analysis being carried at low temperatures, then their value for CGS should also include an approximate 5$cm^{-1}$ shift when compared with that reported by Neumann et al. [202]. This assumes that the temperature co-efficient for the samples analyses by both groups are identical [207].

If one compares the Raman spectra of the flash evaporated samples with their respective x-ray diffraction spectra, a good correlation is found. A less intense XRD <112> diffraction line of the sample deposited at room temperatures labelled 'a' yielded a broad and small $A_1$ mode peak labelled 'b' in the Raman spectrum. However, the Raman peak becomes more distinctive for samples with a high intensity XRD <112> diffraction line, deposited at substrate temperatures of 100 and 200°C respectively. This indicates that the crystallinity of the films is improved at higher substrate temperatures and the increased intensity of the Raman peak results in a reduced FWHM value of about 20 $cm^{-1}$. Yamanaka et al have also reported that the formation of single and strong $A_1$ mode peak for the samples prepared or annealed at higher substrate temperatures was attributed to an improved crystallinity of their films [203].

Further considerations of the effect of composition on the Raman spectra, shown in figure 4.14, revealed that the $A_1$ mode peak also depends on the composition of the as-

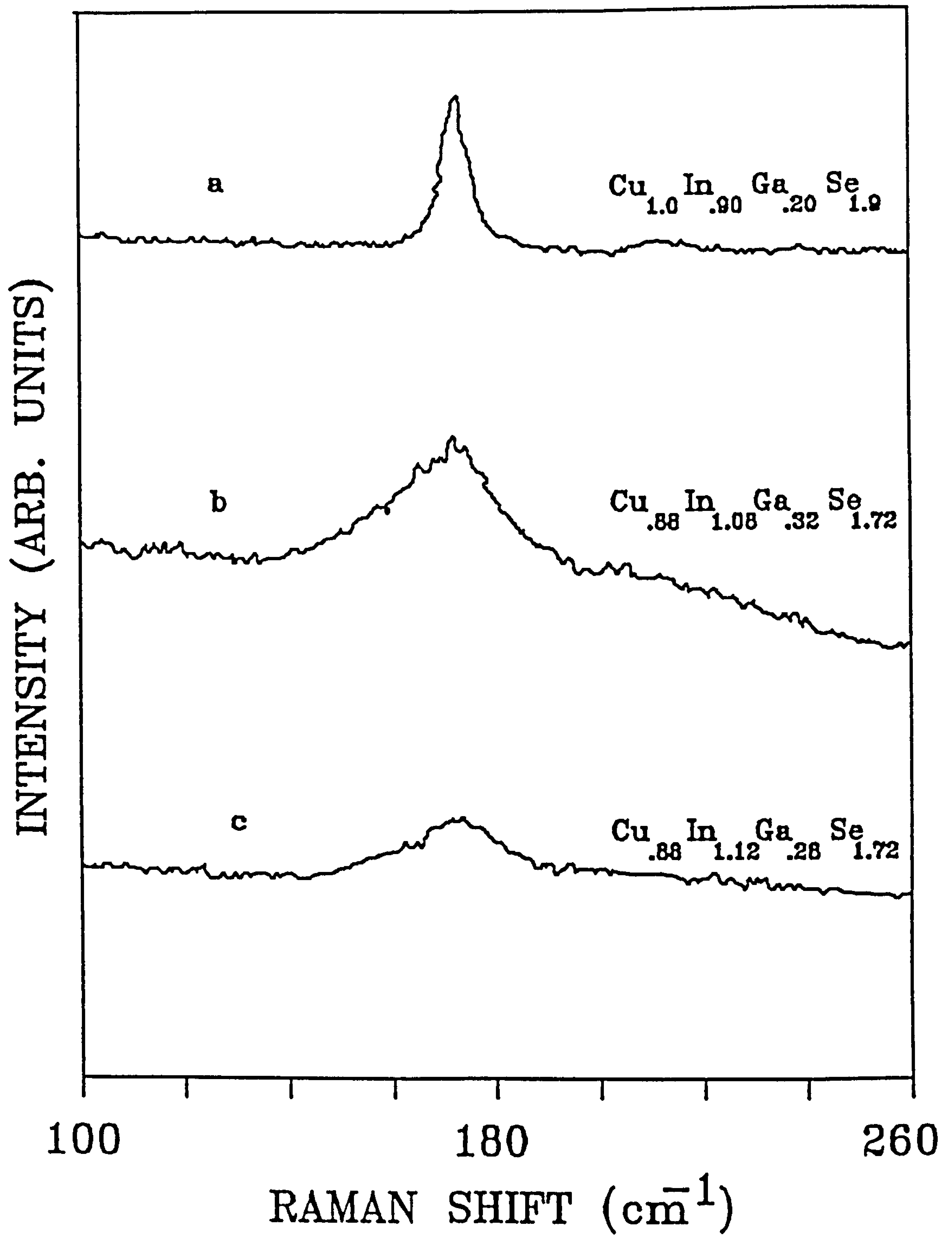


Figure 4.14: Effect of film composition on the Raman spectra of CIGS samples.

grown flash evaporated films. It can be seen that for films with a copper to indium + gallium ratio of 0.63, the peak is small and very broad. As the ratio is increased to 0.91, the intensity of the peak also increases. This trend has also been observed in Raman spectra of co-evaporated CIS thin films [208].

### 4.5.3 Scanning electron microscopy

The effect of substrate temperature on the structural properties of thin films was also investigated using SEM. Figure 4.15c shows an example of an SEM micrograph of an as-grown film (room temperature). It can be seen that there are many small grains of less than 0.2 μm which are separated by a significant number of voids. For the films grown at a higher substrate temperature (100°C) the surface morphology is changed considerably and it can be seen from figure 4.15 (middle) that the grains are closer to each other with a corresponding reduction in the number and size of the voids. However, most of the grains are still very small, of the order 0.1 μm, with a few larger grains of approximately 0.4 μm. A further increase in substrate temperature resulted in a more uniform distribution and grain size, of the order 0.15 μm. The number and size of the voids is further reduced.

The effect of substrate temperature on the microstructural properties can be understood by considering the nucleation and growth process of thin film. At pressures commonly used for evaporation processes, atoms travel in straight lines from the source to the substrate without collisions or loss of energy due to a larger mean free path (about 50cm

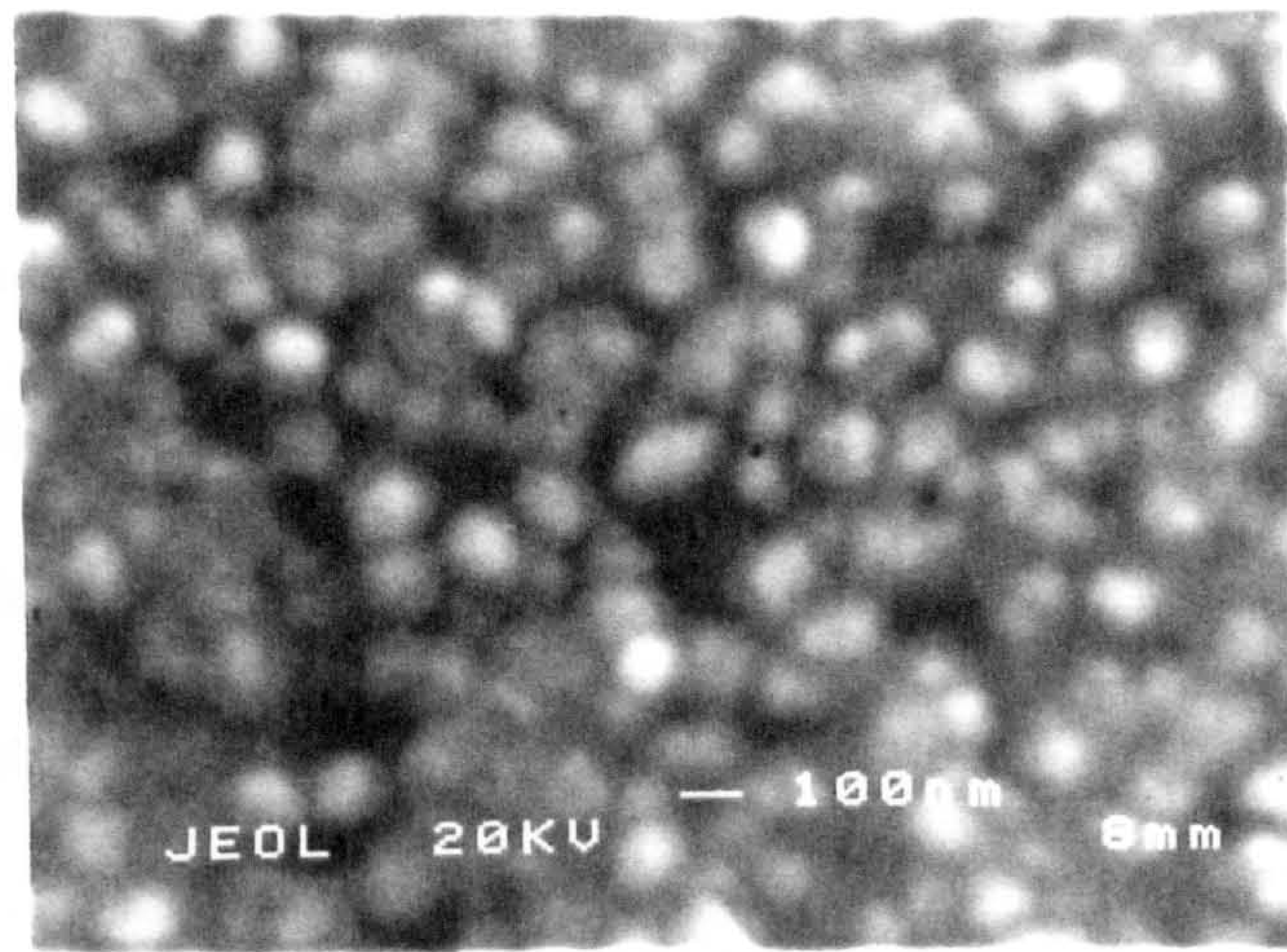


a

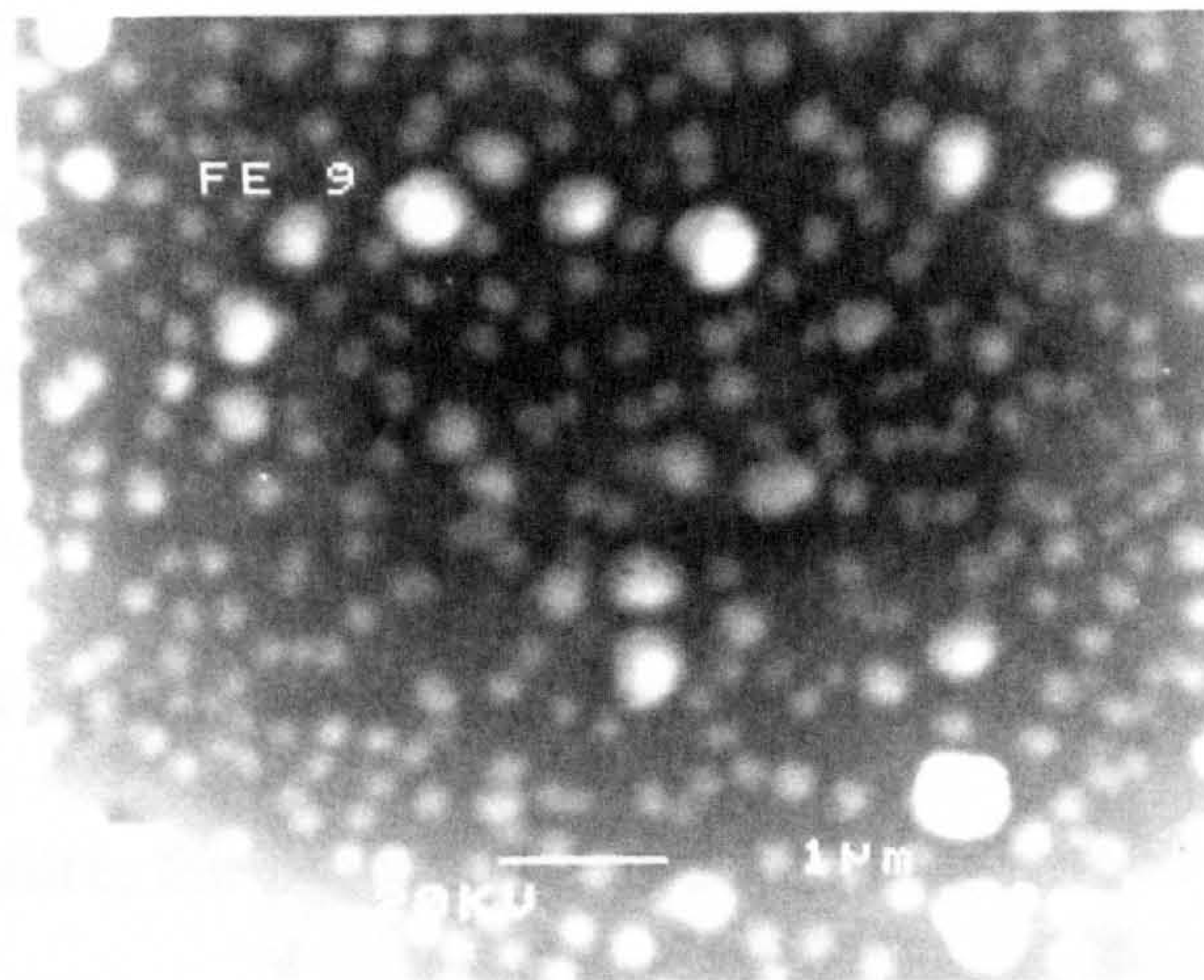


b

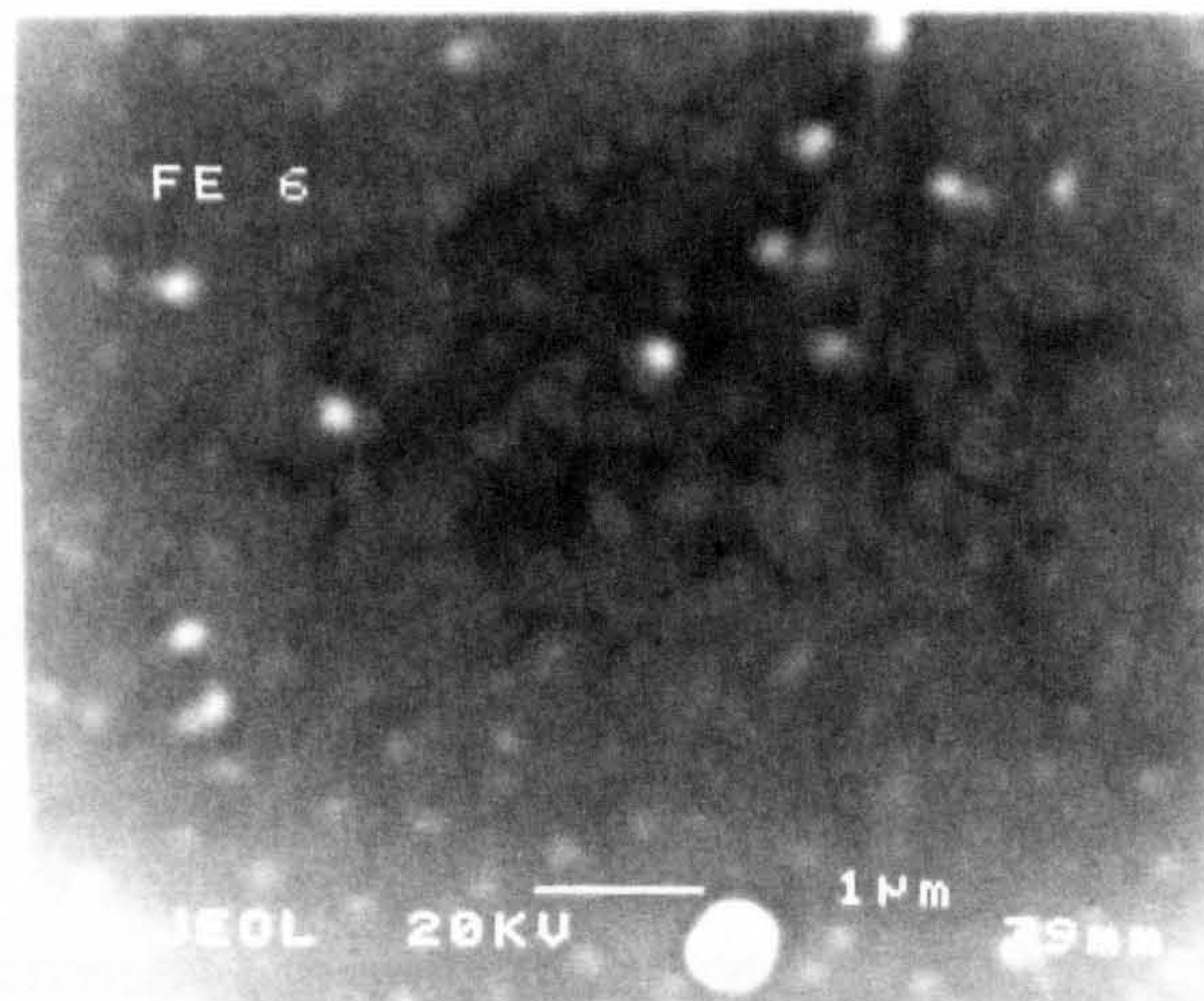


c

Figure 4.15: Scanning electron micrographs of CIGS films deposited at substrate temperature of 200°C (a), at 100°C (b) and at Room temperature (c).

at $10^{-5}$ mbar) compared to the typical system dimensions (source to substrate distance=12cm). When these atoms approach the substrate surface they experience several types of interactions including reflection, adsorption, desorption and associations with species already adsorbed on the substrate surface.

After the atom species have either been adsorbed or have joined another evaporant atom on the substrate surface, they may undergo several other processes such as desorption, surface diffusion and chemical adsorption which all involve energy changes. Surface diffusion does not require bonds to be broken and in general requires less energy than that needed to remove the atom from the substrate. For physically adsorbed atoms, the activation energy of migration is typically of the order one-fourth of the desorption energy [209]. Therefore, the probability of desorption is low.

In the early stages of deposition, adsorption occurs at discrete nucleation sites. As more atoms reach the surface islands are formed which continue to grow in size until they link with neighbouring islands to form a continuous coating as shown in figure 4.16. The probability of surface migration of the adsorbed atoms is small at low substrate temperatures and, therefore, this can result in the formation of small, isolated grains with a significant number of associated voids. The surface migration of the adsorbed atoms will increase with increased substrate temperature, resulting in an increased probability of interaction of the adsorbed atoms with each other to form larger grains. This will also have a major effect on the size and number of the voids. At higher substrate temperatures, grain growth becomes more dense and uniform as shown in figure 4.15 (top).

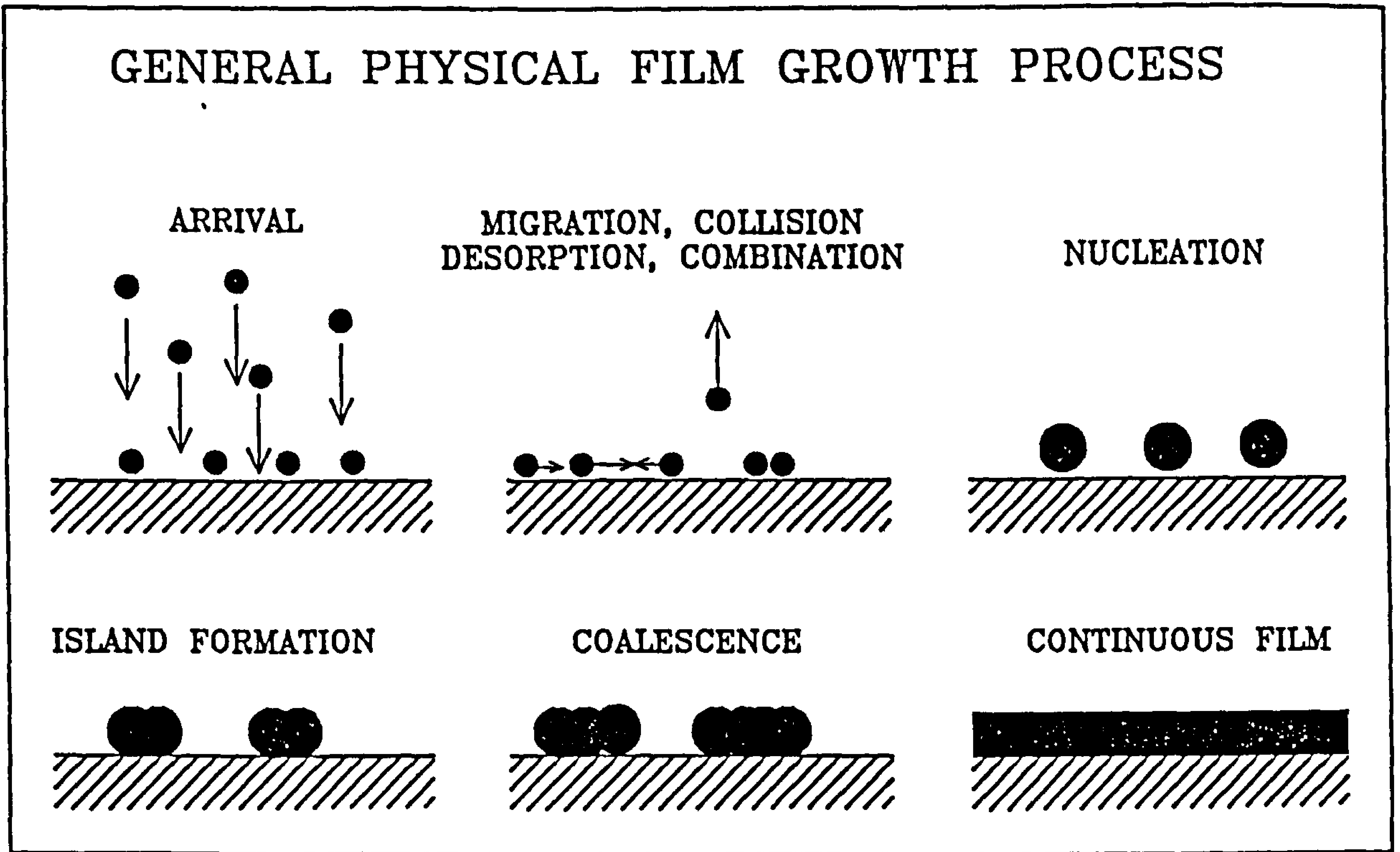


Figure 4.16 Nucleation and physical film growth process.

In our as-grown flash evaporated films it is revealed that the substrate temperature has a significant effect on the grain growth and follows the general process of nucleation and film formation described above.

## 4.6 Depositions under optimised conditions

As stated in section 4.1 the deposition process was investigated to produce films with a chalcopyrite structure, a grain size of > 1 μm and a composition which is comparable to the starting material. It was found that to obtain these ideal properties in the as-grown films was very difficult and therefore the process was optimised to deposit reproducibly films with characteristics as close to the ideal as possible.

The above analysis revealed that the deposition parameters should be set as follows:

| | |
|---|---|
| The source temperature | ≥ 1500°C |
| The powder feed rate | 4-5 mg/min |
| The substrate temperature | > 200°C |
| Source to substrate distance | 12cm |
| Pressure | $10^{-6}$ mbar |

In addition the use of twin chimney type Molybdenum source was found to be beneficial, reducing surface roughness and the probability of pin hole creation. Thin film samples of both CIGS and CIS were deposited using these parameters to examine the reproducibility of this process.

### 4.6.1 Structural properties

To obtain the structural information from the as-grown thin films of both CIS and CIGS, grown under the optimised deposition conditions, samples were characterised using XRD and SEM techniques. The acquired results are correlated with the growth parameters.

**XRD analysis**

Representative XRD spectra of CIGS and CIS are shown in figure 4.17 and 4.18 respectively. The structure of the films shows a strong orientation in the <112> plane as expected. The comparison of the CIGS spectra, figure 4.17, revealed that the structure is reproducible in terms of the preferred orientation. However, it is difficult to say any thing about the existence of the chalcopyrite structure because in strongly oriented films identification of the characteristic chalcopyrite peaks is difficult due to the sensitivity limits of the XRD technique.

The XRD spectra obtained from the CIS thin films, figure 4.18, also shows the <112> preferred orientation. However, when comparing the spectra shown in figure 4.18c with those obtained for CIGS it can be seen that the structure is more relaxed. The intensity of the diffraction lines corresponding to <220,204> and <312,116> are better resolved.

Occasionally, the formation of a more relaxed structure was achieved in the as-grown films. Spectrum 'c' in figure 4.18 shows an example of one of these films. In the

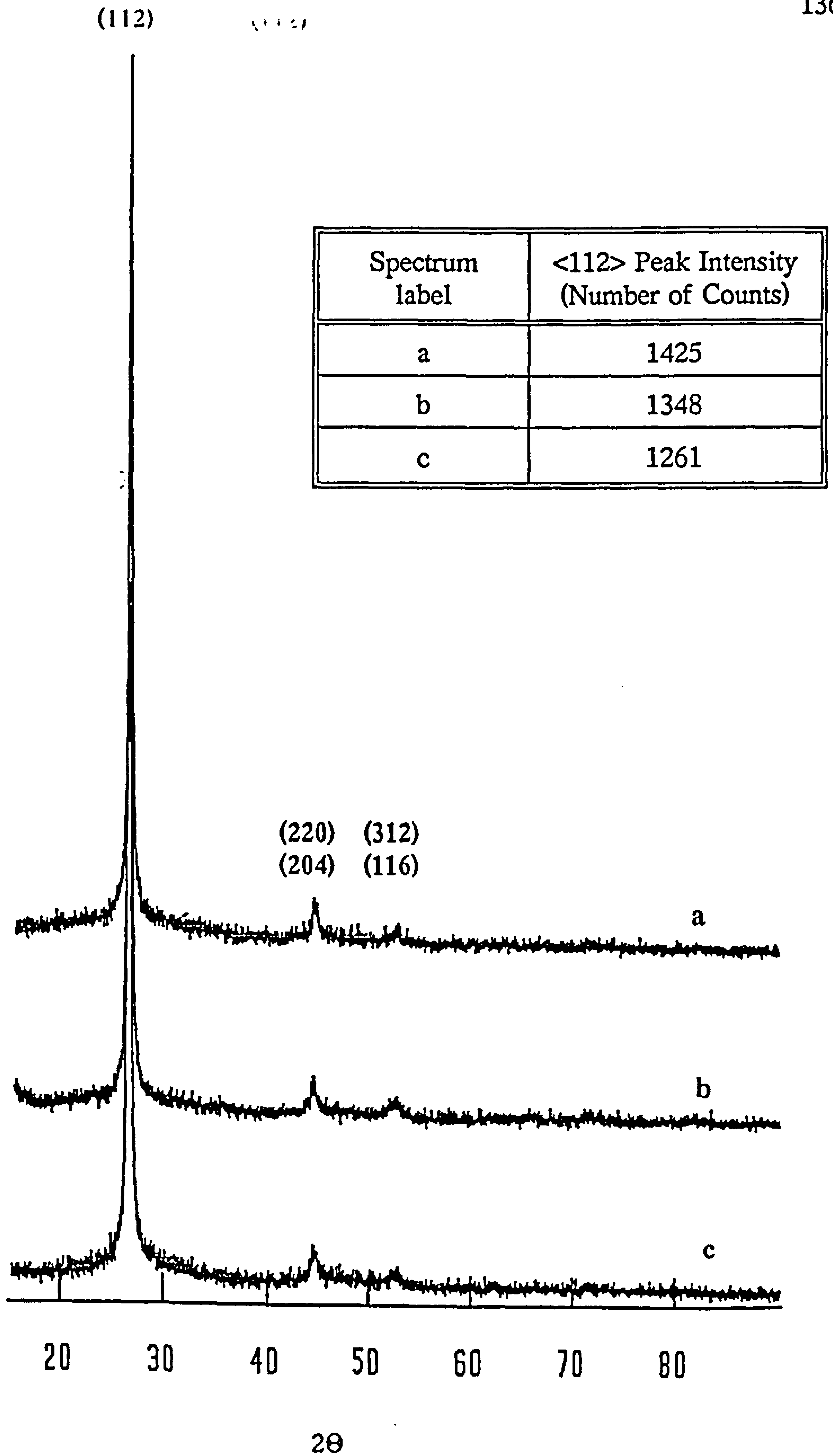


| Spectrum label | <112> Peak Intensity (Number of Counts) |
|---|---|
| a | 1425 |
| b | 1348 |
| c | 1261 |

Figure 4.17: Representative x-ray diffraction spectra of three CIGS thin films prepared under optimised deposition conditions.

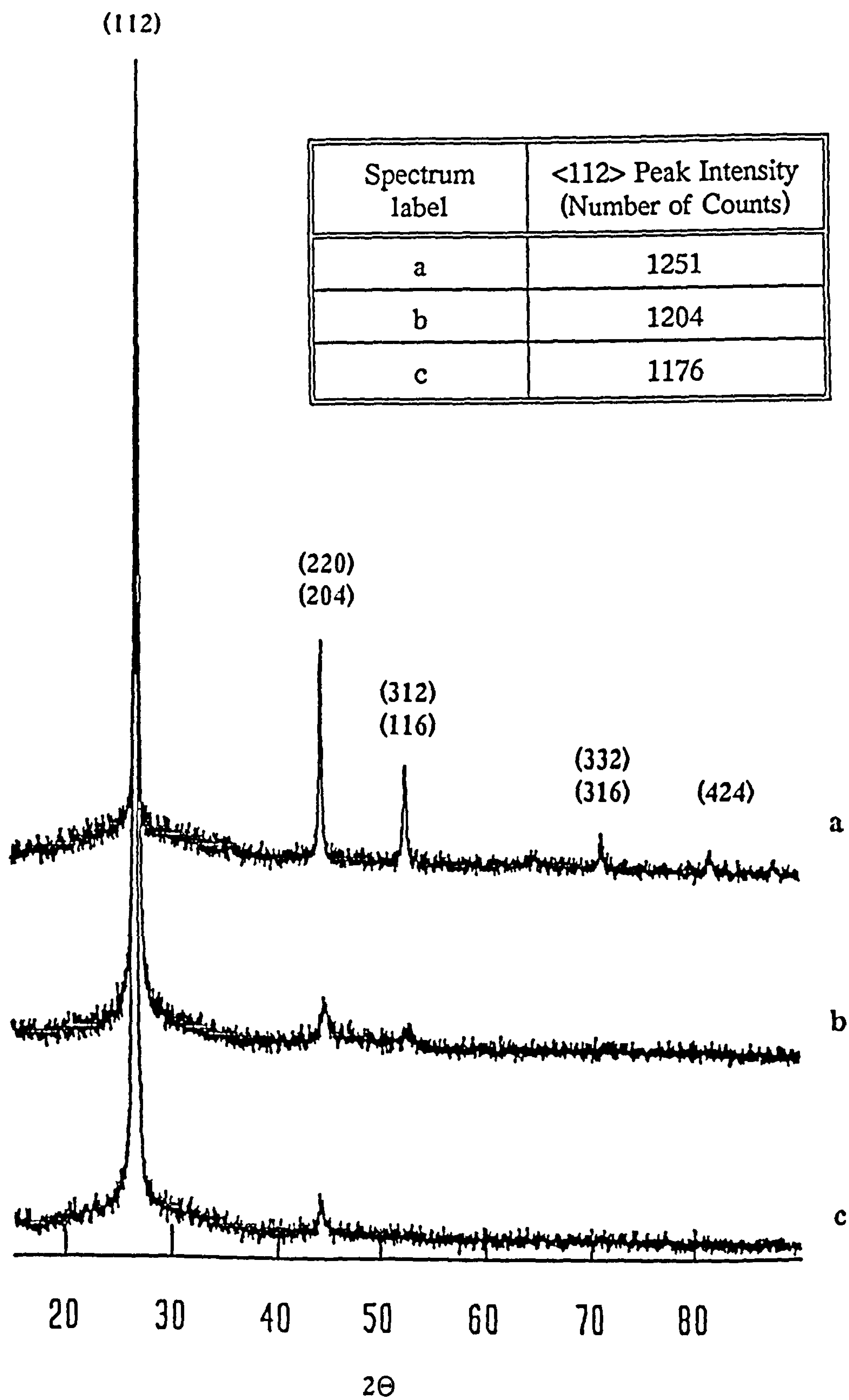

| Spectrum label | <112> Peak Intensity (Number of Counts) |
|---|---|
| a | 1251 |
| b | 1204 |
| c | 1176 |



Figure 4.18: Representative x-ray diffraction spectra of three CIS thin films prepared under optimised deposition conditions.

deposition of this film the substrate temperature was kept at 200°C for 10-15 minutes, after the film had been deposited, and it is believed that this short in-situ anneal is the reason for the observed structure.

As previously outlined, the identification of the chalcopyrite structure in polycrystalline thin films of CIS or CIGS is only possible if either the analysis is carried out by a more sensitive technique than XRD or the film structure is more relaxed. In-situ annealing procedures were adopted to try to produce a relaxed structure so that the identification of the chalcopyrite peaks could be made possible using routine XRD technique, but without success.

**Scanning Electron Microscopy**

The scanning electron micrographs of the samples prepared under optimised deposition conditions are shown in figure 4.19. These correspond to a. CIGS (top) and b. CIS (bottom).

It can be seen that the grains in the SEM micrograph of the CIGS sample are distributed uniformly throughout the film. However, the relatively large spacing between the grains indicated that the film consists of a number of individual grains incorporating a significant number of voids. Similar observations were noticed in other samples. The grain size of these as-grown samples was estimated from the SEM photographs and was found to be of the order 0.1-0.2 microns.

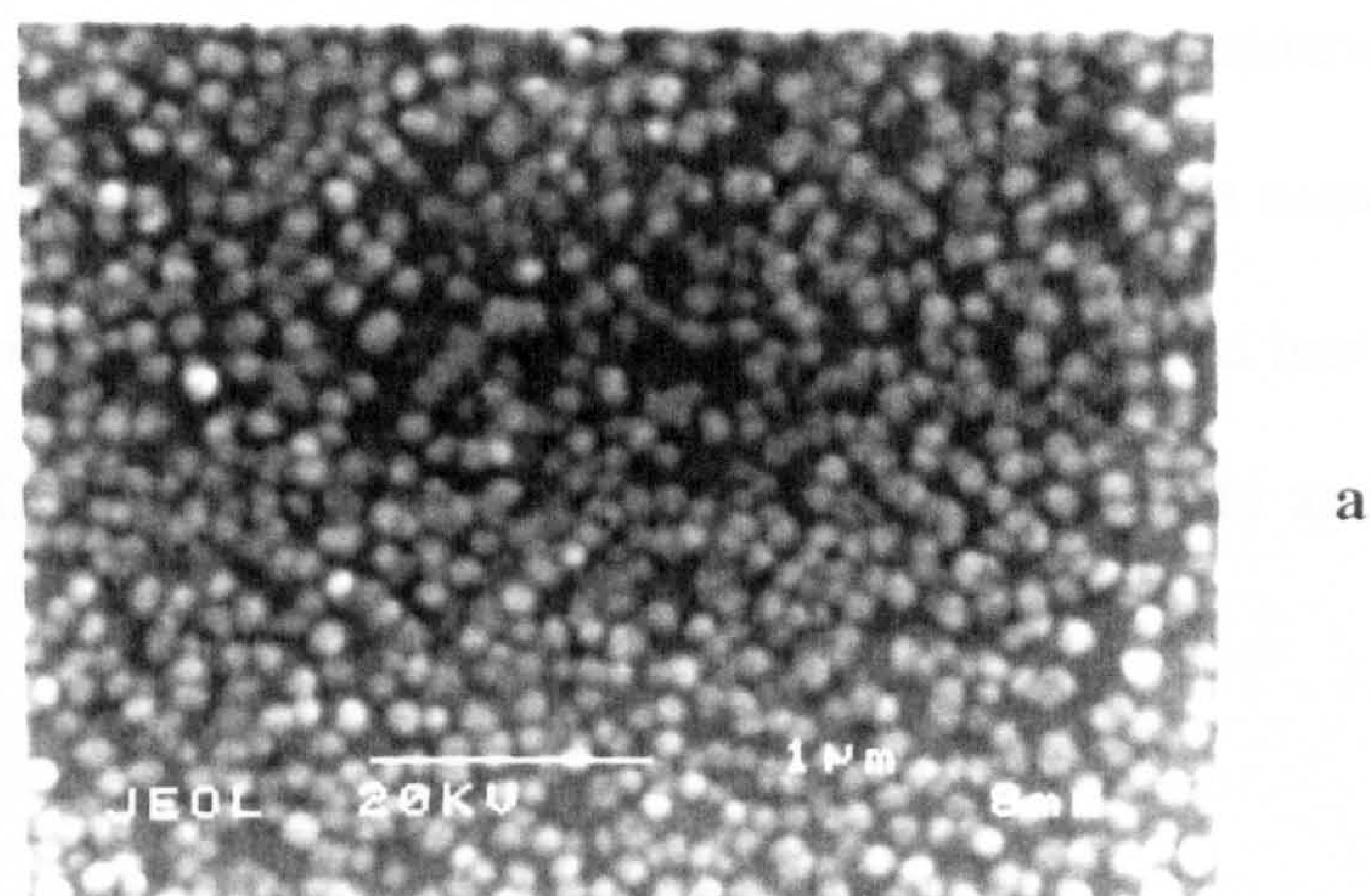


a

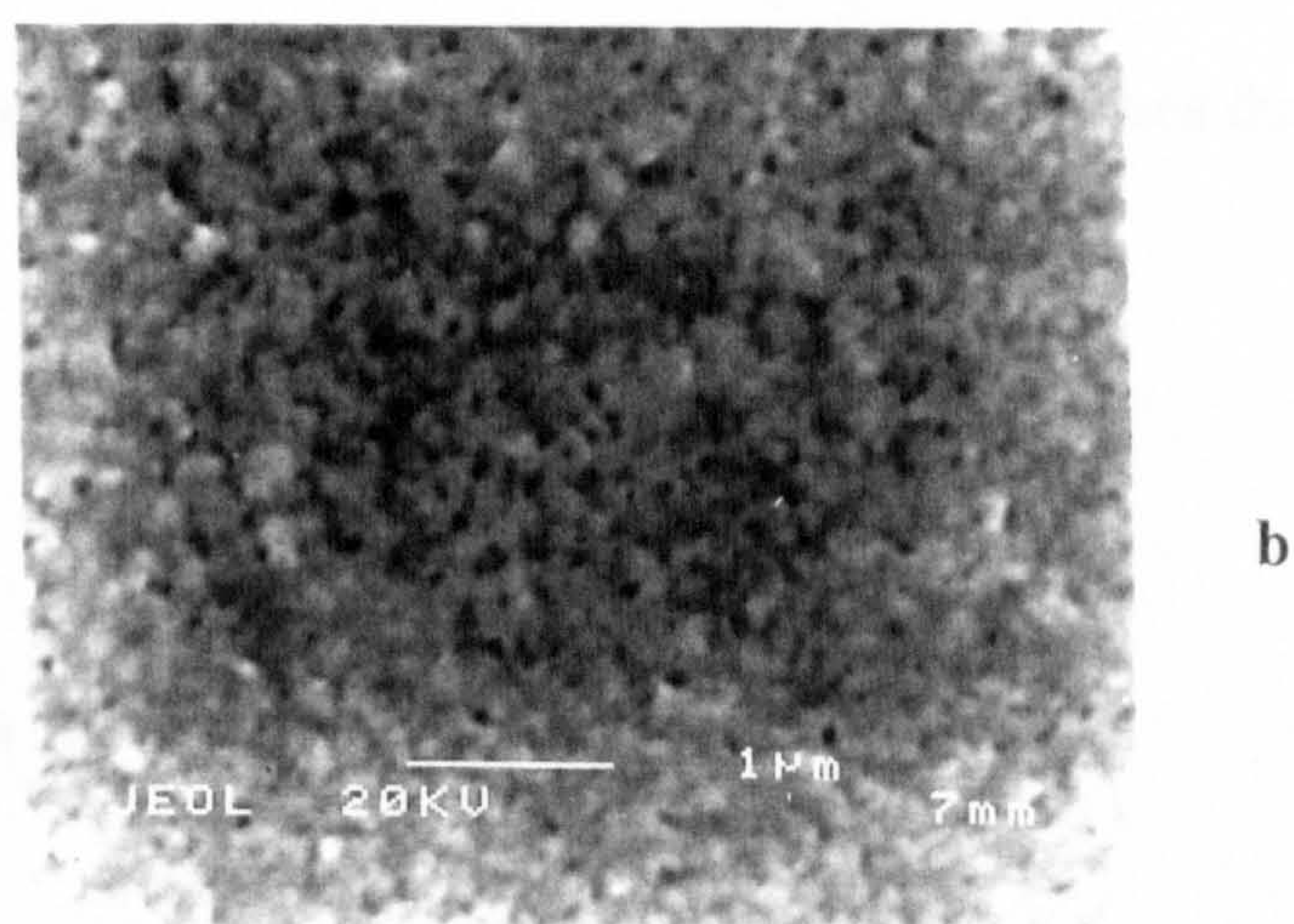


b

Figure 4.19 Scanning electron micrographs of CIGS (a) and CIS (b) thin films prepared under the optimised deposition conditions.

The SEM micrograph of the CIS thin film, however, showed a more dense sponge-like structure with a significantly reduced number of voids. By considering the deposition conditions, it can be concluded that the in-situ annealing affect mentioned above has resulted in a more relaxed and more dense structure. The observed increase in grain size, to approximately 0.3 μm, adds weight to the argument for in-situ annealing.

### 4.6.2 Compositional analysis

The as-grown films of CIGS were analysed both quantitatively and qualitatively for the elemental composition using three different techniques XRF, EDAX and RBS. The CIS thin films were only analysed by the EDAX and RBS techniques due to a lack of XRF machine time.

**X-ray fluorescence spectroscopy**

Figure 4.20 shows the weight percent composition (measurement accuracy of ±3%) for a range of total weight of deposit for different samples of CIGS thin films. The apparent measurement error could be due to the fact that the sample area for analysis was restricted and the calibration conditions and those of the analyses were not identical. In order to obtain more accurate measurements, the preparation of the samples onto Millepore filters was suggested. However, it was found that this was difficult due to the extreme sensitivity of the Millepore filters to heat. It can be seen from figure 4.20 that

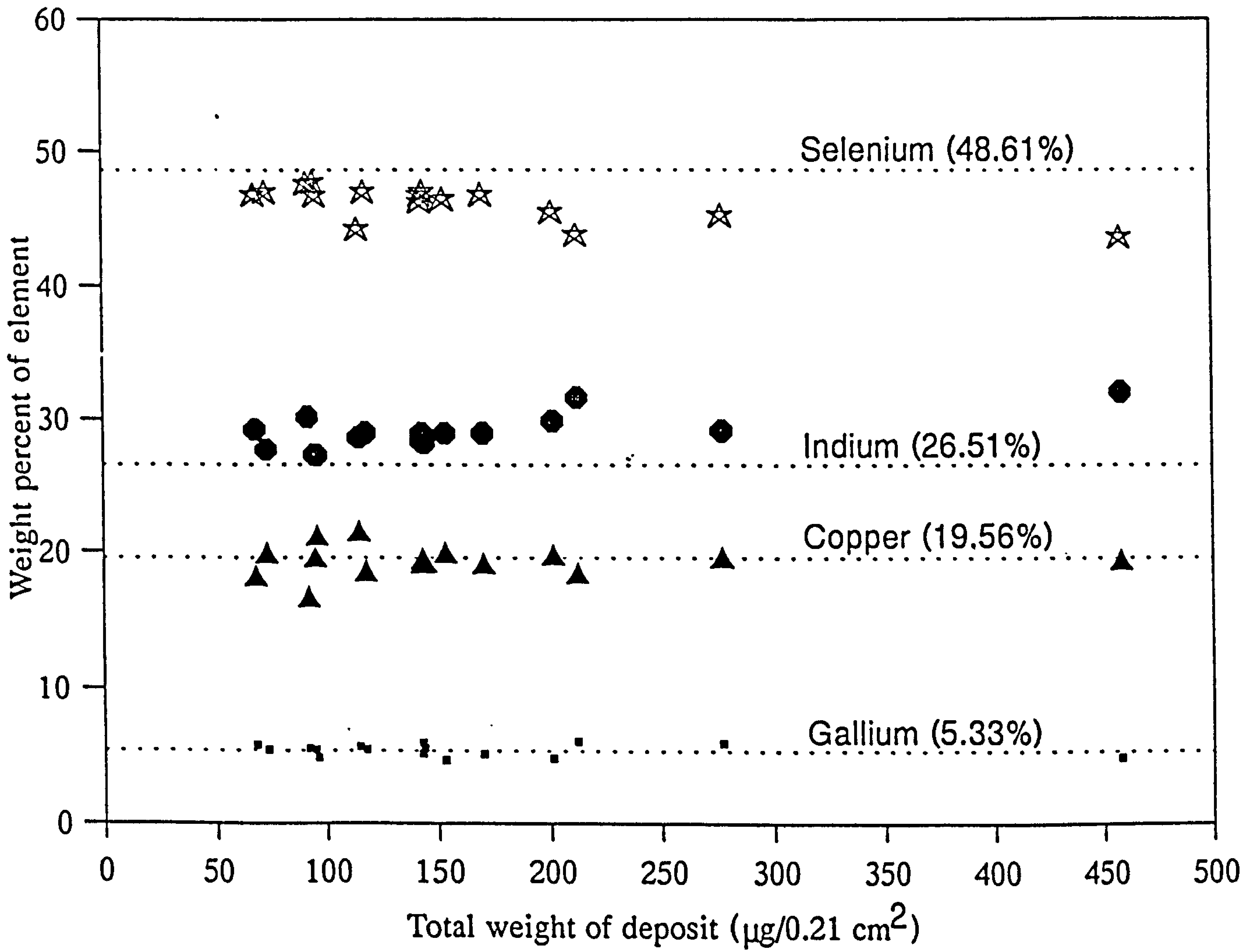


Figure 4.20: Weight percent of elements in polycrystalline CIGS films as measured by XRF technique.

the gallium and copper contents are very consistent and close to the theoretical values of 5.33 wt.% and 19.56 wt.% respectively. However, the indium wt.% in the film was slightly more than that of the starting material (26.51 wt.%), approximately 4 wt.%. XRF analysis also revealed a slight deficiency of selenium in the films. The maximum deficiency for selenium was calculated to be about 3 wt.%.

The selenium deficiencies can be attributed to it's higher vapour pressure [191,210] and, as expected, the deficiency was more pronounced at higher substrate temperatures.

**Energy dispersive x-ray analysis**

The XRF results for the as-grown films were confirmed using EDAX analysis, which has an accuracy of ±4%. From figure 4.21 it can be seen that the Cu, In, Ga, and Se content are within the range 18.3-19.6 wt.%, 30.2-34.5 wt.%, 4.1-6.2 wt.% and 41.4-45.8 w.t% respectively. These results are similar to those obtained using XRF. Once again these results indicate a slight deficiency of selenium.

An alternative diagrammatic approach to represent the EDAX analysis is a plot of the elemental components on a compositional triangle which incorporates experimentally known device efficiency contours [211]. This results in a simple visual model comparing the samples with each other and the starting material. Figure 4.22 shows the results of a series of typical depositions of as-grown CIGS thin films. Indium and gallium are shown on the same axis as gallium is partially substituted for indium in CIGS materials.

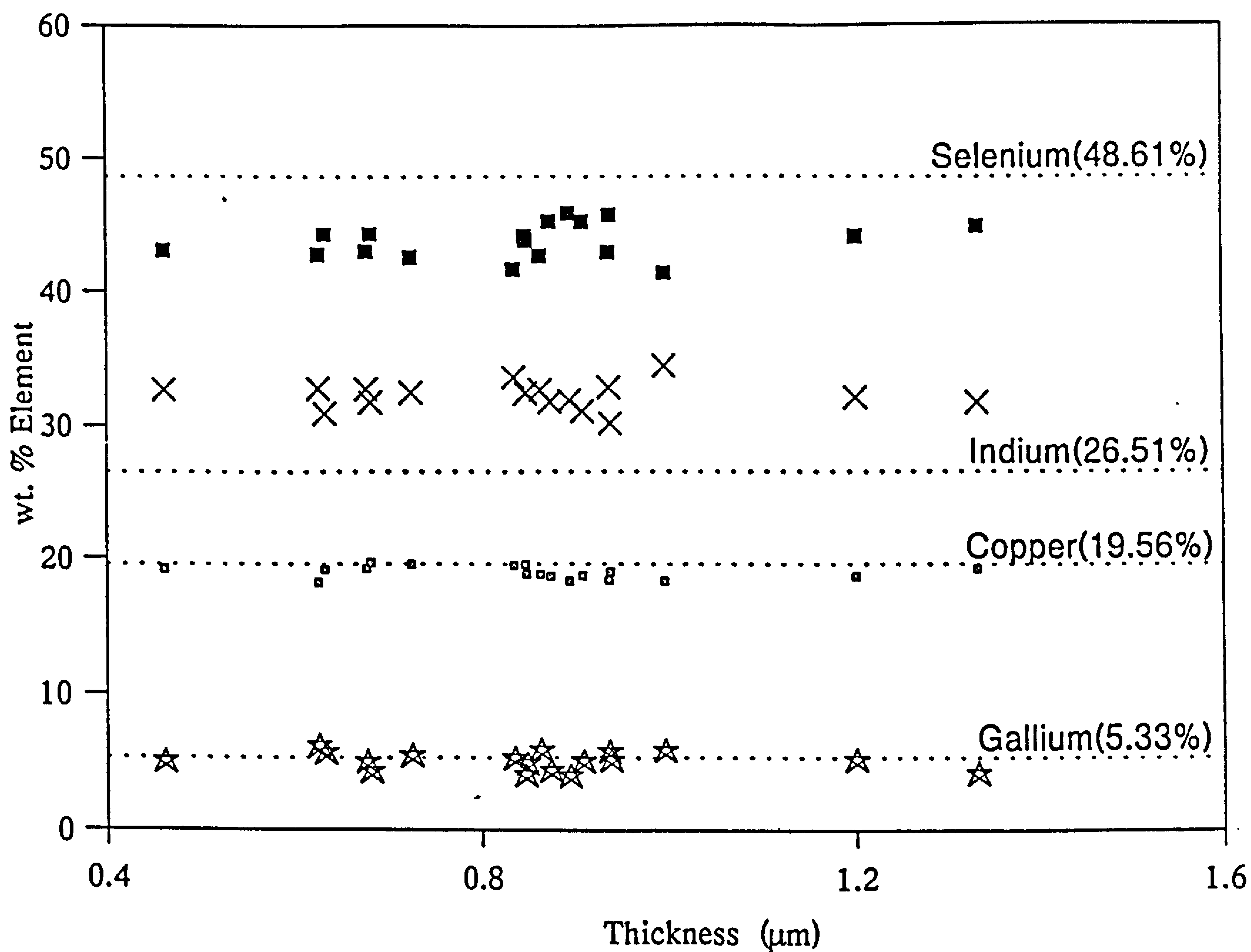


Figure 4.21: Weight percent of elements in polycrystalline CIGS films as measured by EDAX technique.

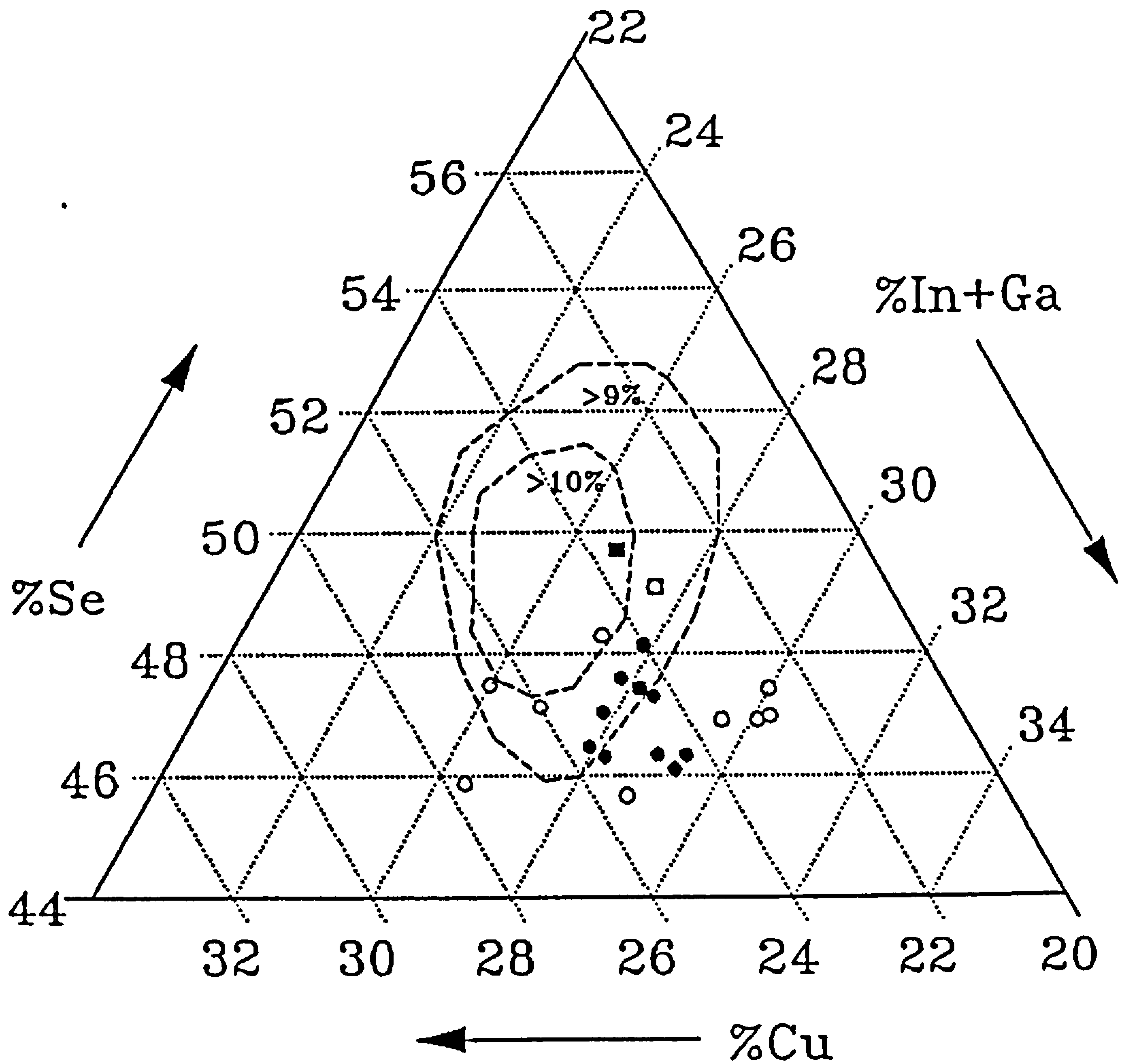


Figure 4.22: Compositional triangle of CIGS and CIS thin films measured by EDAX technique; filled circles (CIGS thin films), filled square (CIGS source material), empty circles (CIS thin films) and empty square (CIS source material).

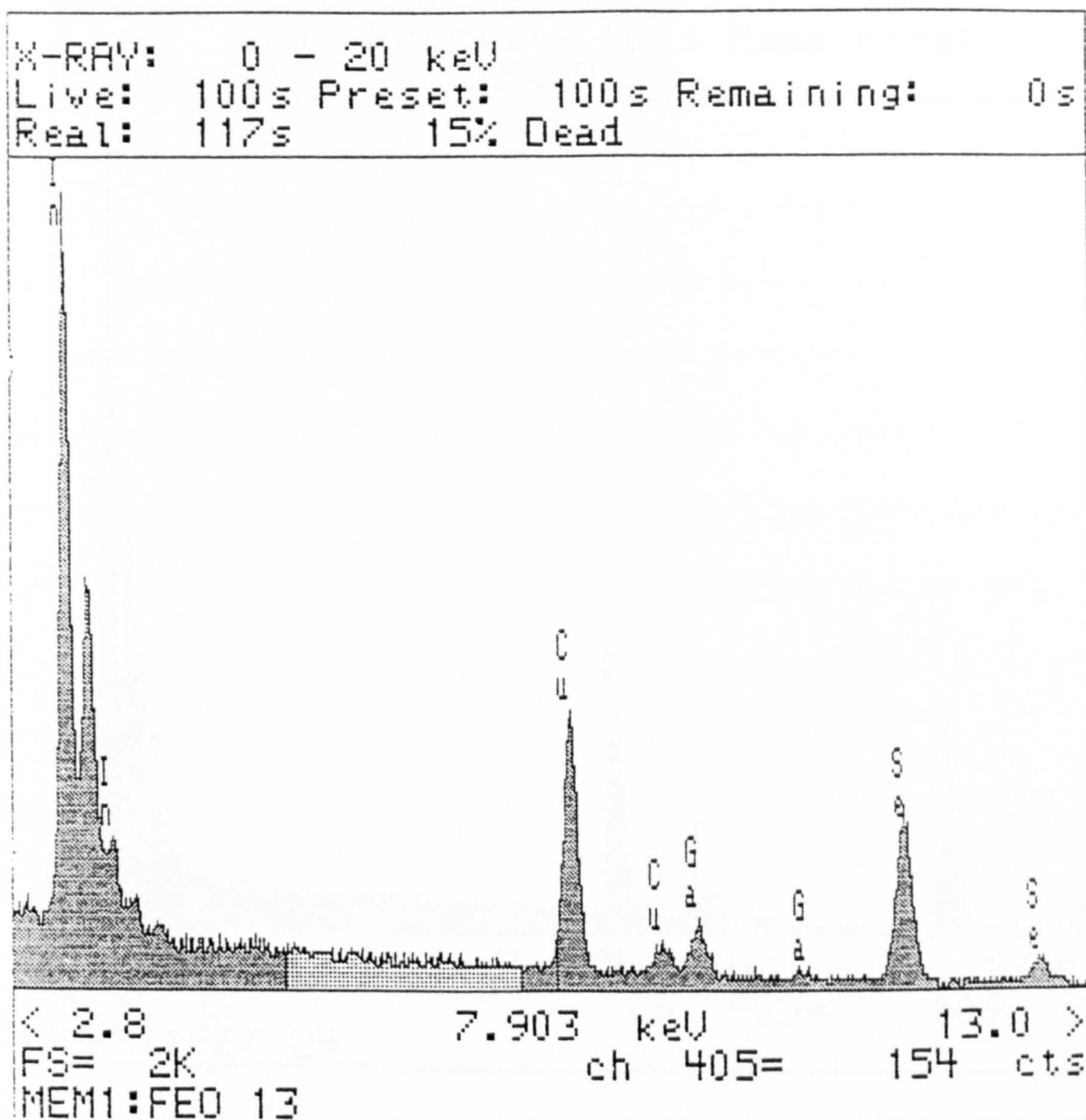


Figure 4.23: EDAX spectrum of the polycrystalline CIGS thin film.

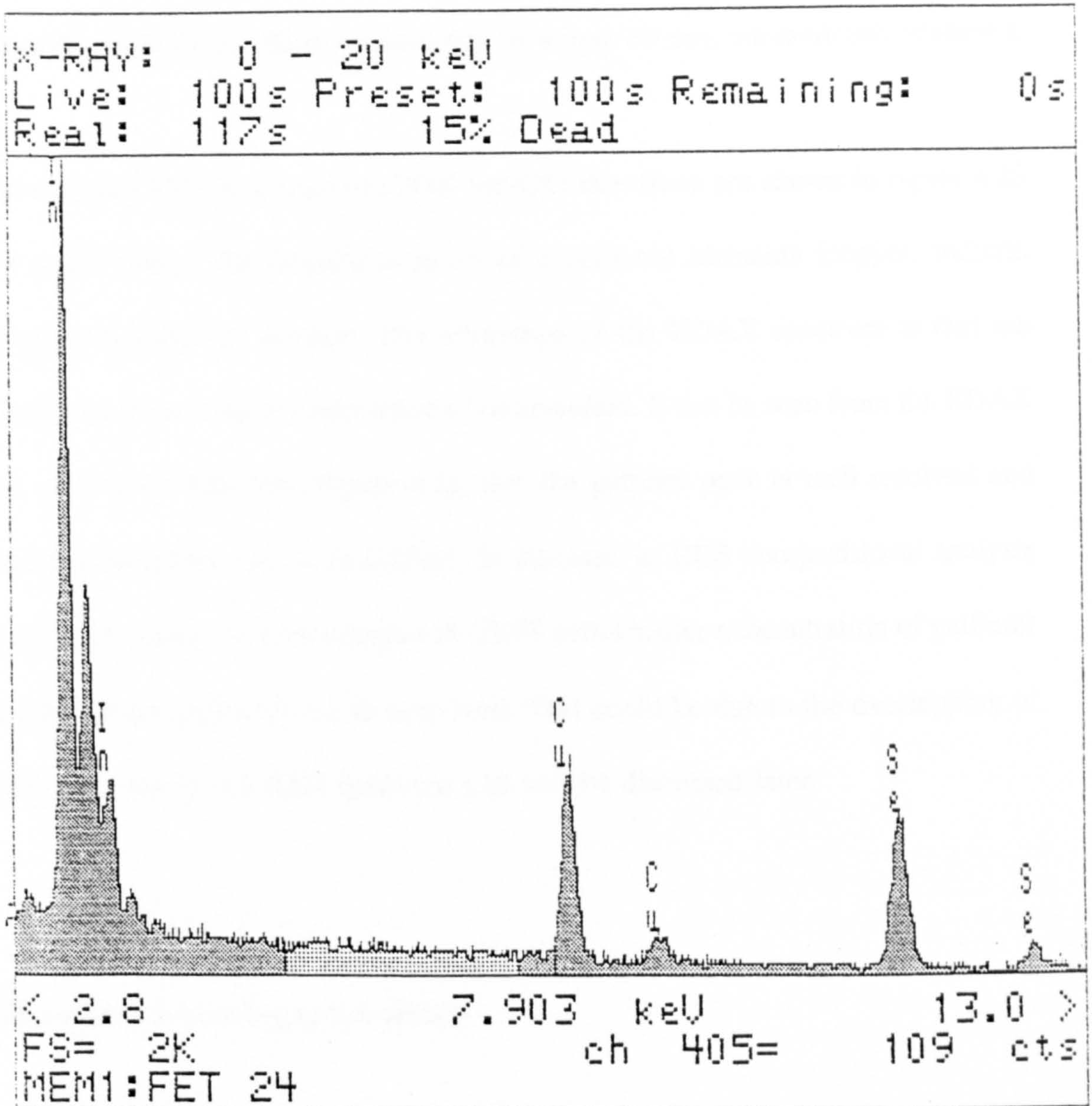


Figure 4.24: EDAX spectrum of the polycrystalline CIS thin film.

From figure 4.22, it can be seen that most of the CIGS (filled circles) samples are grouped together in or around the area where 9-10% efficient solar cells can be fabricated [211]. On the same compositional triangle (by considering Ga=0 for In+Ga) the composition of CIS thin films, represented by empty circles, are randomly scattered.

The representative EDAX spectra of CIGS and CIS thin films are shown in figure 4.23 and 4.24 respectively. The respective peaks of constituent elements (copper, indium, gallium and selenium) are evident. The advantage of the EDAX spectrum is that the identification of microscopic concentration is convenient. It can be seen from the EDAX spectrum of a CIGS thin film, figure 4.23, that the gallium peak is well resolved and elemental concentration can be quantified. In contrast, in RBS compositional analysis techniques (particularly in thick samples of CIGS with smaller concentration of gallium) identification of the gallium peak is very hard. This could be due to the overlapping of the elemental peaks in the RBS spectrum and will be discussed later.

**Rutherford backscattering spectroscopy**

The RBS technique was used not only to determine the elemental surface composition but also to obtain a compositional depth profile of the as-grown films. This is a very useful technique for gaining qualitative information about the film's compositional uniformity (through the film) and quantitative information about the film's surface composition [177]. In RBS spectra, the appearance of peaks corresponding to different elements observes a general rule. Heavy masses appear at high energies giving high

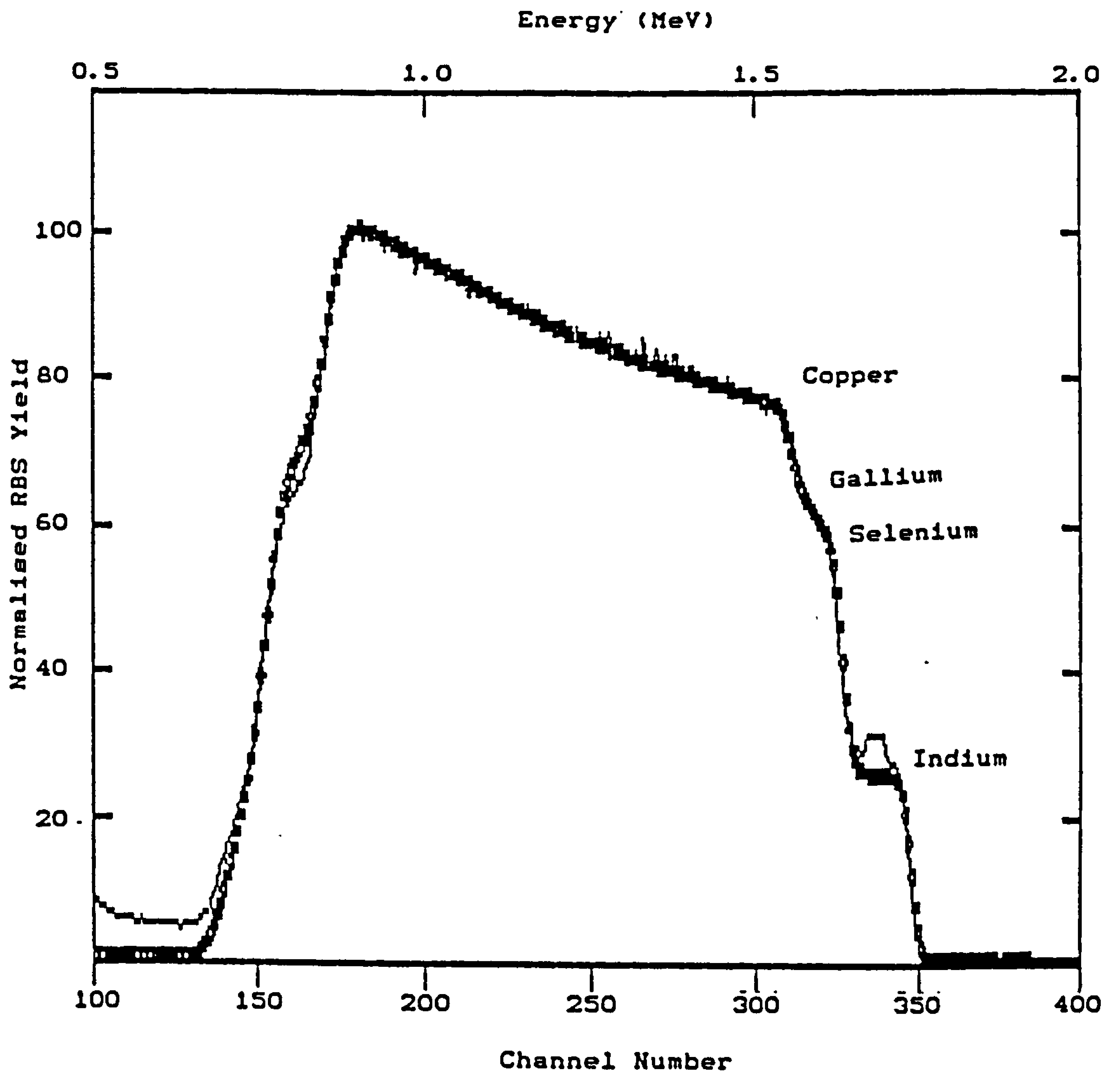


Figure 4.25: Measured and calculated RBS spectra of CIGS thin film.

yield (at higher channel number) and light masses at low energies resulting in a low yield (at lower channel number). For example, in the case of CIGS, indium is the heaviest mass and appears at the highest channel number - 349. At channel numbers - 327, 319 and 311, the respective contribution from selenium, gallium and copper are observed. The thickness of the sample also affects the shape of the spectrum. For thin films (< 20nm) one can observe the resolved peaks for which the percentage error is of the order ±0.2% but, for thicker films, the peaks overlap and the error increases to approximately ±5% [212].

Figure 4.25 shows the measured and simulated backscattering yield of an as-grown CIGS thin film as a function of energy and channel number. On the extreme right hand side, which represents the surface of the sample, the indium peak can be seen at channel number 349. The respective peaks of selenium, gallium and copper are overlapped because the sample thickness was of the order of 0.6 micron. From the rising edges of the peaks one can estimate the channel numbers of the different elements in a compound. However, identification of the gallium peak is difficult. This is due to the low concentration of gallium (25%) and its spectral position within the narrow region between the selenium and copper peaks.

The simulated spectrum was obtained using the 'RUMP' computer software package. The calculated values of elemental composition are summarised in table 4.8 and compared with compositional analysis achieved by XRF and EDAX techniques. Once again the compositional data revealed that films are slightly rich in indium and slightly deficient in selenium.

| Sample No. | Compositional analysis by EDAX (Atm.%) Cu/In/Ga/Se | Thickness (EDAX) Å | Compositional analysis by XRF (Atm.%) Cu/In/Ga/Se | Total weight (μg/0.21cm²) | Compositional analysis by RBS (Atm.%) Cu/In/Ga/Se | Thickness (RBS) Å |
|---|---|---|---|---|---|---|
| FEO8 | 25.6/22.8/5.1/46.4 | 6817±143 | 27.1/19.3/5.6/48.1 | 96 | 26.7/20.1/6.7/46.5 | 5850 |
| FEO9 | 25.5/23.4/4.8/46.3 | 8454±162 | 25.7/20.6/5.4/48.2 | 153 | 20.6/21.1/7.0/51.3 | 9850 |
| FEO10 | 25.1/22.9/5.0/47.1 | 13342±256 | 25.6/21.4/5.7/47.4 | 201 | 26.5/21.1/7.0/45.4 | 10950 |
| FEO11 | 24.3/23.2/6.1/46.3 | 12002±219 | 25.3/23.2/5.8/45.8 | 458 | 32.8/18.6/6.2/42.4 | 19000 |
| FEO13 | 25.5/24.4/6.3/43.8 | 8336±157 | 25.3/20.8/6.9/46.9 | 277 | 25.8/19.3/6.4/48.5 | 18500 |
| FEO18 | 24.1/25.1/7.0/43.8 | 9949±184 | 24.0/22.8/7.2/46.0 | 212 | 31.3/16.9/5.6/46.2 | 14000 |
| FET22 | 24.0/23.8/6.9/45.2 | 9345±185 | 24.8/20.1/6.5/48.7 | 144 | 26.2/21.1/7.0/45.6 | 9650 |
| FET26 | 24.0/23.1/4.8/48.2 | 8922±180 | 24.7/20.7/6.0/48.6 | 170 | 25.5/22.0/7.3/45.2 | 10650 |
| FET28 | 25.1/23.6/6.0/45.3 | 4605±111 | 25.5/19.7/6.3/48.5 | 73 | 25.7/19.7/6.6/48.0 | 4550 |
| FET29 | 23.8/23.8/7.3/45.0 | 6251±137 | 25.1/19.4/6.3/49.2 | 95 | 25.7/20.9/7.0/46.4 | 6000 |

Table 4.8 Comparative compositional analysis of CIGS thin films using EDAX, XRF and RBS techniques.

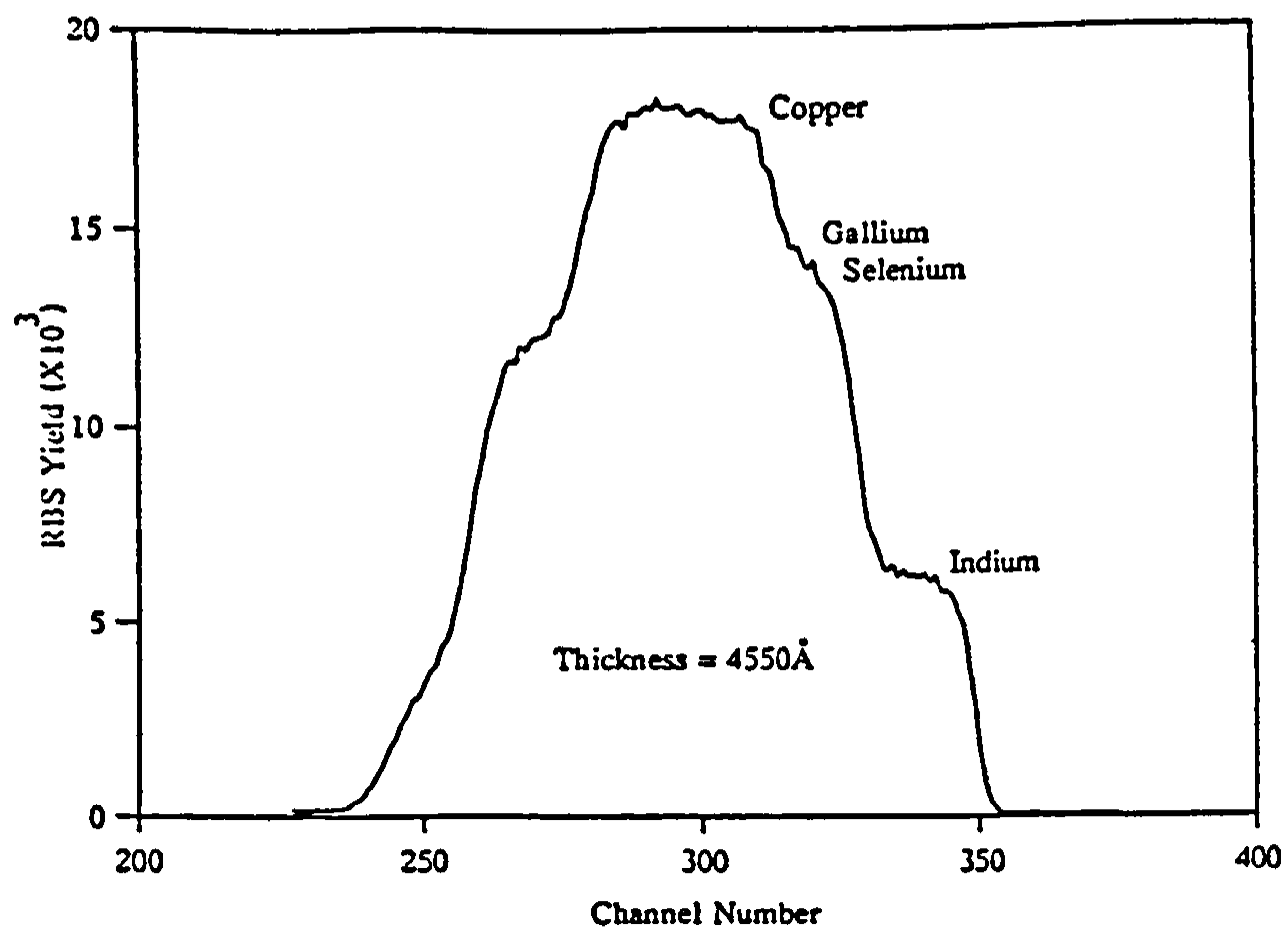


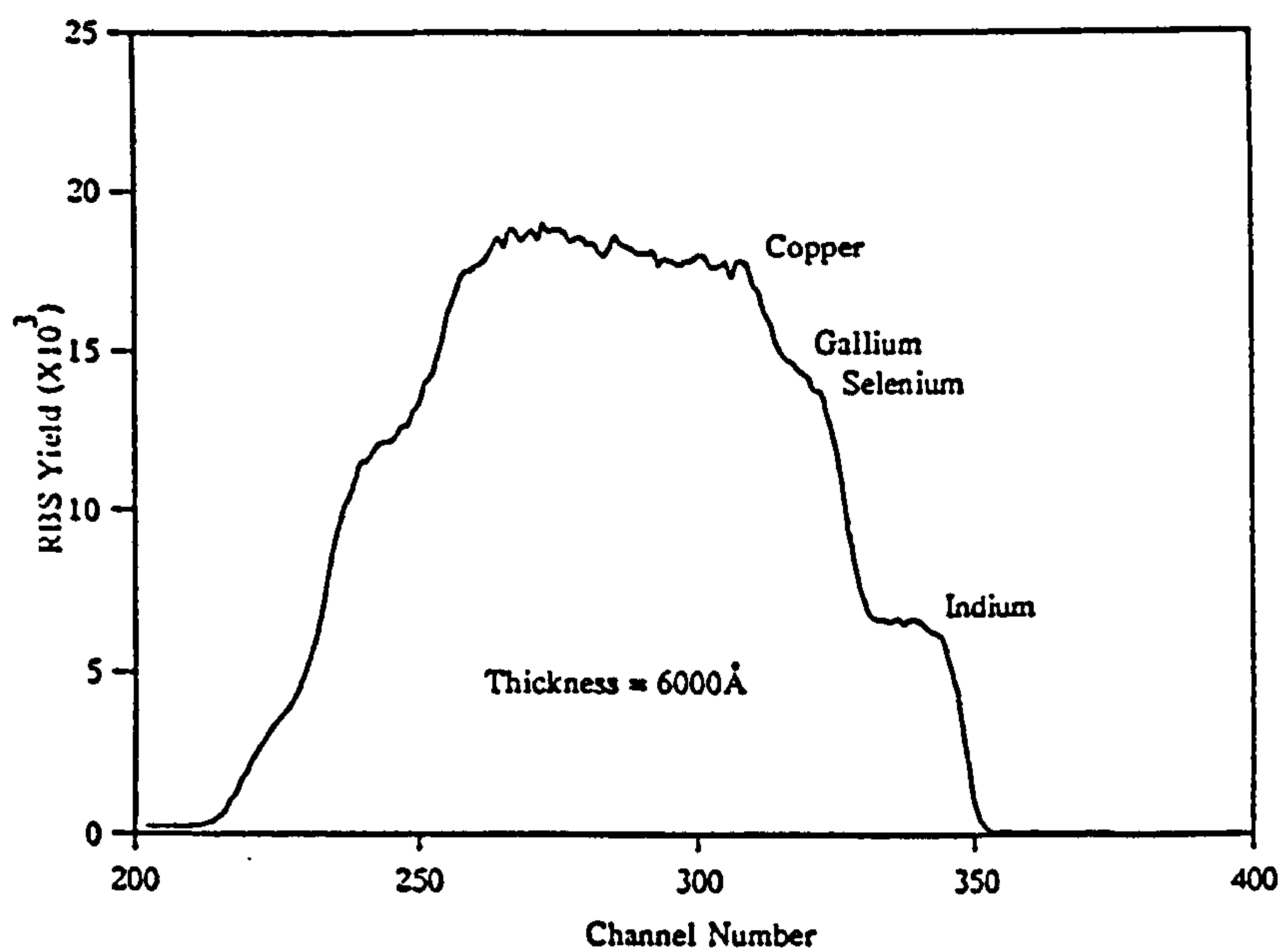


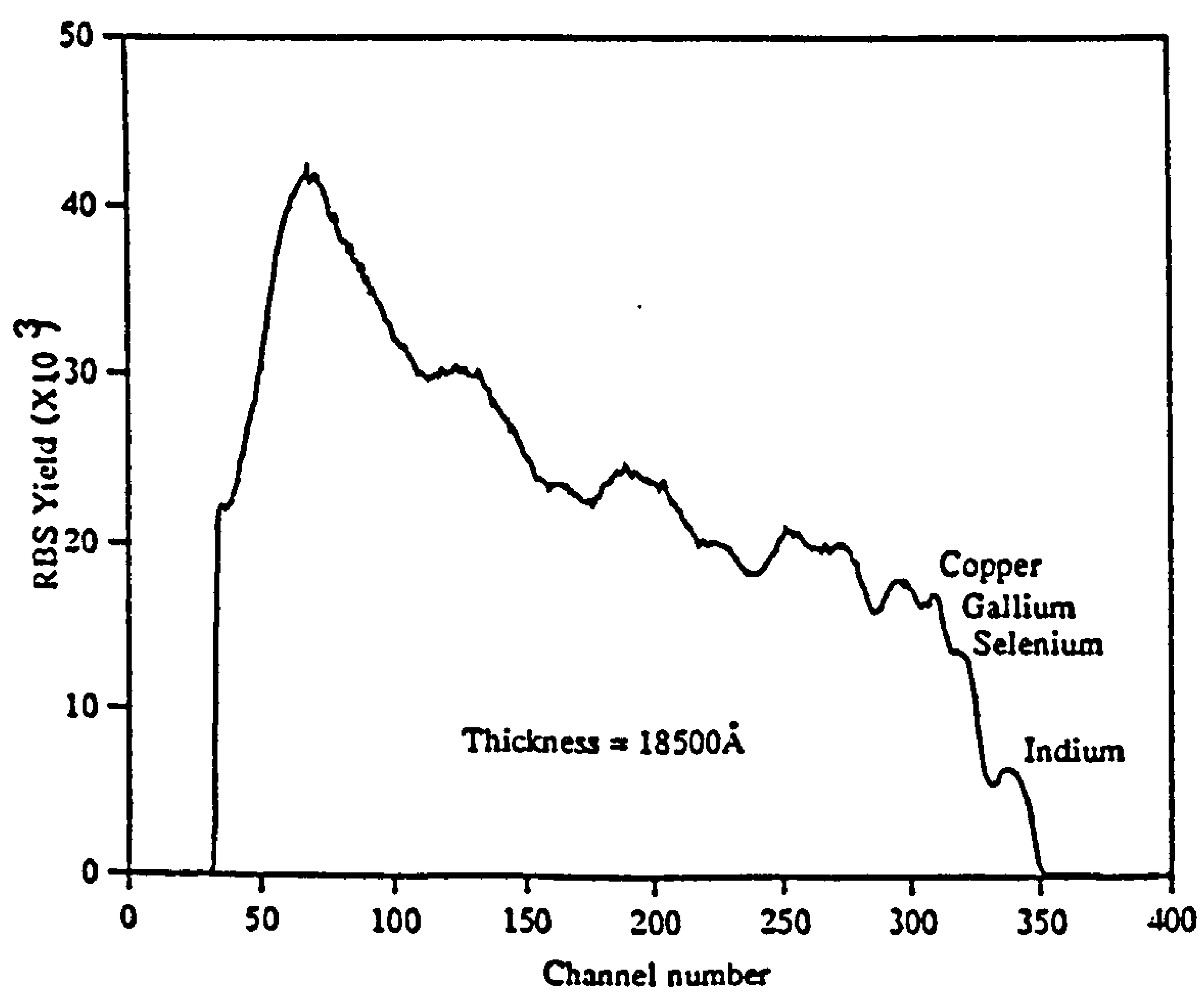


Figure 4.26 Effect of thickness on the RBS spectrum of CIGS thin films.

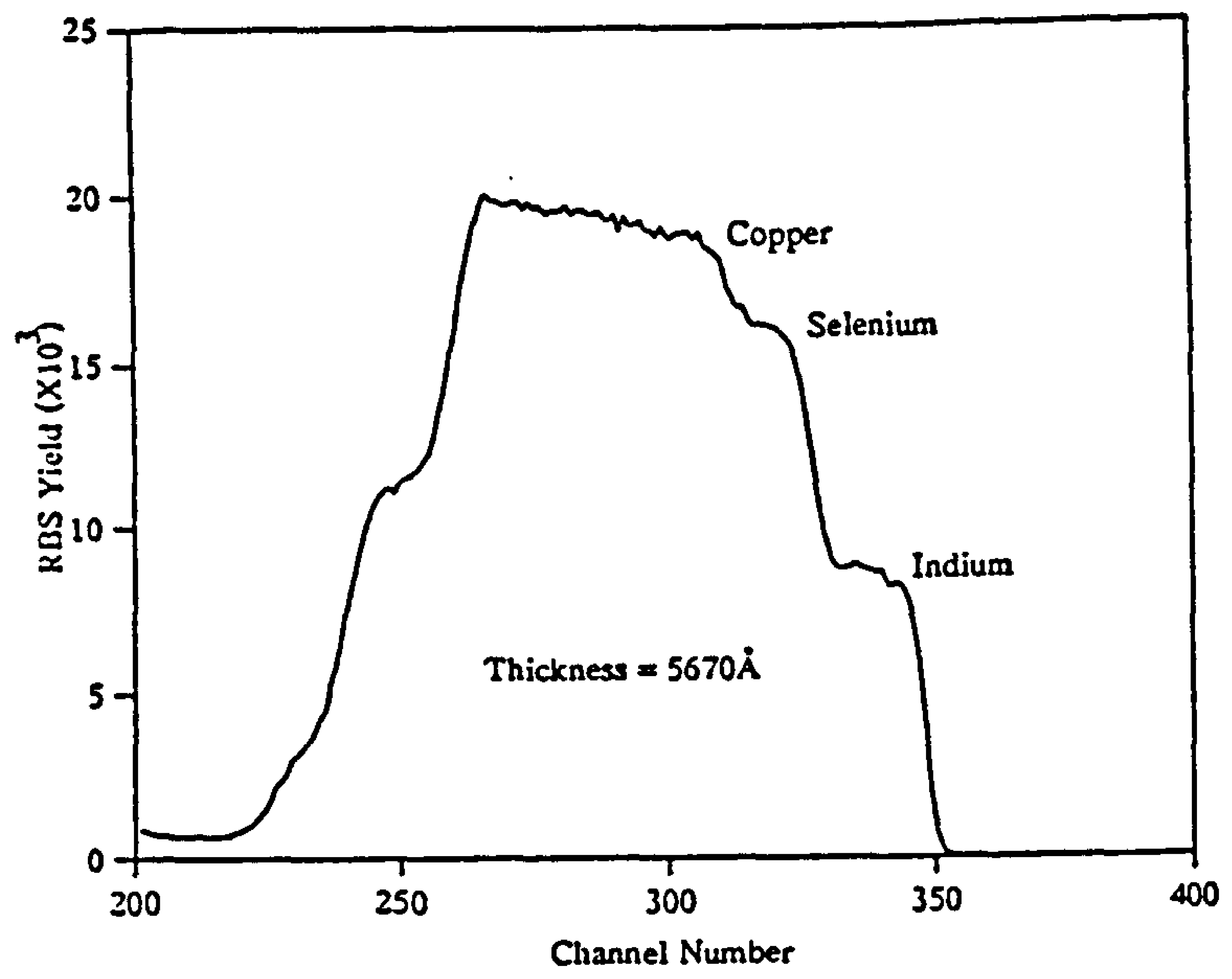


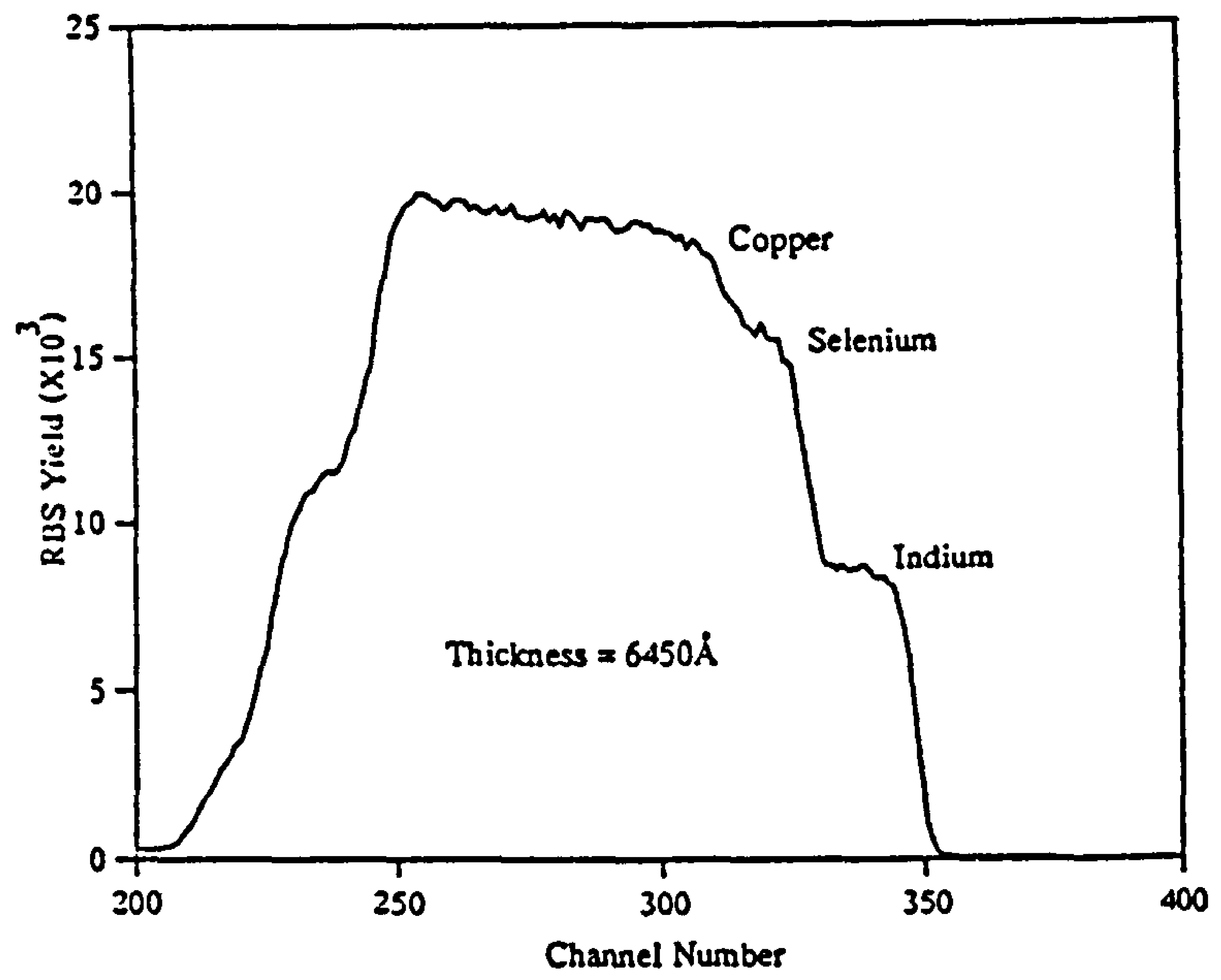


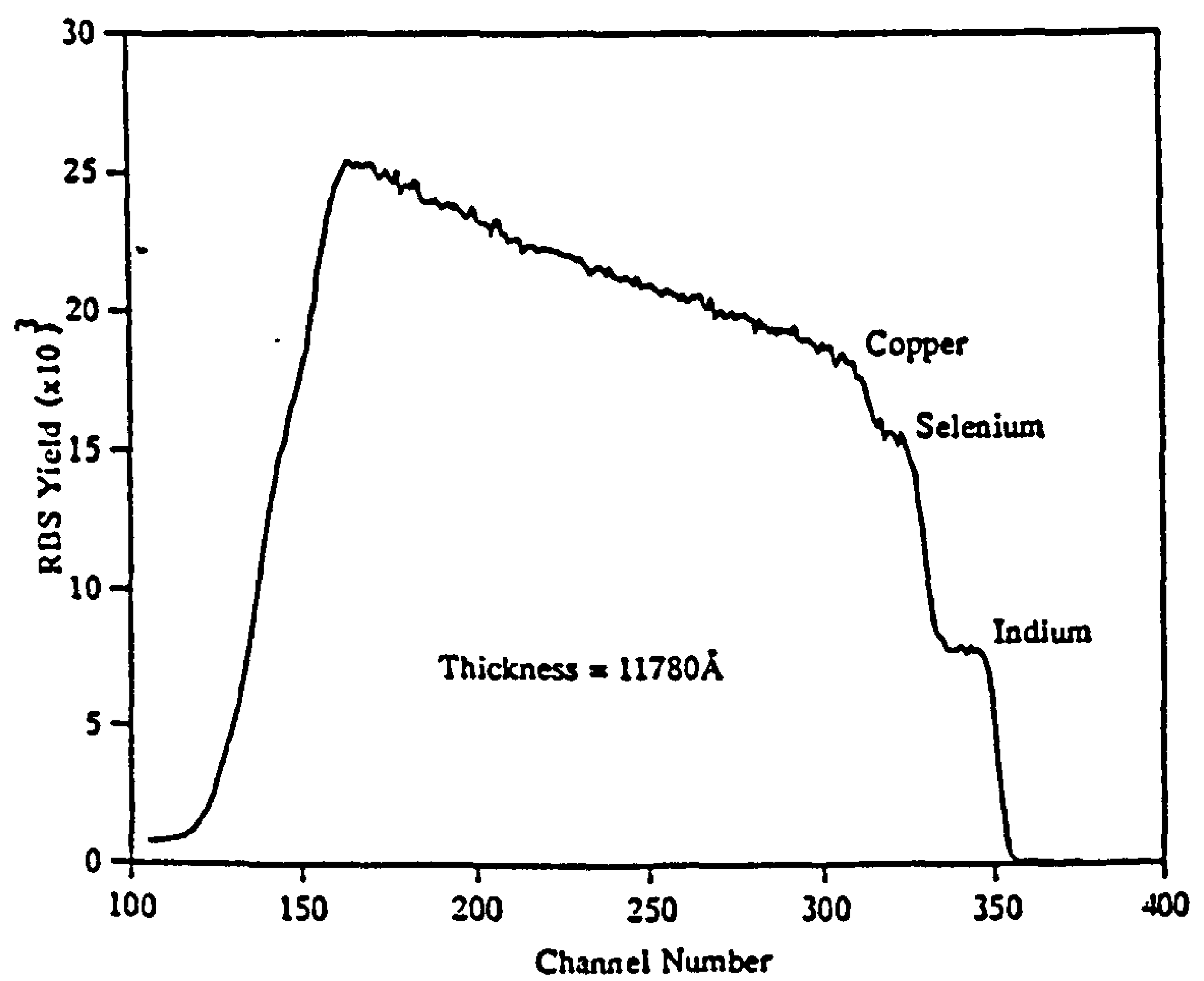


Figure 4.27 Effect of thickness on the RBS spectrum of CIS thin films.

Quantitative measurement of the deposited film thickness can also be achieved by the RBS technique. However, the accuracy of the film thickness strongly depends on the quality of the RBS spectrum. The effect of thickness on the RBS spectrum for CIGS and CIS thin films is shown in figures 4.26 and 4.27 respectively. It can be seen that the separation of front and back edges of the spectrum widened as the film thickness is increased. It was also noticed that for thicker samples a poor back edge is usually observed (see figure 4.27(c)) making it more difficult to measure precisely the film thickness.

Qualitative information about the film uniformity can also be obtained from the spectrum plateau. Large variations in the middle of the plateau can be indicative of a non-uniform, non-homogeneous sample, (example of this can be seen in figure 4.26(c)), whereas, the sample shown in figure 4.27(c) is comparatively more uniform.

### 4.6.3 Comparison of XRF, EDAX and RBS results

It is useful to compare the film composition of the as-grown films with the starting material as the major objective of the deposition process is to obtain a composition in the film which is identical to that of the original material. The films were all found to be deficient in selenium and slightly rich in indium when compared to the starting material. The excess indium in the as-grown films is probably due to the slightly reduced copper and selenium contents (section 4.2.1) which gives an erroneous result. It is believed that the films actual indium content is comparable to that of the starting

material.

A selenium deficiency is a routinely observed phenomenon in most of the deposition technologies investigated by workers thus far [191,210]. In order to overcome this particular problem either a higher percentage of selenium is incorporated in the source material [73,191] or the deposition is carried out under the maximum possible selenium vapour pressure [213]. In many cases this has been achieved by using a separate selenium source which maintains a high selenium vapour pressure level even after the deposition of the other elements has ceased.

Another alternative to reduce the selenium deficiency, involves a post-deposition heat treatment in various atmospheres including selenium [191,210,214]. The results obtained are discussed later in this thesis (chapter 5).

## 4.7 Electrical Properties

The electrical properties of the as-grown films, analyzed by the four point and the hot point probe techniques, showed no reproducible dependence on the deposition parameters. Both n- and p-type behaviour was observed.

Some samples were electrically inhomogeneous, giving both conductivity types within the same sample. These results can be understood by assuming that films were highly compensated with equal donor and acceptor concentrations.

The resistivity values of the as-grown films were in the range of $10^{-1}$ to $10^{3}$ Ωcm. The high values of resistivity can be attributed to structural disorder such as grain boundaries which offers a high resistive path to the movement of charge carriers. In high resistivity samples it was difficult to determine the conductivity type, due to the limited sensitivity of the hot probe technique. The results of this analysis are tabulated in table 4.9.

The high resistivity values and n-type behaviour observed in the CIGS thin films can be ascribed to intrinsic defects, such as selenium vacancies. These intrinsic defects can be due to vacancies, interstitials and antisites and Kroger [215] summarised the way in which these intrinsic defects can behave as either donors or acceptors.

CIGS is an intrinsically doped semiconductor, its conductivity being dependant on the number and type of defect. Two of the most important types of defect are the result of a deviation from molecularity or an excess or deficiency of electrons compared to the number needed to fill the outer orbital of the anion ($Se^{2-}$) [216]. Rincon and Bellabarba [217] reported that these defects can behave as either donors or acceptors. These can be due to anti-sites, indium interstitials and/or selenium or copper vacancies. In some of our as-grown samples, the observed n-type conductivity could be due to one or more of these defects. The probability of the formation of $In_i$ interstitials can be discarded due to their high heat of formation [217]. Defects of the type where indium resides on a copper site are likely to occur. It has been reported [218] that for indium rich CIS this type of defect dominates. However, selenium vacancies are the most likely source for the n-type behaviour [50]. During our depositions, a large amount of radiant heat from the source (before and during the course of deposition) was transferred to the substrate.

| Sample No. | Carrier type | Resistivity $\Omega$ - cm |
|---|---|---|
| FEO8 (CIGS) | n | $2.86 \times 10^{2}$ |
| FEO9 (CIGS) | n | $1.34 \times 10^{2}$ |
| FEO10 (CIGS) | n | $5.46 \times 10^{1}$ |
| FEO11 (CIGS) | n | $1.22 \times 10^{1}$ |
| FEO19 (CIGS) | ? | $4.16 \times 10^{3}$ |
| FEO20 (CIGS) | ? | $3.8 \times 10^{3}$ |
| FET15 (CIGS) | p | $2.00 \times 10^{2}$ |
| FET18 (CIGS) | p | $1.83 \times 10^{1}$ |
| FET21 (CIGS) | p | $8.30 \times 10^{-1}$ |
| FET25 (CIGS) | p | $6.04 \times 10^{1}$ |
| FET23 (CIS) | p | 1.69 |
| FET24 (CIS) | p | $2.76 \times 10^{-1}$ |
| FE103 (CIS) | n | $9.71 \times 10^{-2}$ |
| FE105 (CIS) | p | $3.63 \times 10^{2}$ |

Table 4.9 Electrical properties of flash evaporated CIGS and CIS thin films.

This is in addition to the energy of the evaporant. Both could cause the re-evaporation of selenium from the film and therefore influence the number of selenium vacancies.

## 4.8 Conclusions

X-ray diffraction analysis of the pre-reacted starting materials of both CIGS and CIS revealed the presence of the chalcopyrite structure. The composition of the powder was found to be slightly indium rich with a corresponding deficiency of copper. The segregation process, discussed in section 4.2.1, is the likely cause for this observed deficiency.

CIGS and CIS thin films have been successfully deposited onto glass substrates using flash evaporation of the pre-reacted material at substrate temperatures in the range from room temperature to 200°C.

The structural, compositional and electrical properties of the as-grown films were studied using a variety of analytical techniques. The as-grown CIGS and CIS thin films, deposited at room temperature, were shown to have a strong <112> preferred orientation. At higher deposition temperatures the film crystallinity improved and the preferential orientation along the <112> direction was enhanced along with the appearance of other CIGS/CIS related peaks. Raman spectra of the as-grown CIGS thin films (for all deposition temperatures) exhibited only the $A_1$ mode peak. An increase in the sharpness of this peak was observed as the composition of the films approached that of the starting

material. As the substrate temperature was increased from room temperature, the intensity of the $A_1$ mode peak was enhanced.

Results from XRF, EDAX and RBS all indicated that the as-grown films were slightly deficient in selenium. A complete absence of copper was found in films deposited at source temperatures below 1100°C. It was found that the percentage of copper gradually increased to a level comparable to that of the starting material when samples were prepared at elevated source temperature (>1100°C). Under our experimental conditions, a compensated source temperature of approximately 1500°C was found to be the minimum evaporation temperature for the successful deposition of thin films with a composition comparable to that of the starting material.

Both n and p-type conductivities were observed and this behaviour has been explained in terms of the formation of donor and acceptor states. It is proposed that the observed n-type conductivity is due to a selenium deficiency. Resistivity values in the range $10^{-1}$ to $10^{3}$ Ωcm were measured.

# Chapter 5

# Effect of post-deposition annealing on the film properties

## 5.1 Introduction

The efficiency of solar cells, utilising copper ternary compounds such as $Cu(In,Ga)Se_2$ as the photovoltaic active layer, is to a large extent dependent upon the micro-structure of the films. It is in particular limited by crystalline defects of the semiconducting material such as the density of grain boundaries and the number and type of dislocations. These can vary considerably and are primarily dependent on the fabrication/deposition process. There are several ways of reducing the population of these defects and thus improve the properties of the deposited films. The most common methods involve the optimisation of the deposition parameters and the use of post deposition heat treatments.

The effects of the deposition parameters on the film characteristics were described in chapter 4. This chapter, however, focuses mainly on results obtained by using various post deposition heat treatments to improve the structural, compositional and electrical properties of the flash evaporated CIGS, and CIS as-grown thin films.

Films deposited by the evaporation of pre-reacted polycrystalline starting material onto glass substrates were subsequently processed under several sets of annealing conditions including various ambients such as vacuum, selenium, inert and forming gas and at different temperatures and times.

## 5.2 Structural properties

The effects of post deposition annealing on the structural properties of flash evaporated CIGS and CIS thin films were studied in detail using x-ray diffraction (XRD) and scanning electron microscopy (SEM).

### 5.2.1 X-ray diffraction analysis

**CIGS**

As reported in chapter 4, the as-grown thin films of CIGS and CIS showed a highly preferred <112> orientation with very little evidence of other diffraction lines. It was therefore difficult to identify the film structure (sphalerite or chalcopyrite) of the deposited material by using routine XRD measurements. Information about the film structure can be obtained if it is more relaxed so that other diffraction lines can be seen. This can be achieved either by depositing the films at higher substrate temperatures (about 500°C) or by subjecting samples to post deposition heat treatments. Due to substrate temperature limitation, as mentioned in section 3.3.5, it was not possible to deposit films at temperatures greater than 200°C and so it was not possible to obtain films with a relaxed structure using this technique. It was therefore necessary to use post deposition heat treatments in various ambients at different temperatures and times.

Figure 5.1 shows XRD spectra of the as-grown and vacuum annealed samples of CIGS films. The vacuum anneal was performed at 300°C for one hour. It can be seen from figure 5.1 that the structure of the annealed film is comparatively more relaxed than that

(112)

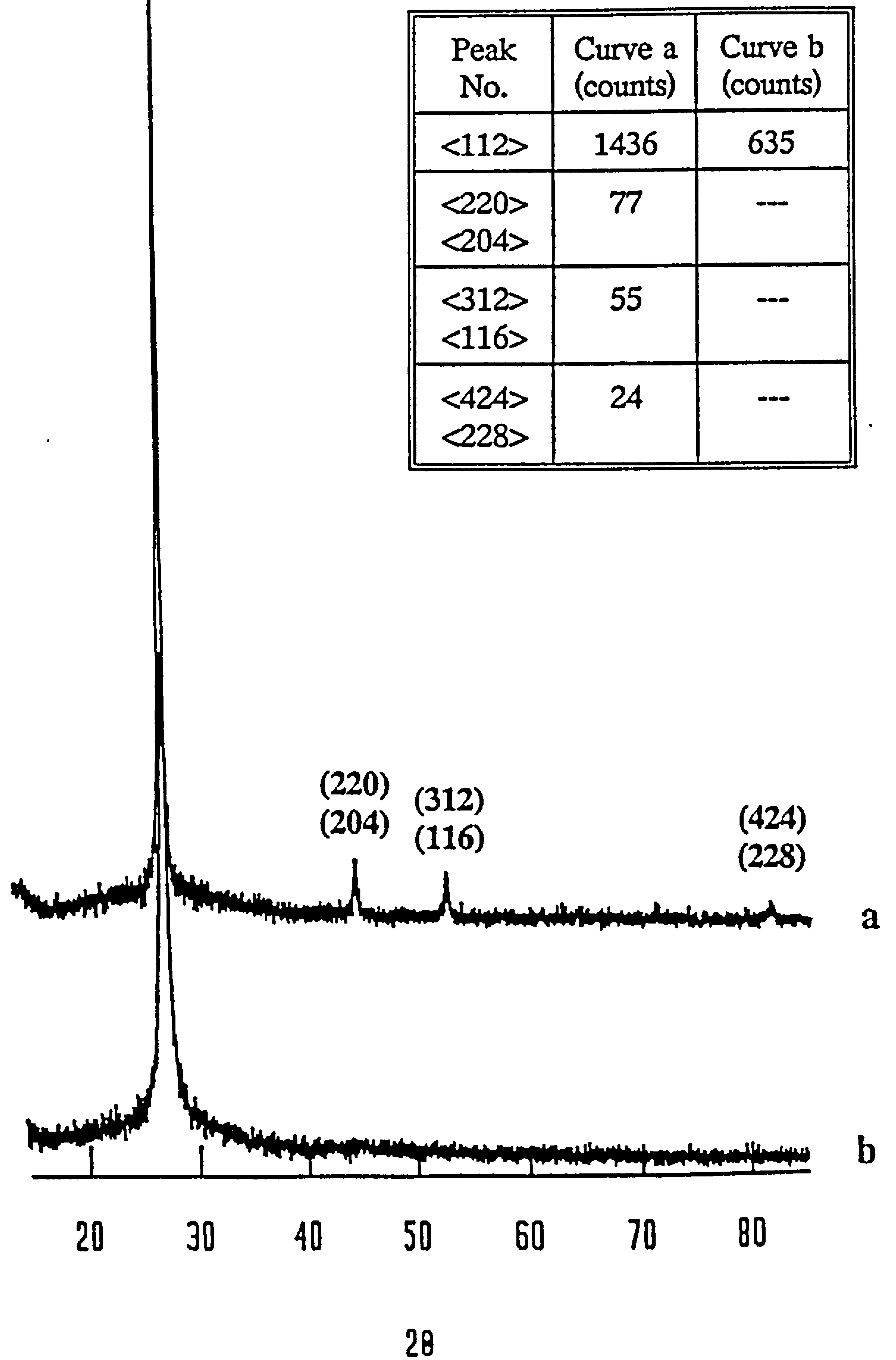

| Peak No. | Curve a (counts) | Curve b (counts) |
|---|---|---|
| <112> | 1436 | 635 |
| <220> <204> | 77 | --- |
| <312> <116> | 55 | --- |
| <424> <228> | 24 | --- |



Figure 5.1: XRD spectra of CIGS thin films; (a) vacuum annealed at 300°C for one hour, (b) the as-grown.

of the as-grown film - the diffraction peaks corresponding to <220,204>, <312,116> and <424,228> are now present. In the case of a vacuum anneal at 250°C, the last peak in the spectrum (appertaining to a d spacing of 1.17Å corresponding to <424,228>) was not observed and the intensities of the other peaks were relatively small. This indicates that, at higher annealing temperatures, the surface migration of the adsorbed atoms is enhanced, creating a more relaxed structure. Further increase in annealing temperature could result in a more relaxed structure and hence form the chalcopyrite structure. However, annealing temperatures exceeding 400°C were not tried because of the possibility of degrading the compositional properties by re-evaporation of selenium from the film and the formation of micro-cracks due to thermal stresses.

Figure 5.2 displays spectra relating to films annealed in a 9:1 mixture of $N_2$:$H_2$ (forming gas) at 300°C for 2 hours and films annealed in selenium at 300°C for 2 hours. Once again, changes in the film structure and orientation due both annealing processes are clearly evident. The <112> peak intensity increases together with the appearance of the <220,204> and <312,116> diffraction lines. A small diffraction peak at a 2Θ value of 38° can also be noticed. However, it can be clearly seen that the intensity of this peak is more pronounced in the selenium annealed film than in the $N_2$:$H_2$ annealed film. This peak could be due to the formation of a secondary phase related to $CuIn_2Se_{3.5}$ [219,220]. The formation of this compound is more likely under selenium annealing conditions as the un-annealed samples were rich in indium and deficient in selenium. Other than the formation of secondary phases, the behaviour of the relaxed structure is identical to that observed for the samples deposited at higher substrate temperatures or annealed in vacuum.

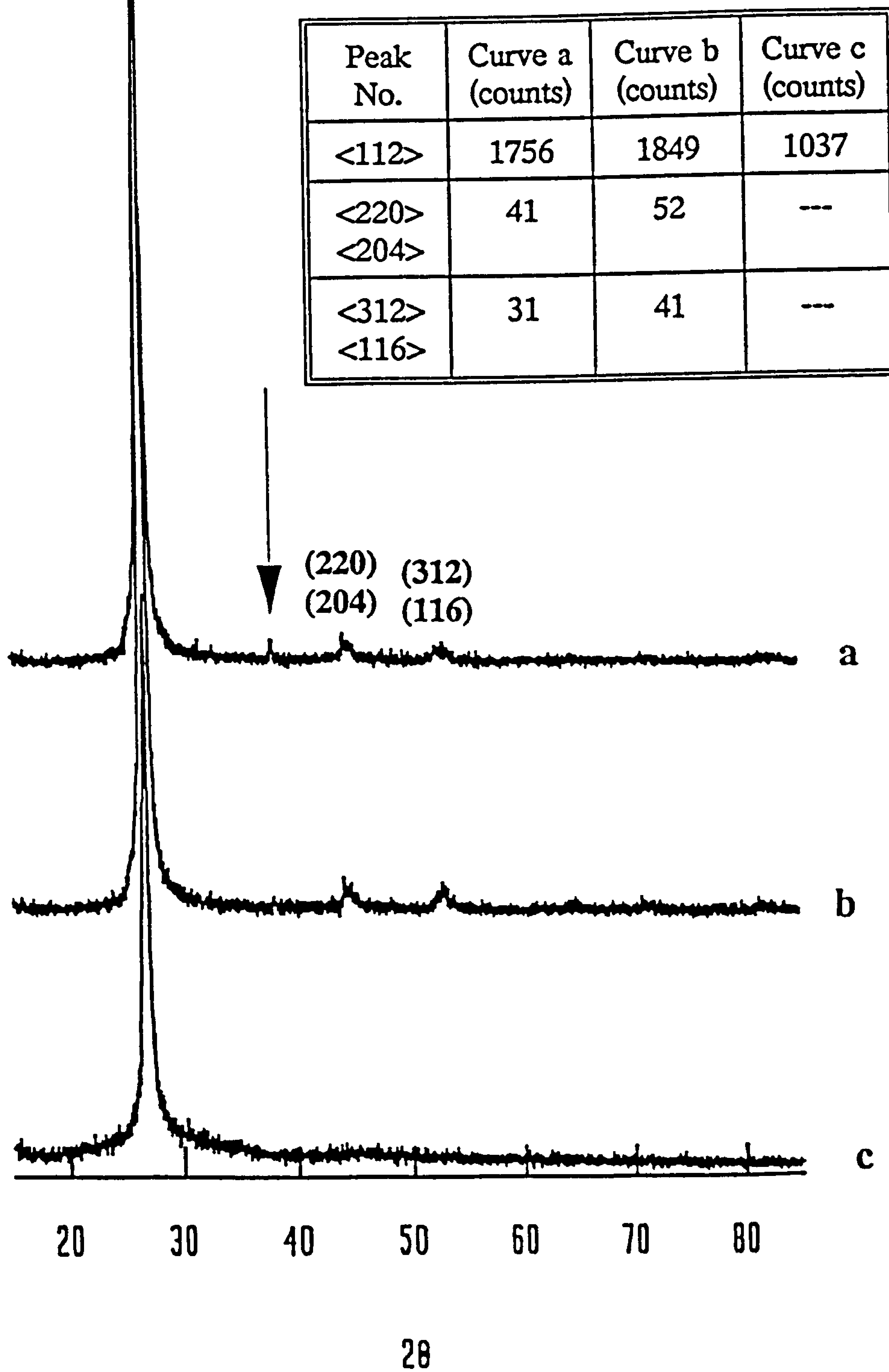


| Peak No. | Curve a (counts) | Curve b (counts) | Curve c (counts) |
|---|---|---|---|
| <112> | 1756 | 1849 | 1037 |
| <220> <204> | 41 | 52 | --- |
| <312> <116> | 31 | 41 | --- |

Figure 5.2: XRD spectra of CIGS thin films; (a) annealed in selenium at 300°C for two hours, (b) $N_2$:$H_2$ annealed at 300°C for 2 hours and (c) the as-grown.

In all the annealing processes discussed above, the structures of the thin film samples were more relaxed with the appearance of other diffraction peaks, but confirmation of the existence of the chalcopyrite structure could never be proved. To overcome this problem it was decided to use a two stage annealing process involving an initial anneal in selenium followed by an anneal in $N_2$:$H_2$ or Argon.

In figure 5.3 the XRD spectra of a two stage annealed film is compared with that of the as-grown film. The first stage of the annealing process was performed in selenium at 300°C for two hours; this was followed by an anneal in a 9:1 mixture of $N_2$:$H_2$ at 300°C for half an hour. A second two stage anneal was carried out using selenium at 300°C for two hours followed by argon at 300°C for half an hour. It can be seen that the two stage annealing process not only resulted in a more relaxed structure, but also revealed the presence of the chalcopyrite structure, indicated by the existence of the <101> and <211> peaks. The characteristic peaks of the chalcopyrite structure can be identified at $2\theta$ values of 17.2° and 35.7° respectively. The intensity of the <112> diffraction peak, which is the only peak observed in the as-grown samples, also increased. In addition, other CIGS related peaks were observed as shown in table 5.1. When comparing the two stage anneals using Se/$N_2$:$H_2$ and Se/argon it can be seen that there was little difference in the intensities of the peaks. This demonstrates that the nature of the second annealing ambient is not an important parameter in the overall annealing process. The structural effects observed are predominantly temperature related. This argument is supported by experimental evidence obtained from films grown by laser ablation at different substrate temperatures [221].

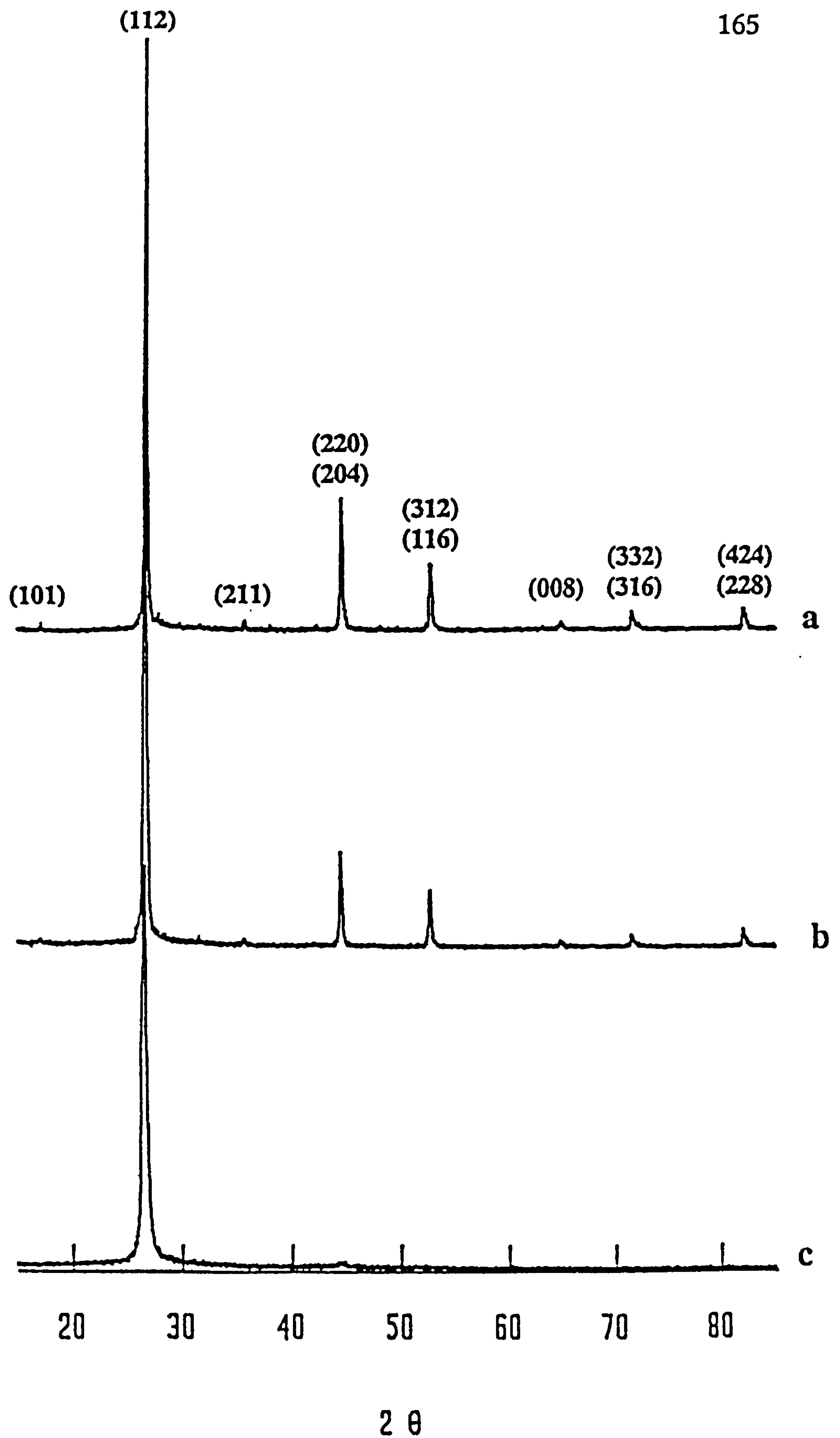


Figure 5.3: XRD spectra of CIGS thin films; (a) selenium annealed at 300°C for two hours + argon annealed at 300°C for half hour, (b) selenium annealed at 300°C for two hours + $N_2$:$H_2$ annealed at 300°C for half hour and (c) the as-grown.

| Peak No. | hkl | Pre-reacted material | | CIGS thin films | |
|---|---|---|---|---|---|
| | | d-value (meas.) | $I/I_{max}$ (%) | d-value (meas.) | $I/I_{max}$ (%) |
| 1 | 101 | 5.14 | 12.2 | 5.15 | 0.94 |
| 2 | 112 | 3.32 | 94.81 | 3.32 | 100 |
| 3 | 103 | 3.19 | 2.89 | 3.19 | 1.91 |
| 4 | 211 | 2.51 | 8.52 | 2.51 | 1.50 |
| 5 | 213,105 | 2.13 | 2.20 | 2.13 | 0.74 |
| 6 | 220,204 | 2.03 | 100 | 2.03 | 21.08 |
| 7 | 301 | 1.88 | 2.89 | 1.89 | 0.20 |
| 8 | 312,316 | 1.72 | 67.33 | 1.73 | 11.70 |
| 9 | 305,323 | 1.46 | 1.37 | 1.47 | 0.52 |
| 10 | 008 | 1.43 | 7.18 | 1.43 | 1.40 |
| 11 | 411,217 | 1.38 | 1.43 | ---- | ---- |
| 12 | 332,316 | 1.31 | 11.06 | 1.31 | 2.95 |
| 13 | 424,228 | 1.17 | 15.21 | 1.17 | 3.40 |

Table 5.1: Comparison of the x-ray powder diffraction data of the polycrystalline pre-reacted starting material and CIGS thin films.

However, if a reactive atmosphere, such as selenium, is employed then other effects have a bearing on the film structure and need to be considered carefully. For example, using a selenium atmosphere results in changes in the observed diffraction peaks and film composition which leads to changes in the electro-optical properties.

## CIS

Figure 5.4 shows a typical XRD spectrum of as-grown and two stage annealed (selenium anneal at 300°C for two hours followed by an anneal under 9:1 mixture of $N_2$:$H_2$ at 300°C for two hours) CIS thin films. Again the characteristic chalcopyrite peaks <101> and <201> are clearly evident in the annealed film. The comparison of the x-ray powder diffraction data of CIS thin films and of the starting material is shown in table 5.2.

The literature contains a number of articles reporting the relaxation of CIS thin film structures and the ultimate formation of the chalcopyrite phase by annealing at different temperatures under various ambients. For example, it was reported that copper and indium rich as-grown electro-deposited thin films [148,222] were micropolycrystalline with weak and broad diffraction peaks corresponding to sphalerite CIS phases, with some possible $Cu_xSe$ and $In_2Se_3$ phases. However, the chalcopyrite structure was identified without any secondary phases after annealing the copper and indium rich films in an argon ambient at temperatures >350°C and in selenium ambients at 450°C respectively. The characteristics peaks of the chalcopyrite phase were only observed in annealed samples.

The influence of annealing on the structural properties of stacked elemental layers (SEL)

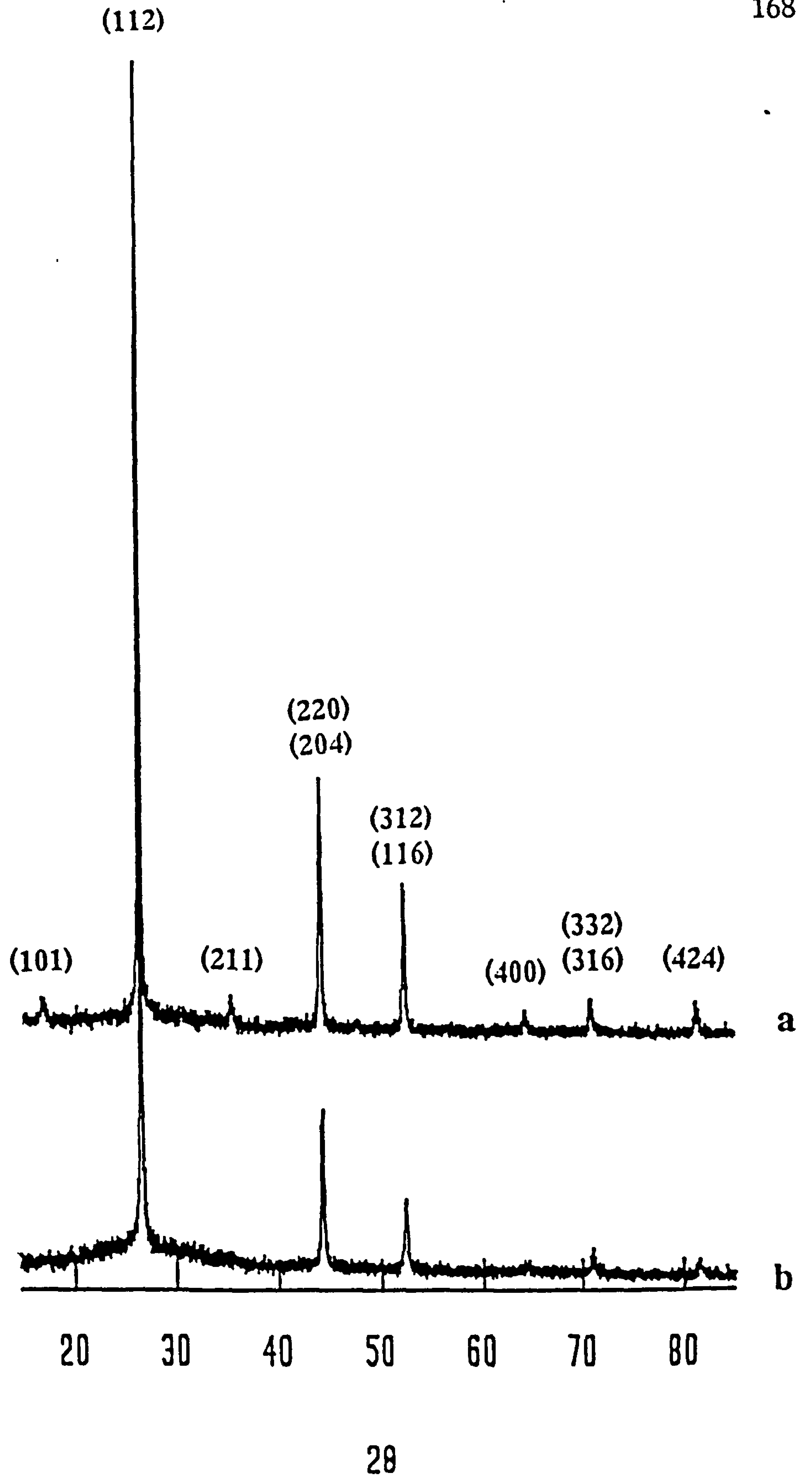


Figure 5.4: XRD spectra of CIS thin films; (a) selenium annealed at 300°C for two hours + $N_2$:$H_2$ annealed at 300°C for two hours and (b) the as-grown.

| Peak No. | hkl | Pre-reacted material | | CIS thin films | |
|---|---|---|---|---|---|
| | | d-value (meas.) | $I/I_{max}$ (%) | d-value (meas.) | $I/I_{max}$ (%) |
| 1 | 101 | 5.204 | 11.95 | 5.22 | 2.42 |
| 2 | 112 | 3.343 | 100 | 3.352 | 100 |
| 3 | 103 | 3.224 | 7.75 | 3.208 | 1.86 |
| 4 | 211 | 2.530 | 7.62 | 2.532 | 2.76 |
| 5 | 213,105 | 2.157 | 3.62 | ---- | ---- |
| 6 | 220,204 | 2.047 | 87.43 | 2.05 | 26.05 |
| 7 | 301 | 1.899 | 3.45 | 1.90 | 0.73 |
| 8 | 312,116 | 1.747 | 37.52 | 1.747 | 15.96 |
| 9 | 305,323 | 1.482 | 1.40 | 1.484 | 0.77 |
| 10 | 400 | 1.447 | 6.75 | 1.448 | 1.73 |
| 11 | 411,217 | 1.395 | 1.35 | ---- | ---- |
| 12 | 316,332 | 1.328 | 15.74 | 1.33 | 3.76 |
| 13 | 109,307 | 1.257 | 1.09 | ---- | ---- |
| 14 | 415 | 1.200 | 1.09 | ---- | ---- |
| 15 | 424 | 1.182 | 17.44 | 1.18 | 3.24 |

Table 5.2: Comparison of the x-ray powder diffraction data of the polycrystalline pre-reacted starting material and CIS thin film.

[223], co-evaporated [224] and DC magnetron co-sputtered [225] thin films of CIS have also been observed. In all cases the annealing times and ambients were different. However, the annealing temperature was always greater than 300°C.

These reports further support our discussion that structural changes observed in annealed CIGS and CIS samples are temperature related, independent of ambient and deposition technique employed.

### 5.2.2 Scanning electron microscopy

The surface structure of CIGS and CIS films, subjected to a variety of annealing regimes, have been investigated using scanning electron microscopy. The as-deposited films revealed a relatively small grain structure with grain sizes being small and uniform and the grain voids being pronounced, as discussed in detail in chapter 4.

The effects of annealing in selenium at a number of different temperatures for periods of two hours are shown in figure 5.5. As expected, increasing the annealing temperature to between 250 and 300°C resulted in grain growth. In addition, the density of the grains increased with selenium being deposited on the surface. However, a further 100°C increase in temperature resulted in the appearance of micro-cracks in the annealed films due to thermal stress as discussed earlier in section 5.2.1. The grain sizes are not as uniform as in the case of as-deposited samples.

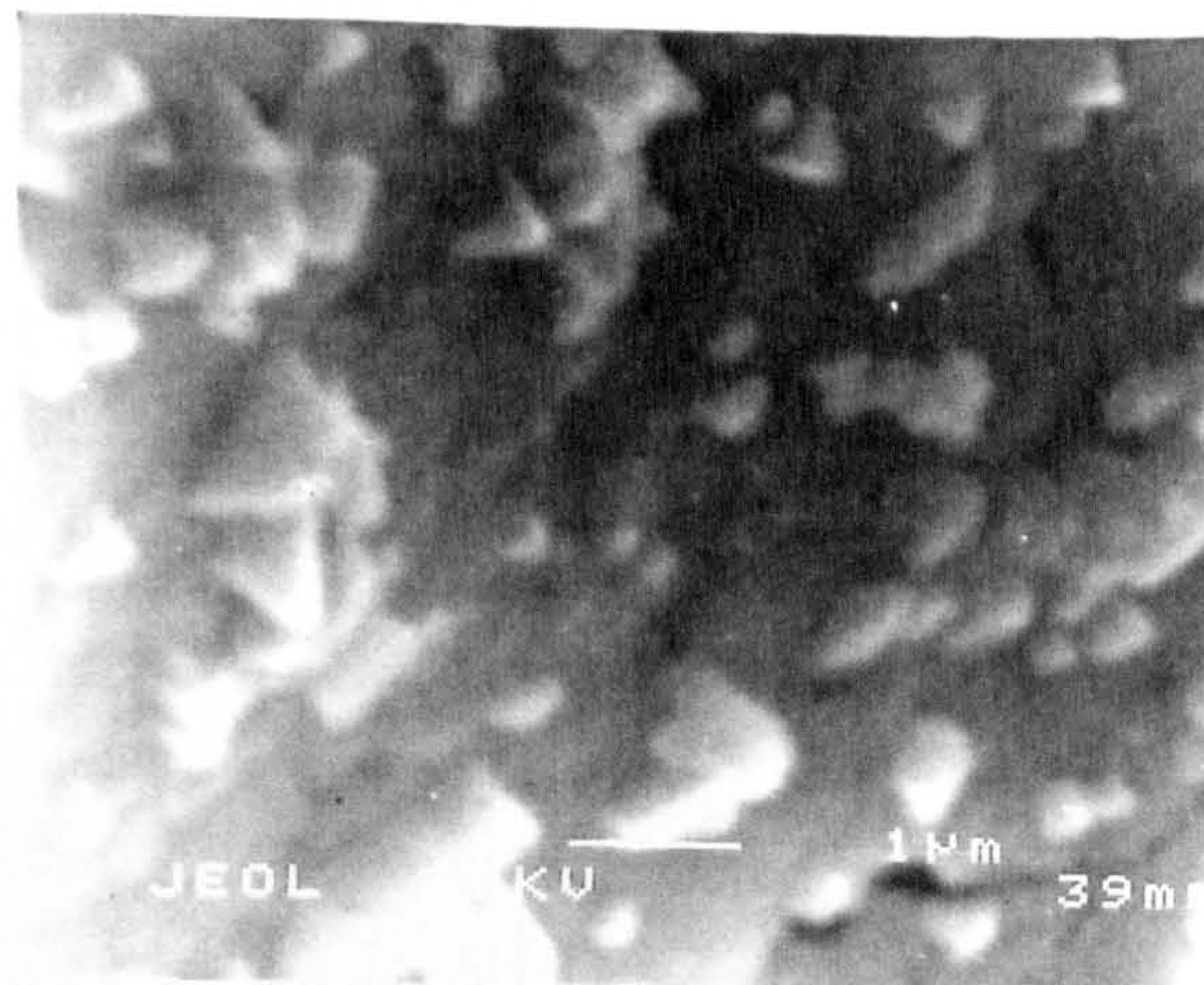


a

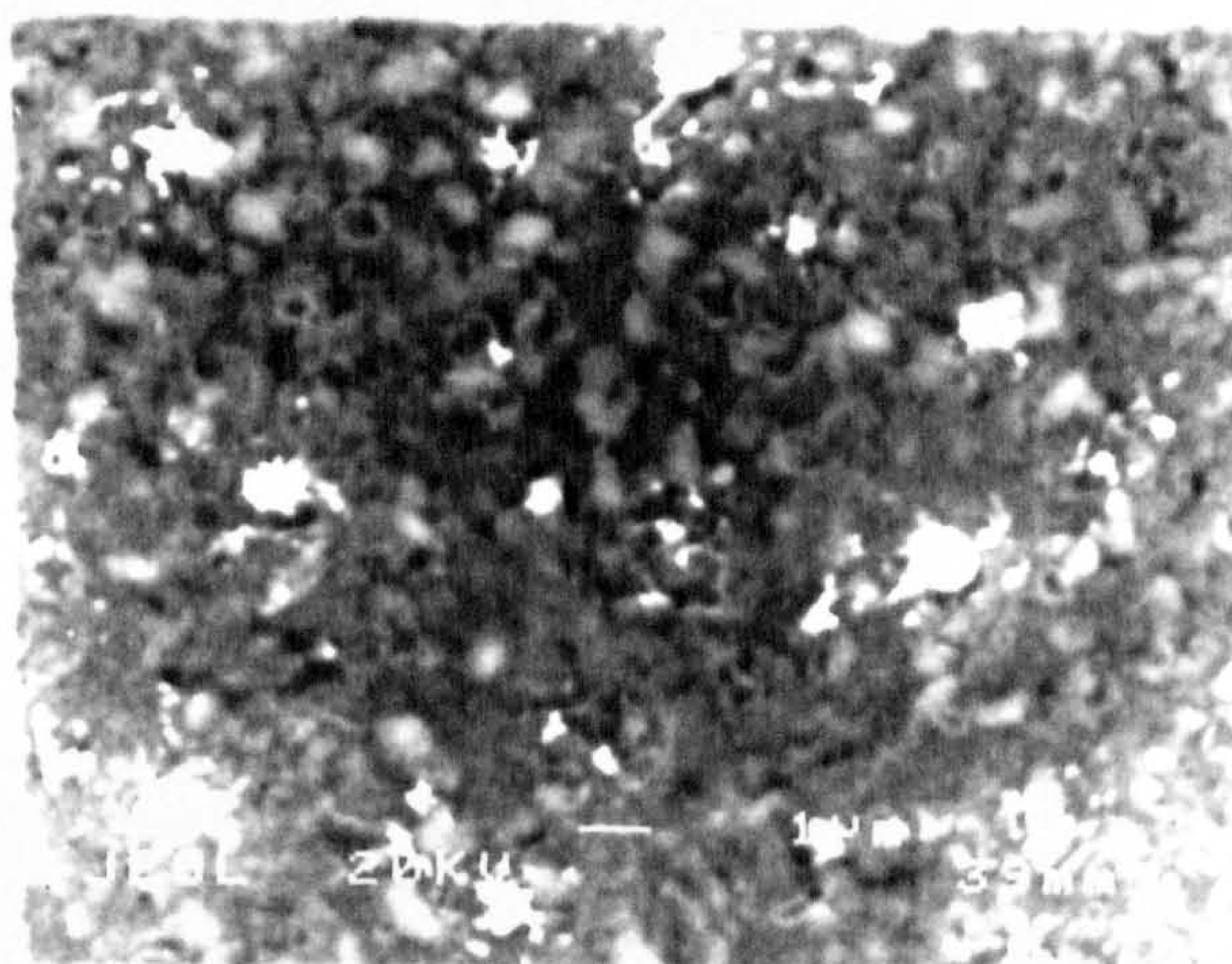

b

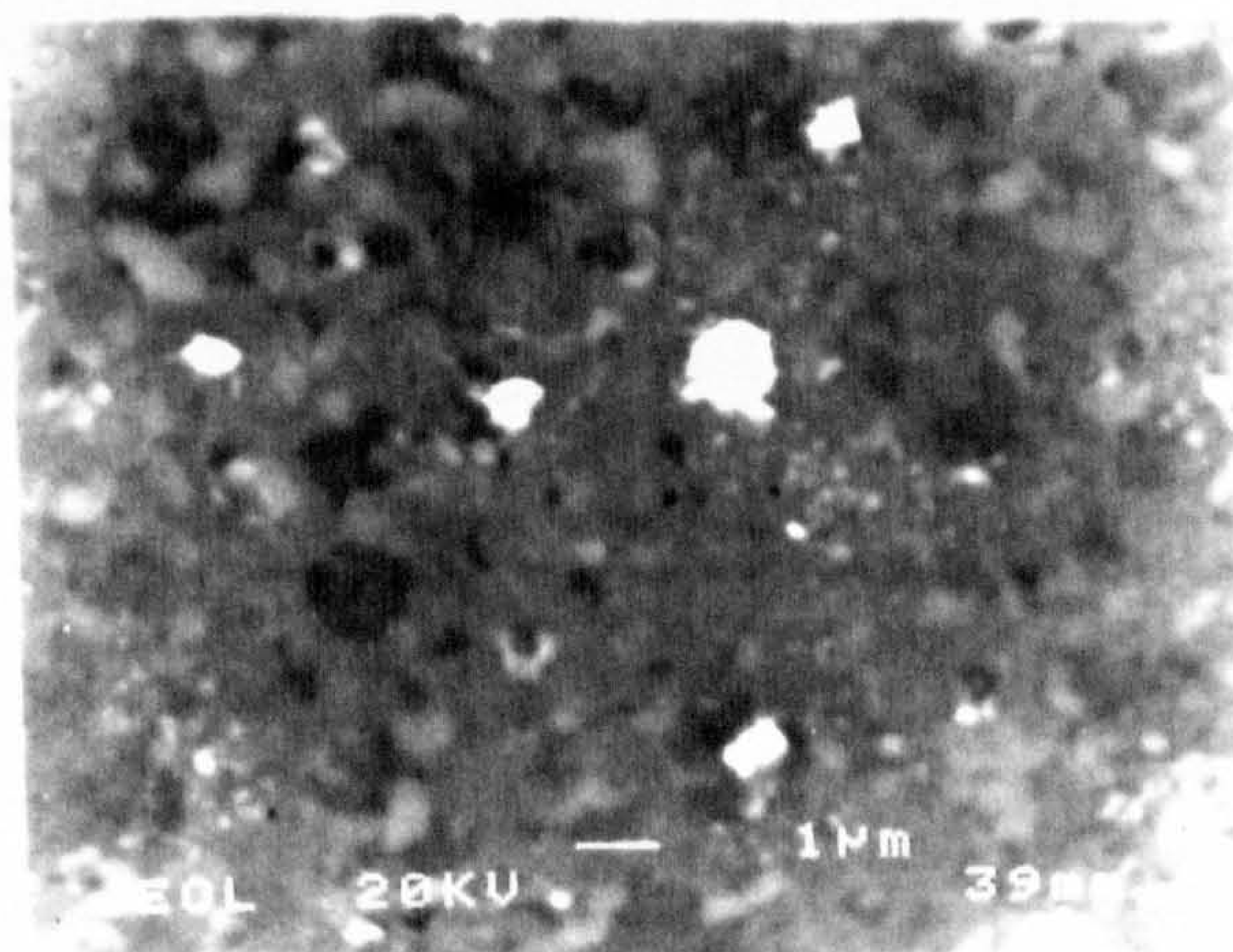


c

Figure 5.5: Scanning electron micrographs of CIGS thin films annealed in selenium a) at 400°C, b) at 300°C and c) at 250°C for two hours.

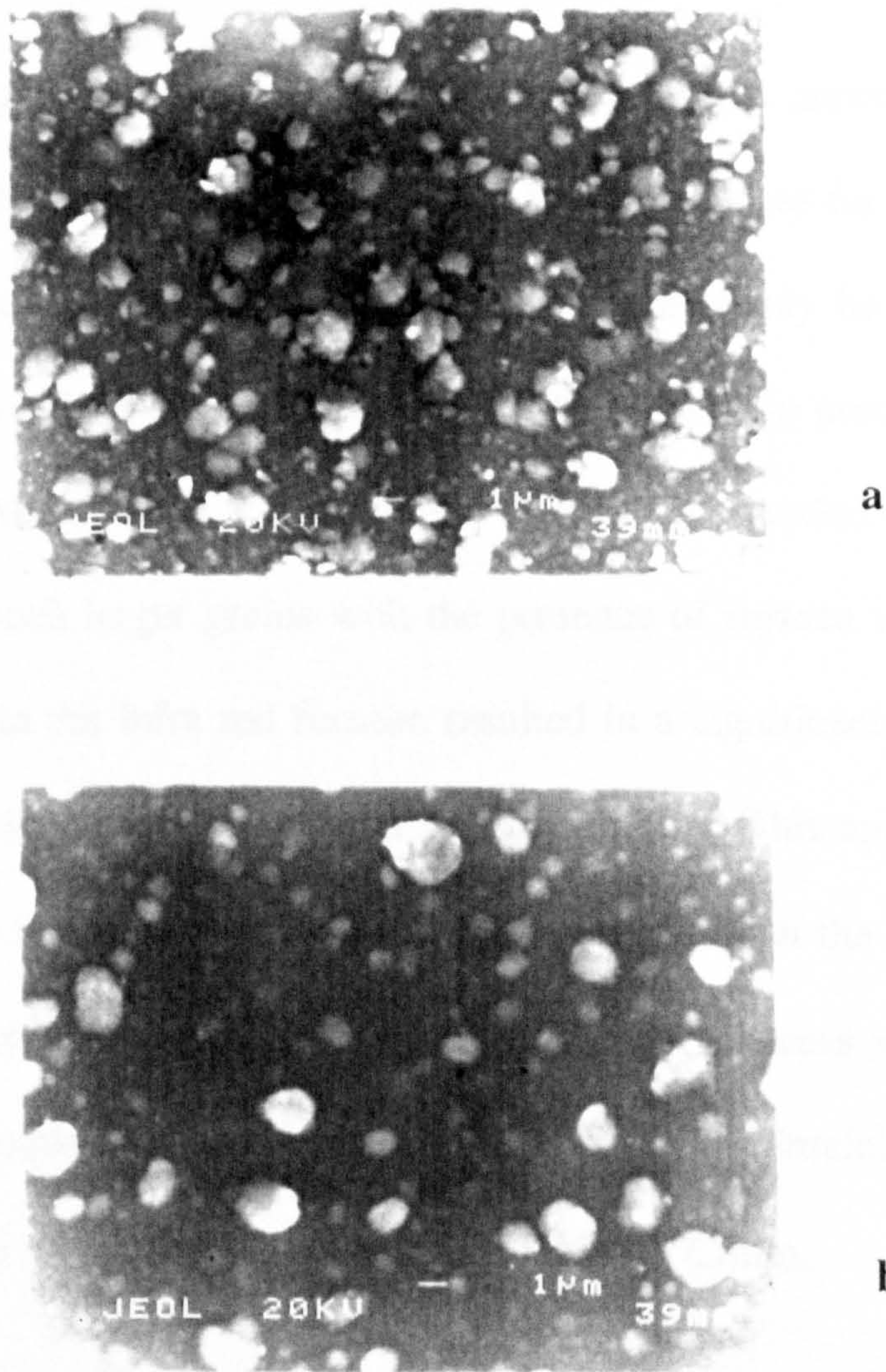


Figure 5.6: Scanning electron micrographs of CIGS thin films; (a) annealed under 9:1 mixture of $N_2$:$H_2$ ambient at 300°C for two hours and (b) at 300°C for one hour.

Annealing in forming gas for 1 and 2 hours respectively showed that an increase in the annealing time resulted in a more granular deposit (see figure 5.6). When compared to the selenium annealed samples these were seen to be more granular.

A two stage annealing process was investigated with an initial anneal in selenium at 300°C for 2 hours. The sample was then divided into two pieces for annealing under $N_2$:$H_2$ (9:1 ratio) for one hour; one was annealed in a resistively heated furnace, the other in a pulsed infra red annealing furnace. Using this two stage process larger grains (ca. 2μm) were observed - figure 5.7. However, the sample annealed in the resistively heated furnace had much larger grains with the presence of surface voids. In contrast the sample annealed in the infra red furnace resulted in a significant reduction in the number of surface voids and a larger grain size distribution. This apparent difference could perhaps be due to the difference in the heating rates. With the infra red heating method a rate of approximately 20°C/min was employed, whereas with the resistive heating system the sample was inserted inside the oven after maintaining a temperature of 300°C. which gave an approximate heating rate of 300°C/min.

For comparative purposes some samples of CIS films were also subjected to this two stage annealing process. The effects observed are shown in figure 5.8; similar effects of the annealing processes on grain growth were observed, however the increase in grain size was small when compared to that of the CIGS samples. It was also noted that the two stage anneal did not eliminate the deposited selenium from the surface of the samples.

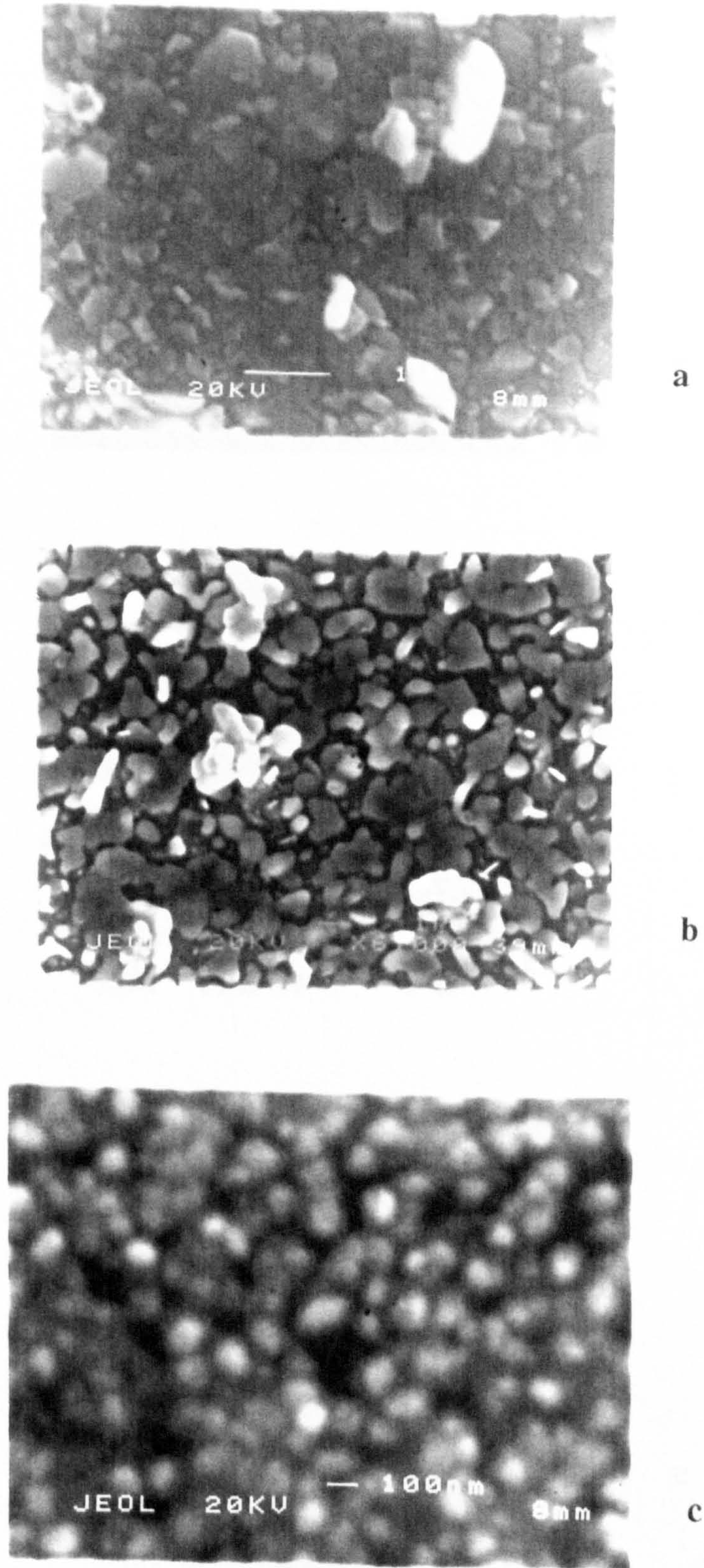


Figure 5.7: Scanning electron micrographs of CIGS thin films; (a) selenium annealed at 300°C for two hours + $N_2$:$H_2$ annealed at 300°C for two hours in a infra-red heater, (b) in a constant resistive heater at 300°C for two hours and (c) the as-grown.

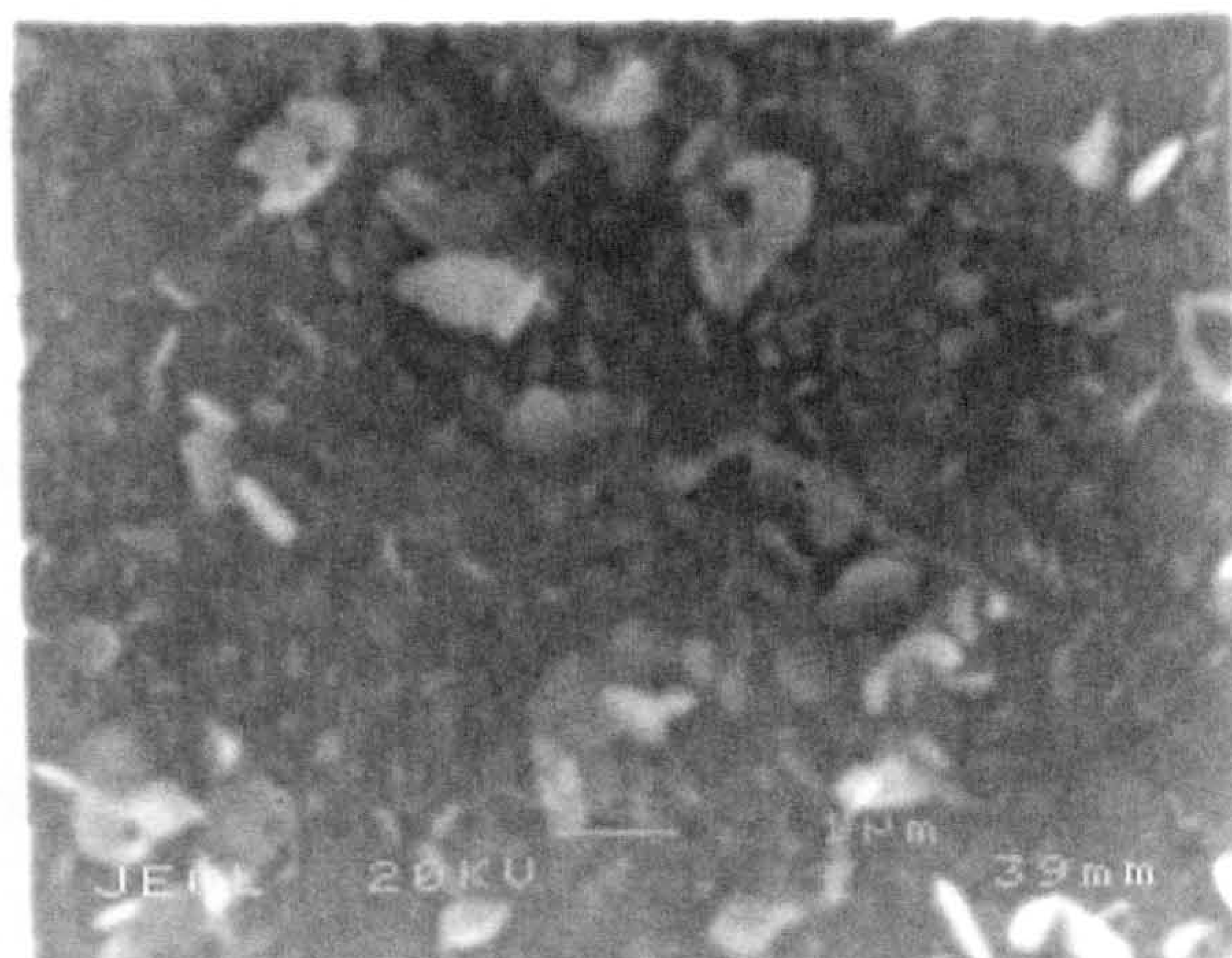


a

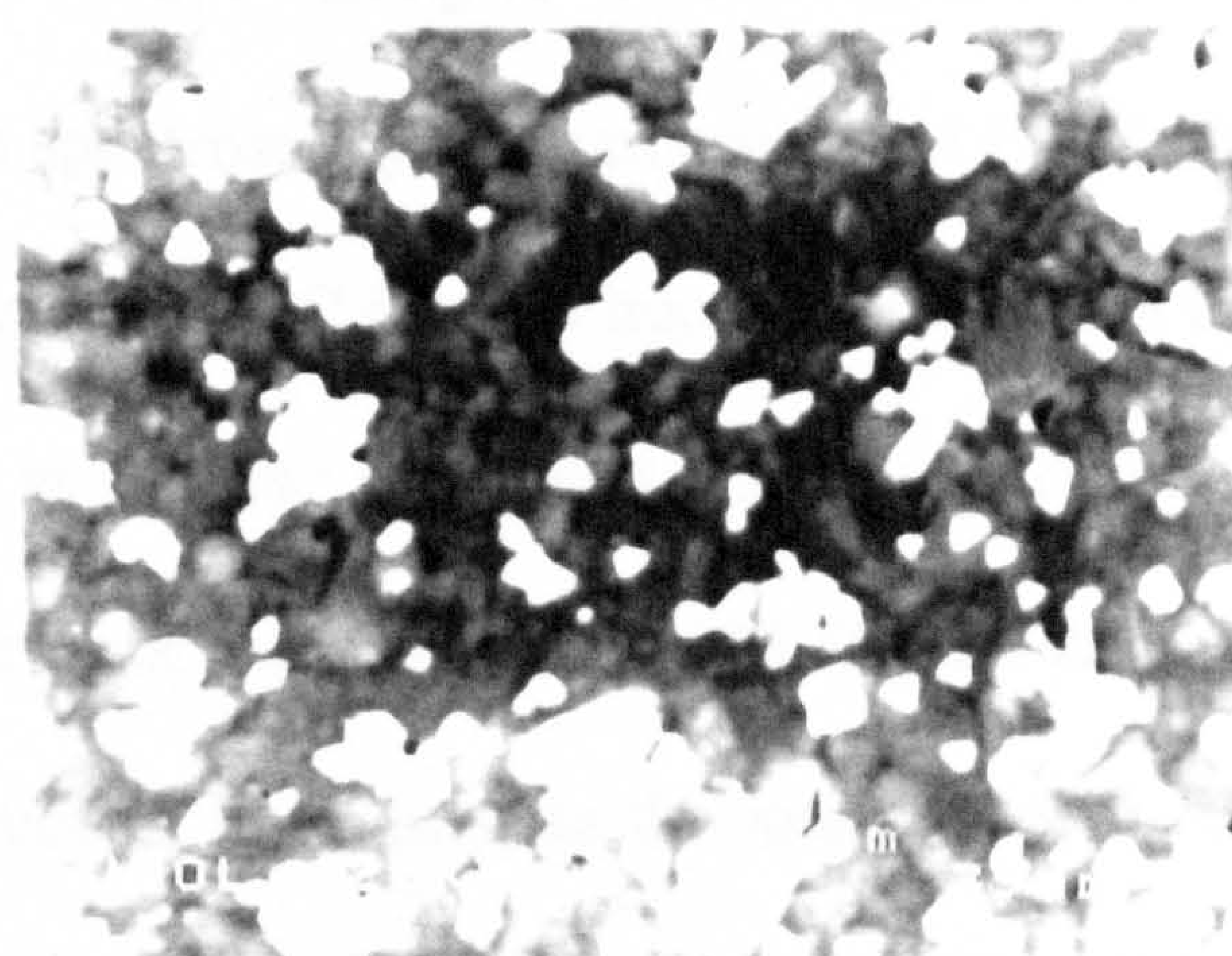

b

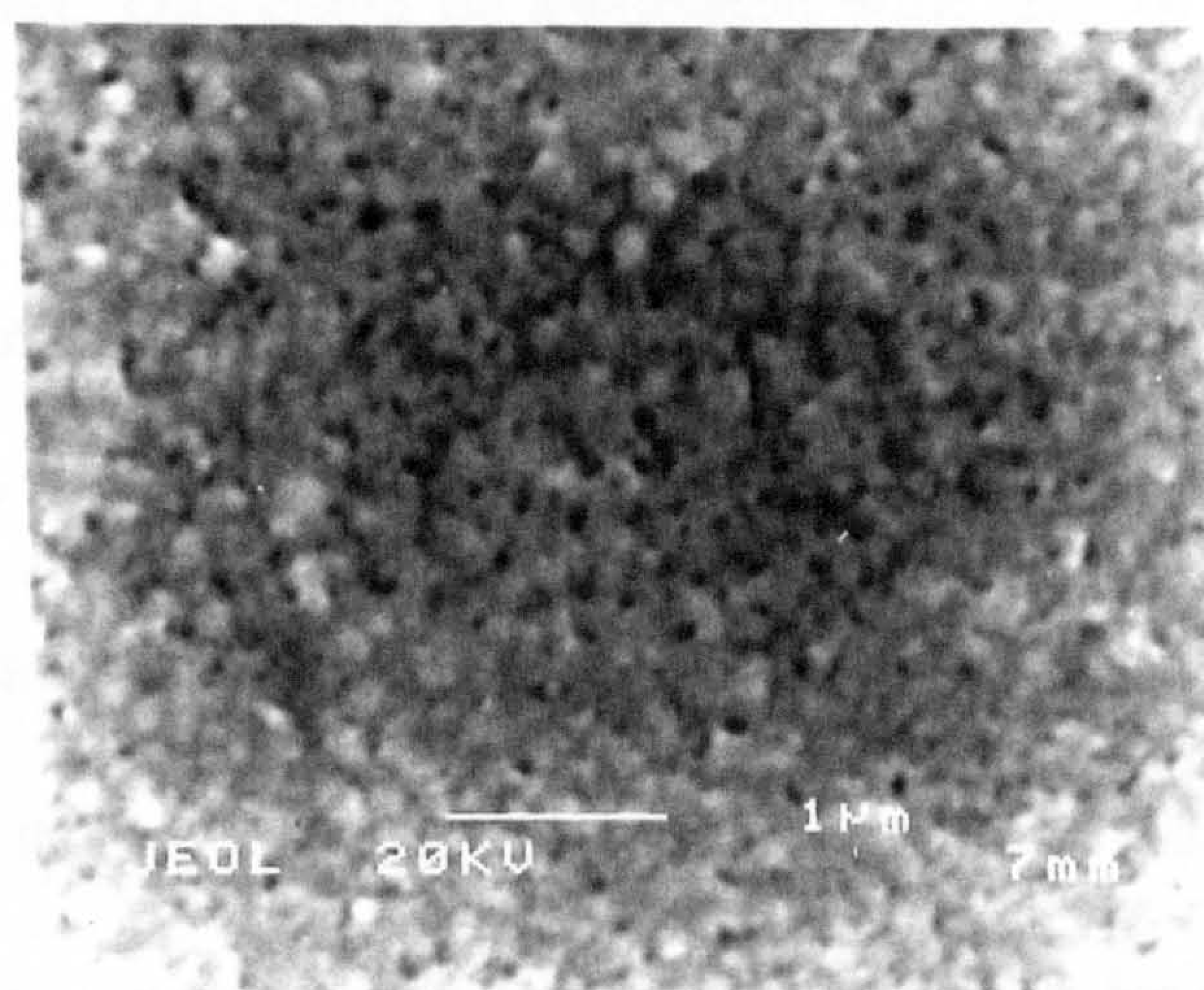


c

Figure 5.8: Scanning electron micrographs of CIS thin films; (a) selenium annealed at 300°C for two hours + $N_2$:$H_2$ annealed at 300°C for two hours, (b) selenium annealed at 300°C for two hours and (c) the as-grown.

### 5.2.3 Raman spectroscopy

Due to the reliance on the microelectronic and materials physics laboratories, University of Oulu, Finland for the Raman analysis, only a small number of samples of CIGS thin films both as-grown and two stage annealed were analyzed.

The structural changes observed using XRD and SEM were further investigated and confirmed using Raman spectroscopy. Raman spectra of CIGS thin films both as-grown and annealed in selenium at 300°C for two hours are shown in figure 5.9. Only a sharp single peak is observed at 175cm$^{-1}$ associated with the $A_1$ mode. The FWHM of the as-grown sample $A_1$ mode peak was found to be 16.35cm$^{-1}$. After annealing a significant improvement in the structure is evident, as the intensity of $A_1$ mode peak is increased and the resultant FWHM value is reduced to 11.32cm$^{-1}$. In addition, another weaker peak at 212cm$^{-1}$ has appeared. This could be associated with "$B_2$" or "E" modes [204].

Figure 5.10 shows the Raman spectra of the as-grown CIGS film (b) and two stage annealed film (c). For comparison the Raman spectra of single crystal CIGS (a) is also included (not at the same scale). The $A_1$ mode peak, for as grown samples, was small and relatively broad, suggesting that the structure of this film is poor (confirmed by SEM). However, after a two stage anneal the $A_1$ peak is larger and better resolved, implying that the annealing process reduces the number of defects and voids resulting in an improvement in both the composition and structure. Two weak peaks at 212 and 230cm$^{-1}$ were also present and it is speculated that the peak at 240cm$^{-1}$ could be due to surface selenium [203]. The effects of annealing can be better understood by comparing

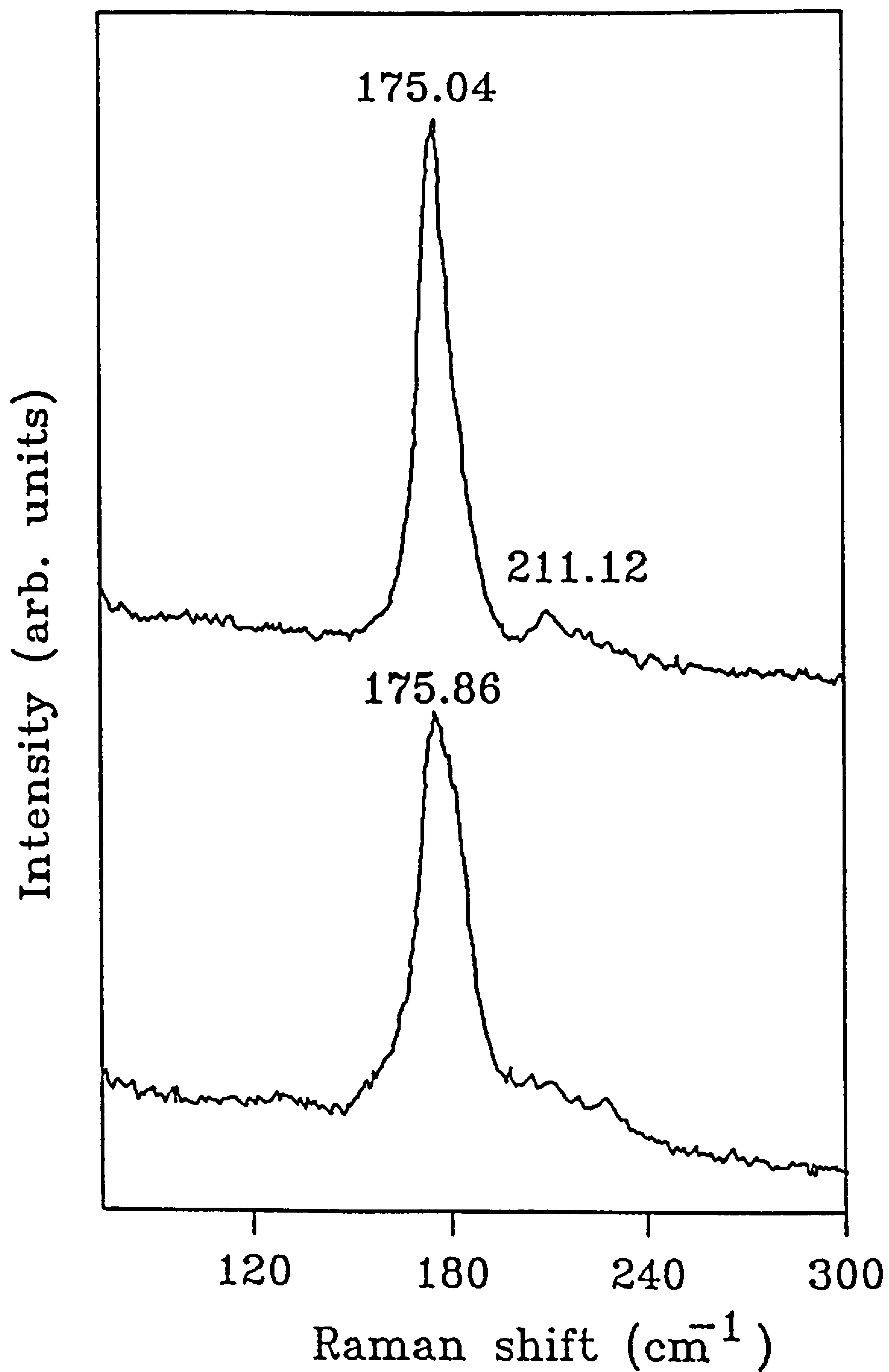


Figure 5.9: Raman spectra of CIGS thin films; (a) selenium annealed at 300°C for two hours and (b) the as-grown.

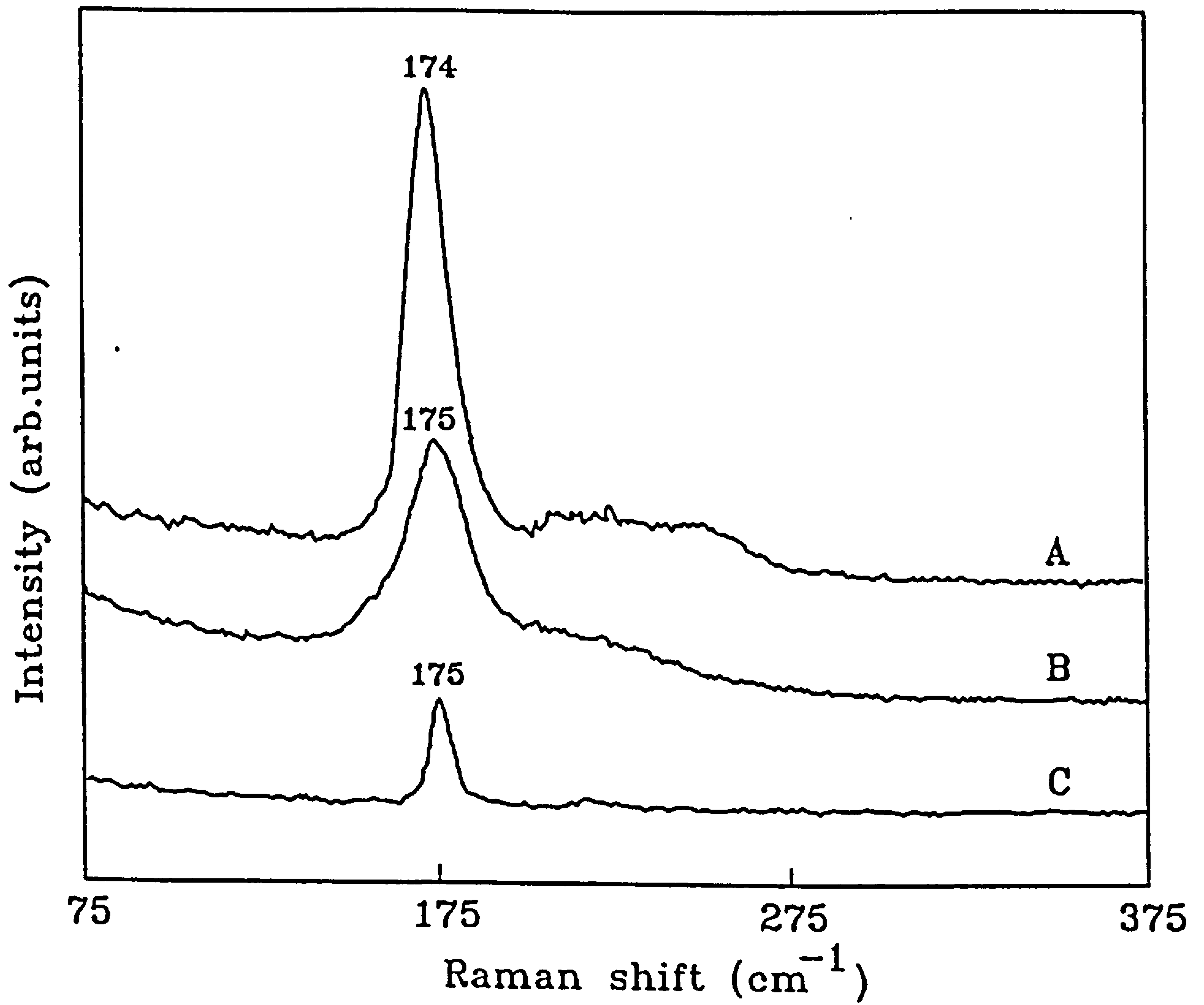


Figure 5.10: Raman spectra of CIGS thin films; (a) selenium at 300°C for two hours + $N_2$:$H_2$ annealed at 300°C for two hours, (b) the as-grown and (c) a standard CIGS single crystal.

the full wave half maximum (FWHM) values, which were found to be, 20cm$^{-1}$ for the as-grown sample, 11cm$^{-1}$ for the annealed sample and 5cm$^{-1}$ for the single crystal. The significance of these values is discussed in section 3.7.

As discussed earlier, the two stage anneal has a significant effect on grain growth, of the order 2 μm. However, a careful examination of the SEM micrograph revealed the existence of surface voids. In an attempt to remove these voids the sample was again annealed in forming gas at 300°C for one hour. The results from Raman analysis are shown in figure 5.11. It appears that further annealing has produced an additional phase. The $A_1$ mode peak is shifted towards a value 185 cm$^{-1}$ (CGS) and a well resolved new peak at 258 cm$^{-1}$ is now present. It is proposed that this new peak is due to the formation of an oxide surface layer of Indium [207].

The XRD spectrum also showed a new diffraction peak at 2θ=32° confirming the presence of an $(Ga,In)_2O_3$ phase [226,227]. It appears that during the annealing process, oxygen has entered into the annealing chamber resulting in the formation of an indium oxide layer on the surface of the film (the natural oxide of CIS and CIGS).

The oxidation of indium (in the CIGS group of compounds) results in the formation of an $In_2O_3$ surface layer and $CuGaSe_2$. This is in agreement work carried by Neuman et al. [207]. In order to confirm these observations it is necessary to investigate the chemical states and composition using techniques such as x-ray photoelectron spectroscopy and secondary ion mass spectra. It would be instructive to carry out depth profiles of the main constituent elements to obtain depth dependent information.

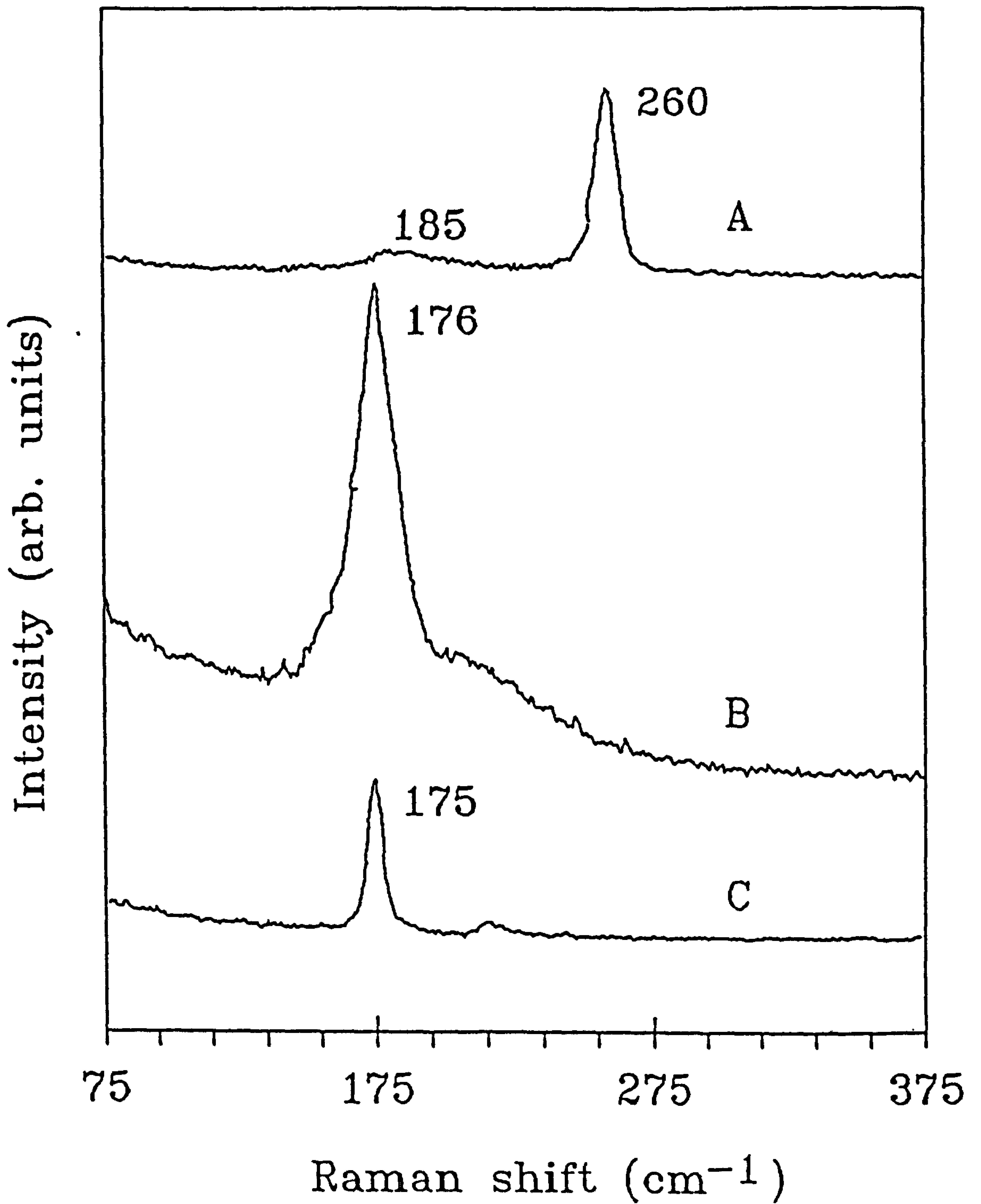


Figure 5.11: Raman spectra of CIGS thin films; (a) $N_2$:$H_2$ annealed at 200°C for two hours, (b) selenium annealed at 300°C for two hours + $N_2$:$H_2$ annealed at 300°C for two hours and (c) a standard CIGS single crystal.

## 5.3 Compositional properties

Compositional analysis of the annealed samples was again investigated using EDAX and RBS.

### 5.3.1 Energy dispersive x-ray analysis

**CIGS**

The effects of annealing on the film composition using various ambients and temperatures were investigated further using EDAX. These results are shown in the composition triangle for both as-deposited and annealed samples of CIGS, figure 5.12. The as-grown samples, produced at a substrate temperature of 200°C (a) were always slightly indium rich and deficient in selenium. However, the values for copper and gallium are close to those of the starting material.

Vacuum annealing (b) of the films at 300°C showed little change in the composition from that of the as-grown, table 5.3. The apparent changes observed are within the measurement error (±4%) for this technique [194]. However, data from other workers [210] have shown loss of selenium from the surface when vacuum annealing was used. This is due to the fact that the selenium vapour pressure is much higher than that of the other elements in the material. This contrast could be due to the variations in the experimental conditions used in this work and those employed elsewhere. Other workers have used longer annealing times in excess of 2 hours [64] compared to 1 hour used in this work, and higher annealing temperatures (400-500°C compared to 300°C) [210].

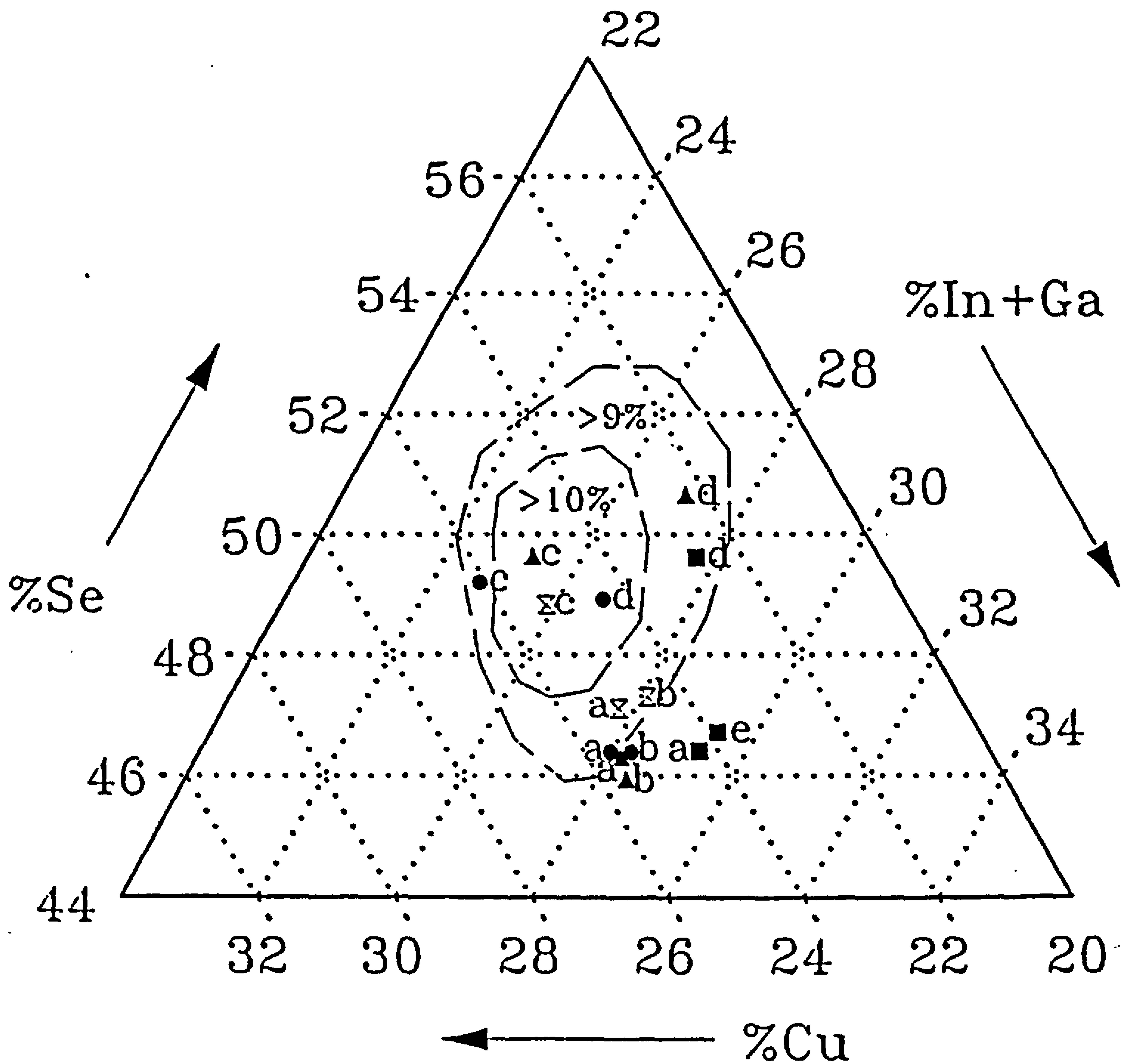


Figure 5.12: Compositional triangle for CIGS thin films; (a) the as-grown, (b) vacuum annealed at 300°C for one hour, (c) annealed under selenium ambient at 300°C for two hours, (d) two stage annealed at 300°C for two hours and (e) annealed under $N_2$:$H_2$ ambient at 300°C for two hours.

The elemental composition of the samples annealed in nitrogen/hydrogen ambients (e) at 300°C also showed no appreciable changes in composition (within the measurement error), table 5.3. Annealing in selenium atmosphere at 300°C (c) resulted in a dramatic change in composition, shifting it towards that of the pre-reacted starting material. This could be due to incorporation of selenium into the film, compensating for the deficiency observed in the as-deposited films. Increasing the temperature, with the other conditions being kept constant, the Se/Cu/(In+Ga) ratio was seen to change, with an increase in the percentage of selenium and a corresponding decrease in the percentages of copper and indium/gallium. A subsequent anneal in forming gas after an initial selenium anneal had very little effect on the final composition of the film, table 5.3.

CIS

Comparison of EDAX compositional analysis for both as-grown and the two stage annealed (selenium + forming gas) thin films of CIS is shown in table 5.3. The first stage anneal under a selenium ambient generally increased the selenium content in the samples due to its incorporation into selenium vacancies. However, the second stage anneal in a forming gas ambient showed a small decrease in the final selenium content. It is possible that this loss of selenium from the film could result from a reaction with hydrogen forming hydrogen selenide which is carried away from the surface. To elucidate this effect further it would be informative to carry out residual gas analysis using a qaudrupole mass spectrometer during the annealing process to analyse the composition of the ambient close to the surface of the sample.

| Sample No. | As-grown thin films Cu/In/Se atm.% | Selenium anneal at 300°C, 2 hours Cu/In/Se atm.% | 2nd anneal in $N_2$:$H_2$ at 300°C, 2 hours Cu/In/Se atm.% |
|---|---|---|---|
| FE105 | 24.5/27.3/48.1 | 24.8/25.4/49.8 | 24.7/26.1/49.2 |
| FE106 | 26.5/26.0/47.4 | 25.7/24.4/49.9 | 25.4/24.3/50.3 |
| FE108 | 25.5/28.9/45.6 | 25.9/24.4/49.7 | 25.2/26.1/48.7 |
| FE110 | 26.8/25.6/47.5 | 26.1/24.6/49.3 | 25.9/24.9/49.2 |
| FE112 | 22.3/31.1/46.6 | 23.7/27.9/48.4 | 23.5/27.8/48.7 |
| FET23 | 22.9/30.8/46.3 | 23.8/27.5/48.7 | 23.5/28.0/48.5 |
| FET24 | 23.5/29.9/46.6 | 24.7/24.7/50.6 | 24.4/25.0/50.6 |

Table 5.3: Compositional analysis of the as-grown, annealed under selenium ambient and two stage annealed thin films of CIS.

### 5.3.2 Rutherford backscattering analysis

Rutherford backscattering spectroscopy (RBS) was also used to analyze the compositional changes on the surface of CIS and CIGS samples caused by the post deposition annealing processes.

Figure 5.13 shows the RBS spectra of the as-grown and vacuum annealed thin films (annealed at 300°C for one hour). The RBS spectrum of the as-grown sample is non-homogeneous in composition throughout its thickness with a number of humps being identified on the central plateau region of the spectrum. The spectrum obtained from the vacuum annealed sample is also shown in the same figure. It can be seen that there is hardly any change in the composition, both on the front (the film surface) and back edge (the film/substrate interface) of the film, as both spectra to a first approximation overlap. The surface composition before and after annealing revealed Cu/In/Ga/Se atm.% values of 24.8/20.4/6.7/48.1 and 25.1/20.2/6.5/48.2 respectively. However, there is a significant change in the central plateau region of the spectrum which is now smoother. It appears that the vacuum anneal has improved the homogeneity of the film composition as a function of thickness. This is as expected as annealing helps to redistribute the constituent atoms into their most stable states.

The effects of annealing under 9:1 mixture of $N_2$:$H_2$ and selenium ambients at 300°C for two hours are shown in figure 5.14. For comparison the RBS spectrum of the as-grown thin film is also considered in the same figure. Once again it is evident that the film uniformity (through the film) has improved. In addition, significant changes in the

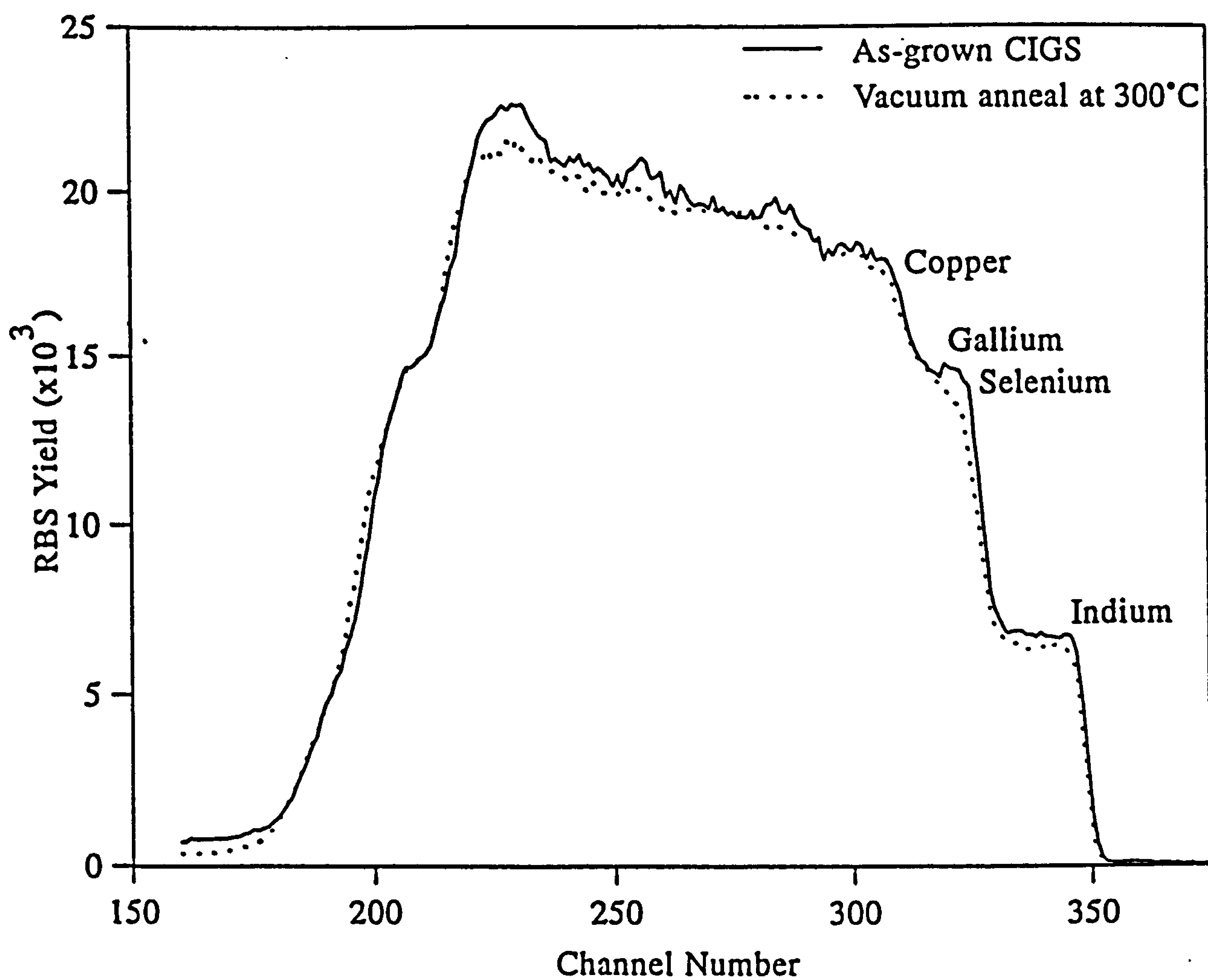


Figure 5.13: RBS spectra of CIGS thin films before and after vacuum anneal at 300°C for one hour.

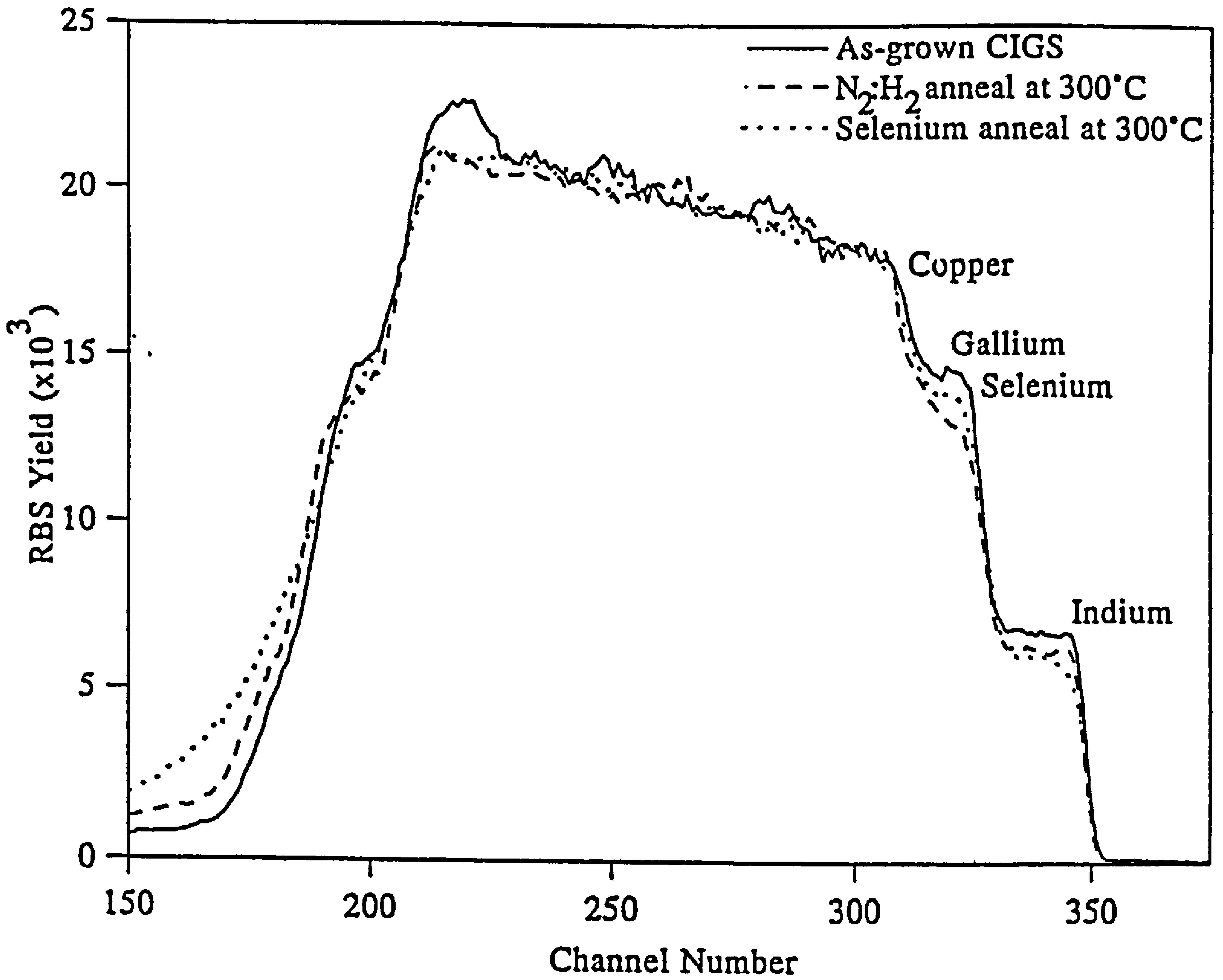


Figure 5.14: RBS spectra of CIGS thin films; the as-grown (full line), annealed under 9:1 mixture of $N_2$:$H_2$ (dashed line) and annealed under selenium ambient (dotted line) at 300°C for two hours.

composition of the front and back edges are also visible. On the front edge of the spectrum, the height of the indium peak is reduced for the annealed samples indicating a reduction in the indium content on the surface. The peak height corresponding to selenium is correspondingly larger in the spectrum of the selenium annealed thin film. Furthermore, the spectrum width (between front and back edge) is also increased [228] attributed to the incorporation of selenium in vacancies existing within the as-grown films - the film thickness has increased from 833 to 909 nm. This effect was repeatedly observed in a number of samples annealed under the same conditions. The surface composition values of as-grown and films annealed separately under forming gas and selenium ambients were 24.8/20.4/6.7/48.1, 25.3/20/6.5/48.2 and 25.2/19.7/4.9/50.2 atm.% respectively.

Figure 5.15 shows the effects of the two stage anneal, selenium at 300°C for two hours followed by a 9:1 mixture of $N_2$:$H_2$ or argon at 300°C for half an hour, on the composition as determined by RBS. At channel number 348 (indium) the RBS shows the as-grown film to be indium rich as a small peak is visible. After the two stage anneal this peak is reduced due to the increase in the selenium. In addition, an improvement in the uniformity of the film is observed.

Hence, as expected, the two stage anneal resulted in structural changes (as found by XRD analysis) as well as compositional changes, which could be beneficial to device performance.

Although this chapter has focused on CIGS, similar effects, of two stage annealing, are

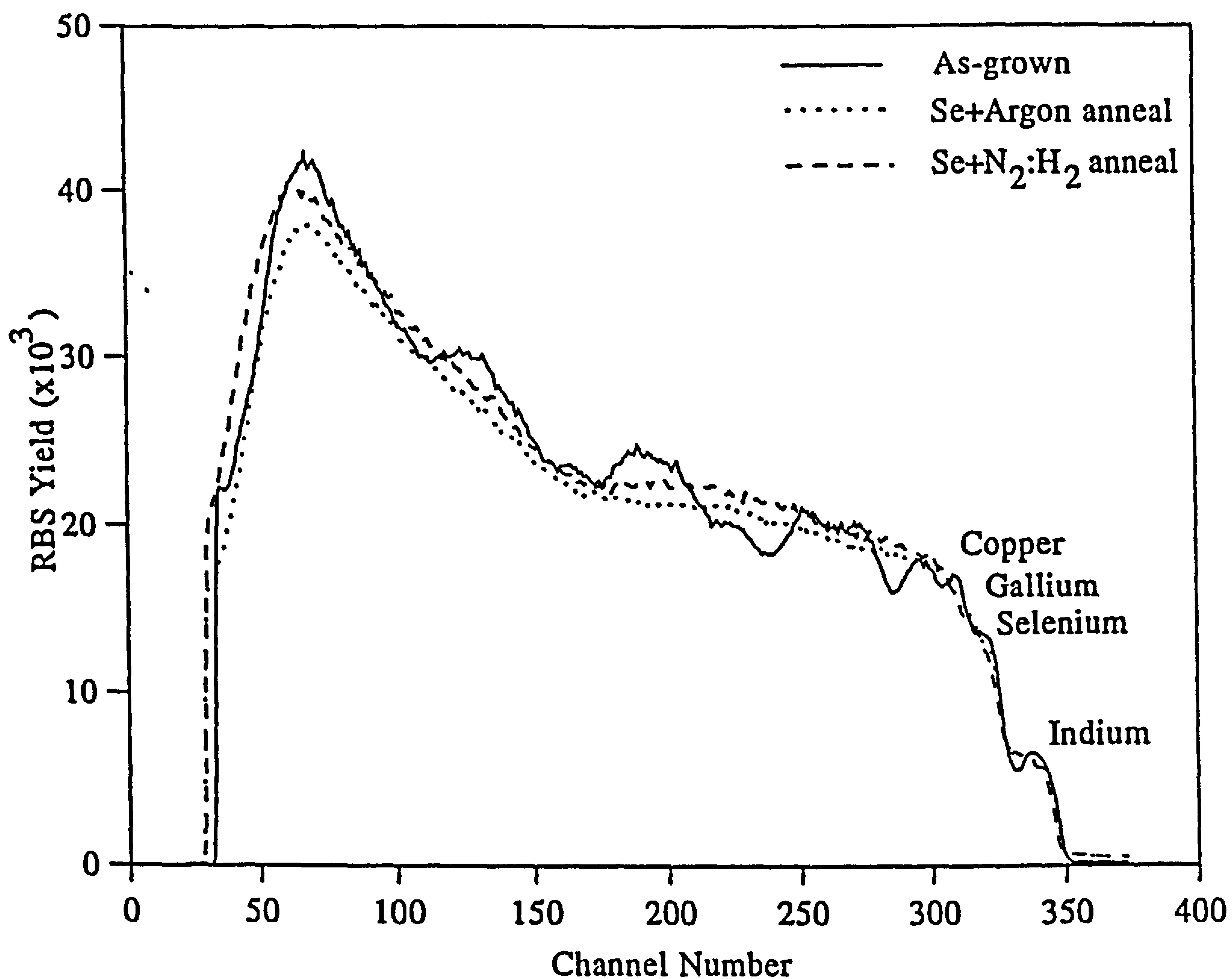


Figure 5.15: RBS spectra of CIGS thin films annealed under selenium ambient at 300°C for two hours followed by an anneal in 9:1 mixture of $N_2$:$H_2$ (dotted line) or argon (dashed line) at 300°C for half an hour.

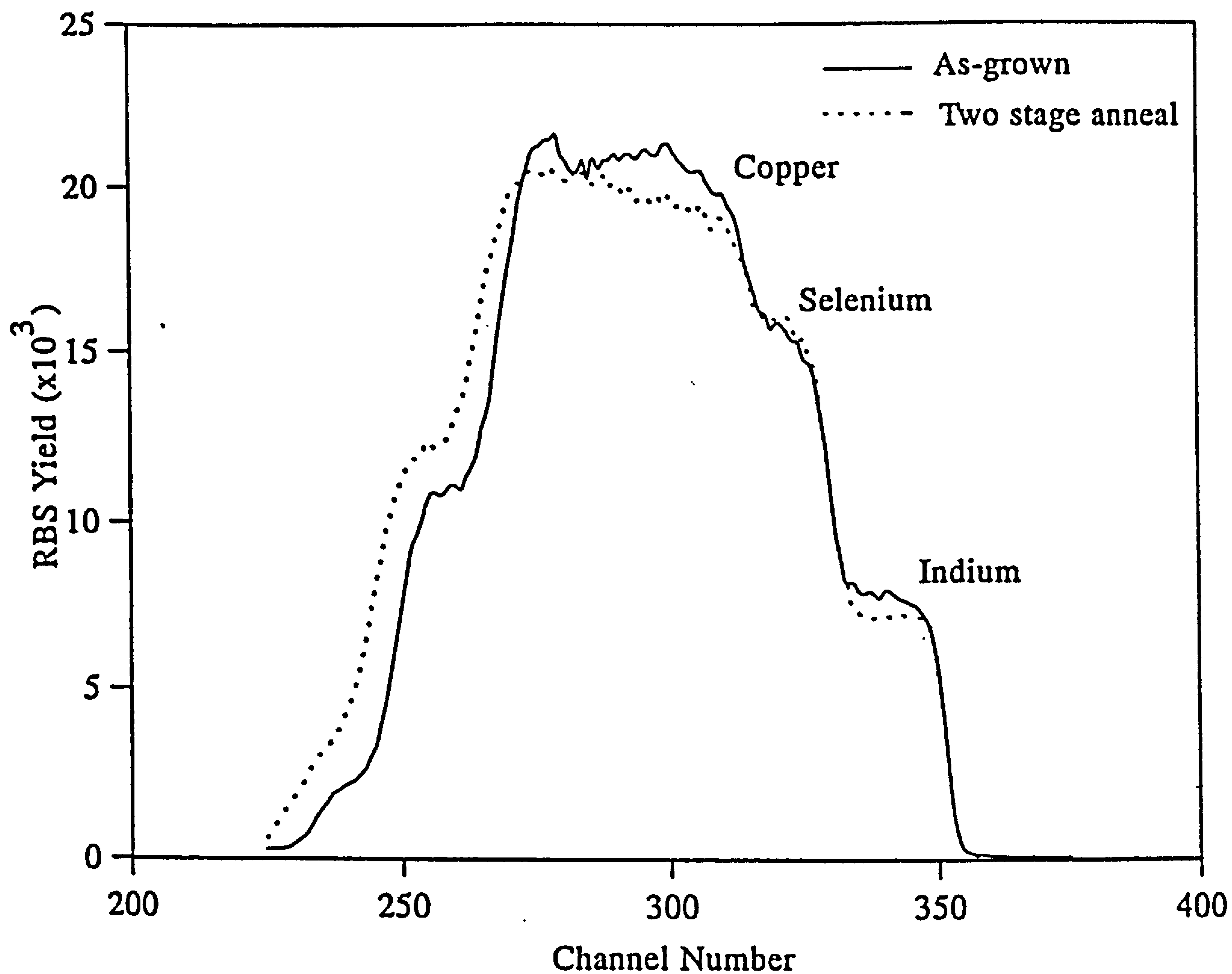


Figure 5.16: RBS spectra of CIS thin films annealed under selenium ambient at 300°C for two hours followed by an anneal in $N_2$:$H_2$ ambient at 300°C for one hour.

observed in the case of CIS thin films. This suggests that the majority of arguments presented for CIGS can also be applied to CIS. The partial substitution of gallium for indium does not therefore significantly alter the response of the material to annealing. A representative RBS spectrum of a two stage annealed film is shown in figure 5.16.

## 5.4 Electrical properties

The resistivity and conductivity type of both the as-grown and annealed CIGS films were measured by using four point and hot-point probe techniques respectively. It was found that the resistivity values of the as-grown films were in the range of $10^{-1}$ to $10^{3}$ Ωcm and both n and p-type conductivities were observed. As described earlier in chapter 4, the conductivity type can be related to the various defect levels present in the films.

A detailed analysis of post deposition heat treatments was carried out to identify the possible origin of the n-type conductivity. The effects observed are summarised below:

a) Post deposition heat treatments at temperatures at or below 300°C, in vacuum, resulted in no change to the conductivity type. The resistivity values either remained constant or showed a very small decrease. A change in conductivity type from p to n-type is usually attributed to selenium loss. However, under our experimental conditions no significant selenium loss was observed.

b) Samples annealed in a 9:1 mixture of $N_2$:$H_2$ again showed no change in the

conductivity type. However, an appreciable decrease in the resistivity from $6.34 \times 10^2$ to 1.10 Ωcm was found.

c) Annealing in selenium always resulted in a change in the conductivity type from n to p. A considerable variation in the resistivity was also observed. This could be attributed to the increase in grain size and the decrease in defect levels (see chapter 6).

From these experimental results the relationship between resistivity and annealing temperature (under selenium) was deduced, figure 5.17. A representative as-grown n-type film (deposited at a substrate temperature of 200°C) had a resistivity value of 12.2 Ωcm. After annealing in selenium at various temperatures between 250 and 475°C, the resistivity initially decreased with a corresponding change in conductivity type from n to p. At temperatures in excess of 300°C the resistivity increased very sharply, and at 475°C it attained a value of $1.32 \times 10^2$ Ωcm.

The initial decrease in resistivity can be attributed to an improvement in both the crystallinity and the grain size. At low temperatures, a relatively large spacing between crystallites offers a high resistive path to the movement of charge carriers. The increased growth of the crystallites at higher annealing temperatures should, in theory, decrease the number of grain boundaries and therefore decrease the resistivity. At temperatures >300°C the increase in resistivity could be due to deviations from stoichiometry. As described earlier, high temperature anneals resulted in damage i.e cracks and peeling were noticed which resulted in a non-continuous film. Another possible explanation for

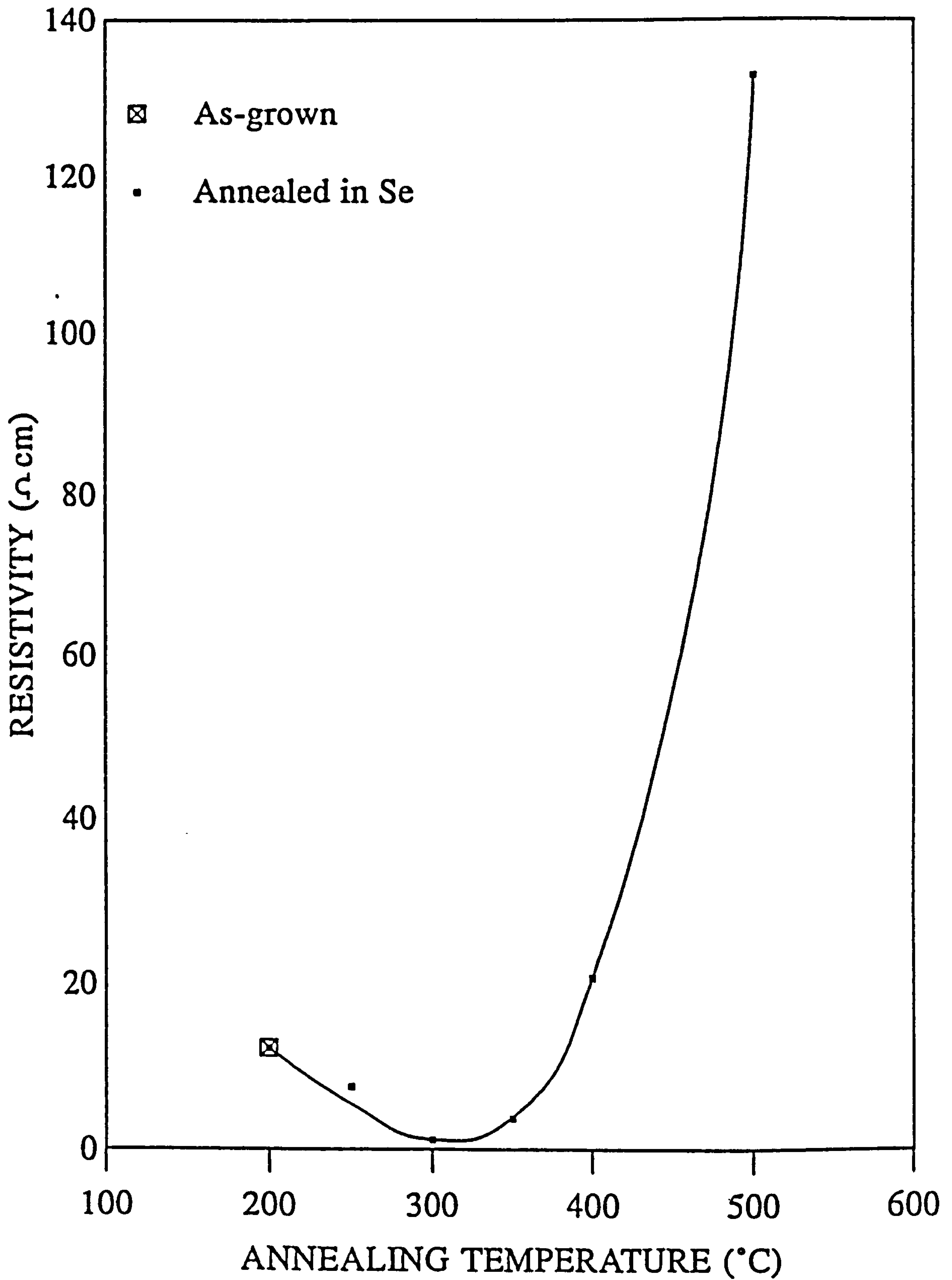


Figure 5.17: Resistivity against the annealing temperature for CIGS film annealed under selenium ambient.

the observed increase in resistivity relies on experimental evidence that copper is the most mobile species within copper ternary compounds [229]. It is proposed that at temperatures of the order 350°C copper migrates to the grain boundaries resulting in an increase in the number of intrinsic defects ($N_A$) within each grain, causing a decrease in the resistivity. Above 350°C, grain growth occurs which reduces the number of grain boundaries so that some of the copper migrates back into the grains and reduces the overall population of intrinsic defects ($N_A$). This consequently increases the resistivity.

To ascertain if the observed increase in resistivity was primarily caused by the formation of a non-continuous film (due to thermal stress) another set of anneals was undertaken using a lower temperature ramp rate and a shorter annealing time. The results of this set of experiments are shown in figure 5.18. As the annealing temperature was increased from 200°C to 300°C there was a dramatic decrease in the resistivity from $2x10^6$ to 4 Ωcm. A further increases in temperature resulted in only a slight reduction in the resistivity. These results can be summarised as follows. Annealing at around 250°C had no observable effect on the resistivity, this temperature is possibly too low to cause diffusion of selenium into the film. At 300°C a dramatic decrease was observed due to selenium activation and growth in the crystallites. Thus it was concluded that 300°C is the minimum temperature required for the annealing to change the conductivity type. At this temperature the resistivity stabilised.

These results are now consistent with those expected and it was therefore concluded that the initial annealing conditions were too harsh as they resulted in the formation of a non-continuous film.

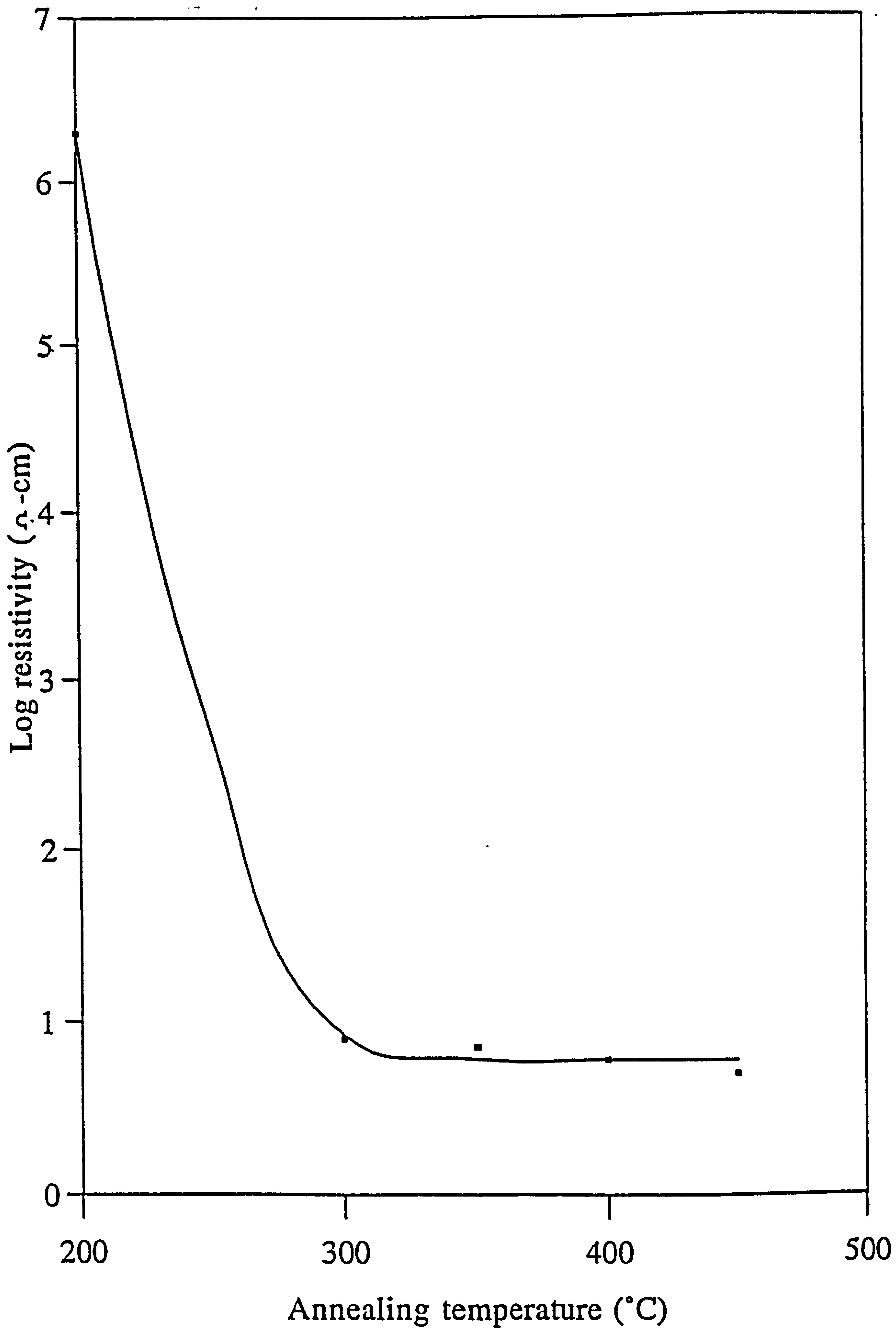


Figure 5.18: Log of resistivity against the annealing temperature for CIGS film annealed under selenium ambient.

| Sample No. | Before annealing | | After annealing | |
|---|---|---|---|---|
| | Conductivity type | Resistivity (Ωcm) | Conductivity type | Resistivity (Ωcm) |
| FET23 | p | 1.69 | p | $3.16 \times 10^{-1}$ |
| FET24 | p | $2.76 \times 10^{-1}$ | p | $5.27 \times 10^{-2}$ |
| FE103 | n | $9.71 \times 10^{-2}$ | p | $1.73 \times 10^{-2}$ |
| FE105 | p | $3.63 \times 10^{2}$ | p | $2.50 \times 10^{1}$ |

Table 5.4: Electrical properties of CIS thin films before and after annealing under selenium ambient at 300°C for two hours followed by an anneal under $N_2$:$H_2$ ambient at 300°C for two hours.

In general, a decrease in resistivity has been observed for most types of thin films independent of annealing ambients due to grain growth and the activation of charge carriers. The effects of the annealing processes on the electrical properties of selected CIS samples are shown in table 5.4. Most of the as-grown samples were p-type and as expected this characteristic was enhanced after annealing in selenium and forming gas ambients.

## 5.5 Conclusions

The response of flash evaporated thin films of CIGS and CIS to various annealing processes under several sets of conditions including vacuum, selenium, inert and forming gas ambients at different temperature and times have been investigated.

Annealing under vacuum, selenium and forming gas ambients resulted in a relaxation of the structure and enhancement of the <112> preferred orientation. However, evidence of the existence of chalcopyrite structure was only observed for the samples processed using the two stage annealing process. SEM measurements confirmed that the grain size increased from 0.1 to 0.5 μm with a corresponding increase in film density. In a number of samples grains of up to 2 μm were found.

Both EDAX and RBS compositional analysis revealed that annealing in selenium was beneficial in respect of the film composition and structure.

Raman analysis confirmed that annealing under selenium and forming gas ambients shifts the composition towards that of the starting material. The spectra also revealed the existence of larger polycrystalline grains, a reduced grain boundary area and a reduced defect density.

The electrical properties, such as conductivity type and resistivity, were also altered by annealing. Vacuum and forming gas anneals resulted in a reduction in resistivity while conductivity type remained unaltered. A change in conductivity type from n to p and a decrease in resistivity to a constant level was observed only for the samples annealed under maximum selenium vapour pressure. P-type samples showed enhanced p-type conductivity.

# Chapter 6

# Photoacoustic spectroscopy and Photoconductivity analysis

## 6.1 Introduction

Despite a great deal of worldwide research on the understanding of the fundamental properties of CIS and related materials, the complex intrinsic defect structure is still not well understood and requires further detailed investigations [228]. Existing experimental work, including electrical and optical measurements, have displayed the existence of several donor and acceptor levels originating from intrinsic defects [230]. In addition, to maximise the efficiency of thin film solar cells and optimize their production, knowledge of the optical properties near and above the fundamental absorption edge is necessary. The application of analytical techniques such as photoacoustic spectroscopy (PAS) and photoconductivity analysis (PC) to the analysis of non-radiative processes in CIS is new with very little published data. However, intensified use of such technologies is likely to yield a great deal of useful scientific and technological information on the defect structure of these and other important semiconductor materials.

In this chapter, the PAS and PC techniques are described and results are presented from the investigation of the optical properties of thin films of CIGS and CIS. The effects of annealing and ion-implantation on the absorption coefficient, energy band gap and the observed non-radiative defect states have been investigated. Information about the defect states was also determined from the PC measurements.

## 6.2 Photoacoustic Spectroscopy (PAS)

The PAS acoustic signal originates from the heat produced when a sample is irradiated by an energetic incident monochromatic light beam. The overall process can be described using thermodynamic considerations [231] such as thermal conductivity, specific heat capacity, latent heat, density, thermal expansion coefficient and the compressibility. The process can be briefly described as the inducement of a temperature rise which results in a pressure wave being transmitted from the sample to a sensitive acoustic detector. The nature of this wave gives information regarding the deep and shallow defect levels as well as data relating to the standard optical parameters. A detailed description of this process is given in section 3.14.

The first theoretical model for photoacoustic emission from condensed matter was reported in 1973 by Parker [232]. This work was followed by the development of a comprehensive model by Rosencwaig and Gersho [233] which is used to interpret experimental results obtained from PAS. This model is based on the evolution of acoustic signals from thick (optical diffusion length smaller than the thickness) samples and therefore considerable modifications were needed in order to apply it to thin films. Several other workers [234-236] have developed models complementary to those mentioned above, but in essence these are all based on the fundamental observations of Rosencwaig. In the following sections, a detailed description of the Rosencwaig and Gersho (RG) model is given. To apply the RG theory to this work i.e. for the analysis of thin films, the model has been developed to take into account the effects of thermal diffusion, multiple reflections and the influence of the substrate.

### 6.2.1 The RG theory

The model [233] is treated in one dimension by considering the production of a photoacoustic signal in a cylindrical cell of diameter D and length L. A schematic diagram of the standard PA cell is shown in figure 6.1. It consists of a solid sample of thickness $l_s$, on a backing material (the base of the cell) of thickness $l_b$. The sample is "coupled" to the acoustic detector by a gas medium of thickness $l_g$. The cell is sealed by a transparent window through which a modulated beam of monochromatic light flux $I_o$ is transmitted. An acoustic detector is mounted in one of the lateral cell walls to detect the acoustic signal produced by the sample. The intensity of the light is sinusoidally modulated at a frequency $\omega=2\pi f$, with an equivalent acoustic intensity I:

$$I=\frac{I_o}{2}(1+\cos\omega t) \tag{6.1}$$

By denoting $\alpha$ as the absorption coefficient of the solid sample, the energy per unit area absorbed along the distance from x to x+dx is:

$$I=\frac{1}{2}\alpha I_o e^{\alpha x}(1+\cos\omega t) \tag{6.2}$$

which is equal to the heat power created in the sample, assuming that the efficiency for the conversion of light to heat is equal to unity [233]. The generated heat then "warms" the sample, gas and the backing material by an amount $\phi(x,t)$ above the ambient temperature $T_o$:

$$\phi(x,t) = T(x,t) - T_o \tag{6.3}$$

The thermal diffusion equation in the solid sample, taking into account the distributed heat source, can be written as

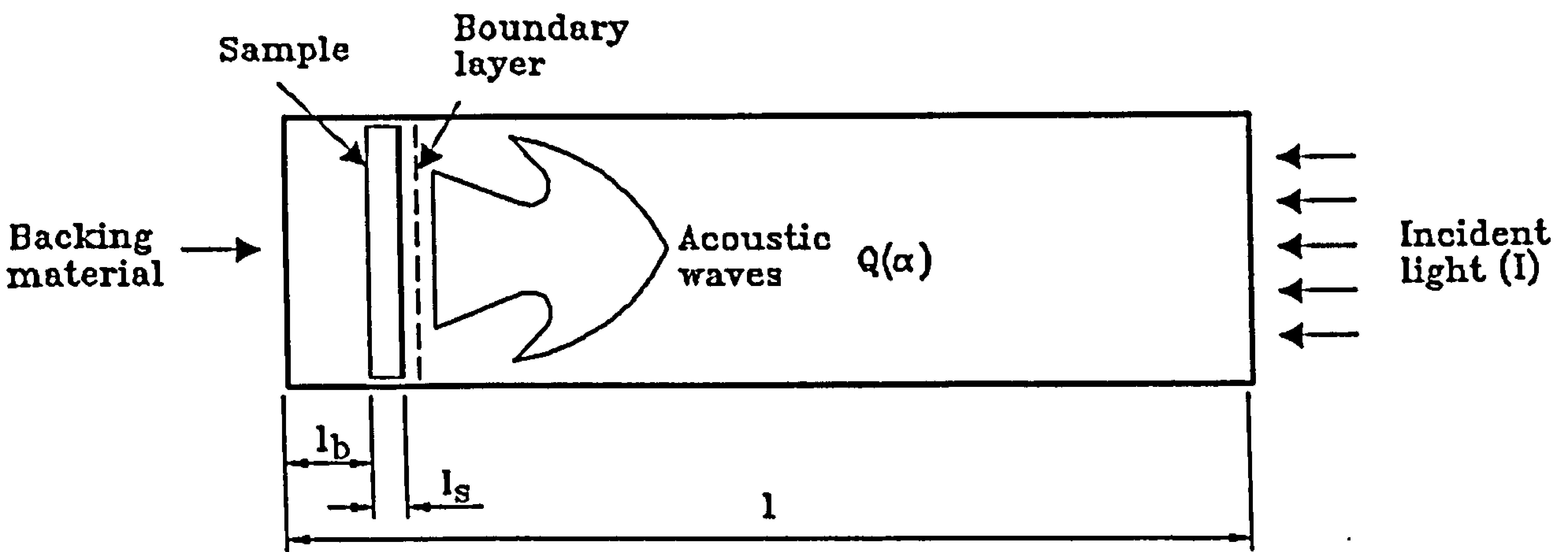


Figure 6.1: Schematic of a standard photoacoustic spectrometer cell [233].

$$\frac{\partial^2\phi_s(x,t)}{\partial x^2}-\frac{1}{\beta_s}\frac{\partial\phi_s(x,t)}{\partial t}+\frac{\alpha I\eta}{\kappa_s}e^{\alpha x}=0 \qquad for -l_s \le x \le 0 \tag{6.4}$$

Where $\eta$ is the efficiency at which the absorbed light at the wavelength $\lambda$ is converted to heat; in most solids $\eta \approx \beta_s$ the sample thermal diffusivity.

For the backing material and gas layer, the thermal diffusion equations are:

$$\frac{\partial^2\phi_b(x,t)}{\partial x^2}-\frac{1}{\beta_b}\frac{\partial\phi_b(x,t)}{\partial t}=0 \qquad for (-l_b-l_s) \le x \le -l_s \tag{6.5}$$

and

$$\frac{\partial^2\phi_g(x,t)}{\partial x^2}-\frac{1}{\beta_g}\frac{\partial\phi_g(x,t)}{\partial t}=0 \qquad for\ 0 \le x \le l_g \tag{6.6}$$

Where $\beta_s$, $\beta_b$ and $\beta_g$ are the thermal diffusivities of the sample, backing material and gas respectively. In general we can use the common symbol $\beta_j$ to represent the three values of $\beta$ i.e. j=s for the sample, j=b for the backing material or j=g for the gas. Using this general notation we obtain the relation:

$$\beta_j = \frac{\kappa_j}{\rho_j\, C_j} \tag{6.7}$$

where $\kappa_j$, $\varrho_j$ and $C_j$ are the thermal conductivity, density and specific heat capacity of medium j, respectively.

From the constraint that the temperature at the cell walls is at ambient, and further assuming that the temperature relative to ambient is zero at the outside face of the cell

walls, the resulting value of $V_g$, which expresses the a.c. component of the temperature change in the gas column, is given by the equation:

$$V_g = \frac{\alpha I_o}{2\kappa_s(\alpha^2-\sigma_s^2)}\left[\frac{(r-1)(b+1)e^{\sigma_s l_s}-(r+1)(b-1)e^{-\sigma_s l_s}+2(b-r)e^{-\alpha l_s}}{(b+1)(g+1)e^{\sigma_s l_s}-(g-1)(b-1)e^{-\sigma_s l_s}}\right] \tag{6.8}$$

where

$$b = \frac{\kappa_b\, a_b}{\kappa_s\, a_s} \tag{6.9}$$

$$g = \frac{\kappa_g\, a_g}{\kappa_s\, a_s} \tag{6.10}$$

and

$$r = (1-i)\frac{\alpha}{2a_s} \tag{6.11}$$

Equation (6.8) evaluated for specific parameter values yields a complex number whose real and imaginary part are $V_{g1}$ and $V_{g2}$, respectively. These determine the in-phase and quadrature components of the periodic temperature variations at the sample surface.

The temperature fluctuations within the solid sample expands and contracts the surrounding gas medium periodically. This can be considered as an acoustic piston acting on the rest of the gas layer. The displacement of the gas piston due to the periodic heating can be estimated by using ideal gas law [233]:

$$\delta_x(t)=\frac{V_g\mu_g}{\sqrt{2}T_o}e^{i(\omega t-\frac{\pi}{4})} \qquad (6.12)$$

By assuming that the total gas volume responds to the action of the acoustic piston adiabatically, the acoustic pressure in the cell due to the displacement of the piston can be derived from the adiabatic gas law:

PV = Constant

Where P is pressure, V is the volume and $\gamma$ is the ratio of specific heats. Thus the incremental pressure will be:

$$P_g(t)=\frac{\gamma P_o}{V_o}\delta V=\frac{\gamma P_o}{l_g}\delta_x(t) \qquad (6.13)$$

Using the value of gas piston displacement obtained from equation (6.12), then

$$P_g(t) = \frac{\gamma P_o V_g}{\sqrt{2}l_g a_g T_o}e^{i(\omega t-\frac{\pi}{4})} \qquad (6.14)$$

where

$$Q=\frac{\gamma P_o V_g}{\sqrt{2}l_g a_g T_o}$$

Theoretical predictions [189] for the photoacoustic effect in opaque materials where optical absorption length is smaller than the thickness of the sample ($\mu_\alpha<l_s$) have shown that the PA amplitude signal will vary as $f^{-1}$ when the thermal diffusion length of the sample ($\mu_s$) is greater than the optical absorption length ($\mu_\alpha$), and as $f^{-3/2}$ when $\mu_s<\mu_\alpha$. For

a strongly absorbing material, such as fine particles of carbon black (particle diameter size in the range of 1-10 μm), where $\mu_\alpha < l_s$ (since $\alpha$ is of the order of $10^6$ $cm^{-1}$) and $\mu_s > l_s$ (given the frequency range of interest 20-5000 Hz), the theory predicts that the PAS signal will vary as $f^{-1}$. Under these conditions equation 6.8 can be written:

$$V_g = \frac{\alpha I_o}{2\kappa_s(\alpha^2 - \sigma_s^2)} \frac{r-1}{g+1} \tag{6.15}$$

By further assuming that g<<1 the resulting PA signal [237] is:

$$P_g(t) = \frac{A\alpha\mu_s}{\omega\sqrt{(\alpha\mu_s+1)^2+1}} e^{i\left[\omega t - \frac{\pi}{4} - \arctan\left(\frac{\alpha\mu_s+2}{\alpha\mu_s}\right)\right]} \tag{6.16}$$

where A is given by the expression:

$$A = \frac{\gamma P_o I_o \sqrt{\beta_g \beta_s}}{2 l_g T_o \kappa_s}$$

### 6.2.2 Determination of the absorption coefficient $\alpha$

The absorption coefficient $\alpha$ of thick samples can be determined either by using the phase or the magnitude of the PA signal. If the PA magnitude is used equation 6.14 can be rearranged to get [237,238]:

$$\alpha = \frac{1}{\mu_s} \frac{q^2 + q\sqrt{2-q^2}}{1-q^2} \tag{6.17}$$

where:

$$q = \frac{|P_g(t)\ \omega|}{A}$$

is the normalised PA signal.

The determination of the absorption coefficient $\alpha$ for thin film samples using the RG-theory is limited, where it was estimated that the gas boundary layer thickness is of the order of the thermal diffusion length [234,239]. Yamasaki et al. [240] extended the RG-theory to the case of thin films by considering the interference effect of light within a sample caused by the multiple reflections at the front and back faces of the sample. Using the same analytical method as the RG theory, they derived an expression for the PAS signal Q($\alpha$):

$$Q(\alpha) = \frac{E}{(b+1)(g+1)e^{\sigma_s l_s} - (b-1)(g-1)e^{-\sigma_s l_s}} \times k_1 \qquad (6.18)$$

with

$$\begin{aligned} k_1 = {} & [(b+1)\{(r-1) - R_b e^{-2\alpha l_s}(r+1)\}e^{\sigma_s l_s} \\ & -(b-1)\{(r+1) + R_b e^{-2\alpha l_s}(1-r)\}e^{-\sigma_s l_s} \\ & +2\{(b-r) + R_b(b+r)\}e^{-\alpha l_s}] \end{aligned}$$

and

$$E = \frac{\alpha I_o \gamma P_o (1-R)}{2\sqrt{2}\kappa_s l_g a_g T_o(\alpha^2 - \sigma_s^2)} \frac{1}{1 + RR_b e^{-2\alpha l} - 2\sqrt{RR_b}\, e^{-\alpha l}\cos(2\delta l)}$$

where R and $R_b$ are the reflections from the gas to sample and from sample to the backing material respectively. Other parameters were defined to be $a_g = (\omega \varrho_g C_g / 2\varkappa_g)^{1/2}$,

$\sigma_s=(1+j)(\omega\varrho_s C_s/2\varkappa_s)^{1/2}$, $b=(\varkappa_b\varrho_b C_b/\varkappa_s\varrho_s C_s)^{1/2}$, $g=(\varkappa_g\varrho_g C_g/\varkappa_s\varrho_s C_s)^{1/2}$, $r=\alpha/\sigma_s$, $\varrho_i$ the density of material i, $C_i$ is the specific heat of material i and i takes the subscripts s, g and b for sample, gas and backing material, respectively. Yamasaki et al calculated $Q(\alpha)$ as a function of $\alpha$ for different film thicknesses and showed that the PAS signal increases linearly with $\alpha$ in the low $\alpha$ range, while it saturated in the high $\alpha$ range tending to a constant value $Q_s$. They found that the key factors affecting the normalised PAS signal were the sample thickness, the penetration depth of the incident light and the thermal diffusion length of the sample. This was independent of whether the sample was a thick or thin film. In the low $\alpha$ range, the normalised PAS signal was found to be nearly proportional to $\alpha$ and was approximated for a thin film as follows:

$$q(\alpha)=\frac{1+R_b}{1-RR_b}(\alpha l), \qquad l\ll\alpha^{-1},\mu_s \tag{6.19}$$

By using $b\approx1$ and $\exp(\sigma_s l_s)\approx1$, The PAS signal for thin films was reported [241] to be:

$$Q(\alpha)=A\frac{\alpha[(r-1)-R_b e^{-2\alpha l_s}(1+r)]+2[(1-r)+R_b(1+r)]e^{-\alpha l_s}}{(\alpha^2-\sigma_s^2)(1+RR_b e^{-2\alpha l_s})}]$$

Its solution leads to:

$$Q(\alpha)=A\frac{\alpha(1-e^{-\alpha l_s})(r-1)+R_b e^{-\alpha l_s}(1+r)(1-e^{-\alpha l_s})}{(\alpha^2-\sigma_s^2)(1+RR_b e^{-2\alpha l_s})}$$

or

$$Q(\alpha)=A\frac{\alpha(r-1)+R_b e^{-\alpha l_s}(1+r)}{(\alpha^2-\sigma_s^2)(1+RR_b e^{-2\alpha l_s})}(1-e^{-\alpha l_s})$$

since $\|r\|>1$ and $r=\alpha/\sigma_s$, Therefore

$$Q(\alpha)=A(1-e^{-\alpha l_s})\frac{1+R_b e^{-\alpha l_s}}{1+RR_b e^{-2\alpha l_s}}$$

### 6.2.3 Modifications to the standard PAS theories - applications to this work

In order to apply the above theories to this work it was necessary to modify relation 6.18 derived by Yamasaki *et al* [240] and is given below:

$$Q(\alpha)=\frac{E}{(b+1)(g+1)e^{\sigma_s l_s}-(b-1)(g-1)e^{-\sigma_s l_s}}\times k_1 \tag{6.18}$$

with

$$\begin{aligned} k_1 = {} & [(b+1)\{(r-1)-R_b e^{-2\alpha l_s}(r+1)\}e^{\sigma_s l_s} \\ & -(b-1)\{(r+1)+R_b e^{-2\alpha l_s}(1-r)\}e^{-\sigma_s l_s} \\ & +2\{(b-r)+R_b(b+r)\}e^{-\alpha l_s}] \end{aligned}$$

and

$$E=\frac{\alpha I_o \gamma P_o(1-R)}{2\sqrt{2}\kappa_s l_g a_g T_o(\alpha^2-\sigma_s^2)}\frac{1}{1+RR_b e^{-2\alpha l}-2\sqrt{RR_b}e^{-\alpha l}\cos(2\delta l)}$$

The interference term relating to the sample substrate is neglected (a detailed discussion is given below). Since $g<<1$ and for thin films $\exp(\sigma_s l_s)\sim 1$;

$$Q(\alpha)=\frac{E}{b}[(1-e^{-\alpha l_s})\{(r-b)+R_b(r+b)e^{-\alpha l_s}]$$

For most backing materials, $b\approx 1$ [242]. Since $r=\alpha\mu_s(1-j)/2$ and $\sigma_s=(1+j)/\mu_s$, the resultant expression is given by:

$$Q(\alpha)=\frac{A\eta(1-R)\alpha\mu_s\sqrt{2}}{(\alpha^2\mu_s^2+2j)}(1-e^{-\alpha l_s})\left[\frac{\frac{\alpha\mu_s(1-j)}{2}-1+R_b e^{-\alpha l_s}\frac{\alpha\mu_s(1+j)}{2}+1}{1+RR_b e^{-2\alpha l_s}}\right]$$

where

$$A=\frac{I_o\gamma P_o}{4\kappa_s l_g a_g T_o}\mu_s$$

let $x = \alpha\mu_s$ and $y = l_s/\mu_s$

$$Q(\alpha)=\frac{A\eta(1-R)}{1+RR_b e^{-2xy}}\frac{x\sqrt{2}(1-e^{-xy})}{(x^2+2j)}\left[\frac{x(1-j)}{2}-1+R_b e^{-xy}\left(\frac{x(1+j)}{2}+1\right)\right]$$

The solution of which leads to

$$Q(\alpha)=\frac{A\eta(1-R)x(1-e^{-xy})}{(1+RR_b e^{-2xy})}\times\frac{\sqrt{(x^2-2x+2)+2R_b e^{-xy}(x^2-2)+R_b^2 e^{-2xy}(x^2+2x+2)}}{\sqrt{(x^2-2x+2)(x^2+2x+2)}}$$

where $q_o = A(1-R)$.

$$Q=q_{\circ}\eta\frac{x}{\sqrt{x^2+2x+2}}\frac{1-e^{-xy}}{1+RR_be^{-2xy}}\sqrt{1+2R_be^{-xy}\frac{(x^2-2)}{x^2-2x+2}+R_b^2e^{-2xy}\frac{x^2+2x+2}{x^2-2x+2}}$$

Finally, the normalised PA signal is given by:

$$q=\frac{Q(\alpha)}{q_{\circ}}=\eta\frac{1-e^{-xy}}{1+RR_be^{-2xy}}\frac{x}{\sqrt{(x^2-2x+2)(x^2+2x+2)}}\times\sqrt{(x^2-2x+2)+2R_be^{-xy}(x^2-2)+R_b^2e^{-2xy}(x^2+2x+2)}$$

By using this relation, the absorption coefficient can be calculated from the normalised photoacoustic amplitude signal generated from the thin film. In order to confirm the validity of this relation with those reported by other workers [240,241], plots of the absorption coefficients versus the normalised photoacoustic amplitude signal were constructed and shown in figure 6.2. The first curve (▲) represents the case where the interference effects of light within a sample (caused by the multiple reflections at the front and back of the sample) are neglected. In the second curve (•) these effects are considered, but the effect of thermal diffusion length is neglected. The absorption curve (■) represents this present work in which all the effects including multiple reflections and thermal diffusion length are considered. It can be seen that the trend of our curve is in good agreement to that reported in the literature [240,241] at medium to high values of PA signal. However, in the low range (0.001 to 0.01) and at the maximum point of the normalised photoacoustic signal, the absorption coefficient is found to be slightly higher. This difference is attributed to the fact that we have considered the effect of thermal diffusion length in the absorption coefficient relation whereas other workers have neglected it.

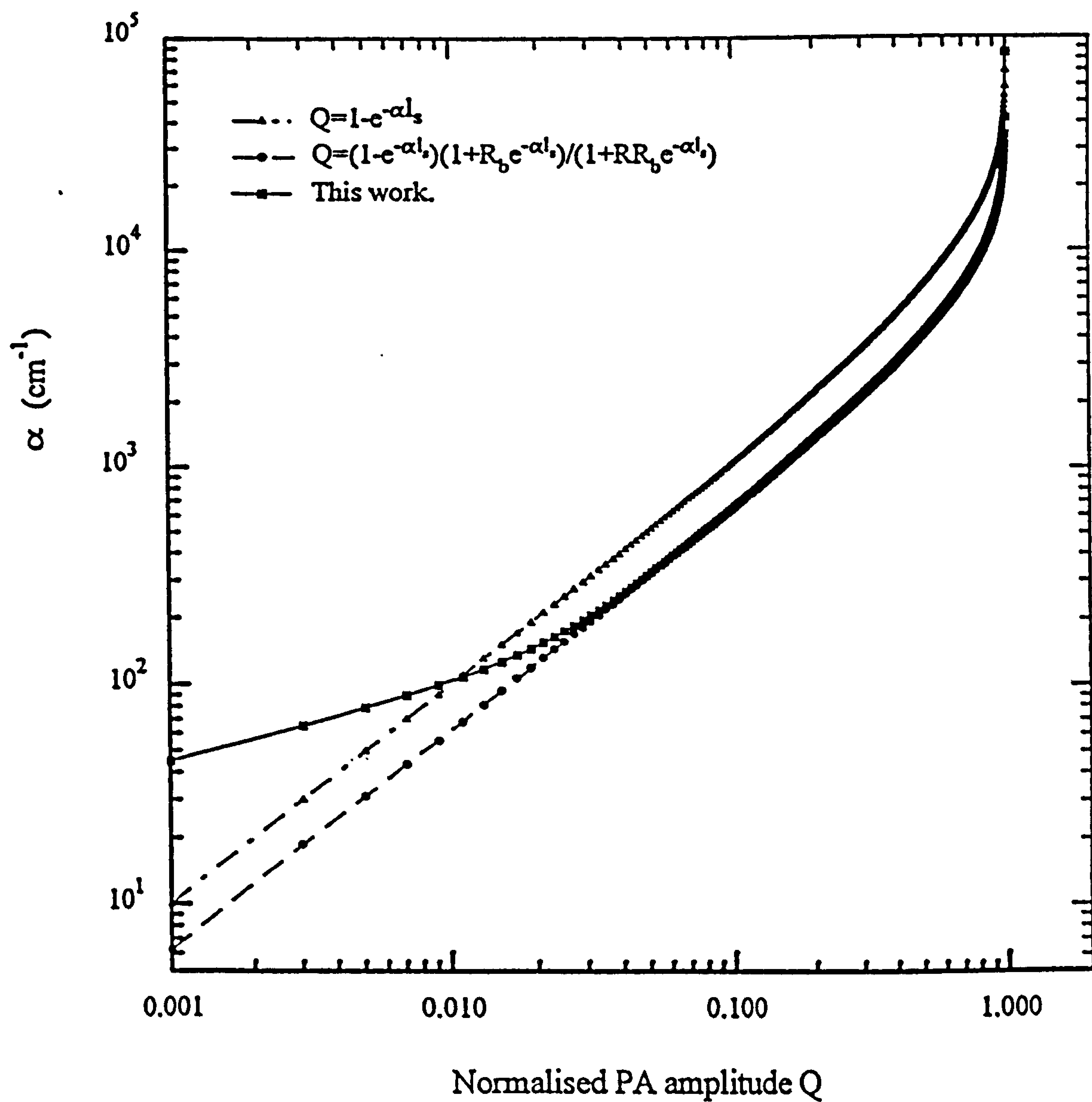


Figure 6.2: Dependence of the absorption coefficient $\alpha$ on the normalised photoacoustic amplitude signal Q; ■ - present work, ▲ - [240] and o - [241].

As stated above, in calculating the absorption coefficient for thin films we made the assumption that the interference term at the film substrate interface could be neglected. If we consider figure 6.3, representing the normalised photoacoustic amplitude signal of a CIGS thin film (deposited onto a molybdenum coated glass substrate - a two layer structure), the resultant photoacoustic signal shows two main peaks marked $\lambda_1$ and $\lambda_2$ at approximately 0.79 and 0.96 eV respectively. The normally observed deep level defects in this range are masked by the large periodic vibrations. The standard relation [243]:

$$d = \frac{1}{2n}\left(\frac{1}{\lambda_2} - \frac{1}{\lambda_1}\right)^{-1} \qquad (6.20)$$

can be used to calculate the layer thickness or the refractive index (n) of the top layer if one of these parameters is known. In the present work the CIGS layer thickness was calculated and found to be approximately 1μm which is in good agreement to that revealed using other analytical techniques such as EDAX and RBS. In addition the band edge maximum (labelled by $E_g$) is observed at approximately 1.19 eV which is close to the reported gap energy for single crystals grown with the same elemental composition [25]. Films deposited onto glass substrates showed no evidence of periodical vibrations which we have attributed to absence of interference effects. This clearly demonstrates that if the films are deposited onto already coated glass substrates, the resultant photoacoustic spectra will be dominated by the interference peaks. Similar spectra were observed for CIS films deposited onto molybdenum coated glass substrates.

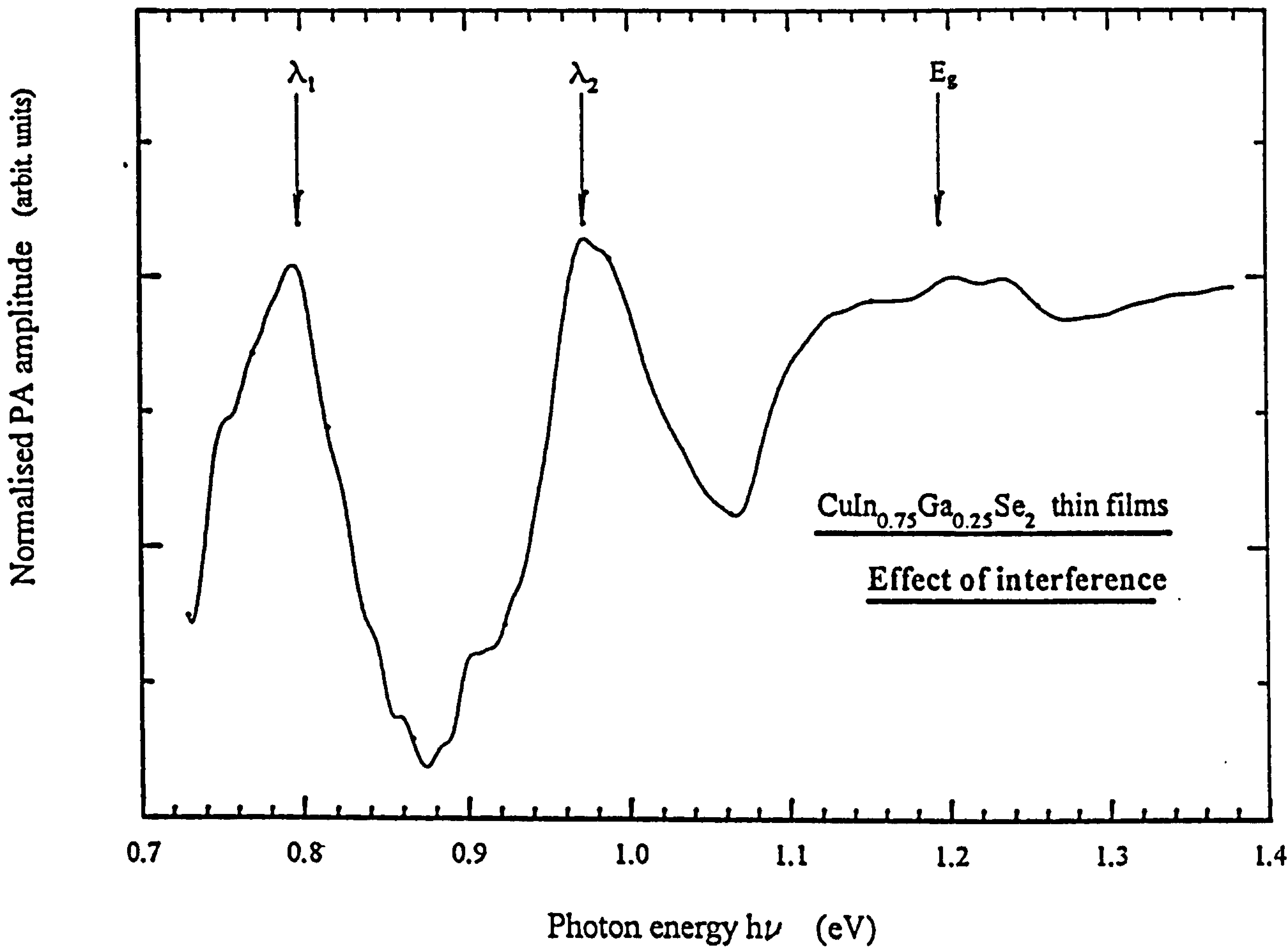


Figure 6.3: The effect of interference from a two layer structure (CIGS thin film deposited onto molybdenum coated glass substrate).

## 6.3 PAS experimental analysis and results

An understanding of the non-radiative processes inherent in semiconductor materials is essential to ascertain the origin and population of active defect states [189] and in turn to improve the overall performance of devices based on these materials [146]. PAS offers the advantage that it is a non-destructive technique for the analysis of these defect states [189].

Figure 6.4 represents the normalised photoacoustic amplitude signal measured from an as-grown CIGS thin film (approximately 1μm), recorded in the photon energy range 0.7 to 1.4 eV. All the photoacoustic spectra were measured at room temperature with a modulating frequency of 112 Hz (unless/otherwise stated) and corrected for the spectral distribution of the optical system and cell by normalizing the response of the specimen to that of carbon black. The photoacoustic spectra shows two distinctive regions at around the band edge at approximately 1.19 eV. The first region, at a photon energy hν of < 1.19 eV, shows transitions (labelled as $E_1$ to $E_5$) due to non-radiative defect states. These could be due to transitions from one defect state to another and/or transitions between defect states and the conduction or valence bands [243] (if the defect state densities are high). The second region is located at photon energies hν > 1.19 eV, where the sample has its highest optical absorption properties. A relatively sharp transition between these two region indicates the fundamental absorption edge. In order to confirm that transitions in the first region of the normalised photoacoustic spectrum are characteristic of CIGS thin film, a virgin 800μm thick cleaned glass slide was also analysed. The normalised photoacoustic amplitude signal (recorded in the same photon

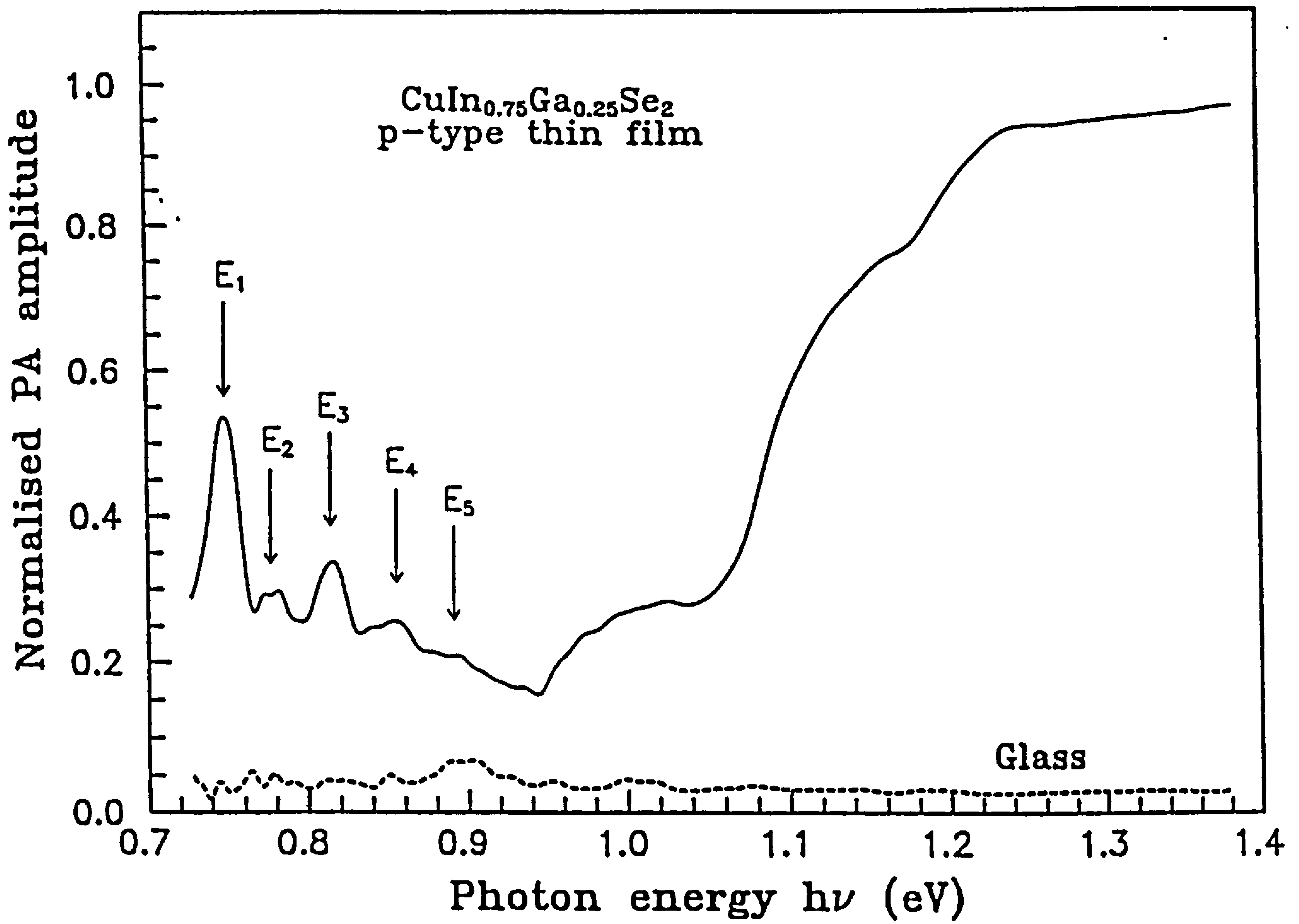


Figure 6.4: Comparative room temperature normalised photoacoustic amplitude signal from p-type CIGS thin film and a specimen of un-coated glass slide.

energy range as for the thin films) is plotted in figure 6.4. It can be seen that for the glass slide the spectrum is almost flat with a maximum normalised photoacoustic amplitude signal of 0.15. An almost similar spectrum, to that of cleaned glass slide, was observed from a high quality (approximately 99% transparent) thin film of indium tin oxide (ITO) prepared by electron beam evaporation techniques [187]. These observations support the idea that the transitions in the first region of the normalised photoacoustic amplitude signal of CIGS thin film are the characteristic of the sample as they do not appear in the PA spectrum of the virgin substrate.

Figure 6.5 shows representative normalised photoacoustic amplitude spectra of as-grown CIGS thin film samples. It can be seen that all the spectra are predominated by defect levels both near the fundamental band edge (1.0 eV to 1.2 eV) as well as in the tails of the spectra. Five main peaks ($E_1$ to $E_5$) in the deeper region (0.7 eV to 1 eV) were always observed. The nature of the fundamental band-to-band transition is difficult to establish as this region is extended across a 300 meV photon energy range. This is due to the presence of one or more shallow defect levels close to the band edge. This was not surprising as the photoacoustic signal depends strongly on the structure and uniformity of the sample. In the case of thin films grown for this work, the existence of voids and grain boundaries and deviations from the stoichiometry (sections 4.5.3 and 4.6.2) gave rise to these defect levels. The structural properties of these samples showed a strong preferred orientation in the <112> plane and the grain size was found to be $<$ 0.2μm. The respective random RBS spectra of these samples further confirmed the observed PAS results as they revealed a non-uniform composition through the depth of the film (Chapter 4 and 5). In contrast, the normalised photoacoustic spectra from the

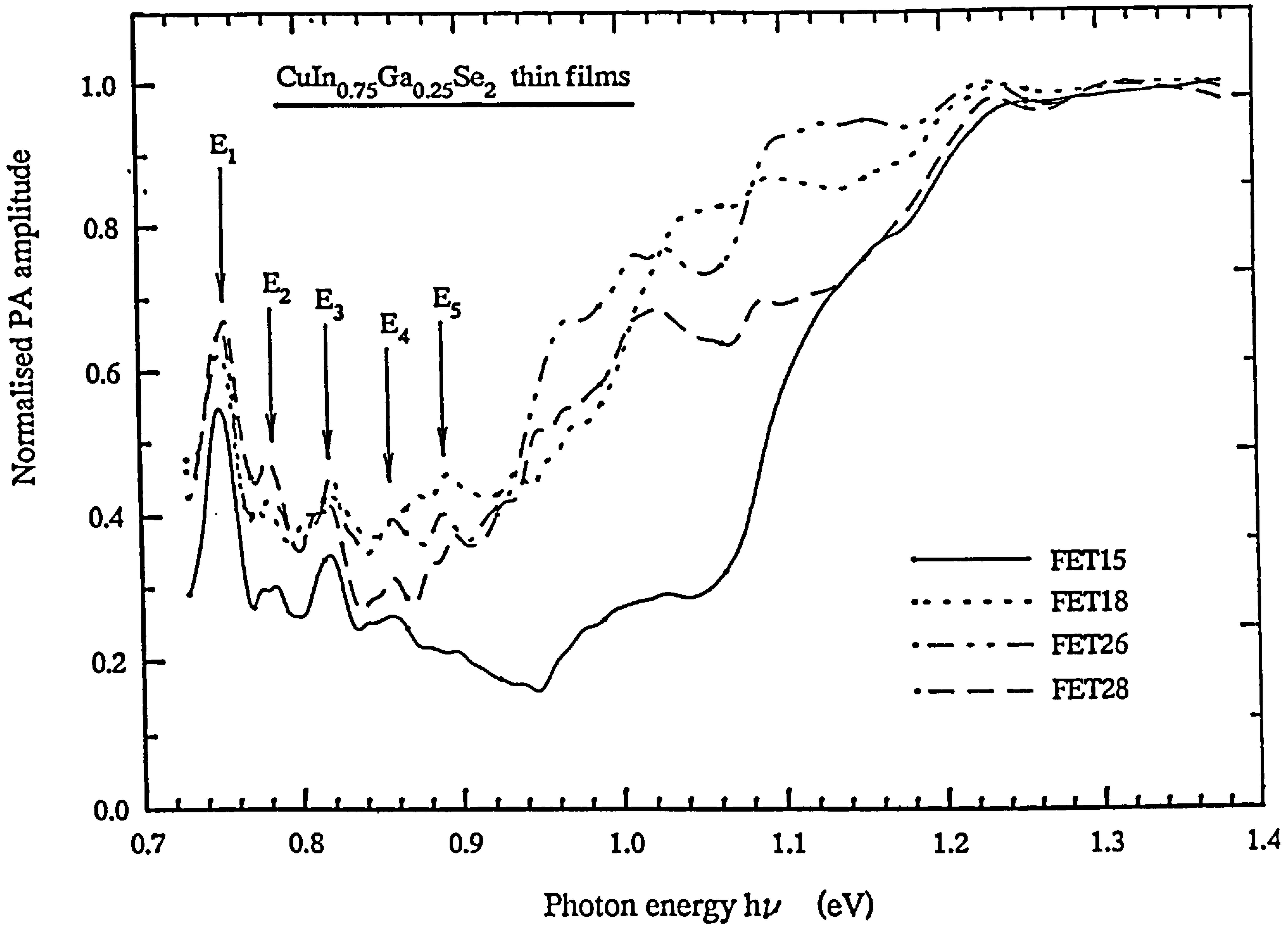


Figure 6.5: Normalised photoacoustic spectra of four representative polycrystalline as-grown CIGS thin films.

CIS and CIGS single crystal samples always showed fewer defect levels in the tail of the spectra [244]. The region near the fundamental band edge of the single crystal samples was always free from defect states and therefore displayed a steep transition edge.

The absorption coefficients evaluated from the photoacoustic spectra of the as-grown CIGS thin film samples are shown in figure 6.6. The defect levels are now better resolved. Near the fundamental band edge it can be seen that there are three or more broad shoulders at approximately 1.0, 1.05 and 1.15 eV. These broad shoulders could be the result of two or more defect levels. All the samples have shown an absorption coefficient of the order of $10^{+4}$ $cm^{-1}$ near the fundamental band gap. The minimum level of the absorption coefficient in the tail of the spectra is different for different samples. It appears that the sample with fewer or less pronounced defect states near the band gap edge (e.g FET15) has a lower minimum level as compared to the other spectra. It is possible that these defect states near the band edge have shifted the minimum of the absorption level in the tail of the spectra to a higher value.

In order to determine the respective band gap energies of the as-grown CIGS samples, $(\alpha h\nu)^2$ was plotted against the photon energy and the representative curves are shown in figure 6.7. The extrapolation of the curves down to a zero $(\alpha h\nu)^2$ level indicated gap energy values of 1.196±0.005 eV. The gap energy of the samples and the ionisation energies of the defect states ($E_1$ to $E_5$) observed in the tail of the PA spectra are listed in table 6.1. The apparent difference of 200 meV in the ionisation energies of the defect levels is due to the difference in fundamental gap energies of CIS and CIGS compounds

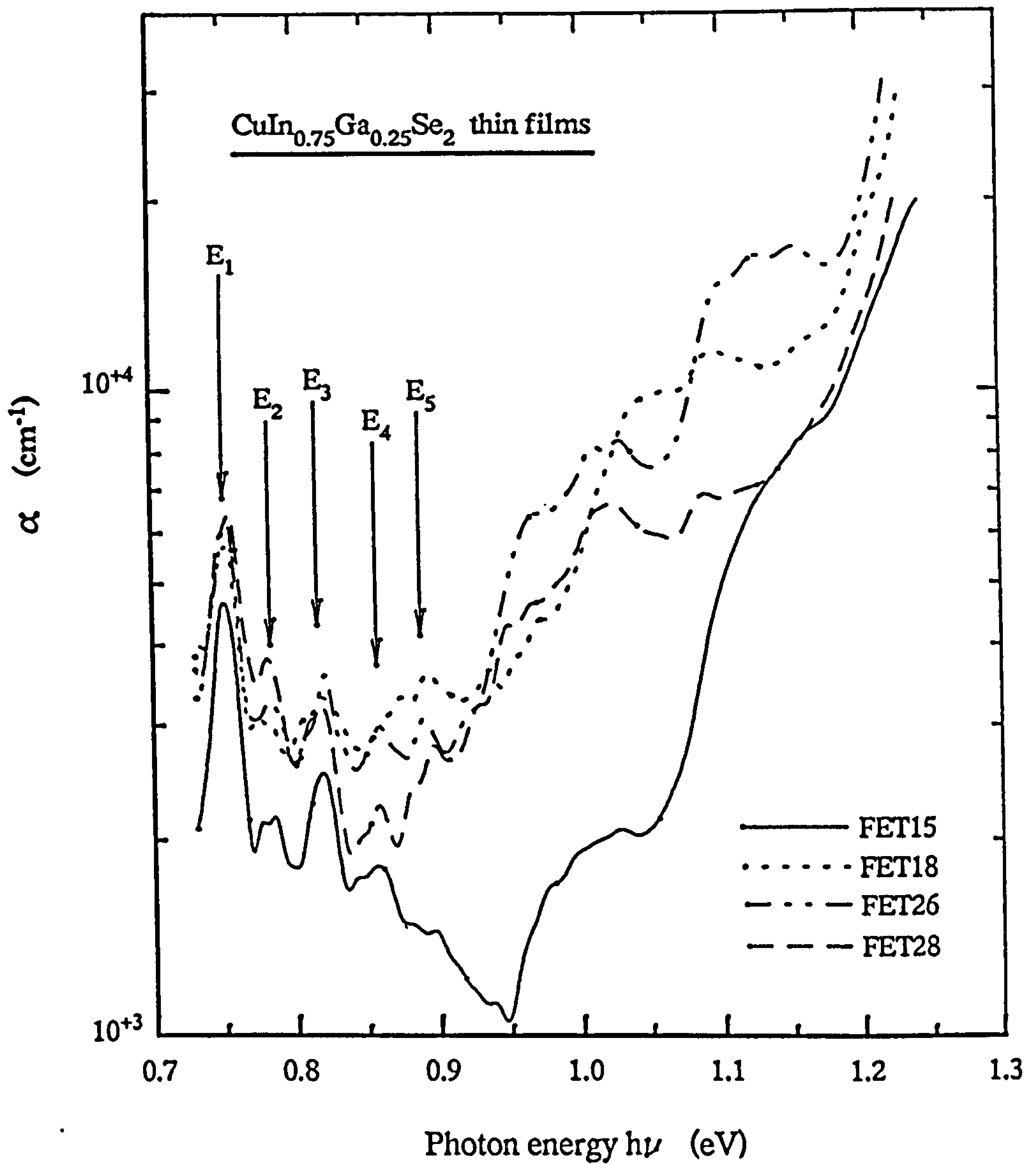


Figure 6.6: Semi logarithmic plot of the absorption coefficient as a function of photon energy calculated from the normalised photoacoustic spectra of figure 6.5.

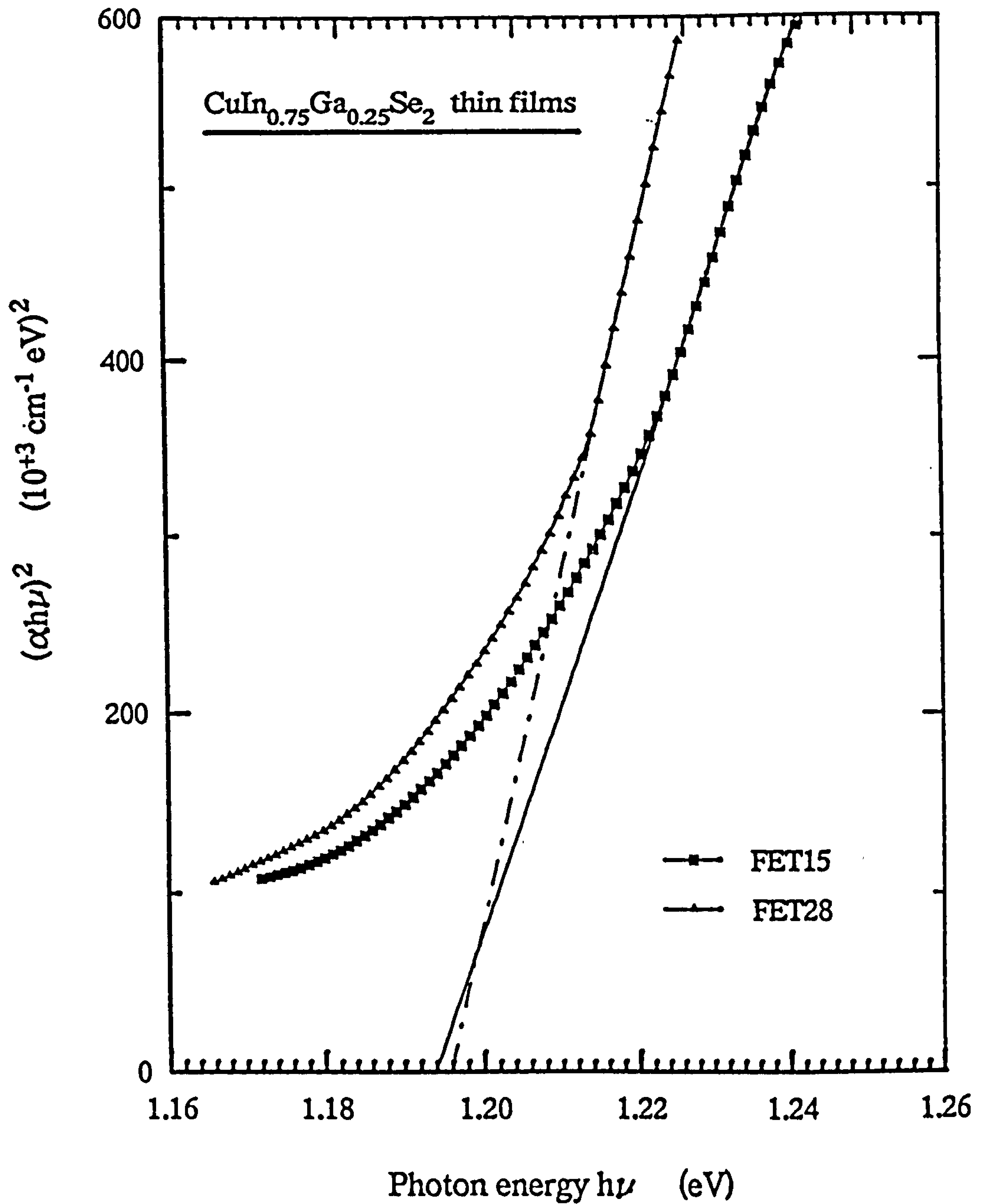


Figure 6.7: Plot of $(\alpha h\nu)^2$ against the photon energy to calculate the band gap of the as-grown polycrystalline CIGS thin films.

| Sample | $E_g$(eV) | $E_g$-hν $E_1$ (meV) | $E_g$-hν $E_2$ (meV) | $E_g$-hν $E_3$ (meV) | $E_g$-hν $E_4$ (meV) | $E_g$-hν $E_5$ (meV) |
|---|---|---|---|---|---|---|
| FET-15 | 1.194 | 444 | 414* | 378 | 337 | 299 |
| FET-18 | 1.201 | 451 | 421* | 390* | 333* | 309 |
| FET-26 | 1.198 | 448 | 416 | 378 | 341 | 308 |
| FET-28 | 1.196 | 446 | 414 | 380 | 341* | 302* |
| FEO-9 | 1.196 | 446 | 415 | 377 | 339 | 289 |
| FEO-13 (Annealed) | 1.197 | 447 | 415 | 377 | 337 | 297 |

Table 6.1: The gap energy and ionisation energies of the defect levels of the as-grown and annealed (under different ambient and temperatures) CIGS thin films.

(approximately 200 meV).

It was noted that the peak positions of the CIGS defect states were similar to those observed in CIS samples [25]. In a recent study, similar spectral behaviour have been observed for both CIGS and CIS single crystals [186]. It can therefore be concluded that the origin of these defects is the same as that of the CIS; this is discussed in section 6.3.1 under laser annealing.

### 6.3.1 The effect of annealing on the observed defect levels

The impact of annealing (under different ambient, time and temperature) on the structural and electrical properties was considered in detail in chapter 5. In this section, however, the influence of annealing on the optical properties is assessed using PAS technique. An initial study of laser annealing and its influence on the optical properties has also been considered.

**Selenium anneal**

Figure 6.8 shows the normalised photoacoustic amplitude signal obtained from the CIGS thin film sample before and after annealing under maximum selenium vapour pressure at 300°C for two hours. It can be seen that the spectrum of the as-grown sample is extended almost linearly in the photon energy range between 0.7 to 1.4 eV. Defect

levels have masked the fundamental band-to-band transitions and, because of this, the estimation of band gap is not possible. It has been reported that the photoacoustic signal strongly depends on the film structure and uniformity [245] and thickness related interference peaks can be observed which makes it difficult to identify the band gap of the thin film sample. A similar shaped photoacoustic spectrum was reported for co-evaporated CIS thin films [245]. In the present case, the reported observations are also true as the XRD spectrum showed a single peak in the <112> direction and the RBS spectrum indicated a non-homogeneous film composition. In contrast, the same sample when annealed under maximum selenium vapour pressure showed significant changes in the behaviour of the photoacoustic spectrum. Near the fundamental band edge the defect related shallow peaks have disappeared and a clear indication of the band edge is now available. However, the peak positions of the defect structure in the tail of the spectra remain unaltered. The changes observed in the photoacoustic spectrum were found to be in good agreement with the improvements in the physical properties of the annealed sample. XRD spectrum showed a dramatic change in the film structure as the characteristic peaks of the chalcopyrite structure appeared. The RBS spectrum of the sample also confirmed the improvements in the film uniformity and homogeneity. An increase in the grain size and a corresponding decrease in the film resistivity have been measured together with an enhancement in the film composition towards that of the starting material. This indicated that the annealing process resulted in a redistribution of the atoms and many of the defect states are annealed out.

Figure 6.9 compares the normalised photoacoustic spectrum of a selenium annealed thin film with that of a standard single crystal. It can be seen that the band edge transition

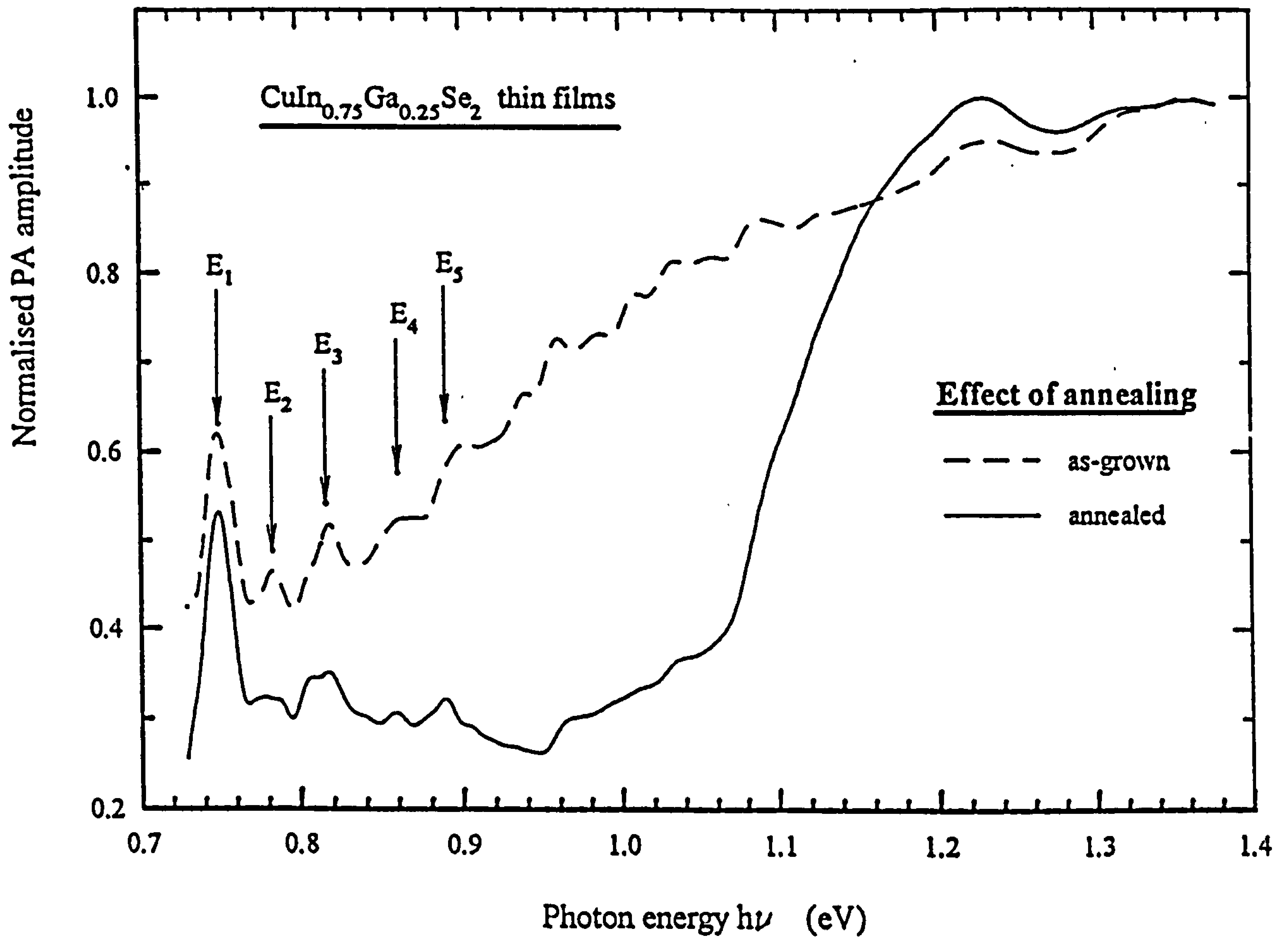


Figure 6.8: Comparative plots of the spectral dependence of the as-grown and selenium annealed at 300°C for two hours CIGS thin films.

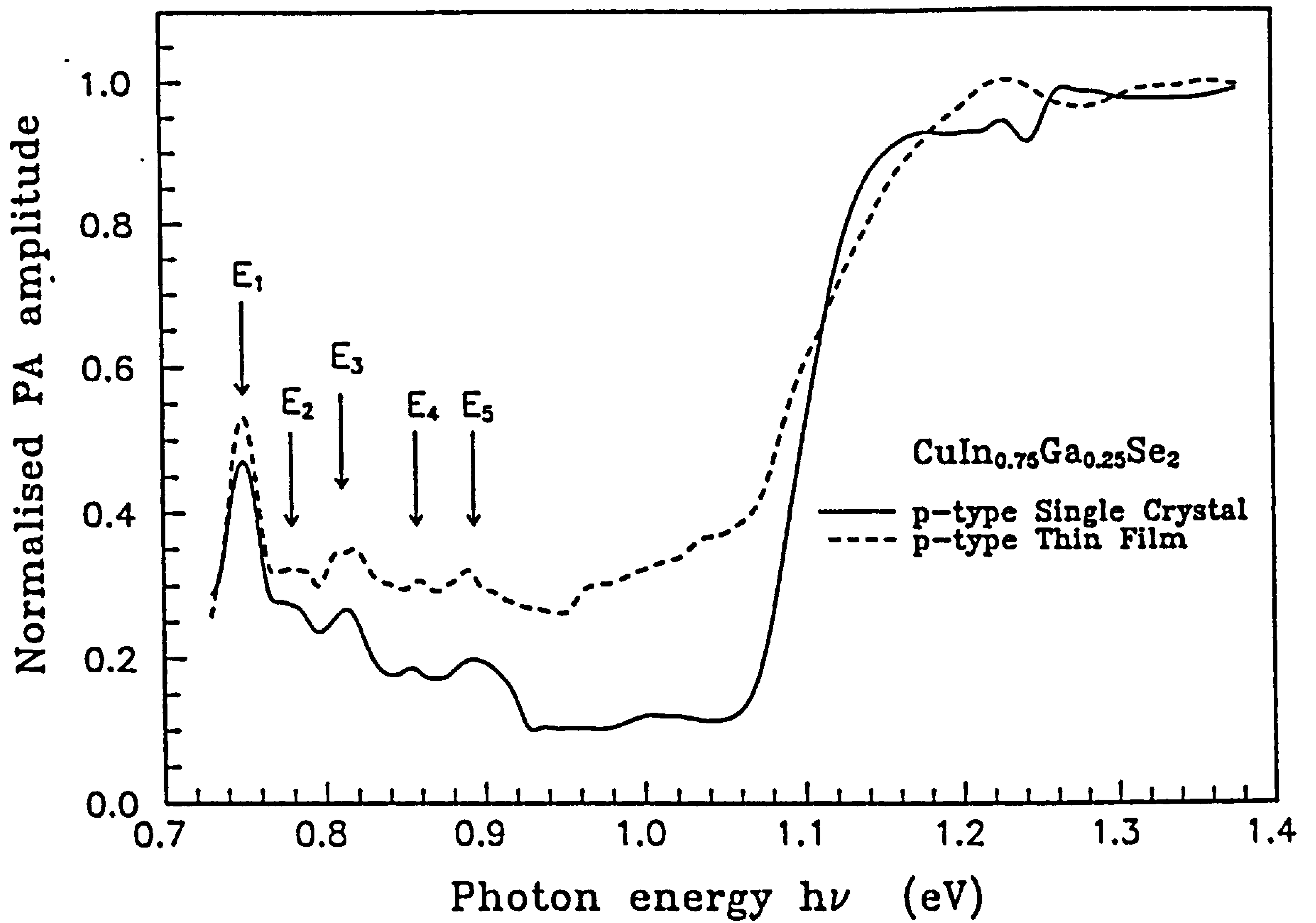


Figure 6.9: Comparative plots of the spectral dependence of p-type single crystal and selenium annealed polycrystalline thin film of CIGS.

in the single crystal spectra is very sharp as compared to that of the selenium annealed thin film. This indicates that the thin film has a number of shallow defect levels which result in a less sharp band edge transition. However, when compared to that of the as-grown thin film, the selenium annealed film is much improved.

The presence of shallow defect levels can be seen more clearly in the absorption spectra. The absorption coefficient, calculated directly from the respective normalised photoacoustic spectra, was divided into two regions (0.7 eV to 1.0 eV and 1.0 eV to 1.3 eV) and is shown in figure 6.10 and 6.11 respectively. The absorption coefficients in the region between 0.7 eV to 1.0 eV indicate the deep level defect transitions which are similar to those observed in the as-grown films as well as both in CIS and CIGS single crystal samples. Since the peak positions are the same in all cases, it can be said that their origin is also the same. However, the peaks could be a composite of more than one peak. At higher photon energy values (1.0 eV to 1.3 eV) the absorption curve revealed two small shallow levels at approximately 0.96 eV and 1.035 eV - figure 6.11. In addition to these peaks, a broad shoulder was observed between 1.08 eV to 1.19 eV. Once again, this could be a single level or a composite of many shallow levels. Finally, at approximately 1.19 eV, a very steep increase in the absorption curve, approaching $10^{+5}$, was observed. This sharp rise is due to the fundamental band to band transition.

The band gap for the selenium annealed sample was calculated to be 1.196±0.005 eV, from a plot of $(\alpha h\nu)^2$ against photon energy, figure 6.12. At present, there is some controversy concerning the true gap energy of 25% gallium containing CIGS alloy. For example, room temperature gap energy values between 1.088 eV [246] to 1.21 eV [247]

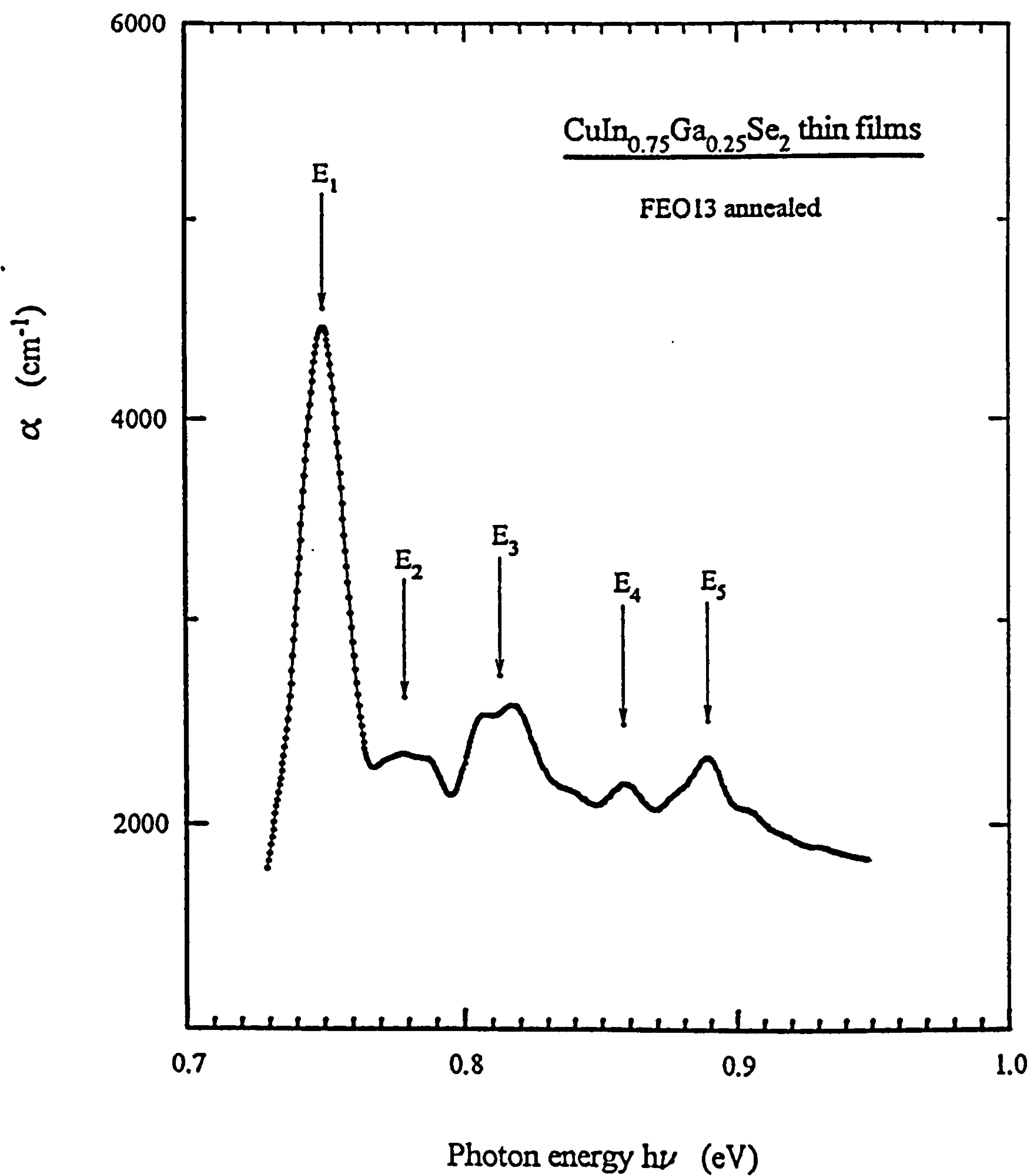


Figure 6.10: Spectral response of the absorption coefficient in the tail of the spectra (0.7 - 1.0 eV) exhibiting the deeper state transitions.

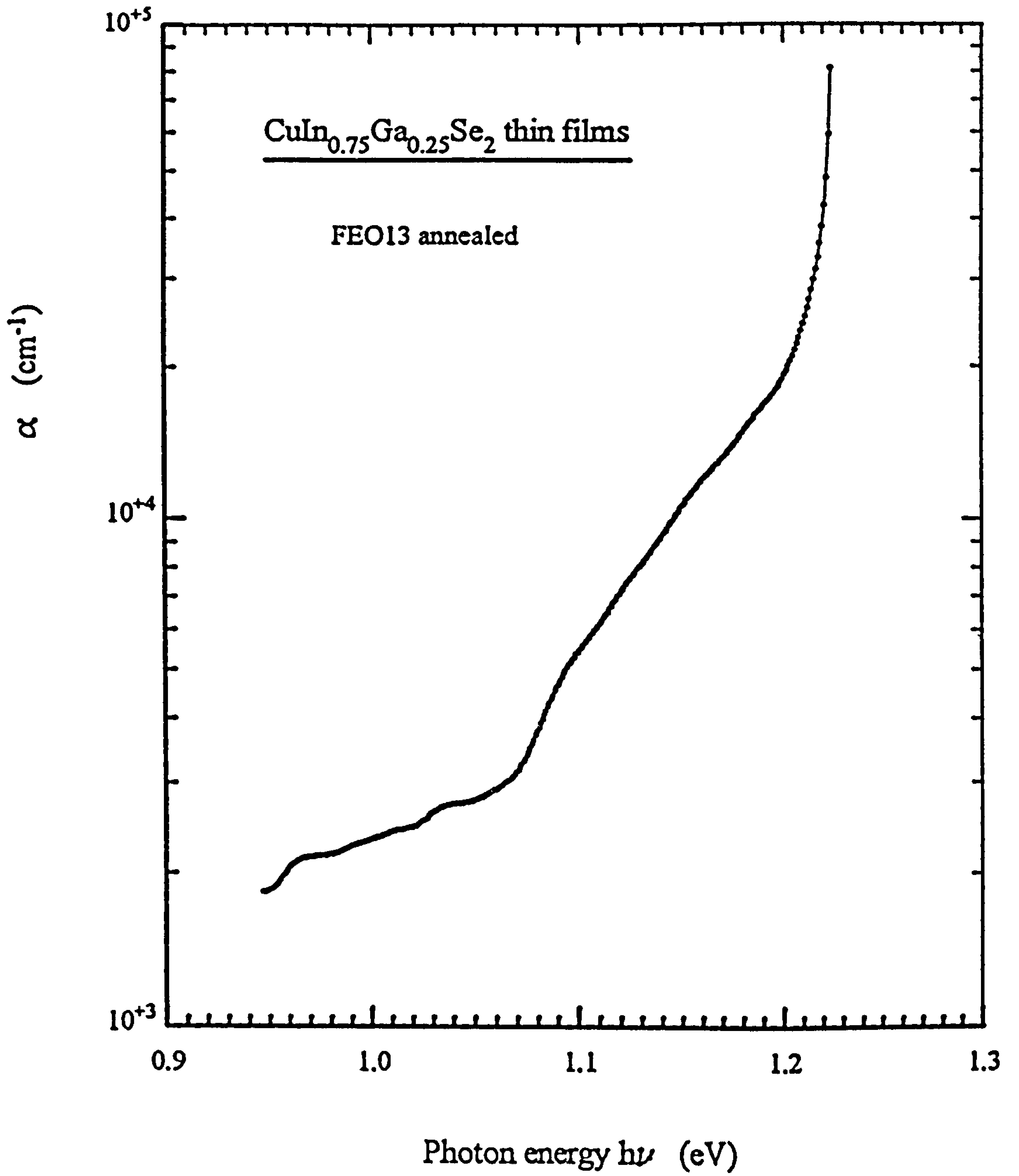


Figure 6.11: Semi logarithmic plot of the absorption coefficient as a function of photon energy (0.9 - 1.3 eV) for a selenium annealed CIGS thin film.

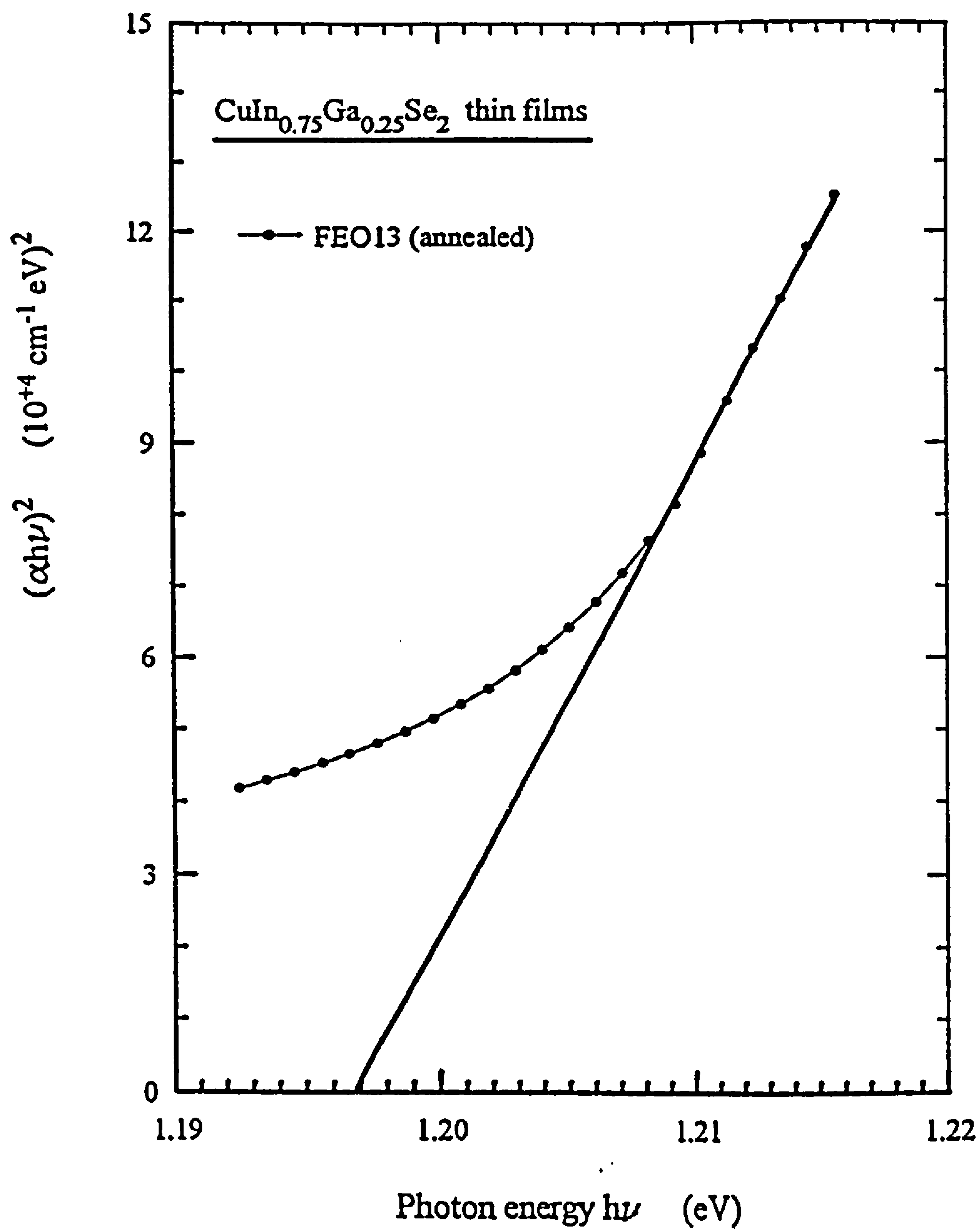


Figure 6.12: Plot of $(\alpha h\nu)^2$ against the photon energy to calculate the band gap of the selenium annealed polycrystalline CIGS thin films.

have been reported for this alloy. Since photoacoustic spectroscopy avoids most of the complications and errors that can be encountered in the routine measurements of transmission and absorption for both single crystal and thin films, this band gap can arguably be the most reliable experimental value available at present.

**Two stage anneal**

Sections 5.2 and 5.3 described the process relating to a two stage anneal, selenium followed by $N_2$:$H_2$, which resulted in an improvement of the compositional and structural properties. To see the effect of the two stage annealing process on the normalised photoacoustic amplitude signal, the sample already annealed in selenium atmosphere at 300°C for two hours was divided into two pieces and one was further annealed in forming gas ambient (9:1 mixture of $N_2$:$H_2$) at annealing temperatures between 200°C to 400°C for half an hour. The second half of the same sample was annealed under argon for the same time and temperature range. The ramp rates for heating and cooling were 20°C/min and 10°C/min respectively.

Figure 6.13 shows the normalised photoacoustic spectra of the sample annealed under the forming gas ambient at 200°C, 300°C and 400°C. It can be seen that the annealing has affected the spectra both near the fundamental band edge and in the tail. However, these changes are more significant in the photon energy range $h\nu < 1.1$ eV where the deeper defect related levels ($E_1$ to $E_5$) were observed. In addition, a new shallow level at approximately 1.10 eV appeared which consistently raised the minimum level of the

photoacoustic signal in the lower photon energy range. Otherwise, the position of the five major peaks ($E_1$ to $E_5$), also observed in the as-grown films, was approximately the same. A number of new defect levels between 0.94 eV and 1.02 eV gradually appeared with increased annealing temperature. An annealing temperature of 400°C showed the worst photoacoustic spectrum in that an increased defect levels intensity and population is evident, figure 6.13. This could be due to the effect of high annealing temperature causing a thermal stress at the surface and or the interface between film and substrate.

The effect of the inert atmosphere (argon) anneal at temperatures in the range 200°C to 400°C on the photoacoustic spectra is shown in figure 6.14. It can be seen that at annealing temperatures up to 300°C there is very little change in the spectra. However, at 400°C there is a significant change in the photoacoustic spectral response. Once again a new shallow level at approximately 1.1 eV is mainly responsible for the increased minimum of the absorption curve. In addition, a number of new defect levels are introduced in the photon energy range $h\nu < 1.05$ eV. The position of the original peaks ($E_1$ to $E_5$) are approximately the same (±5 meV). Some of the peaks are resolved into two separate peaks and some are joined to show a combined effect. For example, the defect level represented by peak label $E_2$ is gradually resolved into two peaks and the $E_3$ is now combined with its nearest neighbour, producing a single well resolved peak. Since argon is an inert ambient it can be said that high temperature annealing is responsible for the observed effects in the photoacoustic spectra of the films as discussed earlier.

The structural and compositional properties of the respective samples showed no change

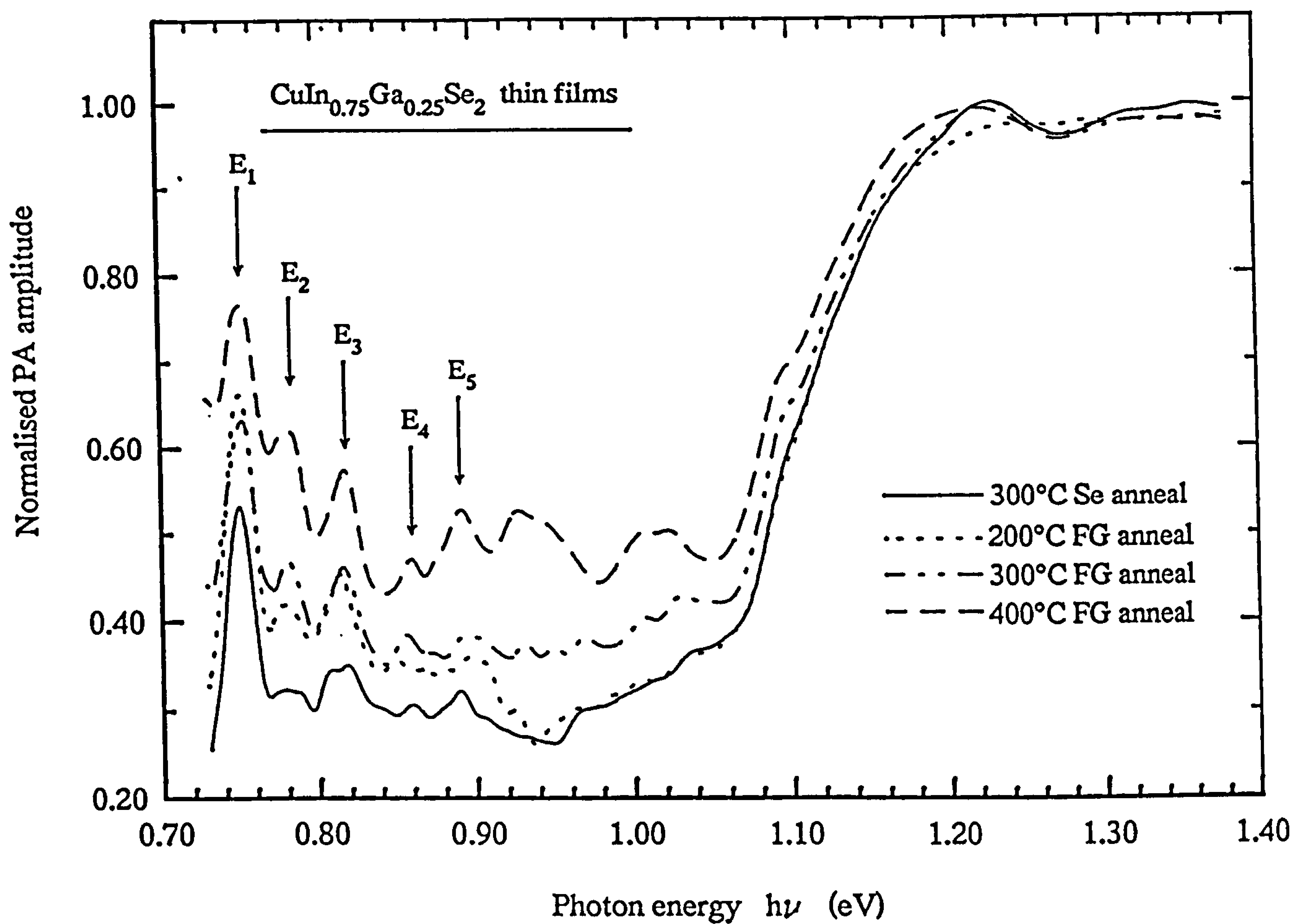


Figure 6.13: Comparative plots of the spectral distribution of CIGS thin films annealed under selenium and $N_2$:$H_2$ (FG) ambient at different temperatures.

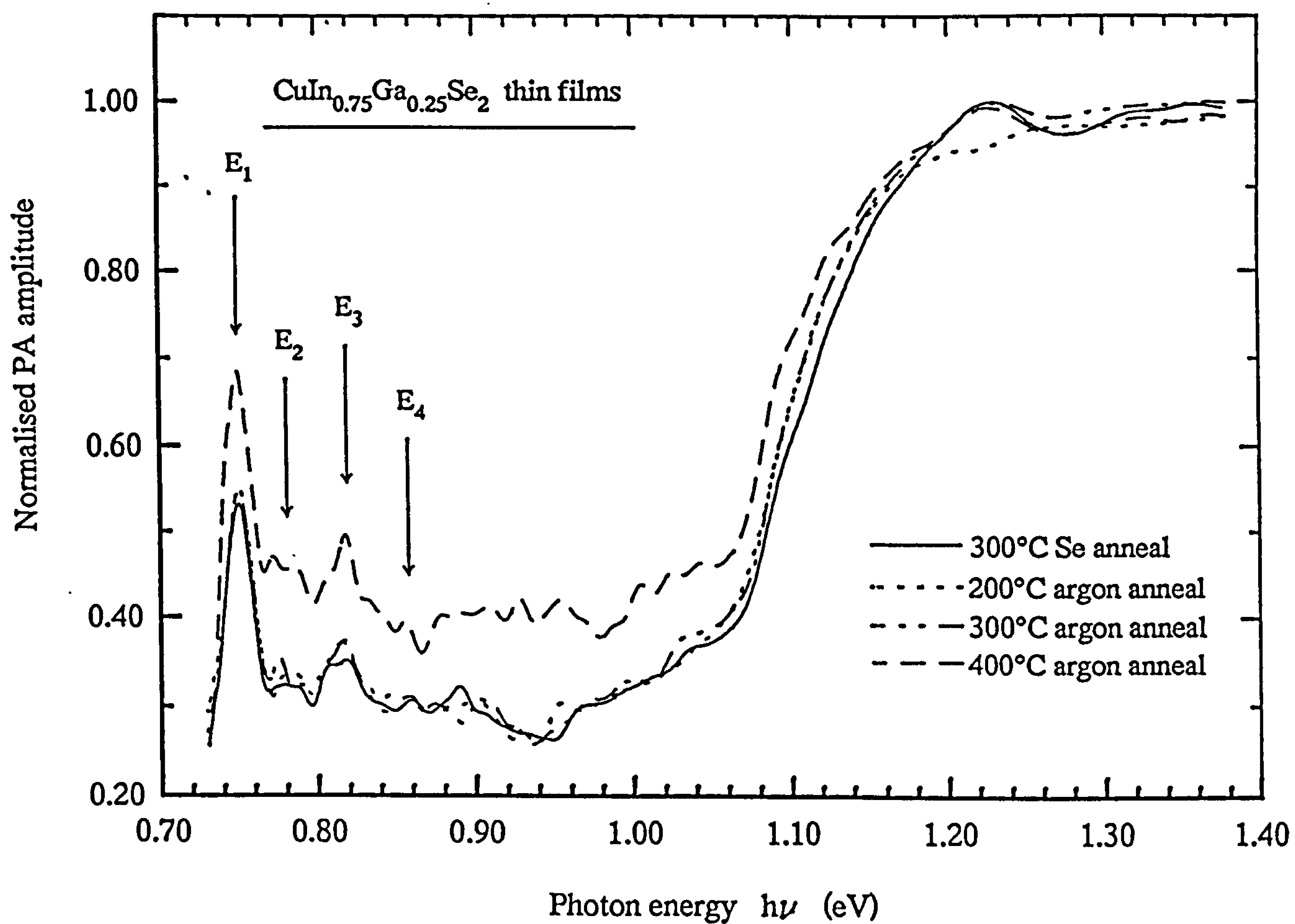


Figure 6.14: Comparative plots of the spectral distribution of CIGS thin films annealed under selenium and argon ambient at different temperatures.

after annealing. Qualitatively, the electrical properties also remained the same. The comparison of the two ambients at 400°C anneal revealed that this temperature is not suitable for the flash evaporated samples (in present study). As discussed in chapter 5, this temperature degraded the film surface due to thermal stresses. However, the visual appearance of the annealed samples, in the present case, was good. This could be due to the fact that samples were annealed for shorter times with slower ramp rates. Other comparison of the various ambients on the electronic structure showed that the deeper states are less affected in argon than in forming gas. This is not surprising as argon is a non reactive gas and should not affect the film, on the other hand, forming gas is known to be reactive with semiconductors. Several reports are available on the hydrogen passivation of semiconductors [248,249].

The changes detected by PAS near the fundamental band edge are better resolved when the absorption coefficients are evaluated from the photoacoustic spectra. Figure 6.15 shows the absorption coefficient spectra of CIGS films annealed in selenium at 300°C and in argon at 300 and 400°C. The absorption curves for the 300°C selenium annealed sample and the 300°C argon annealed sample reveal nearly the same spectra. The absorption curve for the sample annealed at 400°C in argon showed at least two new shallow levels at approximately 1.09 eV and 1.11 eV. A similar observation about the shallow level was noticed for samples annealed in $H_2$:$N_2$ ambients. In spite of these changes, a considerable increase in the absorption coefficient was seen after annealing in selenium, forming gas and argon ambients. All the spectra showed absorption coefficient values of > $10^4$ $cm^{-1}$.

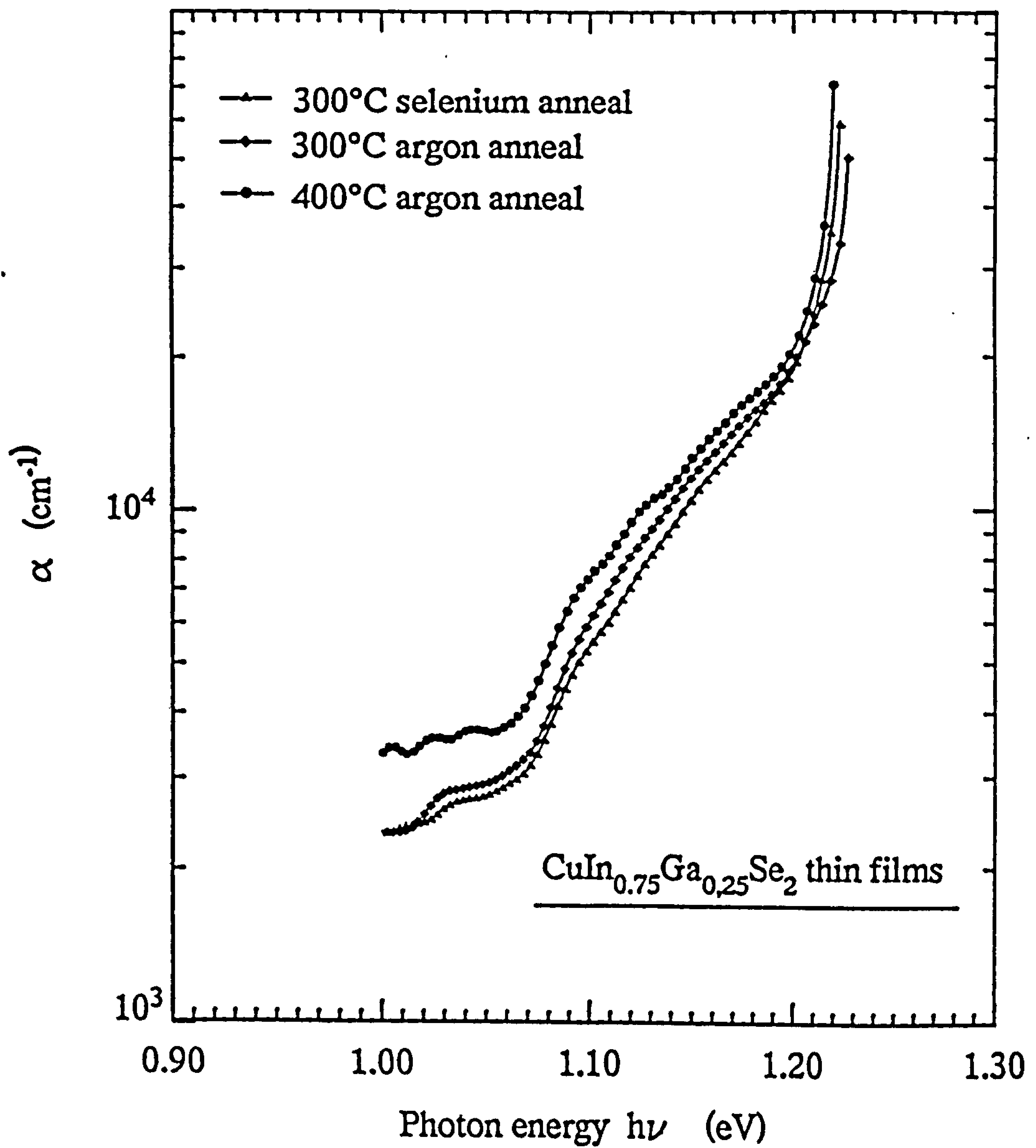


Figure 6.15: Comparative plots of the absorption coefficient of CIGS thin films annealed under selenium and argon ambient at different temperatures.

The band gap energies were determined from the room temperature plots of $(\alpha h\nu)^2$ against the photon energy $h\nu$. Representative curves of these plots are shown in figure 6.16. The band gap energies were determined by extrapolating the curves down to $(\alpha h\nu)^2=0$. The band gap energies for the samples processed under various heat treatments and measured from the photoacoustic spectra at different chopping frequencies are shown in table 6.2. It can be seen that the energy band gap values for most of the CIGS thin films processed under various conditions is 1.196±0.006 eV. A few samples gave energy band gap values which were slightly lower. For example, films annealed in forming gas and argon ambient and analysed with a chopping frequency of 185 Hz showed lower value of the energy band gap of the order of 1.180±0.006 eV. There could be several possible reasons for this observation. Since the thermal diffusion lengths at modulating frequencies of 30, 112, 185 and 312 Hz are 232, 120, 93 and 72μm respectively and the thin film thickness was in most cases of the order 1μm, all the light can pass directly through the sample. It is therefore not possible for the deviated values of band gap (in thin films) to be due to variations in the composition with sample depth. The second possibility is that of a measurement error which, in this study, is approximated to be not more than 0.5%. Another possible cause for the observed change in band gap, which it is felt is the most probable, is the shifting of band gap due to the inclusion of shallow levels which are observed in the photoacoustic spectra of the thin films. This effect is more pronounced when the absorption spectra of the two samples are considered, figure 6.15. It can be seen that a new shallow level near the band edge is changing the slope of the absorption curve as the annealing temperature is increased. Similar effects were observed for the sample analysed with 185 Hz modulation frequency and the corresponding band gap curves revealed a smaller

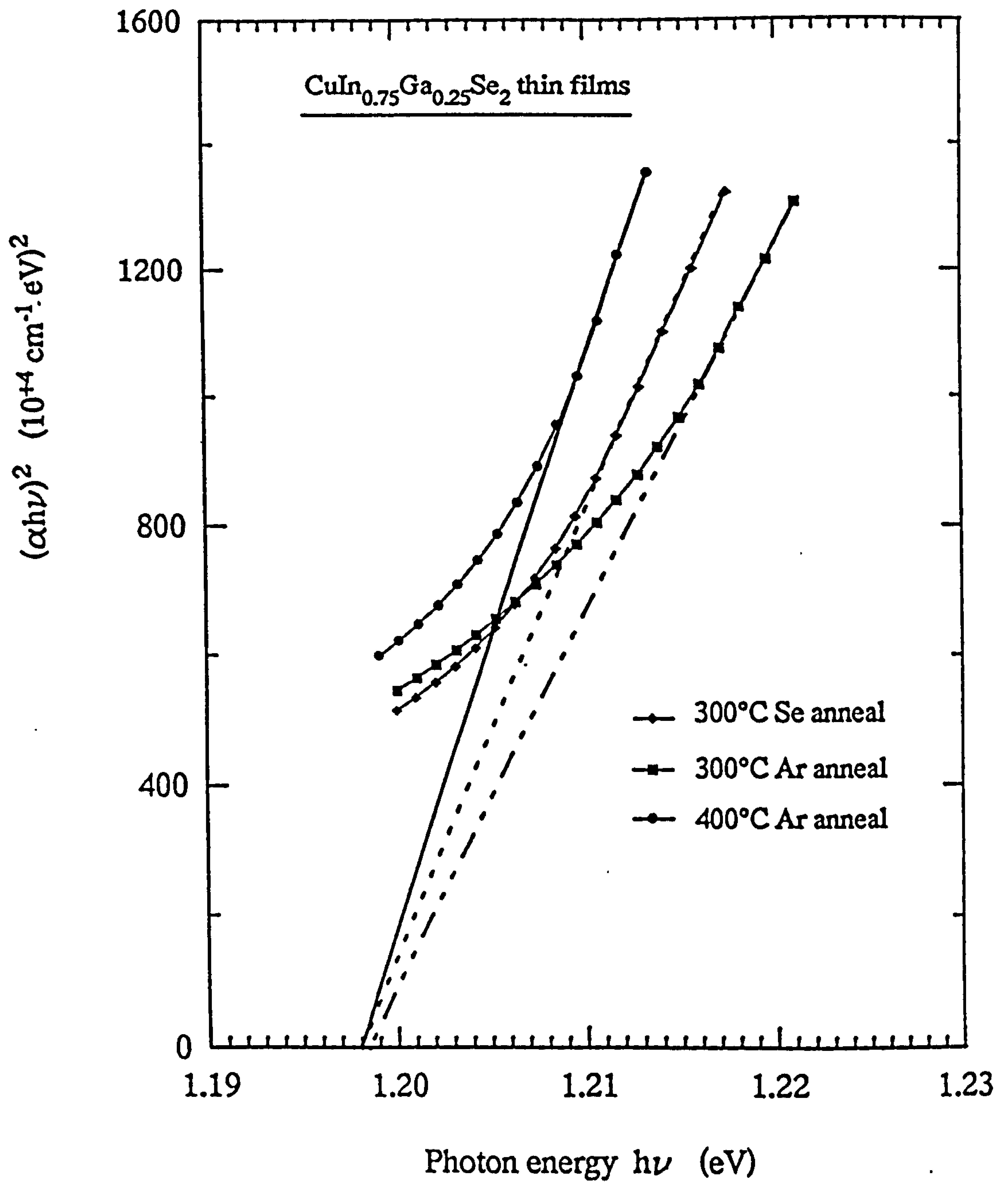


Figure 6.16: Plot of $(\alpha h\nu)^2$ against the photon energy to calculate the band gap of selenium and argon annealed polycrystalline CIGS thin films.

| Process | $E_g$ (eV) at different chopping frequency | | | | Process | $E_g$ (eV) at different chopping frequency | | | |
|---|---|---|---|---|---|---|---|---|---|
| | 30Hz | 112Hz | 185Hz | 312Hz | | 30Hz | 112Hz | 185Hz | 312Hz |
| 300°C selenium anneal | ------- | 1.197 | 1.200 | ------- | 300°C selenium anneal | ------ | 1.197 | 1.200 | ------- |
| 200°C argon anneal | ------- | 1.197 | 1.197 | ------- | 200°C $N_2$:$H_2$ anneal | 1.197 | ------ | 1.180 | 1.196 |
| 300°C argon anneal | 1.196 | 1.196 | ------ | ------- | 300°C $N_2$:$H_2$ anneal | 1.195 | 1.197 | 1.174 | ------- |
| 400°C argon anneal | ------- | 1.196 | 1.181 | ------- | 400°C $N_2$:$H_2$ anneal | ------ | 1.196 | ------ | ------- |

Table 6.2: Energy band gap values of annealed (under different ambient and temperatures) thin films of CIGS at different modulating frequencies.

energy band gap values - table 6.2.

The comparison of the calculated energy band gap values with those reported in the literature is a intricate task. Theoretically, the energy band gap value for CIGS (with 25% gallium) should be 1.14 eV [250]. However, the reported band gap values for single crystals and thin films for the said composition are all very different.

For single crystal samples, optical measurements at room temperature revealed 1.12 eV [251], 1.16 eV [252], 1.19 eV [253] and 1.21 eV [247] etc. In addition, the effect of change in the reported compositions (i.e. copper from 19 atm.% to the near ideal value of 25%) on the energy band gap showed a range between 1.13 to 1.19 eV [254]. More recently, the measured band gap value for single crystal CIGS, using the photoacoustic spectroscopy technique, showed a band gap value of 1.17 eV [25]. The above reported band gap values were calculated from the best fit relations which included the lattice constants, initial band gap values of CIS and CGS and the bowing parameters. The difference in these reported values may be due to the use of different band gap values of CIS (0.995 - 1.02 eV) and CGS (1.62 - 1.68 eV) from which the CIGS alloy is formed. Authors calculated their own values of the lattice parameters, for their materials, and these were then used in the second order polynomial relations. This could also contribute to the reported differences in the energy band gap values.

For thin film samples the reported energy band gap values are few and they range between 1.14 to 1.19 eV [143,255,256]. These differences may be due to structural and/or compositional variations present in the thin film samples. When comparing the

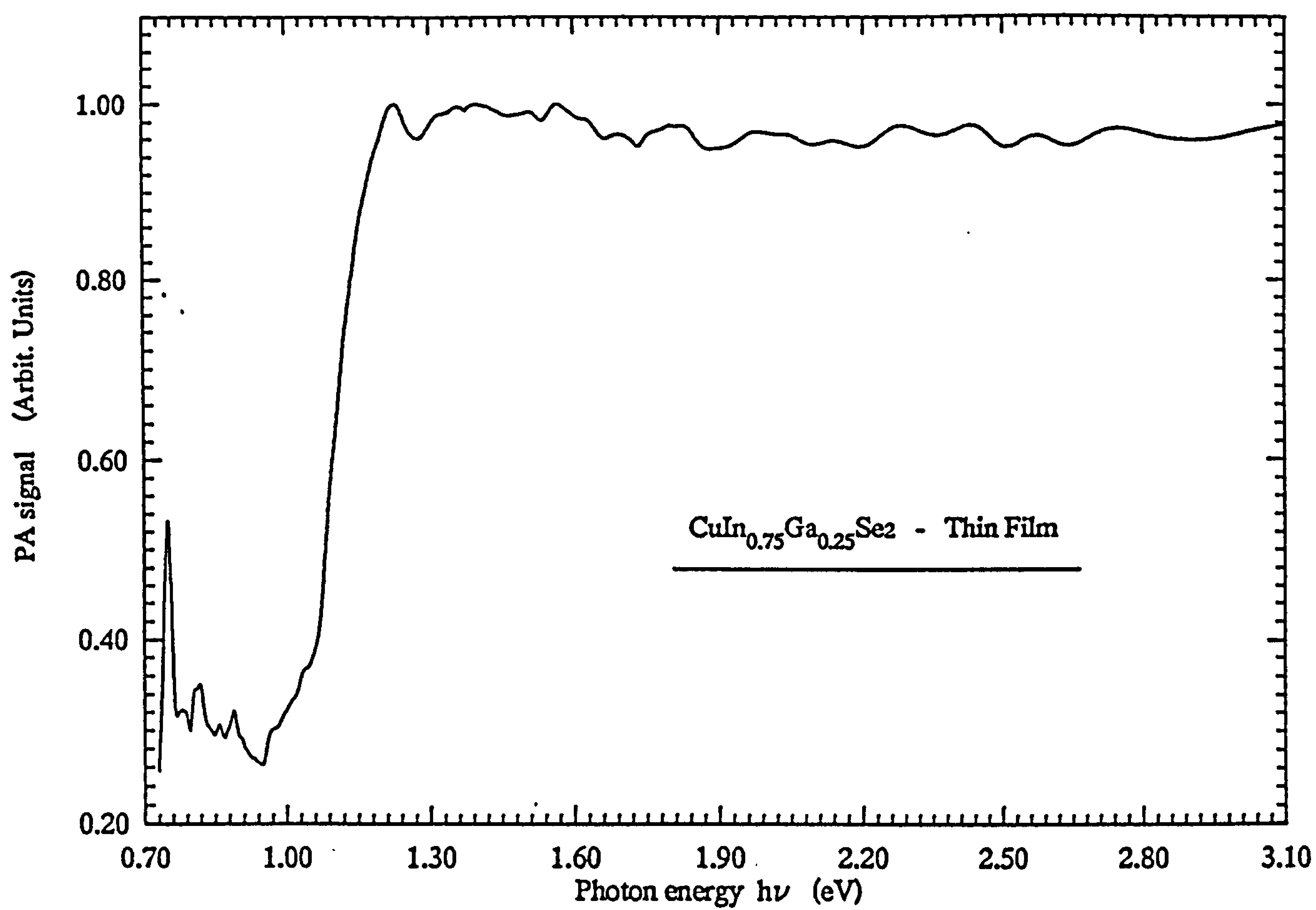


Figure 6.17: Normalised photoacoustic spectrum of selenium annealed CIGS thin film in the photon energy range between 0.7 eV to 3.1 eV.

calculated band gap values of 1.196±0.005 eV from this present work with those reported, it was noted that they matched well with the higher i.e. 1.19 eV values. The observed differences could be due to lower concentration of copper, as reported by Albin et al for 19 at% copper [254]. However, the composition (relative to the copper content) of films used in this study, was found to be extremely close to the ideal i.e. 25 at%. This anomaly in band gap values for CIGS alloys requires further fundamental studies in order to ascertain an absolute value.

The use of photoacoustic spectroscopy is not limited in the near infra-red region, it can also be used in the visible region. The spectrum obtained from CIGS thin films in the photon energy range 0.7 eV to 3.1 eV is shown in figure 6.17. It can be seen that in the visible region between photon energies of 1.4 eV to 3.1 eV there are no major transitions, which indicates the absence of any notable defect states in this region.

**Laser anneal**

The use of lasers in the surface modification of compound semiconductor samples is a well known process. Several reports are available on the successful application of lasers for the synthesis of multi-layered sandwiches of the elemental constituents on suitable thermally insulating substrates [257]. At the research level such layers are generally deposited by sequential vacuum depositions. Recrystallisation of the material deposited by other deposition techniques can also be achieved by laser irradiation. The process involves the interaction of the laser radiation with the surface of the sample which

reorganises the original film structure into an ordered crystalline form. In this section, initial studies of the effect of laser annealing on the optical properties were considered. Thin film samples of both CIS and CIGS were irradiated by a diffused excimer laser in pulsed mode with an energy of 170 mJ.

Figure 6.18 shows an example of the normalised photoacoustic amplitude spectra of laser annealed (5, 20ns pulses) flash evaporated CIS thin films, compared to the as-grown film. In both cases the spectra exhibited two clear regions separated at approximately 1.02 eV, the fundamental band edge of CIS. After laser annealing, significant changes are observed not only near the fundamental absorption edge but also in the tail of the spectrum between 0.7 eV to 1.0 eV. An overall decrease in the minimum of the photoacoustic amplitude is evident. This could be due to a change in the non-radiative quantum yield of the material [243]. It was also noted that a shallow defect level at 1.00 eV was introduced by the annealing process.

In order to compare the deeper state transitions appearing in the tail of the spectra (0.7 eV to 1.0 eV) figure 6.19 was constructed. It shows the absorption coefficient ($\alpha$), derived from the respective sections of the photoacoustic spectra of as-grown thin film, the laser annealed thin film and single crystal. Although the minimum level of the absorption curve in the said photon energy range for the single crystal sample was lower than those for the thin films, for ease of comparison it has been placed above the thin film spectra. As expected, the deeper level states, labelled by $E_1$ to $E_5$, are very clear and well resolved in the case of single crystal. The deeper states are also evident in the thin films but in the as-grown sample these states are not well resolved. In particular, the $E_2$

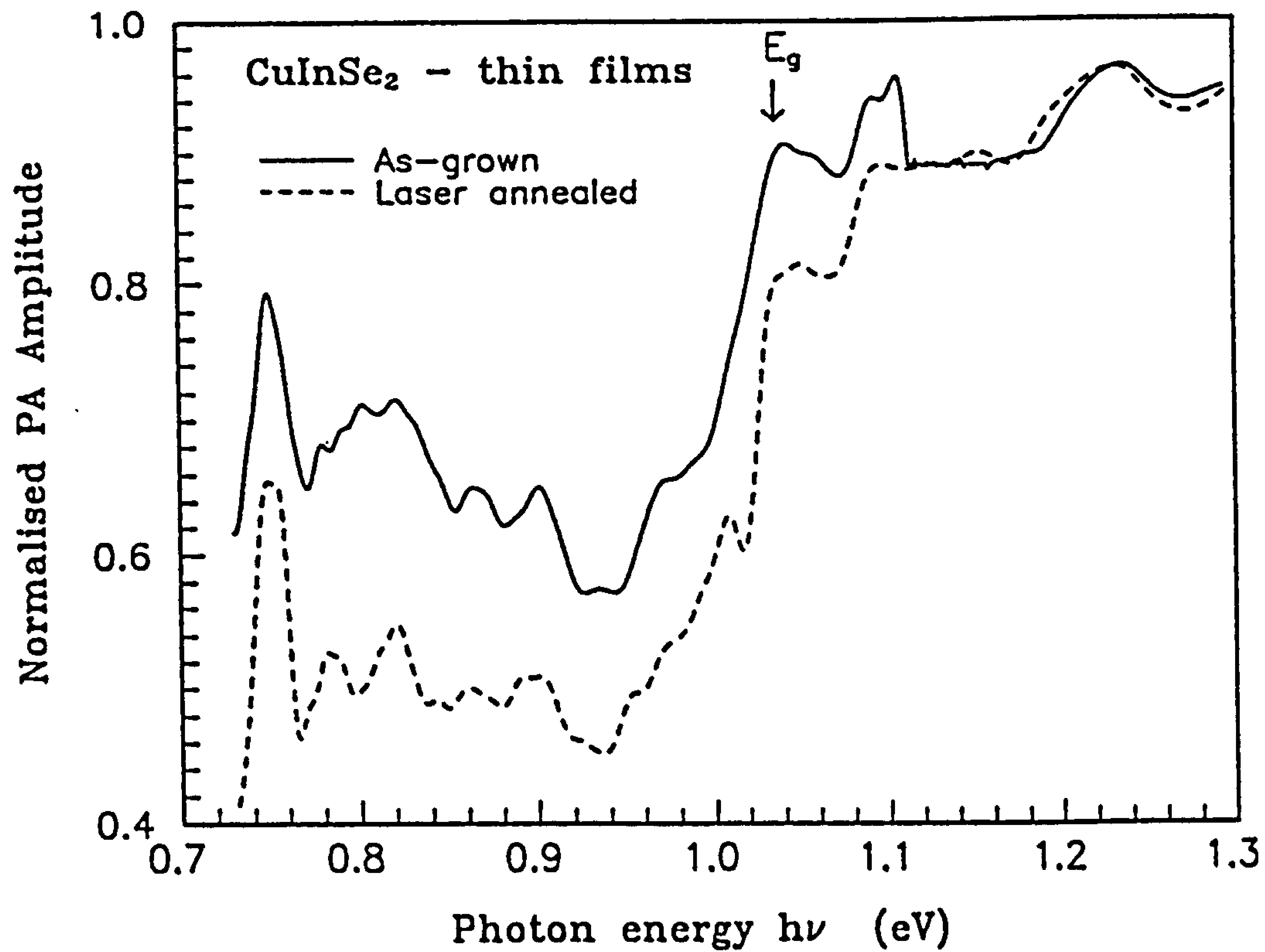


Figure 6.18: Comparative plot of the normalised photoacoustic amplitude signal for polycrystalline CIS thin films before and after laser annealing.

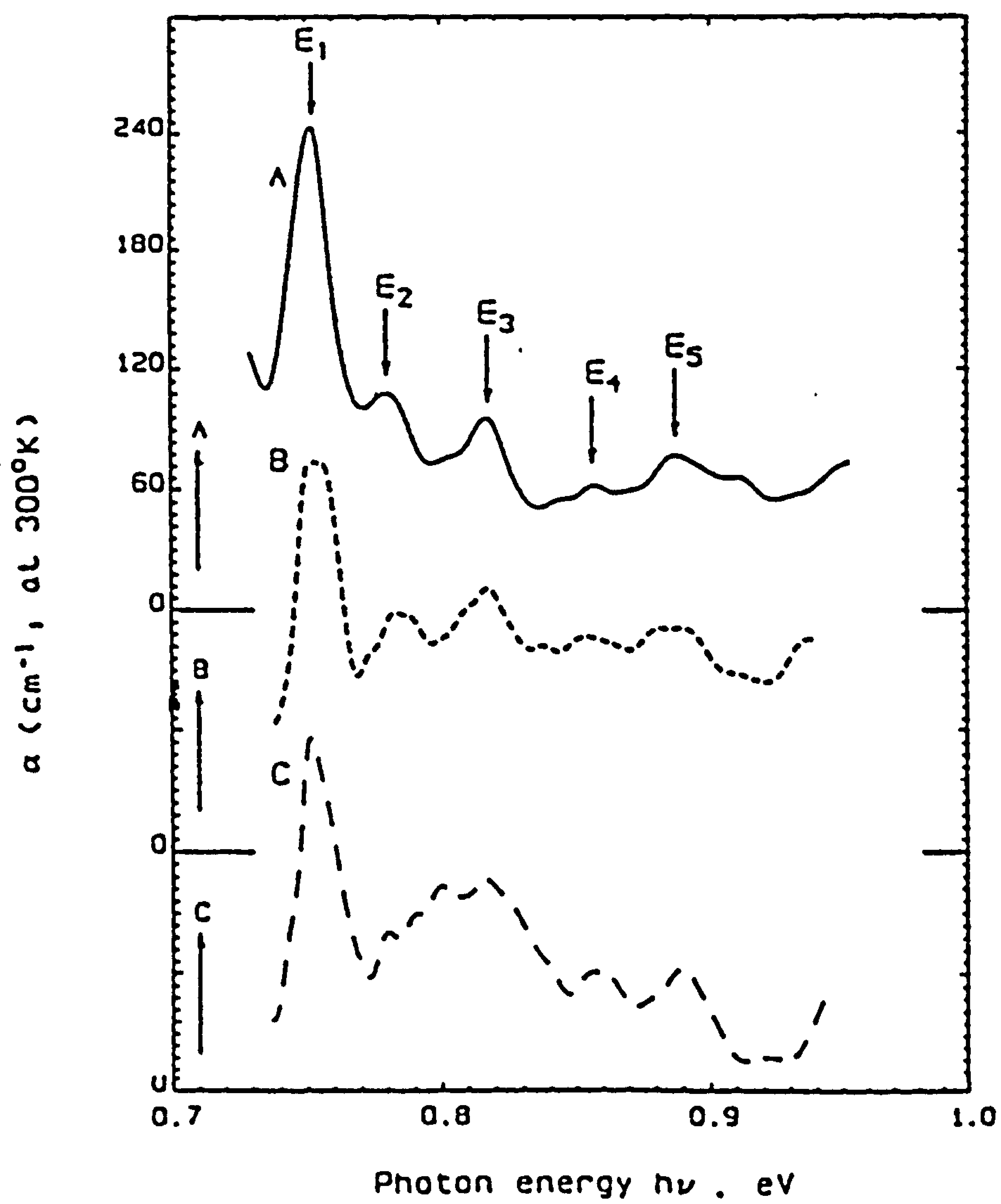


Figure 6.19: Comparative plot of the absorption coefficient of a single crystal (a), polycrystalline CIS thin film before (c) and after laser annealing (b).

and $E_3$ peaks overlap resulting in a broad peak. In contrast, the spectrum obtained from the laser annealed sample, revealed that all the peaks from $E_1$ to $E_5$ are clear and well resolved and are comparable to those from single crystal. The XRD spectrum of the laser annealed sample showed a slight change in structure as compared to that of the as-grown thin film. After laser annealing a number of new CIS related peaks (<204><220>, <116><312> and <217><411>) were evident in the XRD spectrum. Similar effects were observed in the laser annealed CIGS thin films. The film homogeneity was also improved as the RBS spectrum of the latter sample demonstrated. The scanning electron micrographs, however, showed no conclusive evidence of the modification in the grain structure with both the as-grown and laser annealed films having similar grain structures.

In laser annealing, the rate of structural regrowth from the original phase to the crystalline phase is determined by the temperature at the reordering interface. The crystal orientation can also have some effect on the regrowth rate, and because the complete process involves non-equilibrium heating, it is not a simple task to quantify the total procedure. However, it appears from the comparison of the photoacoustic spectra, that laser annealing has redistributed the atoms within the sample and changed the crystal structure. In order to correlate the observed effect with the fundamental properties a more detailed study is required.

The energy band gap value of the as-grown and laser annealed samples were calculated from the room temperature plots of $(\alpha h\nu)^2$ versus the photon energy $h\nu$, figure 6.20. Analysis of the experimental data showed that the near-vertical portion of the $(\alpha h\nu)^2$ curves is due to an allowed direct transition. By extrapolating the linear portion of the

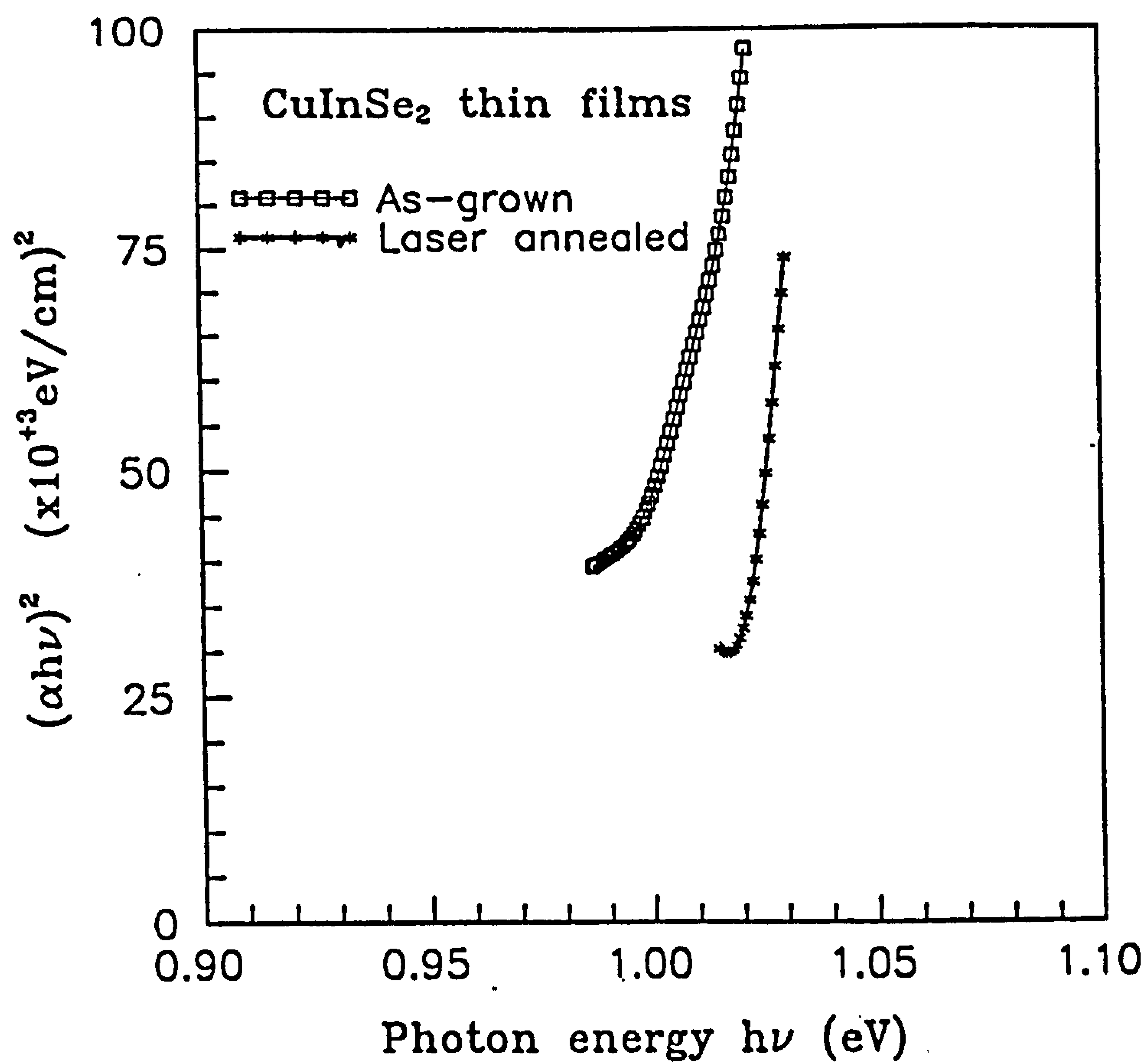


Figure 6.20: Plot of $(\alpha h\nu)^2$ against the photon energy to calculate the band gap of CIS thin films before and after laser annealing.

curves to $(\alpha h\nu)^2 = 0$, the band gap energies were determined. The measured band gap value of the as-grown sample is found to be approximately 0.996 eV. However, in the case of the laser annealed sample, the observed band gap value is slightly higher at 1.015 eV. The energy band gap values of both the as-grown and laser annealed are in good agreement to that measured by the PAS technique [245]. It appears that the new defect levels observed on the linear portion near the fundamental band edge are the probable cause of the band gap shift to this higher value. It should be noted that the sample was not processed under any atmosphere (selenium/CIS powder) before laser annealing.

The ionization energies of the deeper defect levels from the appropriately determined values of the gap energy are derived [190] and are tabulated in table 6.3. The proposed electrical activity (D - donor and A - acceptor) have also been indicated. The strongest peak appearing at 256 meV is an acceptor state and is in good agreement to that reported from DLTS studies on CIS single crystals at 250 meV [258] and on thin films at 260 meV [259]. The peak at 228 meV is due to an intrinsic donor state, reported by Neumann [260], with an activation energy in the range 220-225 meV. Both were determined by electrical measurements and optical absorption studies. The ionization energy of the peak $E_3$, 191 meV, could be either an acceptor or a donor state. An acceptor with an ionization energy of approximately 190 meV has been observed in p-type CIS thin films [261] but recent DLTS measurements confirmed that this defect is a hole and electron trap with ionization energies of 186 meV and 182 meV respectively [258]. The energy $E_4$, 151 meV, can be ascribed to an acceptor state. Within the measurement error, this value agrees with an acceptor activation energy of 160 meV

| Peak number | Peak energy (thin film) | Peak energy (single crystal) | Proposed electrical activity |
|---|---|---|---|
| $E_g$(eV) | 1.015 | 1.008 | |
| $E_1$(meV) | 263 | 256 | A |
| $E_2$(meV) | 235 | 228 | D |
| $E_3$(meV) | 198 | 191 | A/D |
| $E_4$(meV) | 158 | 151 | A |
| $E_5$(meV) | 128 | 120 | A/D |

Table 6.3 The fundamental energy band gap $E_g$ and different defect ionization energies ($E_1$ - $E_5$) of p-type CIS single crystal and thin films as determined by photoacoustic spectroscopy.

determined in indium rich CIS [262] and with 140-160 meV observed in the photoconductivity spectra [214]. In the case of energy $E_5$ the electrical activity can again be ascribed to either an acceptor or a donor. In the literature it is reported to be an acceptor state with energy in the range 110-120 meV [260], determined by electrical measurements on p-type CIS single crystals. In another report by Elfotouh et al [218] this state has been described as a donor state with the same energy of 115 meV, deduced from the photoluminescence spectra. In most of the cases the proposed electrical activity agrees with the reported ones. However, the nature of the defect levels ($E_3$ and $E_5$) are still questionable and, in order to be sure about their electrical activity, a range of samples differing in their structural and compositional properties should be analyzed using the PAS technique.

## 6.4 Effect of ion-implantation

The doping of semiconductors to alter their electrical characteristics is an important process which is normally achieved by adding small amount of impurities to the semiconductor using an appropriate method [263]. One of the most widely used methods is that of ion-implantation [263]. In principle this involves the scanning of an ion beam over the sample surface to achieve a uniform dopant distribution across the sample, at the required depth. The amount of impurities introduced and the depth penetrated depends upon the dose and energy of the beam, which can be controlled very precisely. The major advantage of this process is the precise degree of control and reproducibility achieved. However, high capital costs are incurred in equipping the facility. With the

high throughput obtained by modern implanters, the process cost per specimen is economically viable and competitive with other doping technologies [263]. Following the ion-implantation, high temperature annealing is necessary to activate dopants and to remove surface damage introduced by the ions entering the crystal lattice.

The incorporation of hydrogen into CIS single crystals using both proton implantation and diffusion from a plasma source has been found to modify considerably the electrical properties of the compound [264]. In this section, initial studies on the effect of ion-implantation were carried out. Thin film samples of CIGS already processed under various post-deposition heat treatments (section 6.3.1) were implanted with hydrogen (10 keV, $10^{15}$ ions/cm$^2$) at room temperature.

Figure 6.21 and 6.22 show the normalised photoacoustic spectra of hydrogen implanted CIGS films together with the spectra obtained after the last anneal, in forming gas and argon ambients at 400°C respectively. It can be seen that, for the argon annealed sample, the implantation has improved the structure of the deep states with the defect related peaks ($E_1$ to $E_5$) being well resolved - figure 6.21. An enhanced shoulder at approximately 1.10 eV has raised the minimum level of the photoacoustic signal. However, in the case of the forming gas annealed sample, the implantation effect is not so significant in the low energy range. This could be due to the fact that the sample was already stable in terms of the usual observed deeper state defect population. However, in the case of the argon annealed sample, (figure 6.22) the situation was the exact opposite. The sample before implantation showed a number of extra defect states and therefore the effect of $H^+$-implantation is more pronounced.

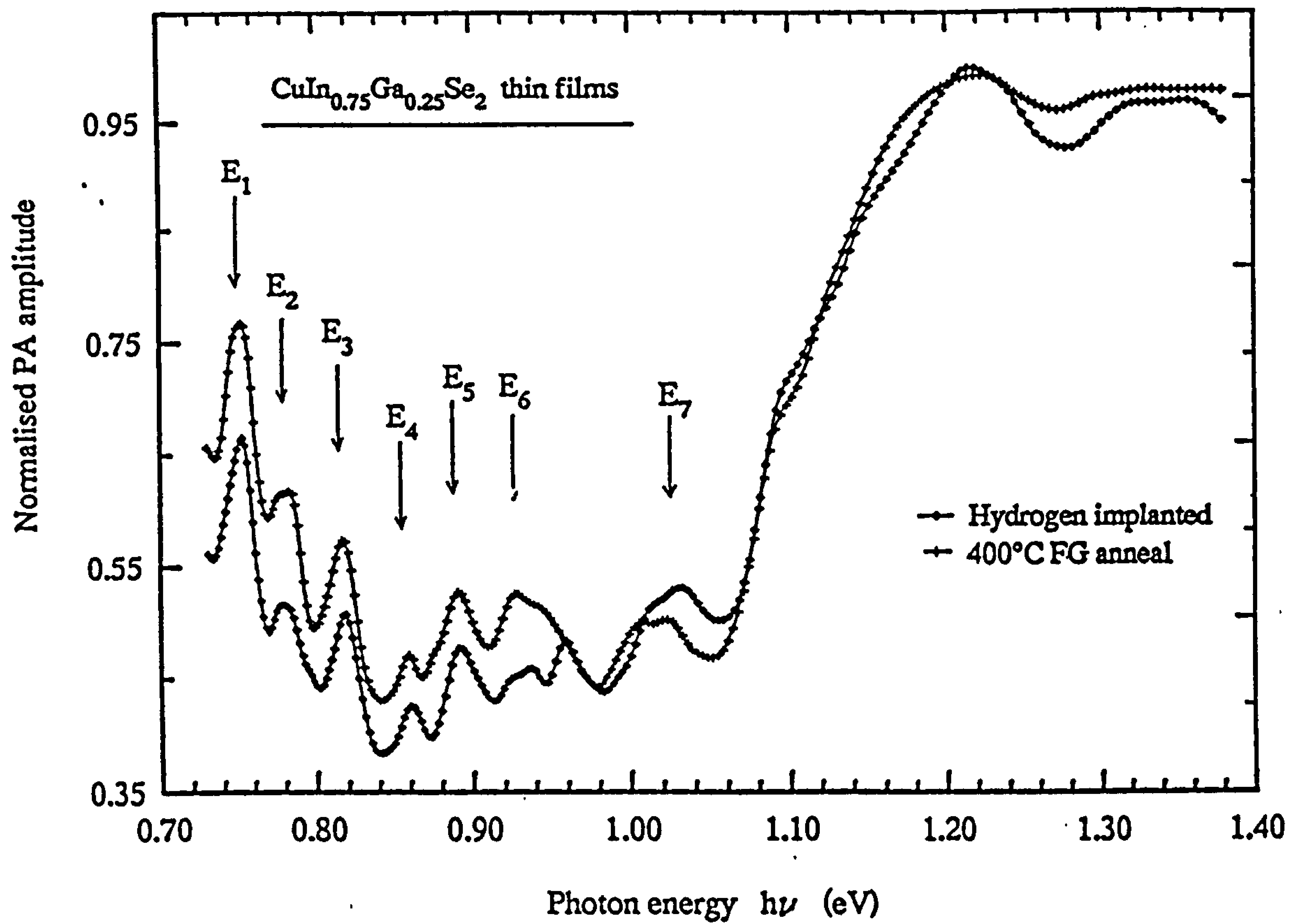


Figure 6.21: Comparative plots of the spectral distribution of CIGS thin films annealed under $N_2$:$H_2$ (FG) ambient at 400°C and $H^+$ implanted.

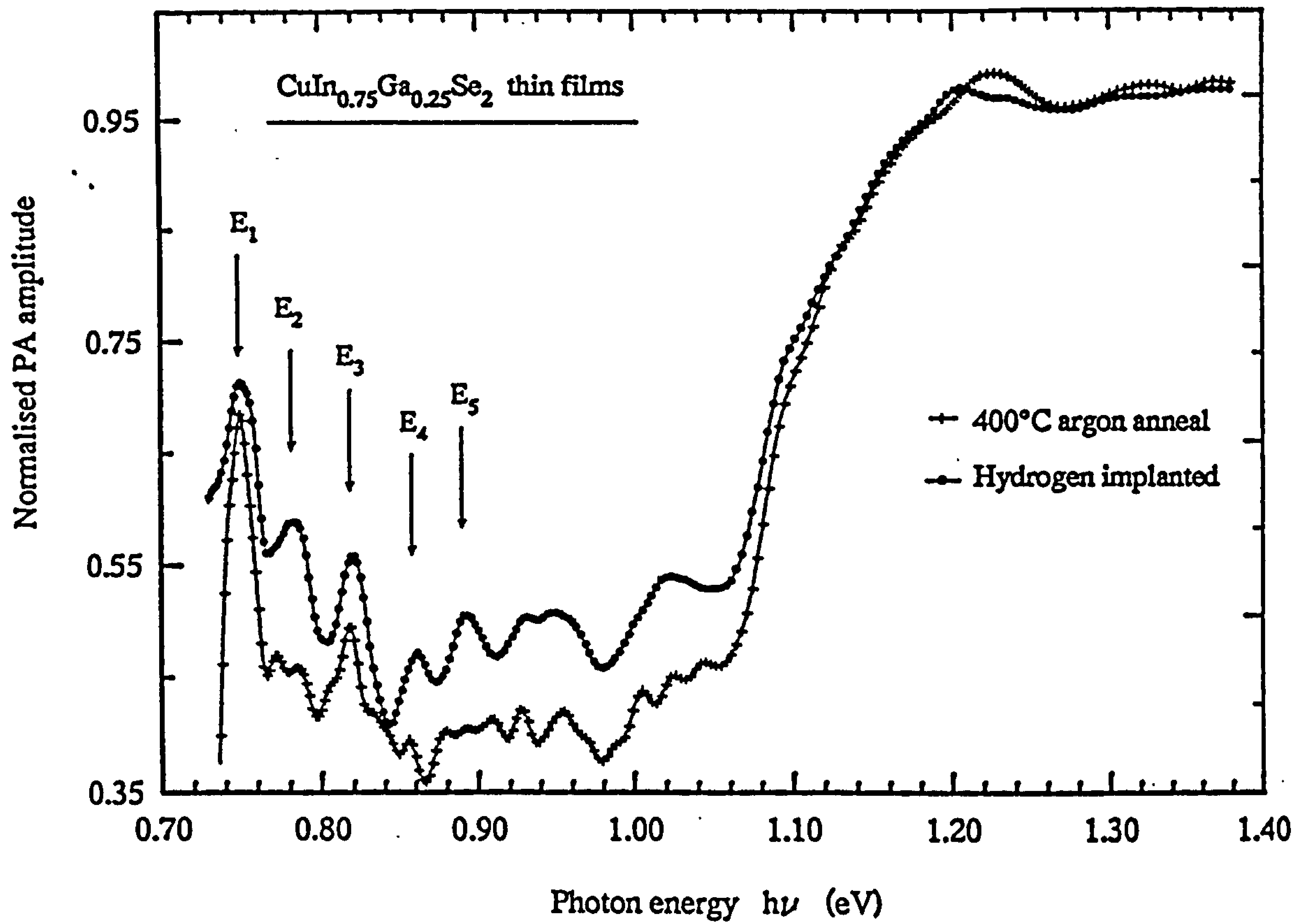


Figure 6.22: Comparative plots of the spectral distribution of CIGS thin films annealed under argon ambient at 400°C and $H^+$ implanted.

Hydrogen has a tendency to interact with other intrinsic or extrinsic defects in semiconductors [248] but, in addition, it can also induce defects [248]. It is well known that all hydrogenation techniques produce some lattice damage [265] which affects the native defect concentrations and thus the electrical and photoelectrical properties. However, post implantation heat treatments can alter these defects. In studying the influence of proton implantation on the electrical properties of p-type CIS single crystals, it has been observed that the implantation induced modifications become thermally unstable at temperatures close to or even below 100°C [266]. It will be interesting to expand this study to ascertain the annealing effect on implanted CIGS films at different temperatures.

## 6.5 Transmission PAS analysis

The conventional methods used to characterise the optical properties of semiconductors are normally based on commercially available spectrophotometers. From there one can get transmission and absorption spectra to observe the behaviour of semiconductor materials in the scanned photon energy range. In the present study, we have tried to use the photoacoustic spectrometer to acquire the transmission spectra. A major advantage of using this approach is the utilisation of the same equipment for both photoacoustic and transmission spectra evaluation.

The basic principle of transmission photoacoustic spectroscopy (TPAS) is quite simple. A gas-microphone type detection cell, containing carbon black powder, is covered by

a suitable window. Thin film or single crystal (<200μm thick) semiconductor material is placed on top of the cell window and exposed to a monochromatic light source, a 400W Xe short arc lamp. The modulated light, after passing through the sample, is absorbed by the carbon black powder. The sample has the effect of filtering out certain wavelengths so that when comparing the spectra obtained from the carbon black with the standard carbon black spectra the missing values of wavelength can be ascertained.

Figure 6.23 shows the TPAS spectra of a CIGS thin film (full line) and that of an un-coated glass slide (dotted line). The spectrum of the glass slide is almost flat within the considered photon energy range. In contrast, the spectra obtained from the thin film sample showed an abrupt transition at around 1.19 eV due to an allowed direct transition between valence and conduction bands. By extrapolating the linear portion of this transition down to the zero level the band edge was found to be 1.196 eV which is identical to that calculated using the standard photoacoustic spectroscopy technique.

In the low photon energy range of CIGS thin film spectra, small peaks are also evident. At present, the nature of these peaks is not clear. However, it can be speculated that these could be due either to an interference effect (usually observed in the routine transmission study) or due to the presence of defect levels. A detailed study of transmission photoacoustic spectroscopy is required to establish the behaviour of semiconductor materials in the low photon energy range.

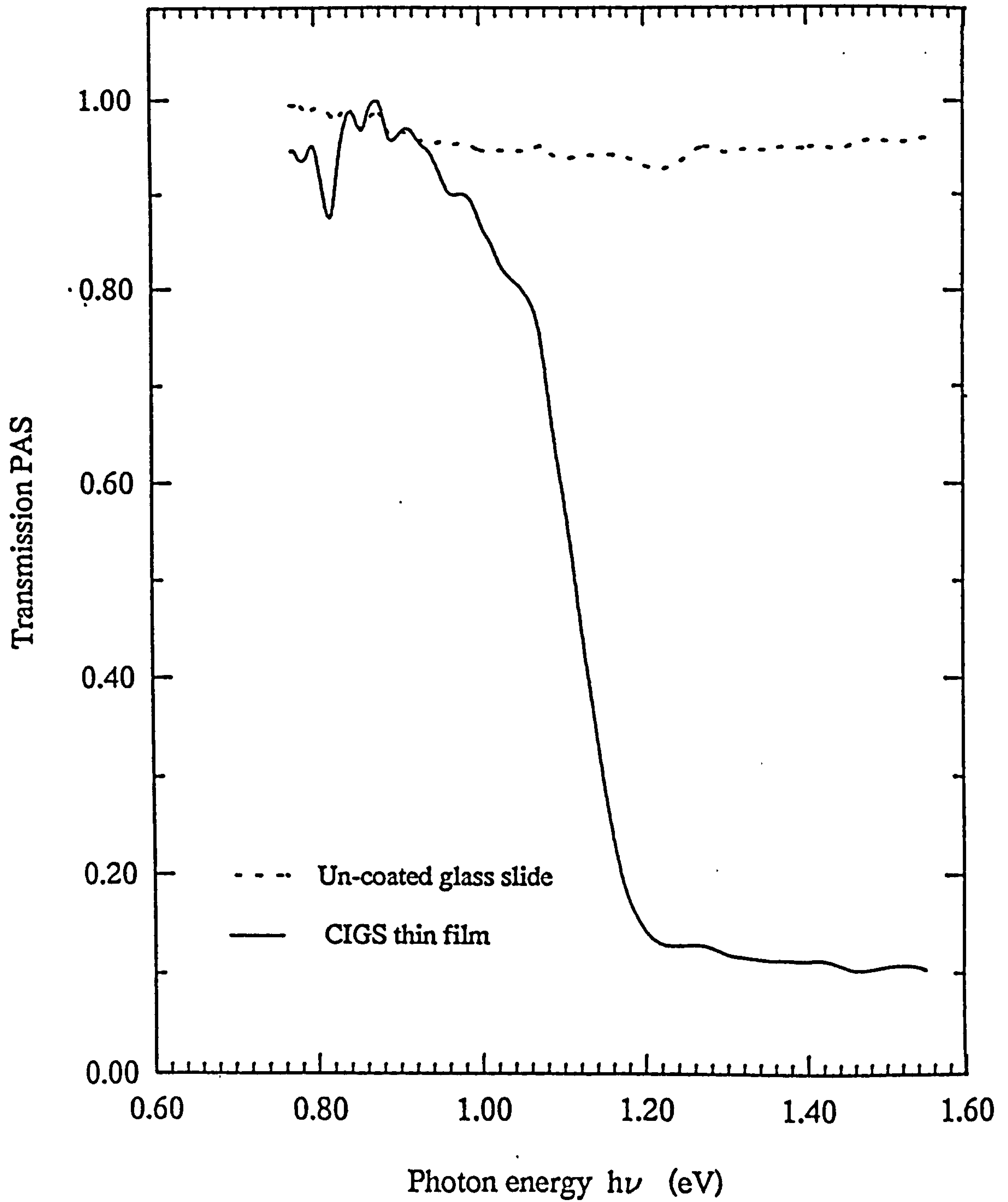


Figure 6.23: Transmission photoacoustic spectra of un-coated glass slide and the as-grown CIGS thin film.

## 6.6 Photoconductivity analysis

It is well established that the properties of CIS are usually determined by the intrinsic defect population [230]. Until recently, optical absorption measurements have constituted the most important means of determining the band structure of semiconductors. Many researchers [53,267,268] have studied the optical properties of copper based ternary compounds near, above and below the fundamental absorption edge. Donor and acceptor states in CIS have been quite widely studied by electrical conductivity [269] and photoluminescence [270,271] techniques. However, very little information is available on photoconductivity investigations for single crystals [271] and thin films [272] of CIS even though this technique is known to be extremely valuable in analysing the mechanisms of photocarrier generation and recombination.

The basic principle of photoconductivity involves the use of light of intensity $I_0$ incident on a material of thickness d with an absorption constant $\alpha$. The intensity of the transmitted light I is given by Beer's law [273]:

$$I = I_0 \exp(-\alpha d) \tag{6.21}$$

The incident light creates photogenerated charge carriers (holes and electrons) which travel towards the contacts. The photo-induced charge carriers can be captured by imperfections in the material which results in transitions associated with intrinsic and extrinsic absorption, capture and recombination and trapping and detrapping. From the photoconductivity spectra, an indication of defect levels can be obtained.

In this section, the results of the optical characterisation of $Cu(In,Ga)Se_2$ both in single crystal and thin film form are reported using the photoconductivity method. The relative photoconductivity of samples was measured between room temperature and 77°K as a function of wavelength using a chopped light source and a lock-in-amplifier. The experimental details are given in section 3.13.

Figure 6.24 represents the photoconductivity spectra of n-type CIS single crystal. It is evident that with increasing the wavelength there are two steep increases in the photoconductivity, these appear between 500 to 700 nm and 850 to 1000 nm respectively. At higher wavelengths, a slow decay of the photoresponse was observed which finally lead to a sharp fall at approximately 1200 nm. In the low wavelength range between 600 and 900 nm, two small peaks A-2 and A-3 were observed at approximately 685 and 783 nm. The energy values corresponding to these peaks (using $E=h\nu=hc/\lambda$) were found to be 1.81 eV and 1.58 eV. Careful examination of the spectra also revealed a very small indication of an A-1 peak at approximately 550 nm (2.25 eV). Similar observations have been reported by Slifkin et al [214] for the n-type CIS single crystals. The energy values are in good agreement to those reported i.e. 1.6, 1.85 and 2.2 eV. Peaks at about 1.6 and 1.9 eV in the photoconductivity spectra of n-type CIS have also been found by Abdinov and Mamedov [274]. This type of spectra has been interpreted [214] as being due to a very thin photosensitive surface layer, and the three additional structures have been ascribed to indirect optical transitions.

These observations were further confirmed from the photoconductivity analysis of another n-type CIS single crystal for which the photoconductivity spectrum is shown in

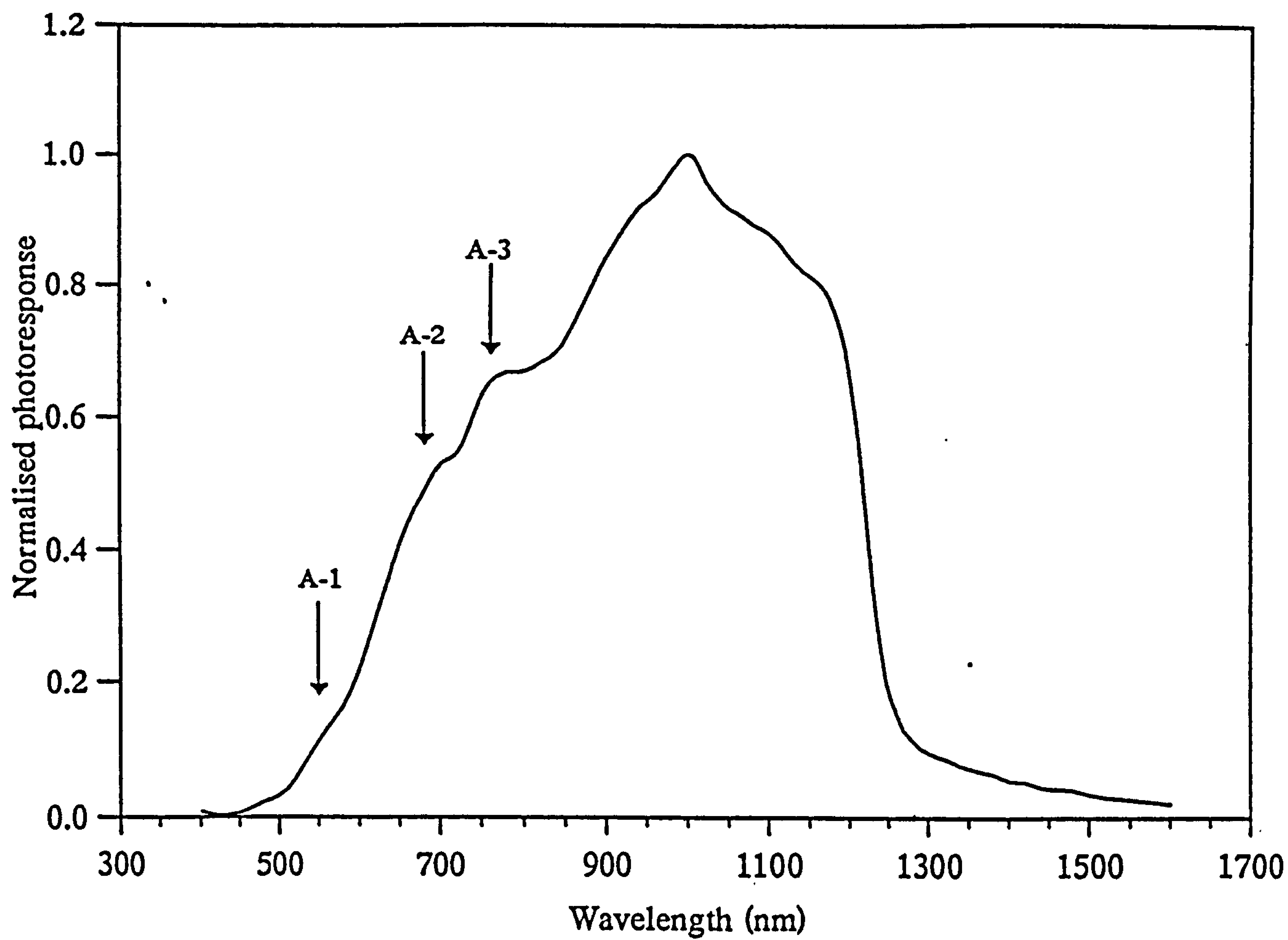


Figure 6.24: Photoconductivity spectrum of n-type CIS single crystal.

figure 6.25. The peaks A-1, A-2 and A-3 at approximately 550 nm, 685 nm and 783 nm respectively are evident. In addition, two extra peaks A-4 and A-5 at around 862 and 1075 nm respectively are also seen. The first three peaks are similar to those observed in the first sample. The nature of the defect level at which these appeared (862 nm) is not completely clear. However, the defect level at 1075 nm (1.15 eV) could be due to selenium vacancies as a similar transition was observed at approximately 1.11 eV [217,275,276] which disappeared when the sample was annealed in selenium vapour.

The spectral dependence of photoconductivity, observed in a p-type CIS single crystal, is shown in figure 6.26. Qualitatively, this spectrum is similar to that observed for the n-type CIS single crystals. Four small peaks A-1, A-2, A-3 and A-4 at wavelength values of approximately 550, 680, 810 and 1020 nm respectively are visible. In addition, a very large and steep peak at approximately 1265 nm (0.98 eV) is also evident. Since the position of this strong peak is very close to the range of the gap energies (0.998 to 1.008 eV) reported for CIS single crystals [190], it is highly likely that this strong peak is due to the fundamental band edge transition of CIS. This was further supported by observations made by Slifkin et al [214] who reported a very similar spectrum of a CIS single crystal annealed under maximum selenium vapour pressure at 600°C for half an hour. The conductivity type of the sample was changed from n to p-type and the observed peaks were attributed to surface effects. Since the position of the photoconductivity peaks are same, it is likely that the origin of the peaks observed in this present work are the same as those reported in the literature [214].

The photoconductivity analysis of thin films was rather difficult. This could be due to

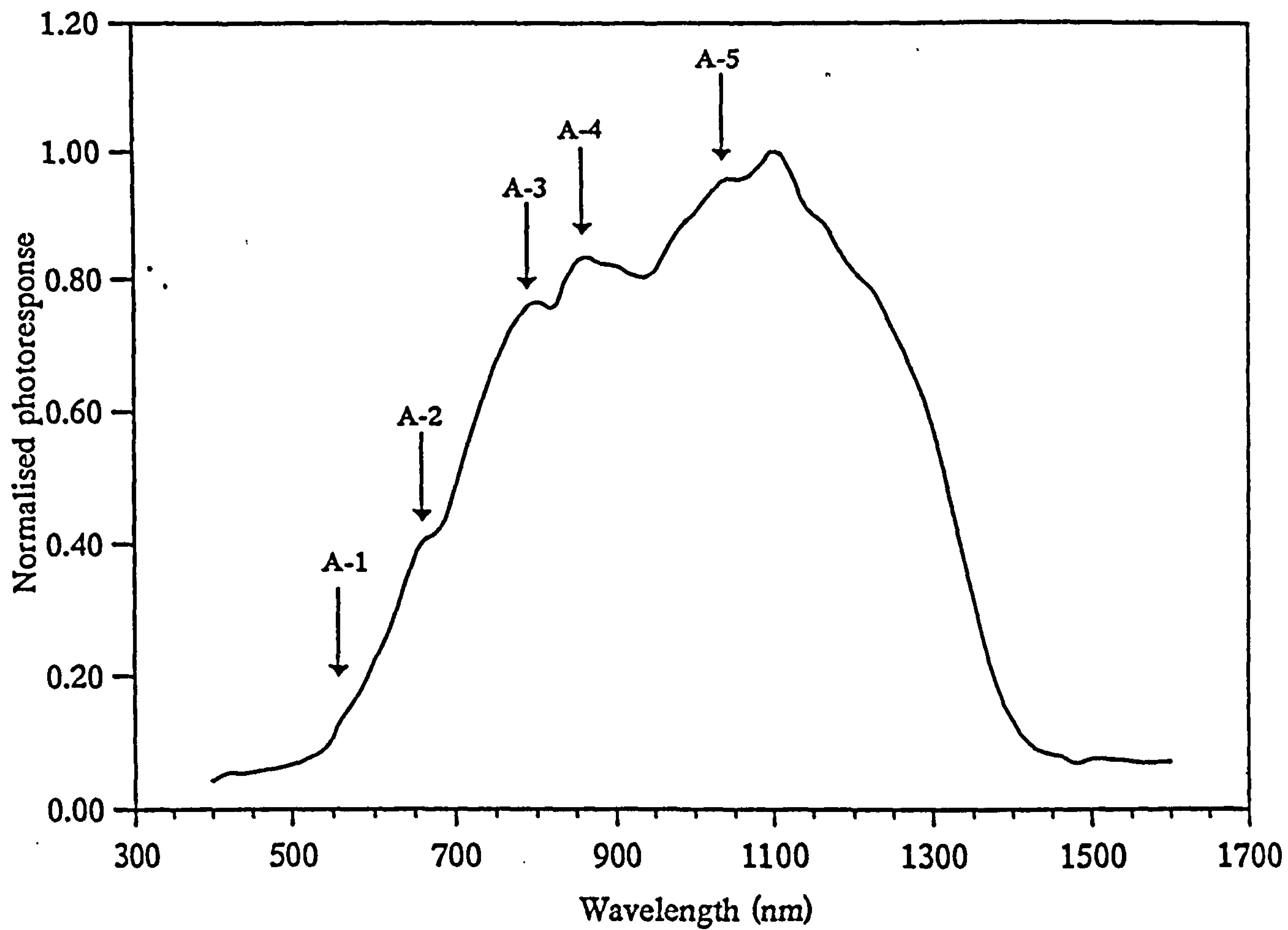


Figure 6.25: Photoconductivity spectrum of n-type CIS single crystal.

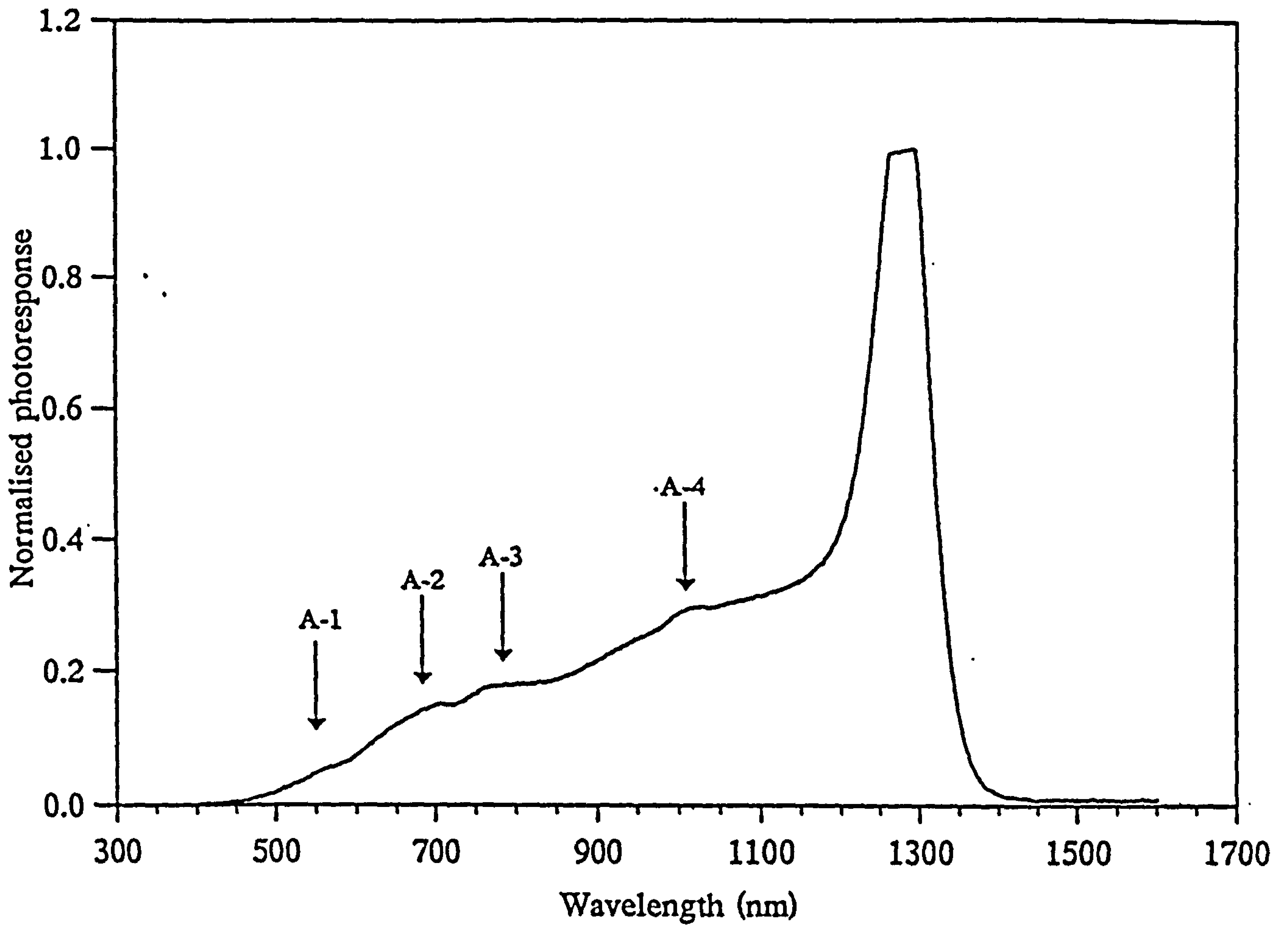


Figure 6.26: Photoconductivity spectrum of p-type CIS single crystal.

a number of reasons including the photosensitivity of the sample, non-uniform thickness and lack of control of experimental technique. In addition, the preparation of ohmic contacts appears to be a major problem in the photoconductivity analysis - non-ohmic contacts can lead to wrong informations in the resultant spectra of thin film and single crystal samples. One can repolish the surface of single crystals if the deposited contacts are non-ohmic, but, this process can not be adopted in the case of thin films.

A representative photoconductivity spectrum of a CIS thin film is shown in figure 6.27. It is clearly evident that the spectral response is much broader when compared to that of single crystals. However, a number of peaks relating to the defect levels associated with structural imperfections and deviations from stoichiometry are visible in the middle of the spectrum. In contrast, a CIGS thin film gave a better photoconductivity spectral response when measured at room temperature, figure 6.28. This spectrum, however, consisted of only two peaks represented by A and B. At higher wavelengths, the tail of the spectrum was extended which indicates the existence of defect levels, capturing and releasing the photo generated charge carriers.

At lower, measurement temperatures, for example 250°K, the extension in the tail of the spectrum was reduced. Further decrease in the measurement temperature again resulted in a steeper tail as indicated in figure 6.29 to 6.31. This suggests that the defect levels which were responsible for the extended tail of the spectrum at higher wavelengths are in-active at lower temperatures. The spectral response of the CIGS film also indicated that the positions and heights of peaks A and B are also affected by the temperature. It can be seen from figures 6.29 to 6.31 that lowering the temperature has resulted in an

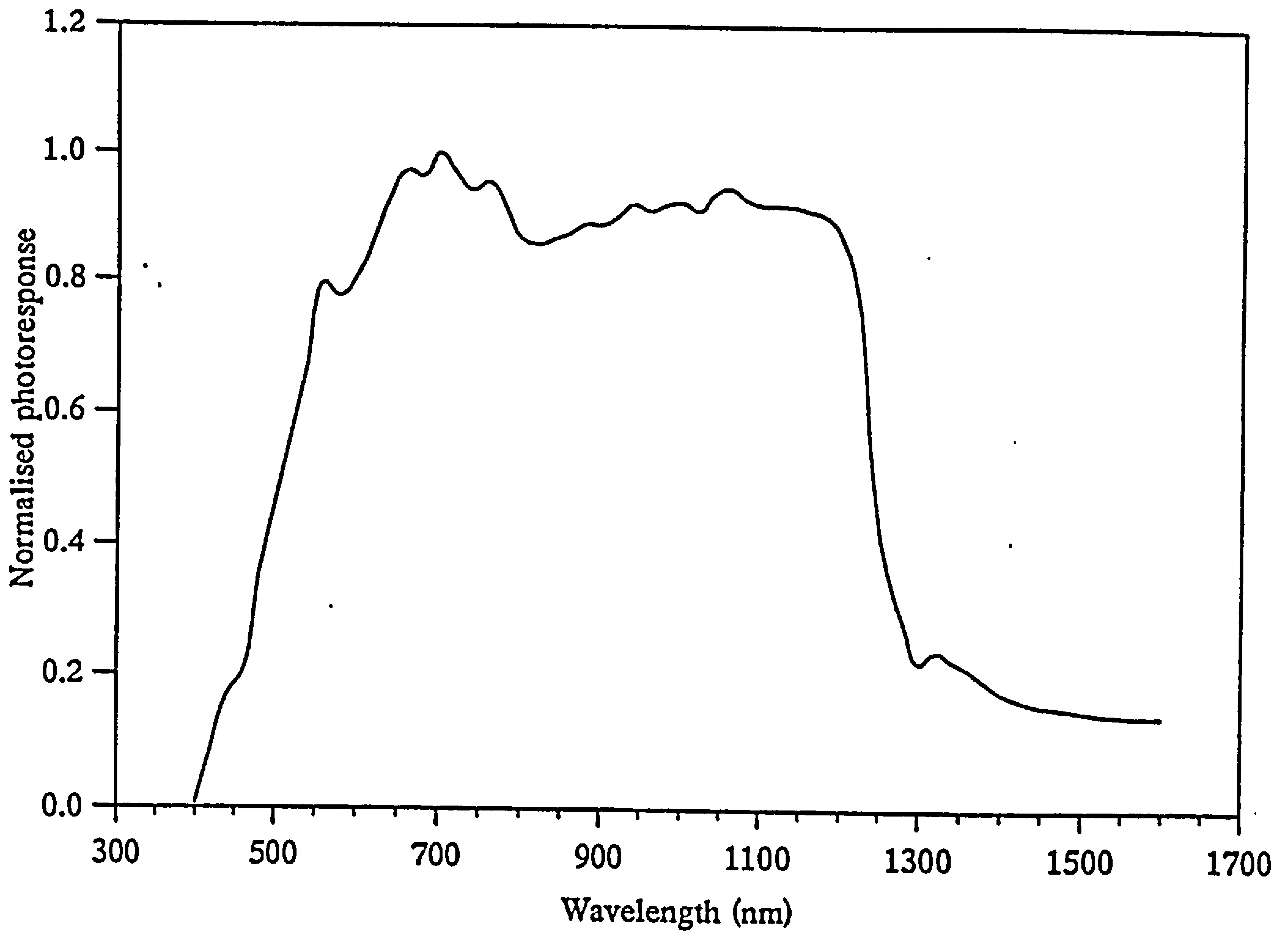


Figure 6.27: Photoconductivity spectrum of p-type CIS thin film.

increase of peak height (peak B). In addition, the peaks are now better resolved (indicated by A1, A2 and B1, B2). The increase in the height of peak B could be due to the reduced extension of the spectrum tail.

During the present work, it was observed that the photoconductivity analysis was limited. This was possibly due to the low power light source (100 W) and/or lack of precise control of the system. The light intensity is probably not high enough to generate the required concentration of photo-carriers. It was therefore decided to explore the use of the photoacoustic spectrometer for the photoconductivity analysis since the light source used in photoacoustic spectrometer was more intense (400 W). The initial study of the photoconductivity analysis on a CIGS single crystal sample is shown in figure 6.32. The spectrum was recorded at room temperature in the photon energy range between 0.95 eV to 1.55 eV. The band gap of the 25% CIGS alloy can be seen at around 1.16 eV. At higher photon energy values the spectrum indicated few peaks which could be the characteristics of the sample or due to the calibration of the system. In order to confirm the origin of these peaks, more analysis is required.

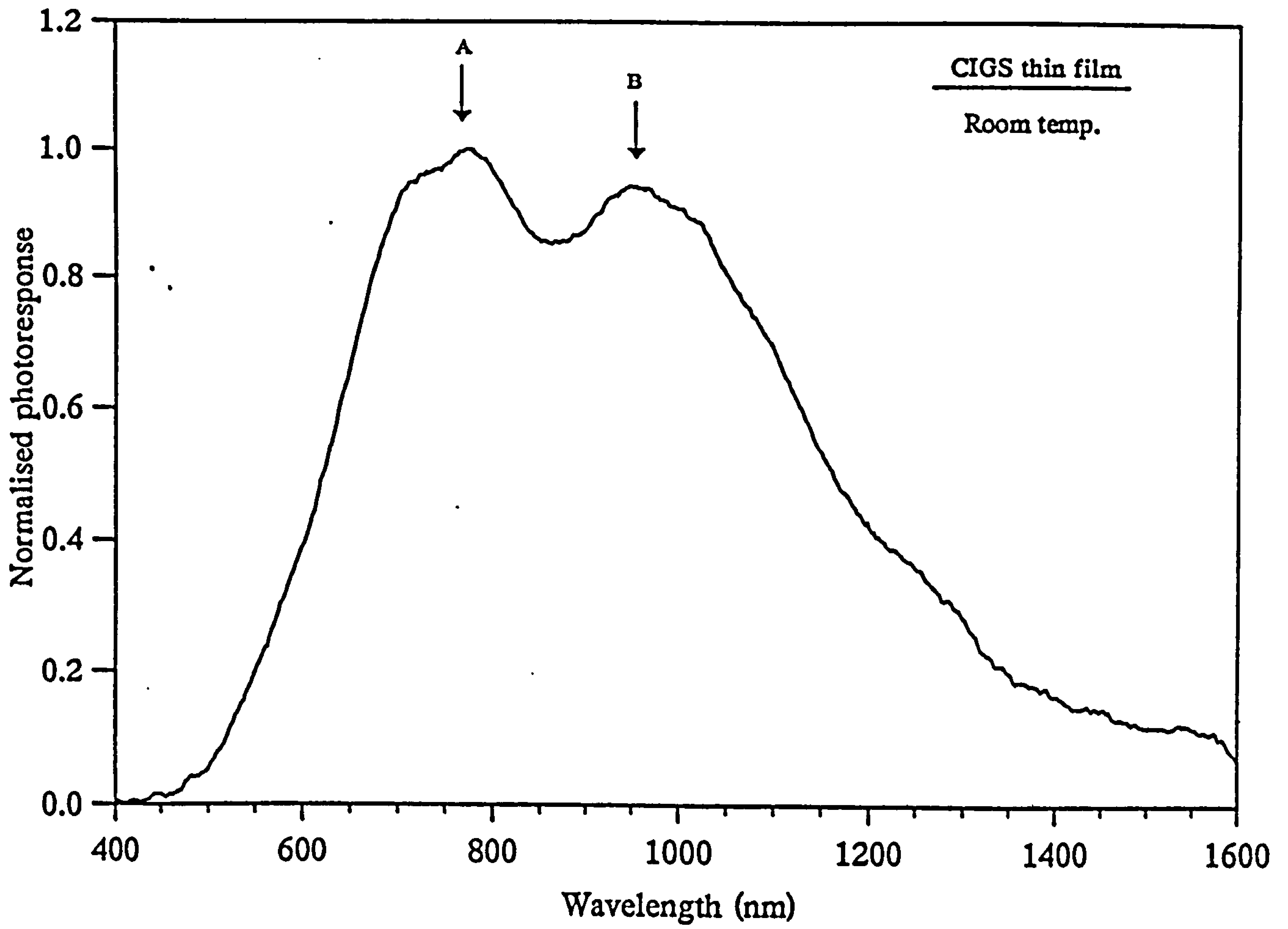


Figure 6.28: Photoconductivity spectrum of p-type CIGS thin film measured at room temperature.

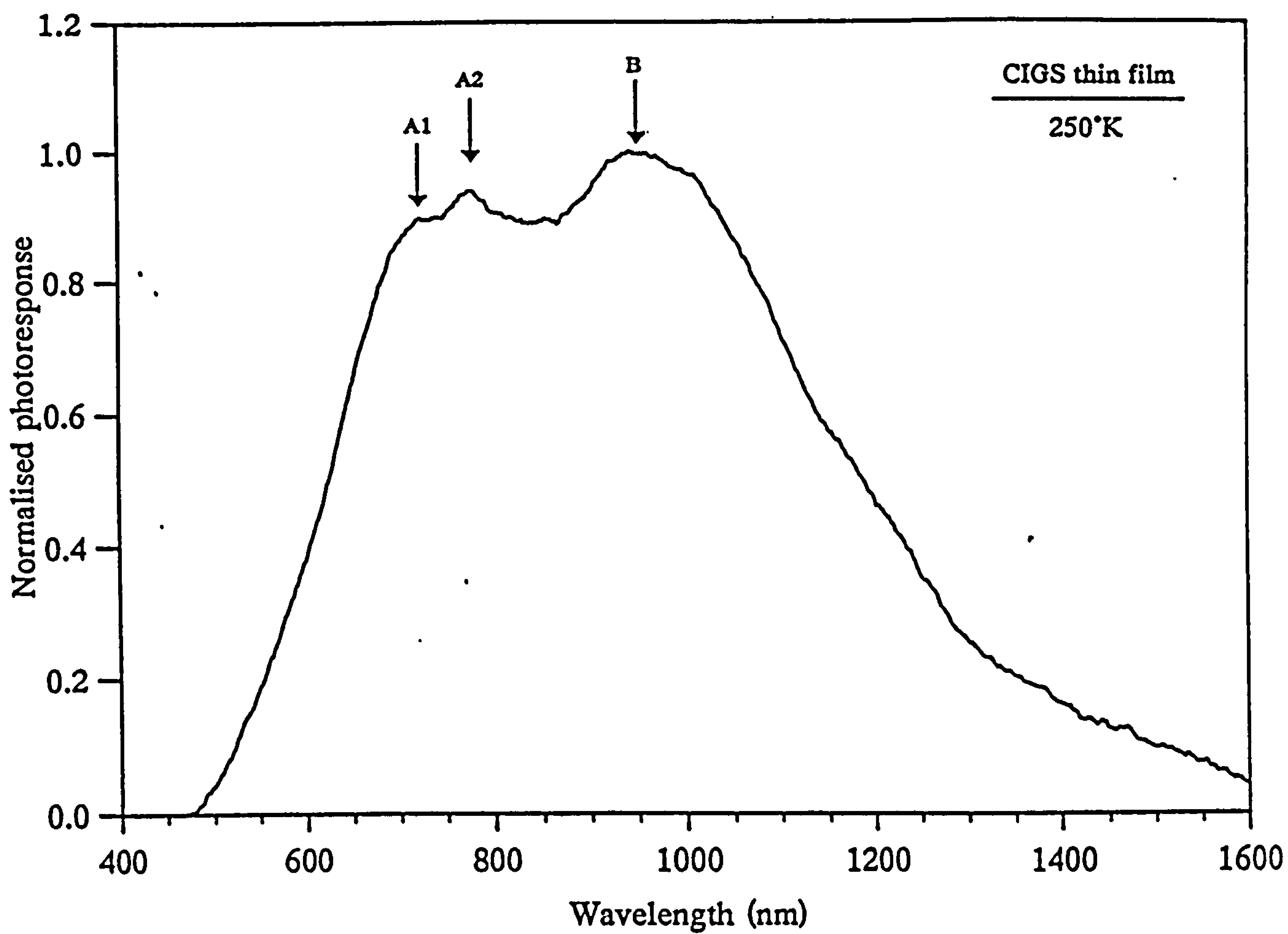


Figure 6.29: Photoconductivity spectrum of p-type CIGS thin film measured at 250°K.

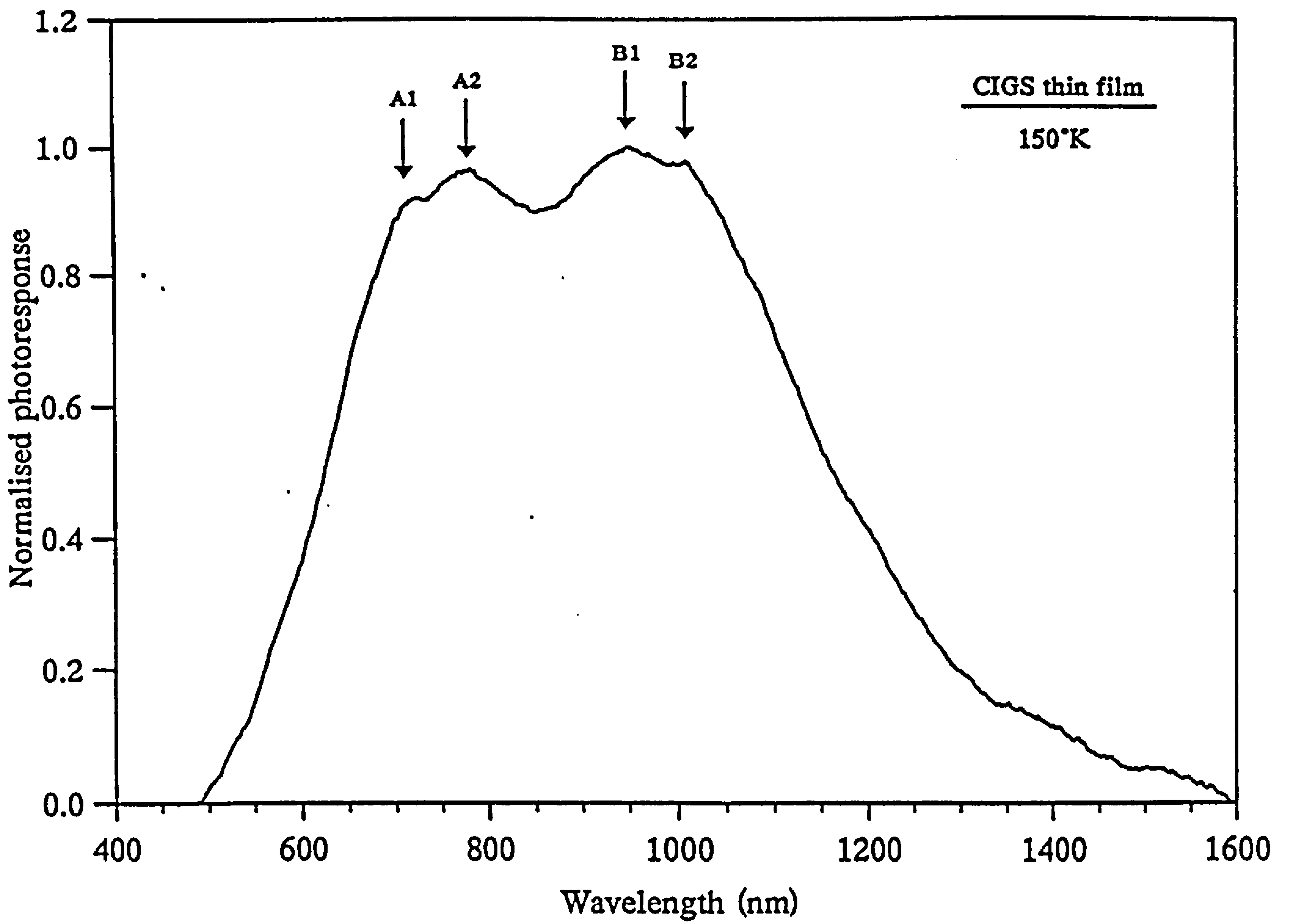


Figure 6.30: Photoconductivity spectrum of p-type CIGS thin film measured at 150°K.

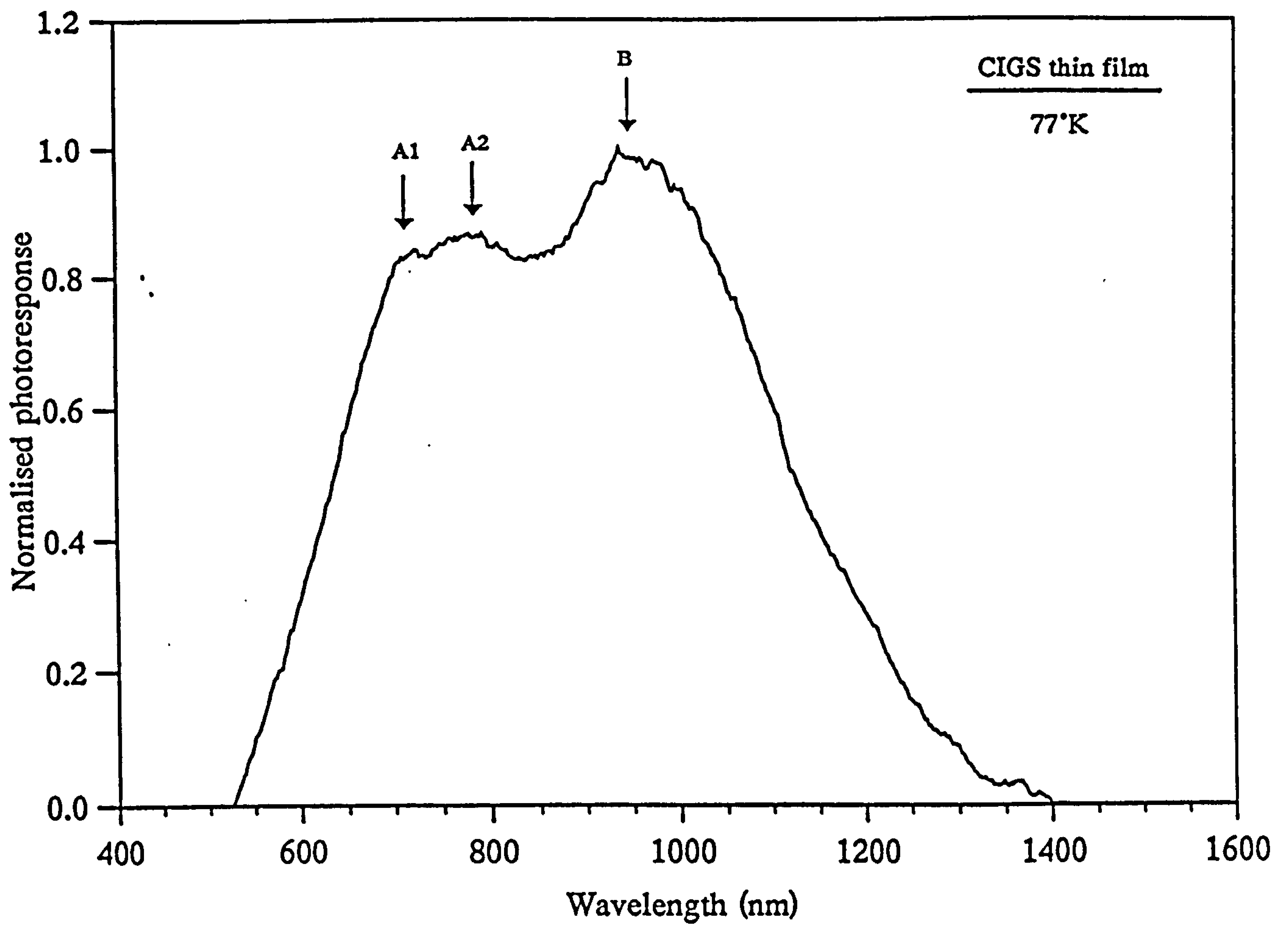


Figure 6.31: Photoconductivity spectrum of p-type CIGS thin film measured at 77°K.

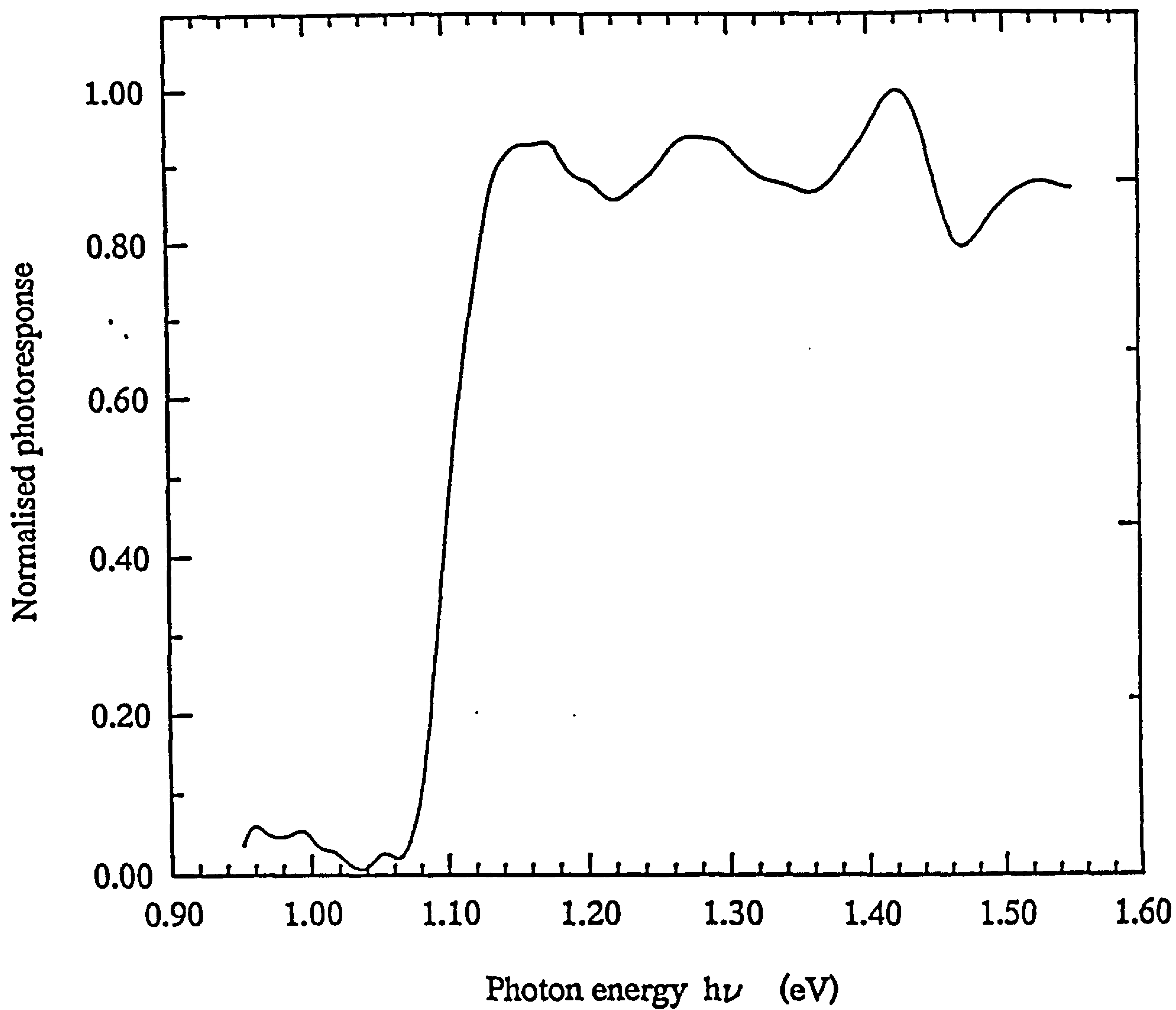


Figure 6.32: Photoconductivity spectral distribution of CIGS single crystal using the photoacoustic spectrometer.

## 6.7 Conclusions

A gas-microphone type photoacoustic spectrometer has been used to investigate the optical properties of both CIS and CIGS thin films in the photon energy range $h\nu = 0.7$ to 3.1 eV. The observed results have shown good agreement with those reported earlier in the literature. It has been demonstrated that PAS is a contact-less, non-destructive, direct, fast and reliable technique for the characterisation of several intrinsic/extrinsic defect levels. In the low photon energy range five major defect levels have been identified which act as either donor or acceptor states. However, in the case of CIGS thin films, more defect states were observed; for these the electrical activity was difficult to assign due to the lack of data regarding the optical properties of this semiconducting compound.

The effect of annealing (under various sets of conditions) on the optical properties of CIS and CIGS have also been investigated using photoacoustic spectrometer. It was noticed that, for the as-grown samples, the fundamental band edge was dominated by defect populations which were only removed by annealing in selenium. However, further annealing under argon and a 9:1 mixture of $N_2$:$H_2$ ambient has shown the formation of a defect level near the fundamental band edge and it is believed that this level was responsible for the increased absorption in the low photon energy range. Initial studies of the effect of ion-implantation and laser annealing on the optical properties of CIGS and CIS films and the use of photoacoustic spectrometer for the transmission measurements have also been described.

Photoconductivity analysis has been carried out on a number of n and p-type samples including CIS and 25% gallium containing CIGS alloys both in single crystal and thin film forms. The observed defect levels have been compared with those reported in the literature. The photoconductivity analysis of thin film samples was found to be difficult when compared to single crystals. The use of a photoacoustic spectrometer has also been explored for photoconductivity analysis.

# Chapter 7

## Summary and future work

## Recommendations

## 7.1 Conclusions

In recent years rapid progress has been made into the research and development of polycrystalline thin film solar cells. This current work forms part of this research and concentrates on the impact of both the deposition and annealing parameters on the electro/optical properties of thin film materials based on copper ternary and multinary compounds. The main objectives of this present work were: to develop a reproducible process for the deposition of high quality $Cu(In_{1-x},Ga_x)Se_2$ thin films by a thermal evaporation process; to investigate various annealing regimes; to develop optical thin film characterisation techniques such as photoconductivity and photoacoustic spectroscopy; and to investigate the relation between the deposition/annealing parameters and the thin film properties.

An improved understanding has been gained of the thin film deposition processes essential to the production of high quality materials for photovoltaic applications. This has led to the design of a new source feed mechanism for controlled film deposition by flash evaporation. Reproducible films of both copper indium diselenide (CIS) and copper indium/gallium diselenide (CIGS) have been deposited, over a range of substrate temperatures, for subsequent evaluation. Various annealing regimes have been investigated in order to produce films with the desired properties. Analysis of both the as-grown and annealed films has been carried out using Rutherford backscattering spectroscopy (RBS), energy dispersive x-ray analysis (EDAX), scanning electron microscopy (SEM), x-ray fluorescence (XRF), x-ray diffraction (XRD), photoacoustic spectroscopy (PAS), photoconductivity and the standard electrical techniques such as

four point probe for resistivity evaluation, and thermal probe for conductivity type etc.

Initially, a basic bell-jar/vacuum system apparatus was completely overhauled and a flash evaporation unit designed. This included both source and substrate temperature measurement facilities, a motorised vibratory hopper for the continuous and controlled feeding of the pre-reacted starting material and the design of the evaporation source. Thin films of CIS and $CuIn_{0.75}Ga_{0.25}Se_2$ were deposited onto glass substrates using the newly developed system to ascertain the optimum conditions for the production of pin hole free thin films. These conditions were found to be: a background pressure of $10^{-6}$ mbar, a source to substrate distance of 12 cm, the use of a twin chimney type molybdenum source, and source material with a grain size between 150 and 250μm.

Thin films deposited under these optimised growth conditions displayed a reproducible composition as measured by the XRF, EDAX and RBS techniques. All the as-grown films had a slight selenium deficiency and a small indium excess. The copper and gallium contents were found to be close to that of the starting material. It was observed that, independent of substrate temperature, the as-grown films had a preferred <112> orientation with no detectable secondary phases. However, the intensity of the <112> peak was found to be strongly dependent on the growth temperature, as was the film morphology. In general, films prepared at low substrate temperatures contained small grains separated by relatively large voids; whereas, at higher substrate temperatures the films consisted of larger grains with fewer, smaller voids. This was also confirmed using Raman analysis.

The effect of post-deposition annealing on the structural, compositional and electro/optical properties was investigated. Several sets of annealing conditions were studied which involved: the use of various annealing ambients such as vacuum, selenium, argon and forming gas, together with the effect of varying both the temperature and the annealing times. The most marked improvements in the composition, optical, structural and electrical properties resulted from annealing in selenium at 300°C for 2 hours. Whereas annealing in either argon or forming gas at 400°C for ½ hour resulted in a major improvement in the morphology. A two stage annealing process was finally adopted to achieve improvements in film properties resulting from both these individual annealing stages.

Photoconductivity and photoacoustic spectroscopy were used to investigate the band gap, absorption coefficients and defect levels in thin films and these results were compared with corresponding data from single crystal samples. The apparatus and analysis procedures for both techniques required extensive development before they could be applied to the analysis of thin films samples. Existing theoretical models for the determination of the absorption coefficient $\alpha$ for single crystals were extended for thin films by considering the effects of multiple reflections and thermal diffusion lengths of the samples. The band gap of CIS and CIGS thin films was established to be in the range of 0.996-1.015±0.006 eV and 1.86-1.96±0.006 eV respectively. The maximum absorption coefficient (at or near the band edge) was found to be in the range $10^4$ - $10^5$ $cm^{-1}$. The most notable information obtained from these techniques related to defect levels, both shallow and deep. Five major deep defect levels were located at low photon energies in thin film CIS at 263, 235, 198, 158 and 128 meV. These levels coincided

with deep levels found in single crystal CIS samples, and were associated with either impurity-to-conduction band or valence band-to-impurity transitions. In the CIGS thin film samples the same five deep levels were observed along with two or three additional shallow levels ascribed to the introduction of gallium into the crystal lattice. After application of the two stage annealing process, changes in photoacoustic spectra were observed and these have been related to changes in composition and structure.

This work has reported the deposition, annealing and analysis of CIS and CIGS thin films. The properties of the optimised films were found to correspond with those of single crystals prepared in our laboratories. These characteristics demonstrated parameters which compared well with the important parameters necessary for the production of high efficiency devices. They include low resistivity, high absorption coefficient and the desired bandgap value.

## 7.2 Future recommendations

1. The design of the flash evaporation system resulted in the production of good quality, reproducible films. However, it is believed that a major improvement could be made by the introduction of a thickness monitor to allow the precise control of the deposition rate and film thickness.

2. The present work revealed that the crystal structure, morphology and compositional homogeneity improved with increased substrate temperature. This

temperature was limited to 300°C and therefore further investigations into the effect of temperature on film quality were limited. The redesign of the substrate heater to allow higher substrate temperatures would alleviate this problem.

3. Preliminary work carried out on the study of films grown onto crystalline substrates, namely silicon, have revealed that after controlled annealing, the films re-ordered into a larger and columnar polycrystalline grains. Further studies are needed to ascertain the mechanisms associated with this observed effect so that this information can be used to adjust the deposition parameters in order to grow films directly of this form. The growth of films on other crystalline substrates should also be investigated.

4. It was observed that the annealing of the as-grown films by a broad beam Excimer laser results in a dramatic reduction in the resistivity. Photoacoustic spectroscopy (PAS) also revealed that the defect structure of the laser annealed films was significantly improved and was comparable with results obtained from single crystal samples. This has been shown to be an extremely reproducible process and more work is certainly required to understand the mechanisms associated with these observed effects.

5. Very little work has been reported in the literature on the use of PAS for the characterisation of ion-implanted thin film semiconductors. It would be useful to implant thin films of both CIS and CIGS with different important ions, such as oxygen and hydrogen, at various energies and implantation doses to relate any consequent changes in electrical and optical activity with the nature and degree of defect levels using the

PAS technique.

6. The most commonly used method for the characterisation of the optical properties of semiconductors utilizes standard transmission and absorption techniques. Initial results have been obtained from a modified photoacoustic spectrometer, in transmission mode, which has indicated that this technique can produce excellent, sensitive spectra. It makes use of an almost perfect 'black body' detector with virtually a flat response over a wide spectral range and has been shown to be effective for both thick ($\approx$ 200 μm) and thin samples ($\approx$ 0.2 μm). This exciting work needs to be extended, with the construction of a dedicated transmission mode PAS to look at a range of semiconductor materials.

7. Photoacoustic spectroscopy, with a gas-microphone detector, is effective with powders and solids having large surface/volume ratios because of the significant heat flow from the sample to the gas. However, it is generally not considered suitable for fast measurements (requiring nanosecond resolution). The system is not only limited by the speed of sound in the sample and gas, but even more so by the slow response of the microphone (<20 μsec.). It has also been observed that during the application of photoacoustic spectroscopy to the analysis of different semiconducting materials, including silicon single crystal wafers and GaAs, that the main limitation in the characterisation was (particularly at higher chopping frequencies) the signal to noise ratio. This was slightly improved after reducing the cell volume. It is felt that the speed of response could be improved and the signal to noise ratio reduced if a piezoelectric detector are incorporated into the apparatus. Further developments could involve the use

of higher chopping frequencies for surface analysis and the use of a better monochromator with an extended range.

# References

References


1. D.M. Chapin, C.S. Fuller and G.L. Pearson, J. Appl. Phys., **25** (1954) 676
2. D.C. Reynolds, G. Leies, L.L. Antes and R.E. Marburger, Phys. Rev., **96** (1954) 533
3. W.H. Bloss, F. Pfisterer and H.W. Schock: in Advances in Solar Energy, Vol. 4, Ed. by K.W. Boer (Plenum Press), 1988
4. G.A. Landis and A.F. Hepp, Proc. European Space Power Conf., 2-6 Sept. Florence, Italy (1991) pp.517
5. R.M. Burgess, W.S. Chen, W.E. Devaney, D.H. Doyle, N.P. Kim and B.J. Stanbery, 20th IEEE PVSC (IEEE, Las Vegas, 1987) 1988, pp.909
6. C. Jennings, 20th IEEE PVSC (IEEE, Las Vegas, 1987) 1988, pp.1225
7. K. Zweibel, 23rd Intersociety Energy Conversion Engineering Conf. Denver, CO, USA, Vol. 3 (1988) pp.97
8. T. Tiedje, E. Yablonovitch, G.D. Cody and B.G. Brooks, IEEE Trans, Electron Devices **ED-31** (1984) 711
9. M.A. Green, Ed., "Solar Cells: Operating Principles, Technology and System Applications", Prentice Hall Inc., 1982
10. T. Markvart, J. Material Science: Materials in Electronics, **1** (1990) 1
11. A.M. Barnett, R.B. Hall and J.A. Rand, MRS Bulletin, (1993) pp.33
12. R.C. Chittick, J. Electrochem. Soc., **116** (1969) 77
13. W.E Spear and P.G. Le Comber, J.Non-Cryst. Solids, **8-10** (1972) 727
14. M. Garozzo, Ceramics International, **19** (1993) 287

15. A.L. Fahrenbruch and R.H. Bube: Fundamentals of Solar Cells, (Academic Press) 1983

16. R. Hill and J.D. Meakin: in Current Topics in Photovoltaics, Ed. by J. Coutts and J.D. Meakin (Academic Press, London. 1985)

17. H.W. Schock, Proc. International Symposium on Polycrystalline Semiconductors and Grain Boundaries, Eds. J.H. Werner, J.H. Moller and H.P. Strunk, Springer-Verlag, Berlin, Heidelberg (1989) pp.246

18. B.M. Basol, Proc. 21st IEEE Photovoltaic Specialists Conf., (1990) pp.588

19. W.H. Bloss and H.W. Schock, 4th International PVSEC Conf., Feb. 14-17, 1989, Sydney, NSW, Australia, 1, pp.39 and the references therein.

20. H. Sobotta, H. Neumann, V. Riede, G. Kuhn, J. Seltmann and D. Oppermann, Phys. Stat. Solidi (a) **60** (1980) 531

21. T. Nakadat, M. Nishioka and A. Kunioka, Proc. 4th. Int. PVSEC, Sydeny, NSW, Australia, (1989) pp.371

22. J. Hedström, H. Ohlesén, M. Bodegård, A. Kylner, L.Stolt, D Hariskos, M. Ruckh and H.W. Schock, Proc. 23rd IEEE Photovol. Spec. Conf. (Louisville: IEEE) 1993, pp.364

23. W. Horig, H. Neumann, B. Schumann and G. Kuhn, Phys. Stat. Sol. (b) **85** (1978) K57

24. H.W. Schock, Proc. 7th E.C. Photovol. Solar Energy Conf., (Sevilla 1986), Reidel, Dordrecht 1987, pp.465

25. A. Zegadi, M.A. Slifkin, M. Djamin, A.E. Hill and R.D. Tomlinson, Phys. Stat. Sol. (a) **133** (1992) 533

26. H. Hahn, G. Frank, W. Klinger, A.D. Meyer and G. Storger, Z Anorg Allg Chem, **271** (1953) 153

27. R.D. Tomlinson, Proc. Material Research Society, (1987) 177

28. R.D. Tomlinson, Conf. Proc. 8th Ternary & Multinary Compounds, Kishinev, USSR, (1990) pp.??

29. J.L. Shay and J.H. Wernick, Ternary Chalcopyrite Semiconductors: Growth, Electronic Properties and Applications (Pergamon, New York, 1975)

30. J. Parkes, R.D. Tomlinson and M.J. Hampshire, J. Appl. Cryst., **6** (1973) 414

31. M. Gorska, R. Beaulieu, J.J. Loferski and B. Roessler, Thin Solid Films, **67** (1980) 341

32. H. Neumann and G. Kuhn, J. Less Common Metals, **155** (1989) L13

33. S.S. Strelchenko, S. Bondar, A.D. Molodyk, L.I. Berger and A.E. Balanevskaya, Izv. Akad. Nauk SSSR, Neorg. Mater., **5** (1969) 593

34. I.S. Palatnik and E.I. Rogacheva, Sov, Phys. Crystallogr., **11** (1966) 191

35. I.S. Platnik and E.I. Rogacheva, Sov. Phys. Doklady, 12, (1967) 503

36. A. Rockett and R.W. Birkmire., EPRI Res. Proj. 2702-1, 1989

37. T.F. Ciszek, J. Cryst. Growth, **75** (1986) 61

38. R.C. Weast, Ed., CRC Handbook of Chemistry and Physics, 60th Edition (CRC Press, Boca Raton, Florida, 1980)

39. B.R. Pamplin and R.S. Fiegelson, Thin Solid Films, **60** (1979) 141

40. S. Endo, T. Irie and H. Nakanishi, Solar Cells, **16** (1986) 1

41. S.M. Wasim and G.P. Sanches, Phys. Stat. Sol. (a), **59** (1980) k175

42. H. Neumann, Solar Cells, **16** (1986) 399

43. H. Neumann, Solar Cells, **16** (1986) 317

44. M. Turowski, M.K. Kelly, G. Margaritondo and R.D. Tomlinson, Appl. Phys. Letts., 44 (1984) 768

45. H.J.V. Bardeleber and R.D. Tomlinson, J. Phys. Chem., 13 (1980) L1097

46. J.D. Meakin, Status of $CuInSe_2$ Solar Cells, Institute of Energy Conversion, University of Delaware, (1985)

47. S.M. Wasim, Solar Cells, 16 (1986) 289

48. D. Hanemann, Critical Reviews in Solid State and Materials Sciences, 14 (1988) 377

49. L.Y. Sun, L.L. Kazmerski, A.H. Clark, P.J. Ireland and D.W. Morton, J. Vac. Sci. & Technol., 15 (1978) 265

50. G. Salviati and D. Seuret, Thin Solid Films, 104 (1983) L75

51. H. Neumann, B. Perlt, N.A.K. Abdul-Hussain, R.D. Tomlinson and A.E. Hill, Cryst. Res. & Technol., 17 (1982) 469

52. W. Horig, H. Neumann and H. Sobotta, Thin Solid Films, 48 (1978) 67

53. O.P. Agnihotri, P.R. Ram, R. Thangarag, A.K. Sharma and A. Raturi, Thin Solid Films, 102 (1983) 291

54. H. Neumann, B. Perlt, W. Horig and G. Kuhn, Solar Cells, 16 (1986) ??

55. J.L. Shay, B. Tell, H.M. Kasper and L.M. Schiavone, Phys. Rev., (b), 7 (1973) 4485

56. L.L. Kazmerski and C.C. Sheih, Thin Solid Films, 41 (1977) 35

57. E. Elliot, R.D. Tomlinson, J. Parkes and M.J. Hampshire, Thin Solid Films, 20 (1974) S25

58. B. Schumann, H. Neumann, E. Nowak and G. Kuhn, Cryst. Res. & Technol., 16 (1981) 675

59. H. Neumann, Cryst. Res. & Technol., 18 (1983) 665

60. N. Romeo, V. Canevari, G. Sberveglieri, A. Bosio and L. Zanotti, Solar Cells, 16 (1986) 155

61. R.D. Pachori, A. Banerjee and K.L. Chopra, Bull. Mater. Sci., 8 (1986) 291

62. R.D. Tomlinson, D. Omezi, J. Parkes and M.J. Hampshire, Thin Solid Films, 64 (1979) L3

63. H. Neumann, E. Nowak, B. Schumann and G. Kuhn, Thin Solid Films, 74 (1980) 197

64. D. Haneman, S.N. Sahu and R.D.L. Kristensen, Thin Solid Films, 163 (1988) 167

65. H.J. Hobler, R. Flagmeyer and B. Schumann, Cryst. Res. & Technol., 18 (1983) 61

66. R. Durny, A.E. Hill and R.D. Tomlinson, Thin Solid Films, 69 (1980) L11

67. N. Romeo, V. Canevari, G. Sberveglieri, O. Vigil and L. Zanotti, Solar Energy Materials, 3 (1980) 367

68. A. Nursalad, N. Romeo, G. Sberveglieri, O. Vigil and L. Zanotti, Mater. Chem. 4 (1979) 549

69. L.L. Kazmerski, M.S. Ayyagari, F.R. White, and G.A. Sanborn, J. Vac. Sci. Technol., 13 (1976) 139

70. H.S. Soliman, M.M. El-nahas, O. Jamaoum and K.A. Mady, J. Mater. Sci., 23 (1988) 4071

71. S. Isomura, A. Nagamatsu, K. Shinohara and T. Aono, Solar Cells, 16 (1986) 143

72. R. Janam and O.N. Srivastava, Cryst. Res. & Technol., 18 (1983) 1475

73. A.F. Fray and P. Lloyd, Thin Solid Films, 58 (1979) 29

74. R.A. Mickelsen, B.J. Stanbery, J.E. Avery, W.S. Chen and W.E. Devaney, Proc. 19th IEEE Photovol. Spec. Conf., (IEEE, New York 1987] pp.1285

75. N.G. Dhere, M.C. Lourenco, R.G. Dhere and L.L. Kazmerski, Solar Cells, 16 (1986) 369

76. E.R. Don, R. Hill and G.J. Russell, Solar Cells, 16 (1986) 131

77. M. Varela, E. Bertran, J. Esteve and J.L. Morenza, Thin Solid Films, 130 (1985) 155

78. J. Szot and D. Haneman, Sol. Energy Mater., 11 (1984) 289

79. J. Piekoszewski, J.J. Loferski, R. Beaulieu, J. Beall, B. Roessler and J. Shewchun, Solar Energy Mater., 2 (1980) 363

80. A.N.Y. Samaan, A.K. Abdul-Hussein, R.D. Tomlinson, A.E. Hill and D.G. Armour, Jpn. J. Appl. Phys., Suppl. 19-3 (1980) 15

81. S.W. Krishnaswamy, A.S. Manucha and J.R. Szedon, J. Vac. Sci & Technol., 1 (1983) 510

82. J.A. Thornton, Proc. 6th Annu. Review meet. on Photovoltaic Advanced R & D, oct. 1984, Seri/cp-211-2507, Solar Energy Research Institute, Golden, Co., 53

83. J. Piekoszweski, J.J. Loferski, R. Beaulieu, J. Beall, B. Roessler and J. Shewchun, Proc. 14th IEEE Photovoltaic Spec. Conf., (1980) pp.980

84. F.R. White, A.H. Clark and M.C. Graf, J. Appl. Phys., 50 (1979) 544

85. S.P. Grindle, A.H. Clark, S. Rezaie-serej, E. Falconer and J. Mcneily, J. Appl. Phys., 51 (1980) 5464

86. B. Schumann, A. Tempel and G. Kuhn, Solar Cells, 16 (1986) 43

87. C.Y. Huang, S.M. Morse, A.H. Clark and L.L. Kazmerski, Solar Cells, 6 (1982) 191

88. M. Gorska, R. Beaulieu, J.J. Loferski, B. Roessler and J. Beall, Solar Energy Mater., 2 (1980) 343

89. B.R. Pamplin and R.S. Fiegelson, Thin Solid Films, 60 (1979) 141

90. C.W. Bates, K.F. Nelson, S.A. Raza, J.B. Mooney, J.M. Recktenwald, I. Macintosh and R. Lamoreaux, Thin Solid Films, 88 (1982) 279

91. C.W. Bates, Jr., M. Uekita, K.F. Nelson, C.R. Abernathy and J.B. Mooney, App. Phys. Lett., 43 (1983) 851

92. A. Vervaet, M. Burgelman, I. Clemminck and J. Capon, Proc. 9th EC PV. Sol. Energy Conf., Freiburg, Fed. Rep. Germany, (1989) pp.480

93. N. Khare, G. Razzini and P.L. Bicelli, Thin Solid Films, 186 (1990) 113

94. H. Oumous, A. Knowles, M.H. Badawi, M.J. Carter and R. Hill, Proc. 9th EC. PV. Sol. Energy Conf., Freiburg, Fed. Rep. Germany, (1989) pp.153

95. T. Walter, M.J. Carter and R. Hill, Proc. 9th EC. PV. Sol. Energy Conf., Freiburg, Fed. Rep. Germany, (1989) pp.115

96. C.P. Chien, S.B. Fine, T.L. Chu, S.S. Chu, Polycryst. Thin Film Rev. Meeting, SERI, Golden, Colorado, (1984) pp.43

97. A.N.Y. Samaan, R. Noufi, A.E. Blakeslee, S.K. Deb, Proc. 7th ICTMC, Snowmass, Colorado, USA, (1986) pp.237

98. A. Saunders, A. Vecht and G. Tyrell, Proc. 7th ICTMC, Snowmass, Colorado, USA, (1986) pp.231

99. B. Schumann, C. Georgi, A. Tempel, G. Kuhn, N.V. Nam, H. Neumann and W. Horig, Thin Solid Films, 52 (1978) 45

100. M. Varela, J.L. Morenza, J. Esteve and J.M. Codina, J. Phy. D: Appl. Phys., 17 (1984) 2423

101. J.J. Loferski, C. Case, M. Kwietniak, P.M. Sarro, I. Castaner and R. Beaulieu, Appl. Surf. Sci., 22/23 (1985) 645

102. L.L. Kazmerski, M. Hallerdt and P.J. Ireland, J. Vac. Sci. & Technol., A1 (1983) 395

103. M. Varela, E. Betran, M. Manchon, J. Esteve and J.L. Morenza, J. Phys. D: Appl. Phys., 19 (1986) 127

104. J.R. Tuttle, R. Noufi and R.G. Dhere, 19th IEEE PVSC, New Orlean, USA, (1987) pp.1494

105. J.P. Roger, D. Fournier, A.C. Boccara, R. Noufi and D. Cahen, Thin Solid Films, 128 (1985) 11

106. S. Wagner, J.L. Shay and H.M. Kasper, J. de Physique, 36 (1975) C3-101

107. L.L. Kazmerski, F.R. White and G.K. Morgan, Appl. Phy. Lett. 27 (1975) 268

108. F.J. Garcia and M.S. Tomar, Jpn. J. Appl. Phy., Suppl. 22-1 (1983) 535

109. S.A. Al-Kuhaimi, and S. Bahammam, Jpn. J. Appl. Phys., 29 (1990) 1499

110. R.R. Potter, Solar Cells, 16 (1986) 521

111. R. Noufi, R.J. Matson, R.C. Powell and C. Herrington, Solar Cells, 16 (1986) 479

112. W.H. Bloss, J. Kimmerle, F. Pfisterer and H.W. Schock, Proc. 17th IEEE Photovoltaic Specialists Conference, Kissimmee, Florida, 1984 (IEEE New York 1984) pp.715

113. K.R. Murali, B.S.V. Gopalam and J. Sobhanadri, J. Mater. Sci. Lett., 5 (1986) 421

114. B. Grzeta-Plenkovic, S. Popovic, B. Celustka and B. Santic, J. Appl. Cryst., 13 (1980) 311

115. C.S. Palatnik and E.K. Belova, Izv. Akad. Nauk. SSSR, Neorg. Mat., 3 (1967) 2194

116. L.S. Lerner, J.Phys. Chem. Solids, 27 (1966) 1

117. B. Tell, J.L. Shay and H.M. Kasper, J. Appl. Phys., 43 (1972) 2469

118. L.Mandel, R.D. Tomlinson and M.J. Hampshire, J. Cryst. Growth, 36 (1976) 152

119. B. Pamplin, T. Kiyosawa and K. Nasumoto, Prog. Cryst. Growth Charac., 1 (1979) 313

120. H.G. Swamy, B.S. Naidu and P.J. Reddy, Vacuum, 41 (1990) 1445

121. I. Martil, J. Santamaria, G. Diaz and F.S. Quesada, J. Appl. Phys., 68 (1990) 189

122. K.T.R. Reddy and P.J. Reddy, Mater. Lett., 9 (1990) 227

123. H. Gopalaswamy and P.J. Reddy, Mater. Lett., 8 (1989) 415

124. I. Martil, G. Gonzalez-Diaz, J. Santamaria, M.L. Lecia, J.L. Hernadez-Rojas and F. Sanchez-Quesada, J. Mater. Sci. Lett., 19 (1990) 237

125. J.L. Annapurna and K.V. Reddy, Indian j. Pure & appl. Phys., 24 (1986) 283

126. K.T.R. Reddy and P.J. Reddy, J. Mater. Sci. Letts., 8 (1989) 110

127. J. Tuttle, D. Albin, J. Goral, C. Kennedy and R. Noufi, Solar Cells, 24 (1988) 67

128. Y.K. Kapur, B.M. Basol and E.S. Tseng, Proc. 18th IEEE PV. Spec. Conf., Las Vegas, Nevada, 1985 (IEEE Press, New York, 1986) 1429

129. B. Schumann, A. Tempel and G. Kuhn, Cryst. Res. & Technol., 18 (1983) 71

130. H. Hallak, D. Albin and R. Noufi, Appl. Phys. Letts., 55 (1989) 981

131. H. Dittrich, U. Prinz, J. Szot and H.W. Schock, Proc. 9th EC. Photovol. Solar Energy Conf., (1989) pp.163

132. B. Tell and P.M. Bridenbaugh, Phys. Rev. B 12 (1975) 3330

133. R.C. Powell, R. Noufi, C. Herrington and T. Coutts, Proc. 18th IEEE Photovolt. Spec. Conf. Las Vegas, NV, USA, (IEEE Press New York, 1986) pp.1050

134. R. Klenk, R. Menner, D. Schmid, D. Cahen and H.W. Schock, Proc. 9th EC Photovoltaic Solar Energy Conf., (1989) pp.469

135. R. Klenk, R. Menner, D. Cahen and H.W. Schock, Proc. 21st IEEE Photovolt. Spec. Conf. (IEEE Press New York, 1991) pp.481

136. K.T.R. Reddy and P.J. Reddy, Solid State Commun., 69 (1989) 693

137. I. Balberg, D. Albin and R. Noufi, Appl. Phys. Letts., 54 (1989) 1244

138. A. Kisilev, A. Jakubowicz, V. Marcu, I. Margulis and D. Cahen, J. Elec. Mater., 18 (1989) 531

139. Y. Aparna, P.S. Reddy, B.S. Naidu and P.J. Reddy, J. Mater. Sci. Letts., 10 (1991) 1258

140. D.K. Suri, K.C. Nagpal and G.K. Chadha, J. Appl. Cryst. 22 (1989) 578

141. D.K. Suri, R.H. Bhawalkar, K.C. Nagpal and G.K. Chadha, J. Mater. Sci., 26 (1991) 3191

142. D. Seuret, O. Vigil and F. Leccabue, Phys. Stat. Sol., (a) 72 (1982) 661

143. Y. Aparna, P.S. Reddy, B.S. Naidu and P.J. Reddy, Phys. Stat. Sol. (a) 125 (1991) K39

144. W.S. Chen, J.M. Steward, B.J. Stanbery, W.E. Devaney and R.A. Mickelsen, Proc. 19th IEEE Photovol. Spec. Conf., New Orleans, (1987) 1445

145. J.M. Stewart, W.S. Chen, W.E. Devaney and R.A. Mickelesen, 7th Int. Conf. Ternary & Multinery Compds. 1986 (MRS 1987) 59

146. R.W. Birkmire, L.C. Dinetta, P.G. Lasswell, J.D. Meakin and J.E. Phillips, Solar Cells, 16 (1986) 419

147. F.O. Adurodija, M.J. Carter, B. Ghosh and R. Hill, Proc. 12th EC Photovoltaic Solar Energy Conf. (1994) In Press

148. C. Guillén and J. Herrero, J. Electrochem. Soc. 141 (1994) 225

149. L.D. Laude, M.C. Joliet and C. Antoniadis, Solar Cells, 16 (1986) 199

150. B.M. Basol, V.K. Kapur and R.C. Kulberg, Solar Cells, 27 (1988) 299

151. J. Szot and U. Pring, J. Appl. Phys., 66 (1989) 6077

152. B. Dimmler, H. Dittrich and H.W. Schock, Proc. 20th IEEE PVSC (1988) 1426

153. H. Dittrich, B. Dimmler, R. Menner and H.W. Schock, Proc. 8th EC Photovoltaic Solar Energy Conf. (1988) 1102

154. L. Harris and B.M. Siegel, J. Appl. Phys., 19 (1948) 739

155. W.S. Chen and R.A. Mickelsen, SPIE, 248 (1980) 62

156. W.E. Devaney and R.A. Mickelsen, Solar Cells, 24 (1988) 19

157. B. Dimmler, H. Dittrich, R. Klenk, R.H. Mauch, R. Menner and H.W. Schock, Proc. 8th EC. Photovoltaic Solar Energy Conf., (Kluwer Academic, Dordrecht, 1988) 1583

158. J. Hedstrom, L. Stolt and M. Jargelius, Proc. 9th EC. Photovoltaic Solar Energy Conf., (Kluwer Academic, Dordrecht, 1989) 473

159. H.M. Smith and A.F. Turner, Applied Optics, 4 (1965) 147

160. J.T. Cheung and H. Sankur, CRC Critical Reviews in Solid States and Materials Sciences, 15 (1988) 63

161. J. Levoska, A.E. Hill, S. Leppävuori, O. Kusmartseva, R.D. Pilkington and R.D. Tomlinson, Jpn. J. Appl. Phys., 32, Suppl. 32-3 (1993) 43

162. A.E. Hill, S. Leppavuori, R.D. Tomlinson, R.D. Pilkington, J. Levoska, E. Ahmed and J. Frantti, MRS Symposium on laser ablation in materials Procedures Fundamentals and Applications. 1992 (Boston, USA) p.483

163. J. Levoska, S. Leppävuori, F. Wang, O. Kusmartseva, A.E. Hill, E. Ahmed, R.D. Tomlinson and R.D. Pilkington, 16th Nordic semiconductor meeting, Iceland, (1994) In Press

164. F.R. White, A.H. Clark, M.C. Gray and L.L. Kazmerski, J. Vac. Sci. Technol., 16 (1979) 287

165. H. Neumann, B. Perlt, N.A.K. Abdul-Hussain, R.D. Tomlinson and A.E. Hill, Solid State Commun., 42 (1982) 855

166. P.A. Jones, A.D. Jackson, P.D. Lickiss, R.D. Pilkington and R.D. Tomlinson, Thin Solid Films, 238 (1994) 4

167. P.A. Jones, A.D. Jackson, P.D. Lickiss, R.D. Pilkington and R.D. Tomlinson, Proc. 12th EC Photovoltaic Solar Energy Conference, Amsterdam, (1994) In Press

168. R.N. Bhattacharya, K. Rajeshwar and R. Noufi, J. Electrochem. Soc., 131 (1984) 939

169. R.R. Chamberlin and J.S. Skarman, J. Electrochem. Soc., 113 (1966) 86

170. J.E. Hill, R.R. Chamberlin, U.S. Pat., 3,148,084 (1964)

171. H. Neumann and R.D. Tomlinson, Solar Cells, 28 (1990) 301 and references therein.

172. H.H. Wieder, Ed., "Intermetallic semiconducting films", Pergamon Press, 1970

173. J. Parkes, Ph.D. Thesis, University of Salford, 1972

174. L.C. Feldman and J.W. Mayer, Eds., "Fundamentals of Surface and Thin film Analysis", North Holland Publisher, 1986

175. S.K. Freeman, Ed.,"Applications of Laser Raman Spectroscopy", John Wiley & Sons., 1974.

176. D.A. Long, Ed., "Raman Spectroscopy", McGraw Hill International, 1977.

177. W.K. Chu, J.W. Mayer and M.A. Nicolet, Eds., "Backscattering Spectroscopy", Academic Press, 1978

178. M.V. Yakushev, G. Constantinidis, M. Imanieh and R.D. Tomlinson, Solid State Commun., 65 (1988) 1079

179. J.R. Tuttle, D. Albin, R.J. Matson and R. Noufi, J. Appl. Phys., 66 (1989) 4408

180. E. Neimi and L. Stolt, ECASIA 89, Antibes, 1989

181. L.R. Doolittle, 'RUMP' user manual, 1985

182. C.W. Oatley, Scanning Electron Microscope, Cambridge University Press, Cambridge MA, 1972

183. M.T. Postek, K.S. Howard, A.H. Johnson and K.L. Macmichael, Eds., Scanning Electron Microscopy, 1980

184. H.A. Liebhafsky et al, "X-ray Absorption and Emission in Analytical Chemistry", John Wiley & Sons, Inc., N.Y, 1962

185. J.M. Bennett and L. Mattsson, Eds., "Introduction to Surface Roughness and Scattering", Optical Society of America, Washington, DC., 1989

186. M. Djamin, Ph.D. Thesis, University of Salford, 1993

187. I.E. Elfallal, Ph.D. Thesis, University of Salford, 1993

188. R.H. Bube, Ed., "Photoconductivity of Solids", John Wiley & Sons., New York, 1960

189. A. Rosenczweig, Ed., "Photoacoustics and Photoacoustic Spectroscopy", Wiley, New York, 1980

190. A. Zegadi, M.A. Slifkin, M. Djamin, R.D. Tomlinson and H. Neumann, Solid State Commun., 83 (1992) 587

191. J.J. Loferski, C. Case, M. Kwietniak, P.M. Sarro, L. Castaner and R. Beaulieu, Application of Surface Science 22/23 (1985) 645

192 H. Neumann, in Optoelectronic Materials and Devices, Ed., M.A. Herman, PWN - Polish Academy of Science, Institute of Physics (1983) p.171-187

193. B.M. Basol, Proc. 9th. Int. Conf. Ternary and Multinary Compounds, Yokohama, 1993, Jpn. J. Appl. Phys., 32 Suppl. 32-3, (1993) pp.35

194. C.A. Faunce, Personal Communication, 1994

195. C.A. Mullan, S.M. Casey, C. Jones, C.J. Kiely, M. Imanieh and R.D. Tomlinson, Materials Research Society, (1992)

196. Balzers evaporation source catalogue.

197. D. Cahen and R. Noufi, J. Phys. Chem. Solids 52, No.8, (1991) 947 and references therein.

198. R.A. Mickelson and W.S. Chen, Appl. Phys. Letts., 36 (1980) 371

199. B. Schumann, C. Georgi, A. Temple and G. Kuhn, Thin Solid Films, 74 (1980) 197

200. M.C. Artaud, F. Ouchen, S. Duchemin and J. Bougnot, Proc. 12th Euro., Photovoltaic Solar Energy Conf., Amsterdam, (1994) 658

201. K.L. Chopra, Ed. Thin Film Phenomenon, Krieger Publishing Company, New York, 1979

202. H. Neumann, R.D. Tomlinson, W. Kissinger and N. Avgerinos, Phys. Stat. Sol. (b) 118 (1983) k51

203. S. Yamanaka, M. Tanda, K. Horino, K. Ito, A. Yamada, M. Konagai and K. Takahashi, proc. 21st IEEE Photovoltaic Spec. Conf., Kissimimee, USA, 1990 (IEEE, New York, 1990) p.758

204. C. Rincon and F.J. Ramirez, J. Appl. Phys., 72 (1992) 4321

205. S. Yamanaka, A. Yamada, M. Konagai and K. Takahashi, Congress of the Int. Solar Energy Society, Pub., Pergamon Press, Oxford, 1 (1989) p.117

206. H. Tanino and H. Nakanishi, Proc. 9th Int. Conf. Ternary and Multinary Compounds, Jpn. J. Appl. Phys. 32 (1993) Suppl. 32-3, pp.436

207. H. Neumann, Personal Communication, 1994.

208. T. Hama, T. Ihara, H. Sato, H. Fujisawa, M. Ohsawa, Y. Ichikawa and H. Saki, Solar Energy Materials, 23 (1991) 380

209. R.W. Berry, P.M. Hall, M.T. Harris, Eds. "Thin Film Technology", D. Van Nostrand Co., Inc., 1968

210. J.J. Loferski, Symp. on Non-Stoichiometry in Semicond. of the Int. Conf. On Advanced Materials - ICAM - 91 Strasbourg, France, 27-31 May, 1991, Eds. K.J. Bachman, H.L. Hwang and C Schwab, (Elsevier Science Publishers, 1992) p.257

211. R.E. Rocheleau, J.D. Meakin and R.W. Birkmire, Proc. 19th IEEE Photovoltaic Spec. Conf., 1987 (IEEE, New York, 1987) pp.972

212. L. Doolittle, Nucl. Instrum. Methods B 15 (1986) 227

213. L. Stolt, J. Hedström, J. Kessler, M. Ruckh, K.O. Velthaus and H.W. Schock, Appl. Phys. Lett., 62 (1993) 597

214. M.A. Slifkin, A. Al-Rahmani, M. Imanieh, R.D. Tomlinson and H. Neumann, Cryst. Res. & Technol., 26 (1991) 109

215. F.A. Kroger, Ed., "The Chemistry of Imperfect Crystals", 2, North Holland Publ. Co. (1974)

216. R. Noufi and D. Cahen, Proc. Material Research Society Sympos., 148 (1989) 451

217. C. Rincon and C. Bellabarba, Physical Review B, (1986) 7160

218. F. Abou-Elfotouh, H. Moutinho, A. Bakry, T.J. Coutts and L.L. Kazmerski, Solar Cells, 30 (1991) 151

219. Schumann et al., Sov. Phys. Crystallog. (Engl. Transl.) 26 (1981) 678

220. Schumann et al., Joint Committee on Powder Diffraction Standard, Card No. 35-1349, 1985.

221. J. Levoska, S. Leppävuori, O. Kusmartseva, F. Wang, A.E. Hill, E. Ahmed, R.D. Tomlinson and R.D. Pilkington, Physica Scripta, (1994) In Press

222. J.F. Guillemoles, S. Massaccesi, P. Cowache, L. Thouin, S. Sanchez, D. Lincot and J. Vedel, Proc. 12th EC. Photovoltaic Solar Energy Conf., Amsterdam, 1994, In Press

223. M.H. Badawi, M. Hyland, A. Knowles, M.J. Carter and R. Hill, Proc. 10th EC Photovoltaic Solar Energy Conf., 1991, pp.883

224. H. Fujisawa, T. Ihara, H. Sato, T. Hama, M. Ohsawa, Y. Ichikawa and H. Sakai, Proc. 10th EC Photovoltaic Solar Energy Conf., 1991, pp.904

225. J.H. Ermer, R.B. Love, A.K. Khanna, S.C. Lewis and F. Cohen, Proc. 18th IEEE PVSE Conf. 1985, 1655

226. Shannon and Prewitt, J. Inorg. Nucl. Chem., 30 (1968) 1389

227. Shannon and Prewitt, Joint Committee on Powder Diffraction Standard, Card No. 21-334, 1971.

228. A. Rocket, F. Abou-Elfotouh, D. Albin, M. Bode, J. Ermer, R. Klenk, T. Lommasson, T.W.F. Russel, R.D. Tomlinson, J. Tuttle, L. Stolt, T. Walter and T. Peterson, Thin Solid Films, 237 (1994) 1

229. K.D. Becker and S. Wagner, Phys. Rev. B, 27 (1983) 5240

230. H. Neumann, E. Nowak and G. Kuhn, Cryst. Res. Technol., 16 (1981) 1369

231. P. Korpiun in "Photoacoustic Effect: Principles and Applications", Eds., E. Luscher, P. Korpiun, H.J. Coufal and R. Tilgner, Vieweg:Braunschweig, (1984) p.40

232. J.G. Parker, Appl. Opt., 12 (1973) 2974

233. A. Rosencwaig and A. Gersho, J. Appl. Phys. 47 (1976) 64

234. L.C. Aamodt, J.C. Murphy and J.G. Parker, J. Appl. Phys., 48 (1977) 927

235. F.A. McDonald and G.C. Wetsel, J. Appl. Phys., 49 (1978) 2313

236. C.C. Ghizoni, M.A.A. Siqueira, H. Vergas and L.C.M. Miranda, J. Appl. Phys., 32 (1978) 554

237. P. Poulet, J. Chambron and P. Unterreiner, J. Appl. Phys., 51 (1980) 1738

238. J. Fesquet, B. Girault and M.D. Razafindrandriatsimaniry, App. Opt., 23 (1984) 2784

239. A.C. Tan and Y.H. Wong, Appl. Phys. Lett., 36 (1980) 471

240. S. Yamasaki, H. Okushi, A. Matsuda, H. Oheda, N. Hata and K. Tanaka, Jpn. J. Appl. Phys., 20 (1981) L665

241. G. Amato, G. Benedetto, L. Boarino, M. Maringelli and R. Spagnolo, IEE Proceedings-A, 139 (1992) pp.161

242. A. Zegadi, PhD Thesis, University of Salford, 1993

243. J.I. Pankove, Optical Processing in Semiconductors (Dover, New York) 1974

244. A. Zegadi, D.M. Bagnall, A.E. Hill, M.A. Slifkin, H. Neumann and R.D. Tomlinson, 12th Euro. Photovoltaic Solar Energy Conf., Amsterdam, (1994) p.1576

245. A. Zegadi, D.M. Bagnall, A. Belattar, R.D. Pilkington, M.A. Slifkin, A.E. Hill and R.D. Tomlinson, Thin Solid Films, 226 (1993) 248

246. T. Tinoco, C. Rincon, M. Quintero and G. Sanchez-Perez, Phys. Stat. Sol. (a), 124 (1991) 427

247. W. Horig, W. Moller, H. Neumann, E. Reccius and G. Kuhn, Phys. Stat. Sol. (b), 92 (1979) K1

248. J.I. Pankove and N.M. Johnson, (Eds.) Hydrogen in Semiconductors 34 Academic Press, 1966

249. M.V. Yakushev, R.D. Tomlinson, H. Neumann, Cryst. Res. Technol. 29 (1994) 125

250. R.D. Tomlinson, Personal Communication, 1991.

251. I.V. Bodnar, A.P. Bologa and B.V. Korzun, Phys. Stat. Sol., 109 (1982) K31

252. G. Antonioli, S. Bini, P.P. Lottici and C. Razzett, J. De Physique, Colloque C8, 47 (1986) C8-431

253. B. Abid, J.R. Gong, H.G. Goslowsky and K.J. Bachmann, Proc. 19th IEEE Photovoltaic Spec. Conf., IEEE, New York, (1987) p.1305

254. D.S. Albin, J.J. Carapella, J.R. Tuttle and R. Noufi, Annual Report, NREL, USA, 1993

255. H.W. Schock, Proc. 12th Euro. Photovoltaic Solar Energy Conf., Amsterdam, (1994) p.944

256. T. Walter and H.W. Schock, Thin Solid Films, 224 (1993) 74

257. I.W. Boyd, Ed. Laser Processing of Thin Films and Microelectronics, Springer - Verlag Berlin, Heidelberg, New York, 1987

258. A.L. Li, I. Shih, J. Electron Mater., 22 (1993) 195

259. M. Igalson and R. Bacewicz, Proc. 11th E.C. Photovolt. Solar Energy Conf., Montreux, 1992, p.874

260. H. Neumann in Verbindungshalbleiter, Ed. K. Unger and H.G. Schneider Leipzig, 1986, p.392

261. S. El-Halawany, R. Bacewicz, J. Filipowicz, R. Trykozko, Phys. Stat. Sol., (a) 84 (1984) K89

262. C.X. Qiu, I. Shih, J. Appl. Phys., 64 (1988) 758

263. S.M. Sze, VLSI Technology, McGraw-Hill, New York, 1983.

264. R.D. Tomlinson, A.E. Hill, G.A. Stephens, M. Imanieh, P.A. Jones, R.D. Pilkington, P. Rimmer, M.V. Yakushev and H. Neumann, Proc. 11th EC. Photovoltaic Solar Energy Conf., Montreux, 1992, p.791

265. S.J. Pearton, J.W. Corbett and M.J. Stavola, Hydrogen in Crystalline Semiconductors, Springer, Berlin, Heidelberg, New York, 1991

266. M.V. Yakushev, H. Neumann, R.D. Tomlinson, P. Rimmer, and G. Lippold, Cryst. Res. Technol., 29 (1994) 417

267. H. Neumann, W. Horig, V. Savelev, J. Lagzdonis, B. Schumann and G. Kuhn, Thin Solid Films, 79 (1981) 167

268. K. Kuriyama and J. Saitoh, Thin Solid Films, **111** (1984) 331

269. H. Neumann and E. Nowak, Thin Solid Films, **102** (1983) 201

270. F. Abou-Elfotouh, D.J. Dunlavey, D. Cahen, R. Noufi, L.L. Kazmerski and K.J. Bachmann, Prog. Cryst. Growth Charact., **10** (1984) 365

271. R.D. Tomlinson, A.E. Hill, M. Imanieh, R.D. Pilkington, A. Roodbarmohammadi, M.A. Slifkin and M.V. Yakushev, J. Elect. Mater., **20** (1991) 659

272. R. Trykozko, R. Bacewicz and J. Flipowicz, Sol. Cells, **16** (1986) 351

273. R.H. Bube, Ed. Photoelectronic Properties of Semiconductors, Cambridge University Press, 1992

274. A. Sh. Abdinov and V.K. Mamedov, Fiz. Tekh. Poluprov., **14** (1980) 892

275. P. Migliorato, J.L. Shay, H.M. Kasper and S. Wagner, J. Appl. Phys., **46** (1975) 1777

276. G. Masse and E. Redjai, J. Appl. Phys., **56** (1984) 1154

# Appendices

# Appendix A

## Cleaning of substrates

Prior to any deposition of thin films, the glass slides underwent a cleaning procedure. This cleaning process is necessary to avoid contamination of the films and to improve the film adhesion with the glass slide. In this process, the glass slides were placed in a special holder inside the glass flask which can hold four slides of 3"x1" size. The flask was then filled with a 5% solution of Decon 75 in de-ionized water and placed in an ultrasonic bath for 15 to 20 minutes. The slides were then removed from the flask and rinsed out several times with fresh running water followed with de-ionized water. A stream of pure dry nitrogen from a liquid nitrogen boiler was passed through another glass flask containing the water rinsed glass slides. The flask was placed in a bath of hot water so that slides should not break due to the condensation. The dried slides were then removed from the flask and used as the substrates for the deposition of CIS and CIGS thin films.

## Appendix B

In the photoconductivity characterisation of CIS and CIGS samples both in thin film and single crystal form, the following BBC control software was used.

The main programme to run the photoconductivity equipment.

```
10    REM***********************************************************
20    REM***                          MENU                        ***
30    REM***********************************************************

40    MODE 0
50    PRINT TAB(20,3)   "--------------------------------------------------------"
60    PRINT TAB(25,4)     "PHOTOCONDUCTIVITY INTERFACE MENU"
70    PRINT TAB(20,5)   "--------------------------------------------------------"
80    PRINT TAB(25,8)   "1.   Collect data from PC apparatus."
90    PRINT TAB(25,11)  "2.   Normalise data."
100   PRINT TAB(25,14)  "3.   Retrieve and plot file."
110   PRINT TAB(25,17)  "4.   Convert to ASCII file."
120   PRINT TAB(25,20)  "5.   Send file to IBM PC."
130   PRINT TAB(25,23)  "6.   Retrieve and plot normalised file."
140   PLOT 4,200,950
150   PLOT 5,1150,950
160   PLOT 5,1150,200
170   PLOT 5,200,200
180   PLOT 5,200,950
190   PRINT TAB(30,30)  "Select option and return"
200   INPUT TAB(56,30)  A
210   IF A=1 THEN CHAIN "COLLECT"
220   IF A=2 THEN CHAIN "NORM"
230   IF A=3 THEN CHAIN "AXIS"
240   IF A=4 THEN CHAIN "STASC"
250   IF A=5 THEN CHAIN "BEEB20P"
260   IF A=6 THEN CHAIN "NAXIS"
270   PRINT TAB(30,30)  "Not a valid option!"
280   GOTO 200
290   CLEAR
300   MODE 0
310   END
```

Subroutine to collect data from the photoconductivity equipment

```
10   REM************************************************************
20   REM***                    COLLECT DATA                      ***
30   REM************************************************************

40   MODE 0
50   DIM S(800)
60   PRINT      "Enter starting wavelength (nm)."
70   INPUT L1
80   PRINT      "Put monochromator on ";L1/2;" , then press return."
90   INPUT Z$
100  VSTA=ADVAL(2)
110  PRINT      "Rewind a little, start motor and press return."
120  INPUT Z$
130  CLS
140  PRINT TAB(0,0)     "Press S to end."
150  IF ADVAL(2)>VSTA THEN GOTO 150
160  N=0
170  LET T=TIME
180  A=ADVAL(2)
190  B=ADVAL(1)
200  R=B/4161
210  V=A/36409
220  X=1240-(V*1000)
230  V=R*80+50
240  S(N)=R
250  PLOT 69,X,Y
260  IF INKEY$(0)="S" THEN GOTO 310
270  IF V<0.1 THEN L2=1600: GOTO 310
280  IF TIME<T+100 THEN GOTO 280
290  LET T=TIME
300  N=N+1: GOTO 180
310  PRINT "Enter finishing value on monochromator."
320  INPUT L2:L2=L2*2
330  INPUT "Name of the file to be stored?" Z$
340  X=OPENOUT Z$
350  PRINT£ X,N,L1,L2
360  FOR W=0 TO N
370  PRINT£X,S(W)
380  NEXT W
390  CLOSE£X
400  MODE 0
410  CLEAR
420  CHAIN "MENU"
```

Subroutine to normalise the collected data from the photoconductivity equipment.

```
10    REM***********************************************************
20    REM***                        NORM                         ***
30    REM***********************************************************

40    MODE 0
50    INPUT      "Name of file to be normalised" Z$
60    INPUT      "Name of normalisation file" Y$
70    CLS
80    X=OPENIN Z$
90    INPUT£X,NZ,L1Z,L2Z
100   CLOSE£X
110   X=OPENIN Y$
120   INPUT£X,NY,L1Y,L2Y
130   CLOSE£X
140   IF NY<NZ THEN N=NY ELSE N=NZ
150   DIM S(N)
160   X=OPENIN Z$
170   INPUT£X,NZ,L1Z,L2Z
180   FOR F=0 TO N
190   INPUT£X,S(F)
200   PRINT TAB(0,0)     "LOADING "F"/"N"  "
210   NEXT F
220   CLOSE£X
230   X=OPENIN Y$
240   INPUT£X,NY,L1Y,L2Y
250   CLS
260   FOR F=0 TO N
270   PRINT TAB(0,0)     "Normalising "F"/"N"  "
280   INPUT£X,PV
290   WL=L1Y+((L2Y-L1Y)*F/N)
300   SS=((3/40)*WL)-12.5
310   S(F)=S(F)/(PV*SS)
320   NEXT F
330   CLOSE£X
340   INPUT      "Normalise to 100% of max signal? (Y/N) "Q$
350   CLS
360   IF Q$="N" THEN GOTO 480
370   IF Q$="Y" THEN GOTO 380 ELSE GOTO 340
380   M=0
390   INPUT      "Select value of N  "A
400   CLS
410   FOR F=A TO N
420   IF S(F)>M THEN M=S(F)
430   NEXT F
440   FOR F=0 TO N
450   S(F)=S(F)*100/M
```

```
460    NEXT F
470    CLS
480    X$=Z$+"N"
490    PRINT        "Saving as "X$
500    X=OPENOUT X$
510    PRINT£X,N,L1Y,L2Y
520    FOR F=0 TO N
530    PRINT£X,S(F)
540    NEXT F
550    CLOSE£X
560    CLS
570    CHAIN "MENU"
```

Subroutine to convert photoconductivity data into an ASCII format.

```
10     REM***********************************************************
20     REM***                   STASC                             ***
30     REM***********************************************************

40     MODE 0
50     PRINT TAB(22,9)   "Enter name of file to be converted."
60     INPUT TAB(40,12) Z$
70     Y$=Z$+"A"
80     CLS
90     PRINT TAB(20,9)   "ASCII file will be stored as ";Y$
100    VDU 23,1,0;0;0;0;
110    PRINT TAB(26,13)  "Loading data"
120    X=OPENIN Z$
130    INPUT£X,N
140    CLOSE£X
150    DIM S(N+3)
160    X=OPENIN Z$
170    FOR W=0 TO (N+3)
180    INPUT X,I
190    S(W)=INT(I*10000+0.5)
200    PRINT TAB(41,13) W;"/";N+3
210    NEXT W
220    CLOSE£X
230    PRINT TAB(20,9)   "ASCII file will be stored as ";Y$
240    PRINT TAB(26,13) "Storing data"
250    X=OPENOUT Y$
260    FOR W=0 TO (N+3)
270    V$=STR$(S(W))
280    FOR D=1 TO LEN(V$)
290    F=ASC(MID$(V$,D,1))
300    BPUT£X,F
```

```
310    NEXT D
320    BPUT£X,13
330    BPUT£X,10
340    PRINT TAB(41,13) W;"/";N+3
350    NEXT W
360    CLOSE£X
370    VDU 23,1,1;0;0;0;
380    CLS
390    PRINT TAB(26,9) "Conversion is complete."
400    FOR N=0 TO 4000:NEXT N
410    CLS
420    PRINT TAB(29,9) "Returning to menu."
430    FOR N=0 TO 4000;NEXT N
440    CHAIN"MENU"
450    END
```

Subroutine to plot the photoconductivity data on the BBC computer screen.

```
10     REM***********************************************************
20     REM***                    AXIS                             ***
30     REM***********************************************************

40     MODE 0
50     VDU 28,2,3,78,0
60     GOSUB 290
70     PRINT TAB(0,0) "Press P to plot data.  Press M to return to menu."
80     VDU 23,1,0;0;0;0;
90     CLEAR
100    PRINT TAB(0,1) "Press C to replot axis."
110    A$=INKEY$(0)
120    IF A$="M" THEN CHAIN "MENU"
130    IF A$="P" THEN GOTO 160
140    IF A$="C" THEN GOTO 40
150    GOTO 110
160    CLS:PRINT TAB(0,1) "Enter name of data file to be plotted."
170    VDU 23,1,1;0;0;0;
180    INPUT TAB(0,2) Z$
190    VDU 23,1,0;0;0;0;
200    GOSUB 620
210    GOSUB 520
220    PRINT "HARD COPY? Y/N":N$=GET$:CLS
230    IF N$="Y" THEN GOTO 77
240    GOTO 70


250    REM***********************************************************
```

```
260   REM***                    SUBROUTINE                    ***
270   REM**********************************************************
280   REM***                    DRAW AXIS                     ***
290   REM**********************************************************

300   VDU 5
310   PLOT 4,100,820
320   PLOT 5,100,100
330   PLOT 5,1250,100
340   FOR W=0 TO 100 STEP 20
350   PLOT 4,90,W*6+100
360   PLOT 5,100,W*6+100
370   PLOT 4,-80,W*6+115
380   PRINT W
390   NEXT W
400   PLOT 4,70,880
410   PRINT "S(N)"
420   FOR W=0 TO 1600 STEP 400
430   PLOT 4,W/1.4-100,100
440   PLOT 5,W/1.4-100,90
440   PLOT 4,W/1.4-240,80
450   PRINT W
460   NEXT W
470   PLOT 4,600,40
480   PRINT "Wavelength (nm)"
490   VDU 4
500   RETURN
510   END

520   REM**********************************************************
530   REM***                    PLOT DATA                     ***
540   REM**********************************************************

550   FOR W=0 TO N
560   Y=S(W)
570   X=(L1+W*(L2-L1)/N)
580   PLOT 69,X/1.4-100,Y*6+100
590   NEXT W
600   RETURN
610   REM

620   REM**********************************************************
630   REM***                    READ DATA                     ***
640   REM**********************************************************

650   CLS
660   PRINT TAB(0,1) "Loading data"
670   G=OPENIN Z$
```

```
680    INPUT£G,N,L1,L2
690    DIM S(N)
700    FOR W=0 TO N
710    INPUT£G,S(W)
720    PRINT TAB(15,1) W;"/";N
730    NEXT W
740    CLOSE£G
750    RETURN
760    END
770    VDU 2
780    *RUN "PLOT"
790    VDU 3
800    GOTO 40
```

Programme to send the ASCII format data from BBC to personal computer.

```
10     REM**********************************************************
20     REM***                     BEEB20P                        ***
30     REM**********************************************************

40     MODE 0
50     INPUT TAB(22,11) "Name of file to be sent",F$
60     CLS
70     PRINT TAB(12,11) "Enter read B:\Filename.ASC A and Return (PC)"
80     PRINT TAB(22,14) "Press R when ready"
90     A$=INKEY$(0):IF A$="R" THEN GOTO 100 ELSE GOTO 90
100    CLS
110    PRINT TAB(22,11) "Data being transferred."
120    H=OPENIN(F$)
130    *FX7,7
140    *FX8,7
150    *FX21,2
160    *FX3,7
170    *FX5,2
180    *FX6,0
190    REPEAT
200    IF EOF£H THEN 250
210    A=BGET£H
220    PRINT CHR$(A);
230    UNTIL EOF£H
240    PRINT CHR$(&1A)
250    CLOSE£0
260    *FX3,0
270    CLS
280    PRINT TAB(22,11) "Returning to main menu."
290    FOR N=0 TO 5000:NEXT N
300    CHAIN "MENU"
```

# Appendix C

During this study, the following work was published.

1. E. Ahmed, A.E. Hill, R.D. Pilkington and R.D. Tomlinson, "Growth and Annealing of $CuIn_{0.75}Ga_{0.25}Se_2$ Thin Films" J. Phys. D: Appl. Phys., 26 (1993) 1787

2. E. Ahmed, A.E. Hill, R.D. Pilkington, R.D. Tomlinson and W. Ahmed, "$CuIn_{0.75}Ga_{0.25}Se_2$ Thin Films for Photovoltaic Applications", Proc. 3rd Int. Symp. Advanced Materials, Islamabad, Pakistan., (1993) p.475

3. A.E. Hill, S. Leppävuori, R.D. Tomlinson, R.D. Pilkington, J. Levoska, E. Ahmed and J. Frantti, "Laser Ablation of $CuInSe_2$ and CuIn/$GaSe_2$ Alloys for Solar Cell Applications" MRS Symposium Proceedings, Eds. B. Braren, J.J. Dubowski and D.P. Norton, "Laser Ablation in Materials Processing: Fundamentals and Applications, MRS Fall meeting, 1-4 Dec. 1992, Boston, Massachustes, USA 285 (1992) p.483

4. A. Zegadi, A. Belattar, C.A. Faunce, E. Ahmed, S. Anwar, M.V. Yakushev, M. Imaneih, M.A. Slifkin, A.E. Hill and R.D. Tomlinson, "An Electron Microscope Study of Near-Surface Damage Caused by Xe and Ne Ion-implantation in $CuInSe_2$ Single Crystals", Nucl. Instr. Methods B, 94 (1994) 429

5. E. Ahmed, A.E. Hill, S. Leppävuori, R.D. Pilkington, R.D. Tomlinson, J. Levoska and O. Kusmartseva, "A Comparative Study of Pulsed Laser Deposition and Flash Evaporation of $CuIn_{0.75}Ga_{0.25}Se_2$ Thin Films", Advanced Mater. for Optics & Elec., 4 (1994) 423

6. J. Levoska, S. Leppävuori, F. Wang, O. Kusmartseva, A.E. Hill, E. Ahmed, R.D. Tomlinson and R.D. Pilkington, "Pulsed Laser Ablation Deposition of $CuInSe_2$ and $CuIn_{1-x}Ga_xSe_2$ Thin Films", Physica Scripta, T54 (1994) 244

7. S. Leppävuori, A.E. Hill, J. Levoska, E. Ahmed, R.D. Pilkington and R.D. Tomlinson, "Copper Indium Diselenide Single Crystal and Thin Film Infra-Red Sensors", J. Sensors & Actuators, (1994) Accepted

8. A. Zegadi, M.V. Yakushev, E. Ahmed, M.A. Slifkin, A.E. Hill and R.D. Tomlinson, "The effect of Se content on defect levels of $CuInSe_2$ Single Crystals detected by Photoacoustic Spectrometry", Proc. $1^{st}$. World Conference on Photovoltaic Energy Conversion, Dec. 5-9 1994 Hawaii, USA.

9. E. Ahmed, A. Zegadi, A.E. Hill, R.D. Pilkington and R.D. Tomlinson, "Optical Properties of Flash Evaporated $CuIn_{0.75}Ga_{0.25}Se_2$ Thin Films", Thin Solid Films, (1994). Submitted

10. E. Ahmed, A. Zegadi, A.E. Hill, R.D. Pilkington and R.D. Tomlinson, "Non-Destructive Characterisation of Defect Levels in $Cu(In,Ga)Se_2$ Compounds", 4th Int. Symp. Advanced Materials, Islamabad, Pakistan (1995). In preparation

# PUBLISHED PAPERS NOT FILMED FOR COPYRIGHT REASONS

Pocket End of Book